Lawrence Berkeley Laboratory

UNIVERSITY OF CALIFORNIA

Materials Sciences Division

Surface Structure Determinations of Ordered Sulfur
Overlayers on Mo(100) and Re(0001) by Low-Energy
Electron Diffraction Intensity Analysis

D.W. Jentz
(Ph.D. Thesis)

November 1992

DISCLAIMER

DISCLAIMER

Surface Structure Determinations of Ordered Sulfur Overlayers

on Mo(100) and Re(0001) by Low-Energy

Electron Diffraction Intensity Analysis

by

David William Jentz

B.S. (Purdue University) 1987

A dissertation submitted in partial satisfaction of the

requirements for the degree of

Doctor of Philosophy

in
Chemistry

in the

GRADUATE DIVISION

of the

UNIVERSITY of CALIFORNIA at BERKELEY

Committee in charge:

Professor Gabor A. Somorjai, Chair
Professor K. Birgitta Whaley
Professor Steven G. Louie

1992

Surface Structure Determinations of Ordered Sulfur Overlayers
on Mo(100)and Re(0001) by Low-Energy
Electron Diffraction Intensity Analysis

by

David William Jentz

ABSTRACT

The surface structure of ordered sulfur overlayers on Mo(100) and Re(0001) was determined by low-energy electron diffraction (LEED) intensity analysis. A newly developed method for surface structure determination, tensor LEED, combined with an automated search was used to analyze the structures presented. The structures on Mo(100) were prepared by depositing sulfur from an electrochemical source and annealing at the appropriate temperature. The structures on Re(0001) were prepared by H_2S adsorption and subsequent dissociation to S and H_2 by annealing the sample at the appropriate temperature. The LEED intensity versus energy (I-V) curves were acquired with a video camera interfaced with a personal computer. The video camera and video processor are discussed in detail. The computer programs used for the data acquisition and analysis are listed in the appendix.

The ordered structures of sulfur on Mo(100) which were studied formed a c(2x2), c(4x2), and p(2x1) periodicities at coverages of 0.5, 0.75, 1.0 ML (monolayers, where 1.0 ML is defined as one sulfur atom per one molybdenum atom) respectively. A Mo_2S-like overlayer, which formed at coverages greater than 1.0 ML, is also discussed. The calculations for the c(2x2) structure gave a best fit geometry with the sulfur adsorbed in a four-fold symmetric hollow site and the second layer buckled by 0.09Å. The S-Mo bond length is 2.45Å and the Pendry R-factor is 0.21. The preliminary calculations for the c(4x2) structure did not yield an acceptable fit. The three models which were tried are discussed. The calculations for the p(2x1) data did not yield an acceptable geometry

either. The five different types of models that were tried are discussed. The implications of this analysis are discussed along with the results of a scanning tunneling microscopy (STM) investigation.

The ordered structures on the Re(0001) surface which were studied have p(2x2) and (2√3x2√3)R30° periodicities and occurred at sulfur coverages of 0.25 and 0.5 ML (where 1.0 ML is defined as one sulfur atom per one rhenium atom) respectively. The best fit structure for the p(2x2) structure has the sulfur adsorbed in a three-fold hollow hcp site and exhibits a buckling of the first and second Re layers. The first layer is buckled by 0.05Å and the second layer is buckled by 0.06Å. The Re-S bond length is 2.32Å and the Pendry R-factor is 0.21. The preliminary results of the dynamical LEED investigation of the (2√3x2√3)R30° structure show reasonable agreement with a model with a six sulfur atom basis.

The theoretical methods used in the calculations are discussed briefly. Also, a review of clean reconstructed Mo(100), H/Mo(100), O/Mo(100), and S/Mo(100) is presented.

Acknowledgements

I would like to thank Gabor Somorjai, my research advisor, who provided me with the opportunity to work in his research group. He has drawn together a rather large and diverse group of graduate students, post-docs, and visiting scientists from all over the world. The international character of the group is an aspect which I have always liked and which has enriched me professionally as well as personally. Most important of all, he taught me to moderate my perfectionistic tendencies with a "get the job done" attitude. For this I am eternally grateful. I would also like to thank Michel Van Hove for always taking the time to answer my questions regarding LEED theory, LEED calculations, surface science, and more general topics. In addition, he was very helpful in suggesting structural models for the tensor LEED analyses that I carried out and in interpreting the results of those calculations. I am deeply indebted to him for taking the time to carefully read and correct one of the later versions of this thesis.

Although many people contributed to my education in experimental surface science, a few stand out among the rest. I must first express my appreciation to Hiroko Ohtani who introduced me to ultra-high vacuum (UHV) technology and surface science techniques. I am extremely grateful to Ian Harrison and Istvan Boszormenyi for aiding me in my struggle to resurrect the video LEED chamber which seemed more of a historical oddity than a vessel in which to conduct research. I must also thank Bob Hwang who helped me set up the video LEED data acquisition system and Chang-min Kim who taught me how to orient, cut, and polish single crystals.

On the theory side of things, I would like to thank Philip Rous for answering my naïve questions about LEED theory. I am indebted to Adrian Wander who tolerated my persistent and often unrelenting barrage of questions concerning the tensor LEED calculations. I must also thank Angelo Barbieri for his helpful and stimulating discussions

about tensor LEED and his suggestions regarding accurate surface structure determinations.

I would like to express my appreciation to Jim Dunphy and Philipe Sautet for their stimulating discussions about the S/Mo(100) system, particularly the Mo(100)-c(2x2)-S structure. I am especially appreciative of Jim Dunphy for acquiring and providing the STM images of the Mo(100)-c(4x2)-3S structure which are presented in Chapter 6.

I am thankful for the support of the technical staff at LBL during my first three years. In particular, I would like to thank Bob Yberra who in addition to fixing my electronic equipment tried to help me understand the workings of my electronics. I would also like to express my appreciation for the support of the technical staff on campus during my last two years. I rarely found them to be discourteous. I would like to thank all the guys in the machine shop for the fast turnaround time and their pleasant demeanors. In addition, I would like to thank Tom Giannotti in the campus electronic shop for repairing my electronic equipment and for occasionally accompanying Glenn Jernigan and me for a few beers at a local "establishment".

I would like to thank all those who made the campus a delightful place to work - Hiroko Ohtani, Istvan Boszormenyi, Ian Harrison, Pedro Nascente, and Glenn Jernigan. I will include Nick Materer, even though he was a "hill person", who was often all too willing to come down to campus to go to dinner and have an interesting discussion about LEED or life in general. As for Glenn, I can never repay the debt that I have incurred in these last four months. I could not have possibly completed this thesis without his helpful critique of the early drafts and comments on the figures.

I would like to thank my parents and sisters for being supportive and understanding that I have been very busy, particularly in the past year, and did not always have the time to participate in family gatherings. Last though not least, I would like to

thank my brother, Brian, for allowing me to borrow his computer so that I could finish my thesis while I was in Chicago.

Table of Contents

Table of Figures

Table of Tables

I.   The LEED Technique

Chapter 1.   The LEED Experiment

1.1. Introduction

Most investigators who study single crystal surfaces under ultra-high vacuum (UHV) use low-energy electron diffraction (LEED) to determine how well ordered their surface is. They use LEED in a very qualitative way, extracting information about the reciprocal lattice. However, a great deal of quantitative information can be obtained from the study of LEED intensities, for instance the local bonding geometry, bond lengths, adsorption sites, etc.. The difficulty of LEED intensity analysis lies in the need for a theory which adequately treats the multiple scattering processes which can not be neglected. A full multiple scattering LEED theory was developed in the late 1960's and early 1970's and more than 150 structure determinations have been performed since that time. The calculations required large mainframe computers and were typically carried out by theoretical physicists. The community of surface scientists who were involved in either the theoretical or experimental side of surface structure determination by LEED intensity analysis was small. After twenty some years since the first surface structure calculations were performed, LEED calculations are becoming accessible to a larger group of surface scientists. This is due mostly to a recent advance in LEED theory - tensor LEED. This method is relatively fast and has the advantage that it can run on a computer work station. Now LEED calculations no longer have to be performed on supercomputers and more importantly the programs have become more general and easier to use. So probably in the future more experimentalists will attempt to analyze their data with the tensor LEED programs.

The LEED experiment involves bombarding a highly ordered surface with a monoenergetic beam of electrons and detecting the elastically back scattered electrons, typically, with a fluorescent screen. Position-sensitive electron counters have also been used to study electron beam sensitive overlayers and insulating surfaces [1.1]. The diffracted electrons exit a highly ordered surface in well defined directions. These beams, as they are often called, strike the detector causing the phosphor to fluoresce; thereby forming a diffraction pattern on the fluorescent screen. The symmetry and shape of the diffraction pattern and the diffraction spot intensities contain detailed information about the long range order and the local bonding geometry of adsorbates on the surface. In addition to atomic and molecular adsorbates, clean reconstructed surfaces of transition metals and semiconductors also can be studied with this technique.

To analyze the intensities of the diffraction spots of a LEED pattern requires a device, a video camera in our case, which can measure the intensity of each diffraction spot in the LEED pattern that is displayed on a conventional LEED optics. In video LEED the entire LEED pattern is imaged and recorded at each energy. An intensity vs. energy (I-V) curve is generated by measuring the intensity of each beam in the LEED pattern as a function of incident electron beam energy. These experimental I-V curves are compared to I-V curves which have been calculated for various model geometries. The model which gives the best fit of the experimental data is taken as the correct surface structure.

This work attempts to explain the current developments in video data acquisition of LEED I-V data and the subsequent analysis with a tensor LEED program which has been run successfully on a work station.

1.2. Apparatus

1.2.1. LEED Optics

The LEED apparatus used in this work was a conventional Varian four-grid LEED optics which is illustrated in Figure 1.1. It is a retarding field analyzer (RFA) which can also be used as a detector for Auger electron spectroscopy (AES). It consists of four concentric hemispherical grids and a fluorescent screen. Each of the grids and the screen have a hole in its center to allow the electron-gun drift tube to be inserted. The first grid is grounded internally to create a virtually field free region between the sample and the detector. The second and third grids are electrically connected. The purpose of these two grids is to provide a homogeneous electric field. The bias applied to the second grid is
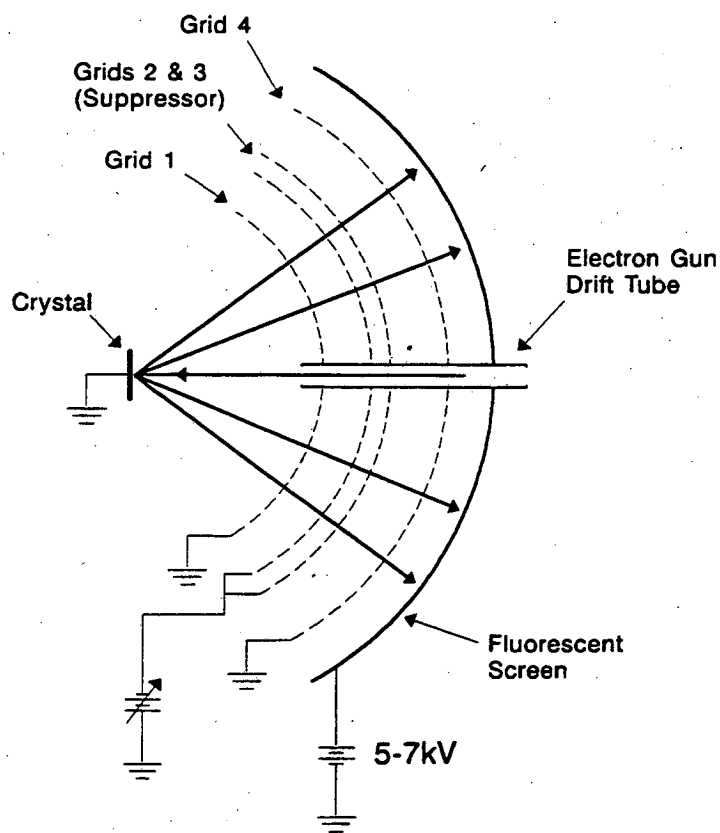
Figure 1.1   Schematic of LEED optics

called the suppressor voltage and it is negative with respect to the electron gun cathode. The suppressor prevents secondary electrons and electrons which have lost energy through other loss mechanisms from reaching the fluorescent screen. This assures that only elastically scattered electrons will make it to the fluorescent screen. However, in practice the elastic peak is asymmetric with a larger tail on the low energy side. Most of the electrons from the entire elastic peak are allowed to pass through the second and third grids. The fourth grid is grounded to prevent field penetration of the high bias on the screen. The fourth grid is more important for AES because it prevents AC coupling between the third grid and the screen. The screen is biased, 5-7 kV, to accelerate the electrons to high enough velocities such that the diffraction beams are visible.

Magnetic fields and electrostatic fields are a concern for experiments with low energy electrons. Magnetic fields from the ion pumps and the earth's magnetic field are potential sources of problems. Insulators near the crystal which cross the plane of the crystal will typically charge up and make the experiment difficult to impossible. The magnetic fields may be dealt with in one of two ways - a set of Helmholtz coils or µ-metal shielding. Mu metal is an alloy with a nominal composition of 77.2% nickel, 14.9% iron, 4.8% copper, and 1.5% chromium and has a high magnetic permittivity if it is properly annealed [1.2]. In the UHV system used in this work a piece of µ-metal surrounded the sample and another surrounded the LEED optics. The effectiveness was questionable because the LEED patterns below 60 eV appeared to have a different angle of incidence based on the I-V work. For this reason all data were acquired above 60 eV where the effect was not observed.

1.2.2. Electron Gun

The electron gun used in these LEED experiments was a Varian off-axis electron gun. The filament assembly is mounted 13° off the gun's main axis [1.3]. This very

effectively reduces the amount of light, emitted by the W filament, that is able to exit from the electron-gun drift tube. The electrons are deflected onto the gun's main axis after they pass through the anode. The beam voltage is the difference in potential between the cathode and the anode. Both the cathode and sample are at earth ground during the experiment. Thus, the beam energy is measured with respect to the Fermi level of the sample.

1.3. Diffraction Patterns

1.3.1. Lattice and Basis

The two dimensional periodicity of a surface may be characterized by a periodic array of points which possesses translational symmetry. The unit cell is a collection of lattice points which has the property of translational symmetry. Associated with each lattice point is the *basis*. The basis specifies the atom or group of atoms associated with each lattice point. *Lattice* and *basis* together define the physical geometric structure of the crystal. In Figure 1.2, an example of the distinction between lattice and basis is shown.

A diffraction pattern provides information about long range order present in the crystal. From the diffraction pattern, the symmetry and dimensions of the unit cell can be determined. Diffraction spot intensities provide information about the *basis*, the contents of the unit cell. Once the lattice and the basis are both determined the geometrical structure of the crystal, or in this case the surface, has been solved.

Translational symmetry means that translating the lattice along any linear combination of the unit cell vectors will bring the lattice points into coincidence much like a point group symmetry. Mathematically this is expressed as

6
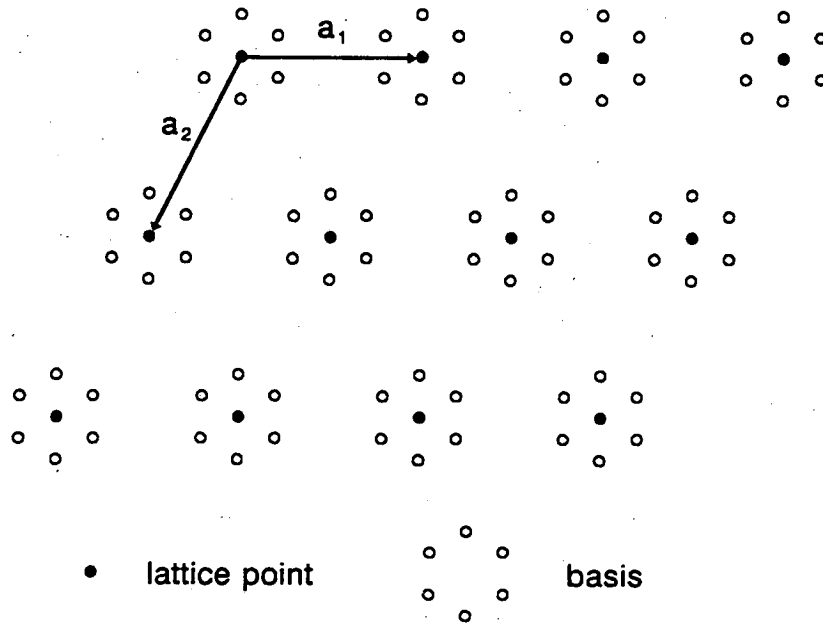
Figure 1.2   Schematic which illustrates the difference between lattice and basis

$$T = n\mathbf{a}_1 + m\mathbf{a}_2 , \tag{1.1}$$

where $\mathbf{a}_1$ and $\mathbf{a}_2$ are lattice vectors and n and m are integers.

Aside from translational symmetry a perfect surface has a point group symmetry associated with it. Most symmetry operations that are possible for the bulk apply to the surface, e.g. rotation, reflection, and glide. The notable exception is a screw axis symmetry operation. Each rotation axis, reflection plane, or glide plane must be perpendicular to the surface to be a valid symmetry element of the surface. Five surface Bravais net unit cells are possible given the constraints imposed by the translational symmetry and the point group symmetry.

An ordered surface has two lattice vectors which define the periodicity of the surface. The following vector relationships relate the reciprocal lattice vectors to the direct lattice vectors

$$\mathbf{a}_1^* = 2\pi \left[\frac{\mathbf{a}_2 \times \mathbf{n}}{\mathbf{a}_1 \cdot (\mathbf{a}_2 \times \mathbf{n})} \right], \tag{1.2}$$

$$\mathbf{a}_2^* = 2\pi \left[\frac{\mathbf{n} \times \mathbf{a}_1}{\mathbf{a}_2 \cdot (\mathbf{n} \times \mathbf{a}_1)} \right], \tag{1.3}$$

7

Direct Lattice   Reciprocal Lattice

(a)

(b)
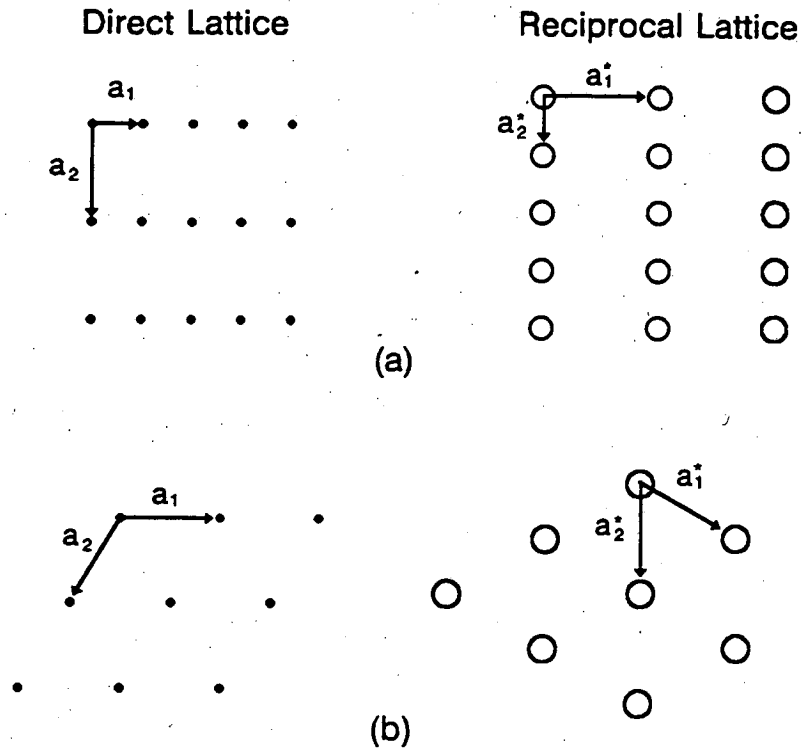
Figure 1.3   Comparison of direct lattice with reciprocal lattice. The direct
lattice is on the left hand side and the reciprocal lattice is on the right hand side
for a) rectangular net and b) hexagonal net.

where n is a unit vector parallel to the surface normal. Remember that $a_1 \cdot (a_2 \times n) = a_2 \cdot (n \times a_1) = A$, where A is the area of the unit cell. The unit cell area, A, is not a vector quantity so the cross product in the numerator determines the direction of the reciprocal lattice vectors. Notice that the cross product rotates a_2 90° clockwise and rotates a_1 90° counterclockwise. In addition, the magnitude of each reciprocal lattice vector is inversely proportional to its direct lattice vector. See Figure 1.3 for two examples of direct lattices and their corresponding reciprocal lattices. In general, a reciprocal lattice vector , g, is defined as

$$g \equiv h a_1^* + k a_2^*,$$
(1.4)

where h and k are integers.

Figure 1.4   Schematic of diffraction from an ordered surface
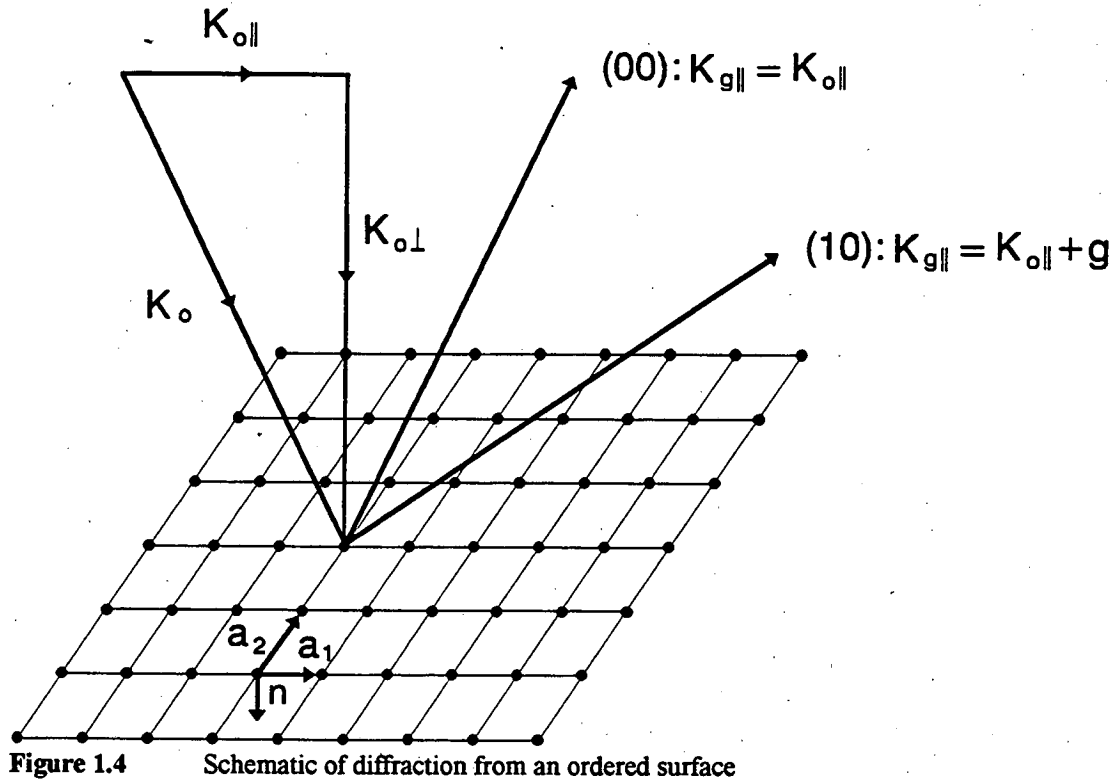
In Figure 1.4 a general case of diffraction is illustrated. A plane wave with wavevector, $\mathbf{K}_o$, is diffracted by the ordered surface. Parallel momentum is conserved, that is

$$\mathbf{K}_{g\parallel} = \mathbf{K}_{o\parallel} + \mathbf{g} \,. \tag{1.5}$$

If $g=0$, $(hk)=(00)$, then the electrons are scattered into the specular direction. Note that $\mathbf{K}_{g\parallel}$ can only have values which are within a reciprocal lattice vector, $\mathbf{g}$, of $\mathbf{K}_{o\parallel}$.

1.3.2. Diffraction Condition

Diffraction is a phenomenon which involves the scattering of electromagnetic waves or particles, which exhibit wave behavior, from a periodic array of scatterers. The incident wave or particle is scattered into well defined directions because the diffracted waves interfere constructively in these directions.

9

The scattered waves obey the conservation of momentum and energy. For diffraction from a three dimensional array (e.g. bulk X-ray diffraction) the relationships are the following:

$$\mathbf{K}_g = \mathbf{K}_o + g, \qquad \text{conservation of momentum} \qquad (1.6)$$

and
$$K_o = K_g, \qquad \text{conservation of energy.} \qquad (1.7)$$

For diffraction from a two dimensional array (e.g. LEED from surfaces) the conditions are

$$\mathbf{K}_{g\parallel} = \mathbf{K}_{o\parallel} + g, \qquad \text{conservation of } \textit{parallel} \text{ momentum} \qquad (1.8)$$

and
$$K_o = K_g, \qquad \text{conservation of energy.} \qquad (1.9)$$

For a surface, the penetration depth of the electrons is relatively small, 10-15Å, compared to the amount of the surface that is sampled. Thus, momentum perpendicular to the surface is said not to be conserved. The perpendicular component of the momentum can be obtained from the two following relationships which result from equations (1.8) and (1.9)

$$K_{g\perp}^2 = K_g^2 - K_{g\parallel}^2 = K_g^2 - \left(K_{o\parallel} + g\right)^2 , \qquad (1.10)$$

$$K_{g\perp} = \sqrt{K_o^2 - \left(K_{o\parallel} + g\right)^2} , \qquad (1.11)$$

Because no constraints exist for the perpendicular momentum, reciprocal space is not composed of reciprocal lattice points but reciprocal lattice rods. This means that many diffracted beams are present at any given energy and angle of incidence, unlike the case of bulk X-ray diffraction.

1.3.3. Energy Dependence of the LEED Pattern

The energy dependence of the LEED pattern can be best understood by considering an incident electron beam at normal incidence. In Figure 1.5a, a vector diagram of the incident electron with wavevector, $\mathbf{K_o}$, and the exiting beam with wavevector, $\mathbf{K_g}$, is shown. The angle, θ, between the two wavevectors $\mathbf{K_o}$ and $\mathbf{K_g}$ is the exit angle of the outgoing electron beam. In Figure 1.5b the situation where the incident wavevector, $\mathbf{K_o}$, is twice the length of that in Figure 1.5a is shown. This corresponds to an energy that is four times that shown in Figure 1.5a. Notice that in both Figure 1.5a and 1.5b the parallel momentum is always equal to $\mathbf{g}$. This is because 1) the incident electron beam does not have a parallel component and 2) we are considering the same diffraction beam at different energies. As the incident electron energy is changed the magnitude of $\mathbf{K_o'}$ changes but not its direction, i.e. the angle of incidence remains the same. Since we are considering only elastic scattering the length of $\mathbf{K_g'}$ equals the length of $\mathbf{K_o'}$. This means that the length of $\mathbf{K_g'}$ is fixed by the incident electron energy and the
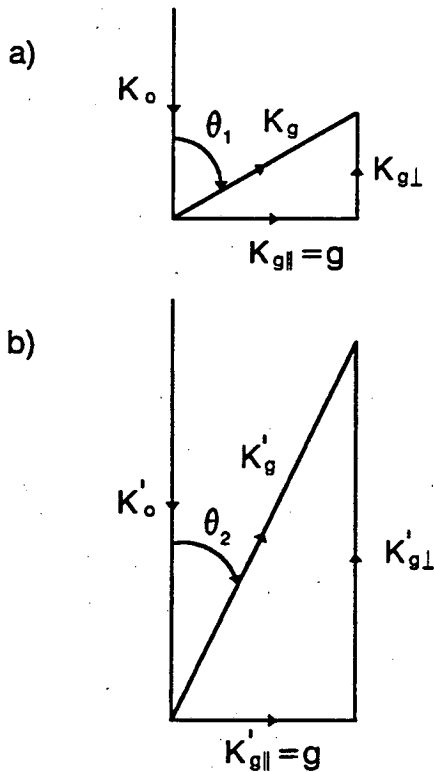
Figure 1.5   Energy dependence of the LEED pattern. Schematic of diffraction a) at one energy and b) at four times the energy

magnitude of $\mathbf{K}'_{g\parallel}$ is equal to that of $\mathbf{g}$ by conservation of parallel momentum. The only vector quantity that is unrestricted is $\mathbf{K}'_{g\perp}$. We can see that as the energy is increased the length of $\mathbf{K}'_{g}$ increases and the exit angle, θ, decreases so that $\mathbf{K}'_{g\parallel}$ always equals $\mathbf{g}$ as demanded by the conservation of parallel momentum. So we can see that in LEED the absence of a third Bragg condition allows diffraction spots to exist at all energies. Sometimes experimentally the beams are too weak to be detected but this is a very different situation than spot extinctions or absences.

1.3.4. Indexing the LEED Pattern

Often the LEED pattern is a superposition of diffraction patterns from different domains and it is not possible to index the whole diffraction pattern. By indexing we mean assigning a notation to the LEED pattern which describes the dimensions and orientation of the direct space lattice. Often the pattern is indexed according to one domain. A domain is a type of long range defect where distinct patches of equivalent but differently oriented surface structure coexist.

A Bravais lattice is a lattice with only one lattice point per unit cell. Only one domain typically can be considered a Bravais lattice. If another domain produces additional spots, as is often the case for rotational domains for example, then the resulting superposition does not form a Bravais lattice. Often the Bravais lattices can be labeled with Wood's notation [1.4] which has the general form $j\left(\dfrac{b_1}{a_1} \times \dfrac{b_2}{a_2}\right)R\alpha$ where j is either a "c", for centered, or a "p", for primitive. The ratios in the parentheses are of the unit cell vectors of the superstructure relative to the unit cell vectors of the substrate. The $R\alpha$ signifies that the superlattice is rotated an angle α with respect to the substrate lattice. This notation requires that the angle between $\mathbf{b}_1$ and $\mathbf{b}_2$ be the same as that between $\mathbf{a}_1$ and $\mathbf{a}_2$. If this is not the case then a more general form of notation must be used.

12

The alternative and more general way of labeling the surface structure is with a matrix notation. The matrix is defined by the equation

$$\begin{bmatrix} b_1 \\ b_2 \end{bmatrix} = \begin{bmatrix} m_{11} & m_{12} \\ m_{21} & m_{22} \end{bmatrix} \begin{bmatrix} a_1 \\ a_2 \end{bmatrix}. \tag{1.12}$$

The superlattice unit cell vectors are b_1 and b_2 and the substrate unit cell vectors are a_1 and a_2.

Indexing a LEED pattern requires that superlattice basis vectors b_1^* and b_2^* and substrate basis vectors a_1^* and a_2^* be defined for the LEED pattern. We use

$$\begin{bmatrix} a_1^* \\ a_2^* \end{bmatrix} = \begin{bmatrix} m_{11}^* & m_{12}^* \\ m_{21}^* & m_{22}^* \end{bmatrix} \begin{bmatrix} b_1^* \\ b_2^* \end{bmatrix}, \tag{1.13}$$

to express the substrate reciprocal lattice in terms of the reciprocal superlattice. This equation can be rearranged into the following form

$$\begin{bmatrix} b_1^* \\ b_2^* \end{bmatrix} = \frac{1}{m_{11}^* m_{22}^* - m_{12}^* m_{21}^*} \begin{bmatrix} m_{22}^* & -m_{12}^* \\ -m_{21}^* & m_{11}^* \end{bmatrix} \begin{bmatrix} a_1^* \\ a_2^* \end{bmatrix}, \tag{1.14}$$

where the inverse of the matrix in equation (1.13) was taken. Now the direct space lattice can be obtained by substituting $b_1^* = 2\pi/b_1$ and $b_2^* = 2\pi/b_2$ for the superlattice basis vectors and similarly for a_1^* and a_2^*. Using some algebra, the result may be put into the simple form

$$\begin{bmatrix} b_1 \\ b_2 \end{bmatrix} = \begin{bmatrix} m_{11}^* & m_{21}^* \\ m_{12}^* & m_{22}^* \end{bmatrix} \begin{bmatrix} a_1 \\ a_2 \end{bmatrix}. \tag{1.15}$$

By comparing this equation with equation (1.12) the following relationships exist between the matrix elements

$$m_{11} = m_{11}^* \qquad m_{12} = m_{21}^*$$
$$m_{21} = m_{12}^* \qquad m_{22} = m_{22}^*$$

The determinant of the matrix is equal to the ratio of the unit cell area of the direct superlattice (b_1 and b_2) to that of the substrate lattice (a_1 and a_2); therefore, the matrix elements, m_{ij}, can only have values for which the determinant is not equal to zero.

This method does not give a unique notation because the coefficient matrix depends on the choice of the vector directions. Therefore, different matrix notations may yield equivalent unit cells.

Typically, the surface structures that are encountered are commensurate which means that the combination of substrate and overlayer lattice produce a finite unit cell that is related to the substrate in a simple way. In matrix notation, none of the matrix elements is an irrational number. The structures that do have irrational matrix elements are, not surprisingly, called incommensurate. In an incommensurate structure the overlayer and substrate almost seem not to be influenced by the presence of the other. Incommensurate structures occur for rare gas atoms physisorbed on various substrates, for example Ag(111)+Incommensurate Xe [1.5]. The weak interaction between the substrate and the overlayer is the reason for the structure being incommensurate. Clean Mo(100) at temperatures less than 200K reconstructs to form an incommensurate structure. The reasons for this are not as obvious as in the previous example. This structure will be discussed in more detail in Chapter 5.

1.3.5. Symmetries in the LEED Pattern

Symmetries in the LEED pattern occur not only for the diffraction spot positions but also for the spot intensities. For an ideal surface the spot intensities have their highest symmetry at normal incidence. Generally, at off-normal incidence angles the spot intensities become asymmetric. For the general case, the symmetries, which show up in the LEED pattern, occur when the symmetry elements are parallel to the incident electron beam. This is because the electron paths are then invariant with respect to the symmetry element.

Although the spot intensities may display high symmetry at normal incidence this does not necessarily indicate a highly symmetrical surface. Domains can complicate the

situation. As stated earlier, a domain is a type of long range defect where distinct patches of equivalent but differently oriented surface structure coexist. The patches of surface are energetically equivalent because the atoms in the respective unit cells have the same bonding geometry. Each domain is generally related to the other by a point group symmetry operation of the substrate. Out-of-phase domains would be an exception, because they have equal orientations. An example of rotational domains is illustrated in Figure 1.6b and an example of out-of-phase domains is illustrated in Figure 1.6c. Steps or other defects with preferred orientations may cause some domains to be more prevalent than others. Sometimes this is intentional; an experimentalist might intentionally misorient a single crystal 1-2° away from a low-Miller index plane for the explicit purpose of studying a particular domain.

In general, the maximum number of distinct domains on an ideal surface is the

(a)

(b)   (c)
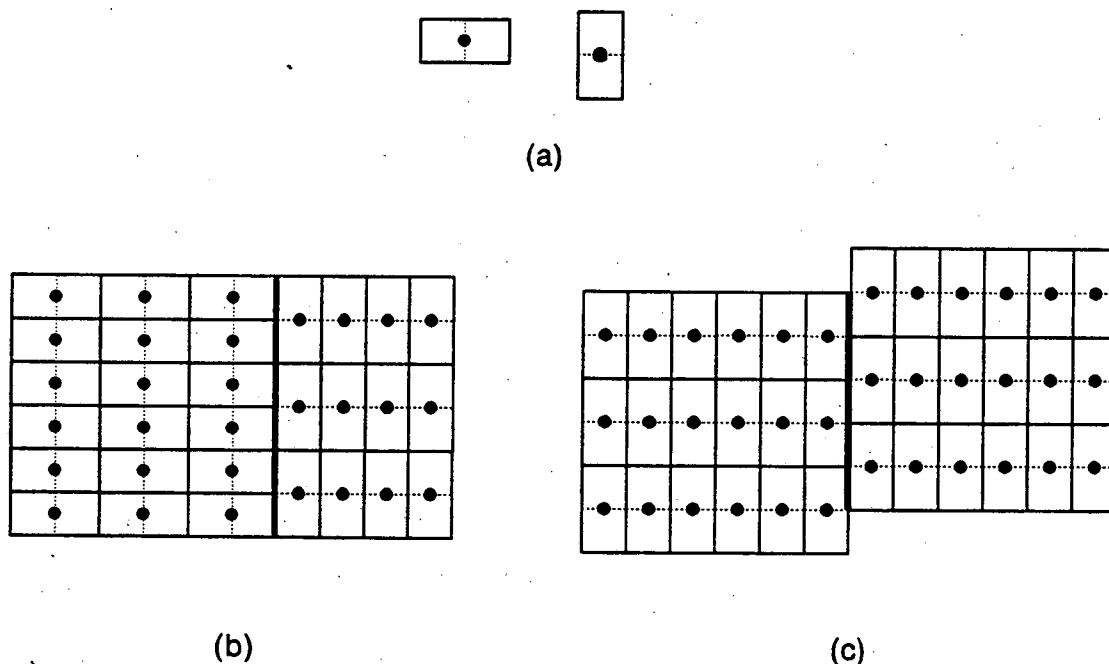
Figure 1.6   Domains of a p(2x1) superlattice on a substrate with a square lattice. In (a) the p(2x1) unit cell (on the left hand side) and the p(1x2) unit cell (on the right hand side). The vertices represent the lattice points and the filled circles represent the basis. The dotted lines represent the part of the underlying 1x1 substrate lattice that does not coincide with the superlattice. In (b) two rotational domains of p(2x1) and p(1x2). In (c) translational domains, this is the specific case of two domains which are exactly out of phase. The dark vertical line in (b) and (c) represents the domain boundary.

number of possible symmetry operations that apply to the surface, excluding translational domains. For example on Mo(100), which has a square lattice, the bulk-terminated surface has four mirror planes and a four-fold rotation axis. This implies that eight symmetry operations apply to the surface; therefore, eight distinct domains may coexist on the surface. This will occur if the basis, i.e. the contents of the unit cell, generates a unit cell with no symmetry. However, if the unit cell has some symmetry this will reduce the number of distinct domains, i.e. some domains will be symmetrically degenerate. This is illustrated in Figure 1.7 for a substrate with a square lattice and a rectangular superlattice with a lower symmetry than the substrate. If the superlattice unit cell possesses the highest symmetry possible, i.e. two mirror planes and a two-fold rotation axis, then only two distinct domains will exist on the surface as is shown is Figure 1.7a. If the symmetry of the unit cell is lower, only one mirror plane, then each of the rotational domains is split into two domains which are mirror images of each other. In Figure 1.7b this is illustrated. Notice that the unit cells have been generated by mirroring one of the unit cells through the mirror plane which is no longer present in the unit cell. If all symmetry is removed from the unit cell then each of the rotational domains splits into four distinct domains. The four p(1x2) domains can be generated by starting with one of the four domains and applying a mirror operation vertical to the page, a mirror operation horizontal to the page, and a two-fold rotation. Each symmetry operation produces one domain. The same applies to the p(2x1) domain. These are merely the symmetry operations which applied to the unit cells in Figure 1.7a. The eight domains, four from the p(1x2) and four from the p(2x1), are depicted in Figure 1.7c.

We have disregarded translational domains since they only need to be considered when interference effects are important such as when the domains are smaller than the electron-beam coherence width. The coherence width can be defined as the distance

(a)   (b)

(c)
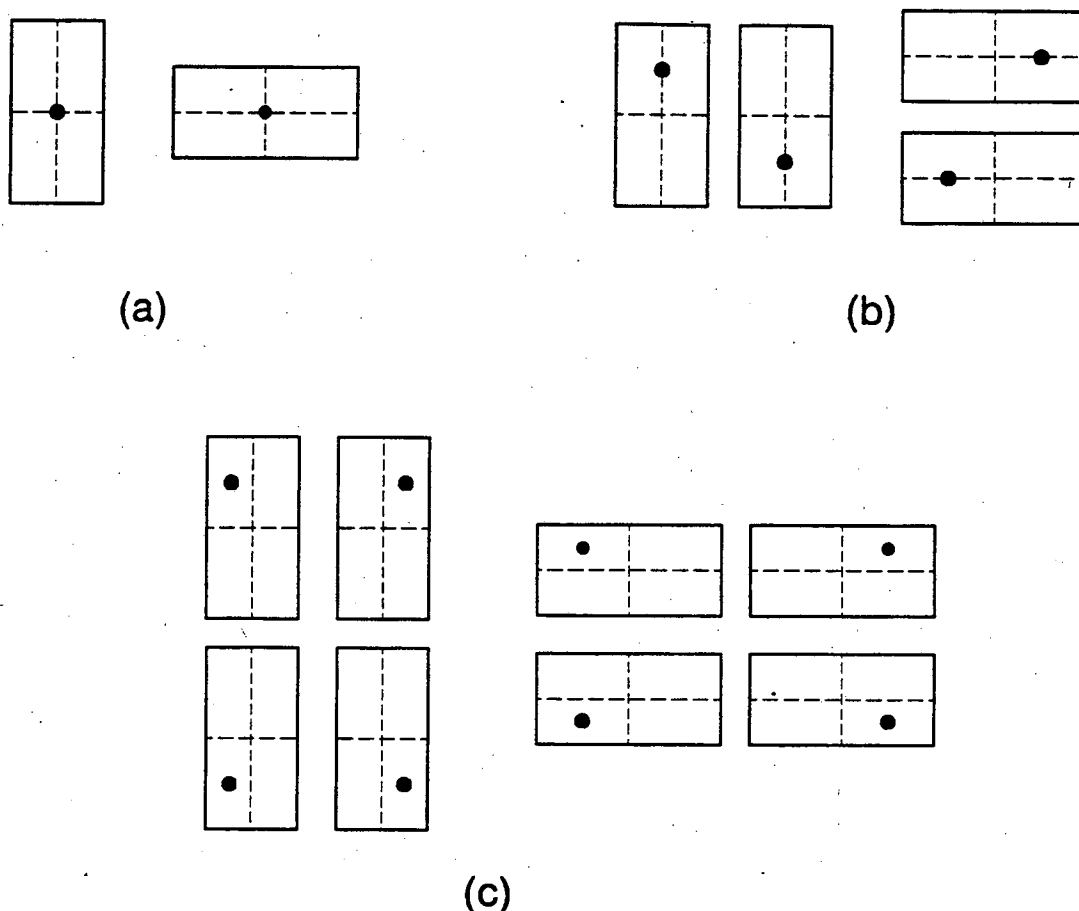
Figure 1.7   The effect of the symmetry of the superlattice unit cell on the number of distinct domains on the substrate. The vertices of the rectangular unit cells represent the lattice points and the filled circles represent the basis. The dotted lines represent the mirror planes perpendicular to the page. As the symmetry of the superlattice unit cell decreases the number of distinct domains increases. This is depicted in (a) for two rotational domains, p(1x2) and p(2x1) respectively, with unit cells with high symmetry, in (b) for four distinct domains with unit cells with lower symmetry, and in (c) for eight distinct domains with unit cells with no symmetry.

beyond which two points on the same wave front have a random phase relationship. For a commercial LEED electron gun, 50-100Å is a typical coherence width.

In the LEED experiment the domains are much smaller, hundreds of Ångströms for a well-ordered surface, than the diameter of the incident electron beam, which is on the order of 1mm, so the resulting LEED pattern is a superposition of the LEED patterns from the individual domains on the surface. This must be accounted for when the calculated intensities are compared to the experimental intensities. In principle, the intensities of the LEED patterns of all the possible domains must be calculated and

averaged. However, at normal incidence only the intensities of the beams from one domain need to be calculated since the LEED patterns from the other domains can be produced by applying the correct symmetry operations to the LEED pattern which was calculated. Then the intensities of the LEED patterns from all the domains are averaged together to yield the intensities which can be compared with the experiment. Typically in the calculations, the assumption is made that the domains are larger than the coherence width of the electron beam. This requires the *intensities* and not the scattering amplitudes to be averaged. An example of a surface with two domains labeled domain 1 and domain 2 which are equal in area and are larger than the coherence width of the electron beam would be treated with an equation with the form

$$I_g = \left|A_g^1\right|^2 + \left|A_g^2\right|^2,$$ \hfill (1.16)

where I_g is the intensity of a LEED beam with label g, A_g^1 is the complex amplitude of an outgoing plane wave from domain 1, and A_g^2 is the complex amplitude of an outgoing plane wave from domain 2. However, if the domains were smaller than the coherence width of the electron beam then interference effects would occur between the two different domains. These interference effects would have to be accounted for by adding the complex amplitudes of the outgoing plane wave from each domain then converting the sum to an intensity in the following manner

$$I_g = \left|A_g^1 + A_g^2\right|^2.$$ \hfill (1.17)

References

1.1   D.F. Ogletree, Ph.D. Thesis, Berkeley, 1986.

1.2   Fred Rosebury, **Handbook of Electron Tube and Vacuum Techniques**
      (Addison-Wesley, 1965) p. 386.

1.3   M.A Van Hove, W.H. Weinberg, and C.-M. Chan, **Low-Energy Electron
      Diffraction** (Springer-Verlag, 1986) p. 18.

1.4   E.A. Wood, Bell Syst. Tech. J. XLIII, 541 (1964); J. Appl. Phys. **35**, 1306 (1964).

1.5   N. Stoner, M.A. Van Hove, S.Y. Tong, and M.B. Webb, Phys. Rev. Lett. **40** 243
      (1978).

Chapter 2.   LEED Theory

Interpretation of the diffraction spot positions in a LEED pattern only requires a kinematic, single scattering, treatment. Single scattering means that an incident electron is elastically backscattered once in the near surface region and exits the surface. However, this is not what physically occurs. Because of the large scattering cross section for low-energy electrons, the electrons may actually experience several scattering events before exiting the surface. The effect of multiple scattering in LEED is not to alter the positions of the diffraction spots but to change the spot intensities, that is multiple scattering redistributes the intensity among the outgoing beams as compared to single scattering. A simple single scattering treatment, in general, will not produce I-V spectra which resemble the experimental data. The main difficulties with a LEED theory which accounts for multiple scattering is keeping track of all the possible scattering paths that a LEED electron may take and calculating the scattering along all those paths.

2.1. LEED Scattering Theory Overview

The objective of LEED scattering theory is to first calculate the theoretical intensities of the backscattered diffraction beams with momentum, k_g, as a function of the incident beam momentum, k_o. Then to compare the calculated intensities with the measured intensities. A surface structure is determined by varying the geometrical parameters of the structural model until the set of calculated intensities agrees with the set of experimental intensities. In general, a structure is determined by trial and error, so many models must be considered to make certain that a particular model gives a best fit of the experimental data.

The general scheme is to calculate the scattering from individual planes of atoms parallel to the surface. This approach takes advantage of the limited penetration depth of the incident electron, 10-20Å. The LEED wave function is composed of a finite sum of plane waves, $\{k_g^{\pm}\}$, which are related to the incident plane wave momentum, k_o, by a reciprocal lattice vector, g. The number of plane waves that are needed depends on both the energy of the incident electron and the spacing between the planes.

Since each plane of atoms has translational symmetry, the incident plane wave can only be diffracted into plane waves with momentum, $k_o + g$. The scattering of an incident plane wave with momentum k_o from a plane of atoms into a set of diffracted plane waves is contained in the plane wave scattering matrix, M. The intra-plane scattering is typically calculated in the spherical wave representation. The incident wave on the ith atom in a plane of atoms is a combination of the incident wave on the plane and the amplitude at the ith atom of all the waves scattered from other atoms in the plane. Once the plane wave diffraction matrices have been calculated for each of the different layers, the scattering between planes is calculated. Various stacking schemes exist to combine the plane wave matrices from the different layers and include multiple scattering effects to generate the theoretical intensities.

2.2. Inelastic Scattering

Only 1-5% of the incident electrons are elastically back scattered from a surface. The electrons lose energy through the generation of secondary electrons, plasmon losses, single particle excitations, etc. LEED theory is only concerned with the elastically scattered electrons but has to account for the inelastic losses. Since the theory is only concerned with the fraction of electrons that are inelastically scattered and not the loss processes, the inelastic losses are accounted for by an electron-mean-free path or an

21

imaginary part of the potential. The equation for the energy of a LEED electron between the ion-cores is

$$\frac{\hbar^2 k^2}{2m} = E + V_{or} + iV_{oi} , \qquad (2.1)$$

where V_{or} is the real part of the potential and V_{oi} is the imaginary part of the potential which simulates the damping of the LEED electrons. Typical values for V_{oi} range from 1-5eV. If the electrons' penetration were not damped and they penetrated deep into the crystal then a third Bragg condition would exist and the peaks in the I-V spectra would become very sharp because the width of the peaks is inversely proportional to the number of participating scatterers perpendicular to the surface. The width of the peaks in the I-V curves provides an estimate of the strength of the damping. A simple relationship can be obtained between the width of the peaks, ΔE, and the imaginary part of the potential, and has the form [2.1]

$$\Delta E \approx V_{oi} . \qquad (2.2)$$

2.3. Elastic Scattering

2.3.1. Atomic Potential Scattering

2.3.1.1.   Muffin-Tin Model

In LEED theory a muffin-tin model has been adopted to describe the potential of the near surface region. The muffin-tin model had been used successfully for electronic band structure calculations prior to its incorporation into LEED theory. The muffin-tin model assumes that all the atomic potentials are spherical and that the atomic potential extends from the center of the ion-core to R_m, the muffin-tin radius. The model is composed of nonoverlapping spheres and a constant potential, called the muffin-tin potential, which exists between the spheres.

Accurate wave functions exist for free atoms but these cannot be used because LEED is sensitive enough to the valence electrons to make these unsuitable [2.2]. The atomic potentials often used in LEED calculations for metal surfaces are those that were calculated by Moruzzi et al [2.3] who performed self-consistent band structure calculations for all the electrons in the crystal. This procedure produces a one-electron potential that can be used for the LEED electrons.

2.3.1.2. Phase Shifts

The incoming and outgoing beams have well defined directions so it is natural to use a plane wave representation, and since the interstitial regions have a constant potential plane waves are also a convenient choice. However, in the case of scattering from the ion-cores the potential is spherical and a natural choice would be a spherical wave representation. To most effectively exploit the scattering from atomic potentials and end up with the scattering amplitudes for each diffraction beam a partial-wave analysis is used. Partial-wave analysis employs a spherical-wave expansion of a plane wave. Since the atomic potential is assumed to be spherical, only the radial part of the Schrödinger equation remains to be solved. The solutions of the radial Schrödinger equation are Bessel functions, j_ℓ, multiplied by spherical harmonics, $Y_{\ell m}$. The phase shifts, δ_ℓ, are obtained by smoothly matching the solution of the radial Schrödinger equation inside the muffin-tin sphere to the solution outside. This can be accomplished by equating the logarithmic derivatives just inside and outside of the muffin-tin radius. The phase shifts, δ_ℓ, are found in the atomic scattering t-matrix which has the form

$$t_\ell = -\frac{\hbar^2}{2m}\left(\frac{1}{k}\right)\sin\delta_\ell \exp(i\delta_\ell) , \qquad (2.3)$$

where $k = \sqrt{\frac{2m}{\hbar^2}(E - V_{or} - iV_{oi})}$.

The basic effect of the atomic potential is to advance the phase of the LEED electron. This can be understood from a simple one-dimensional potential well problem. In

Figure 2.1a a particle with energy greater than zero passes over a square potential well with depth, V_0. The equation for the energy of the particle outside of the well is given simply by

$$E = \frac{\hbar^2 k^2}{2m} \, , \tag{2.4}$$

and for the region inside the well by

$$E = \frac{\hbar^2 k^2}{2m} - V_0 \, . \tag{2.6}$$

Since the wavelength of the particle is inversely proportional to its energy, one can see from Figure 2.1a that the particle moves faster inside the potential well than outside the well. Classically the particle can be thought of as being accelerated through the region of the well and spends less time in the region of the well except at resonance, when it is trapped for a longer time within the well. The other consequence of being accelerated is that the phase of the wave is advanced and the wave is said to be phase shifted. This can be seen in Figure 2.1a.

If the energy of the particle is such that its wavelength is an integral or half integral number of wavelengths then the amplitude of the wave inside and outside the region of the

(a)   (b)
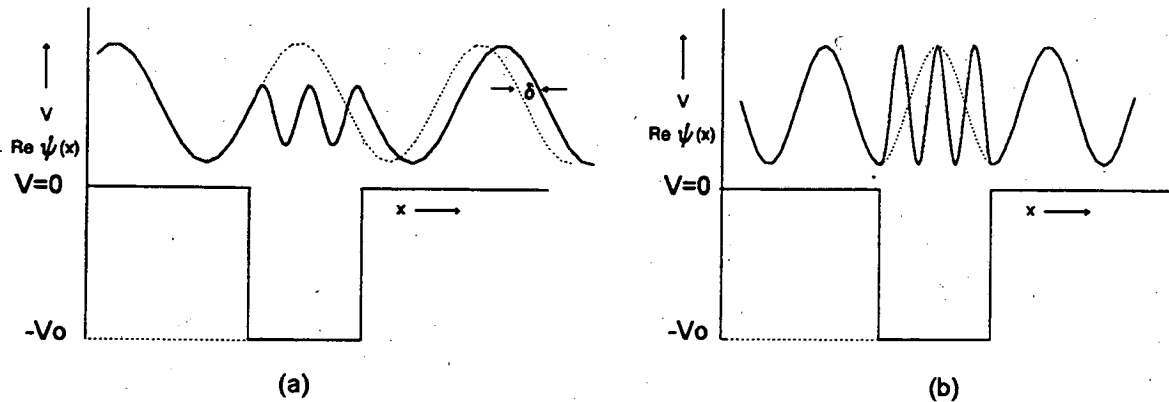
Figure 2.1   Scattering of a plane wave from a one dimensional well. a) a 1-D plane wave phase-shifted by δ and b) a 1-D plane wave at resonance

24

well will be equal. This condition is known as resonance scattering. This is illustrated in Figure 2.1b. Resonances are not true bound states of the well because bound states are localized in the region of the well and the resonances are not.

2.3.2. Potential Step Scattering

When the LEED electron enters the surface it crosses a potential step, from the vacuum level to the inner potential or muffin-tin level, and its kinetic energy changes; this results in refraction of the electron. Refraction is particularly important because the beams have different exit angles; therefore, the refractive effects do not cancel in general as they do for the specific case of the specular beam. The exit angle is of interest in the calculations because the reflectivity, which is defined as

$$R^{th} = \frac{k_{g\perp} |B|^2}{k_{0\perp} |A_0|^2} , \qquad (2.7)$$

depends on it. A_0 is the amplitude of the incident wave and is set equal to unity in the calculations and B is the calculated amplitude of the outgoing wave.

2.4. Conventional LEED Calculations

In practice the spherical and plane wave representations are both used during different parts of the LEED calculation. The plane-wave representation does not work well when interlayer spacings between scatterers become small, on the order of the wavelength of the LEED electron. In this case the spherical-wave representation must be used. Typically, scattering between coplanar or nearly coplanar atoms is calculated using a spherical-wave representation and scattering between layers uses a plane-wave representation. In the plane-wave representation the wave field is expanded conveniently in terms of the reciprocal lattice vectors, g. In principle an infinite number of values of g is

needed; however, only a finite number of beams contribute to the propagation from layer to layer. Beams with large values of g decay exponentially away from the layer and do not contribute.

In general, the atomic scattering is contained in the phase shifts which have to be calculated for each atomic element. The in-layer scattering calculation is the time consuming step. A spherical-wave representation, using a Green's function formalism, is used to calculate the in-layer scattering. Once all the layer diffraction matrices, which basically contain the scattering amplitudes for the transmitted and reflected waves, have been generated, the layers are stacked together and typically plane waves are used to calculate the scattering between layers. Different methods are available; however, only the method used in the calculations presented in this work is discussed below. The inelastic scattering effects are included in the imaginary part of the potential and temperature dependent effects are included through a Debye-Waller factor, similar to the one used in X-ray diffraction. Temperature-dependent phase shifts are generated by multiplying the t-matrix by a Debye-Waller factor.

The calculation is repeated for each surface geometry and for each energy point on the theoretical energy grid. Most of the calculations in this work used 40-44 energy points, over an energy range of ~160eV.

2.4.1. Combined Space Method and Composite Layers

The scattering properties of an atomic layer can be described by scattering matrices, $M_{g'g}^{\pm\pm}$, in the plane wave representation. The subscripts are read from right to left, so $M_{g'g}^{\pm\pm}$ gives the ratio of the amplitude of a scattered wave with momentum $k_{g'}^{\pm}$ to the amplitude of the incident wave with momentum $k_{g}^{\pm}$. This matrix can describe the scattering of a single atomic layer or several layers combined, e.g. a composite layer.

To calculate the plane-wave matrices, $M_{g'g}^{\pm\pm}$, for a layer composed of more than one atom per unit cell, a composite layer, a matrix inversion formalism may be used. This formalism uses a spherical wave representation for the subplanes, which are Bravais lattices (i.e. one atom per unit cell), that comprise the composite layer. The subplanes may be coplanar. The original method due to Beeby [2.4] was generalized by Tong and Van Hove [2.5] to include the incidence of plane waves $k_g^\pm$ for all beams g.

If we consider a composite layer with N subplanes, each with the same Bravais lattice which may contain different kinds of atoms and following Van Hove and Tong [2.6], we define the following quantities in a spherical wave representation $[L=(\ell, m)]$ in atomic units ($\hbar^2 = m = 1$):

$t_\ell^i = \dfrac{1}{2k_0} e^{i\delta_\ell} \sin\delta_\ell$: scattering t-matrix for a single atom in subplane i;

$\tau_{LL'}^i$: scattering matrix which contains all scattering paths within subplane i;

$T_{LL'}^i$: scattering matrix which includes all those scattering paths within the composite layer that end at subplane i;

$G_{LL'}^{ji}$: structural propagator describing all unscattered propagations from atoms in subplane i to atoms in subplane j

The plane-wave diffraction matrix is defined as

$$M_{g'g}^{\pm\pm} = -\frac{16\pi^2 i}{Ak_{g_\perp}^+} \sum_{LL'} Y_L\left(k_{g'}^\pm\right) \sum_{i=1}^{N} \left\{ \exp\left[i\left(\pm k_g^\pm \mp k_{g'}^\pm\right)\cdot r_i\right] T_{LL'}^i \right\} Y_{L'}^*\left(k_{g'}^\pm\right) + \delta_{g'g}\delta_{\pm\pm} , \qquad (2.8)$$

with
$$G_{LL'}^{ji} = \hat{G}_{LL'}^{ji} \exp\left[-ik_g^\pm \cdot \left(r_j - r_i\right)\right] . \qquad (2.9)$$

$G_{LL'}^{ji}$ may be expressed as sum over direct lattice points with

$$\hat{G}_{LL'}^{ji} = -8\pi i k_0 \sum_{L_1} {\sum_{P}}' i^{\ell_1} a(L, L', L_1) h_{\ell_1}^{(1)}\left(k_0 \left| P + r_j - r_i \right|\right)$$

$$\times Y_{L_1}\left(P + r_j - r_i\right) \exp\left[-ik_0 \cdot P\right] , \qquad (2.10)$$

or as a sum over reciprocal lattice points

$$\hat{G}_{LL'}^{ji} = -\frac{16\pi^2 i}{A} \sum_{g_1} \frac{\exp\left[ik_{g_1}^\pm \cdot \left(r_j - r_i\right)\right]}{k_{g_1\perp}^\pm} Y_L^*\left(k_{g_1}^\pm\right) Y_{L'}\left(k_{g_1}^\pm\right) , \qquad (2.11)$$

27

where $h_{\ell_1}^{(1)}$ is a spherical Hankel function of the first kind, P runs over all lattice points of one subplane, excluding the term with $P + r_j - r_i = 0$, r_i and r_j are the positions of arbitrary reference atoms in subplanes i and j, respectively, $Y_{\ell m}$ is a spherical harmonic, and A is the unit cell area.

The Clebsch-Gordan coefficients are defined as

$$a(L_1, L_2, L_3) = \int Y_{L_1}^*(\Omega) Y_{L_2}^*(\Omega) Y_{L_3}^*(\Omega) d\Omega . \tag{2.12}$$

The subplane τ-matrix is defined as [2.1]

$$\tau_{LL'}^i = \left[\left(I - t^i G^{ii} \right)^{-1} \right]_{LL'} t_\ell^i , \tag{2.13}$$

where I is the identity matrix.

The matrices T^1, ..., T^N are obtained exactly according to Beeby [2.4] with the expression

$$\begin{bmatrix} T^1 \\ T^2 \\ T^3 \\ \vdots \\ T^N \end{bmatrix} = \begin{bmatrix} I & -t^1 G^{12} & -\tau^1 G^{13} & \cdots & -\tau^1 G^{1N} \\ -\tau^2 G^{21} & I & -\tau^2 G^{23} & \cdots & -\tau^2 G^{2N} \\ -\tau^3 G^{31} & -\tau^3 G^{32} & I & \cdots & -\tau^3 G^{3N} \\ \vdots & \vdots & \vdots & & \vdots \\ -\tau^N G^{N1} & -\tau^N G^{N2} & -\tau^N G^{N3} & \cdots & I \end{bmatrix}^{-1} \begin{bmatrix} \tau^1 \\ \tau^2 \\ \tau^3 \\ \vdots \\ \tau^N \end{bmatrix} . \tag{2.14}$$

The reflection and transmission matrices can be defined as

$$r^{+-} = M^{+-}, \quad r^{-+} = M^{-+}, \quad t^{++} = M^{++}, \quad \text{and} \quad t^{--} = M^{--}, \tag{2.15}$$

where $M^{\pm\pm}$ is derived from equation (2.8). The superscripts are read from right to left, so for example r^{-+} refers to a wave initially traveling into the surface which is reflected at the layer and travels back towards the surface. If the scattering layer has inversion symmetry, as a coplanar layer does, then $r^{+-} = r^{-+}$ and $t^{++} = t^{--}$. Transmission occurs when the electrons emerge on the opposite side of the layer on which they impinged, whereas reflection occurs when the electrons emerge on the same side of the layer.

2.4.2. Renormalized-Forward Scattering (RFS)

Once the plane-wave diffraction matrices, $M^{\pm\pm}$, have been generated for the different types of layers in the surface, the layers can be stacked together and the

scattering amplitudes for each diffraction beam can be calculated. The Renormalized-Forward Scattering (RFS) perturbation method which was formulated by Pendry [2.8] was the method used for all the calculations in this work. The perturbation is based on the fact that forward scattering or transmission is favored over backscattering or reflection. The total reflectivity of the surface is expanded in terms of the number of reflections. The reflectivity to first order is given by all waves which are transmitted an unlimited number of times and experience one reflection. Second order is given by all waves which are reflected three times - an odd number of reflections is required for the wave to exit the surface. The required number of reflections is 2n-1 where n is the order of the expansion.

The method may be implemented by allowing the incident plane wave to be transmitted through each of the layers until it dies out because of inelastic effects. Then starting at the deepest layer reached, propagate the plane waves toward the surface collecting the reflected waves at each layer. This is done until all the plane waves which were reflected once have emerged to the surface. For the second order the emergent waves are propagated back into the surface and the whole procedure is repeated. This is done until the sum of the amplitudes of the nth-order plane waves changes the total reflectivity from the previous pass by a negligible amount. This method converges because the inelastic effects cause the higher order waves to die out.

The formalism uses two expressions, one for penetration and one for emergence. The one for penetration has the form

$$a_{(i)g}^{new} = \sum_{g'} \left(t_{gg'}^{++} P_{g'}^{+(i-1)} a_{(i-1)g'} + r_{gg'}^{+-} P_{g'}^{-(i)} a_{(i)g'} \right), \qquad (2.16)$$

and the expression for emergence has the form

$$a_{(i)g}^{new} = \sum_{g'} \left(t_{gg'}^{--} P_{g'}^{-(i+1)} a_{(i+1)g'} + r_{gg'}^{-+} P_{g'}^{+(i)} a_{(i)g'} \right), \qquad (2.17)$$

where $a_{(i)g}$ represents the plane-wave amplitudes in the ith interlayer spacing and $P_{g'}^{\pm(i)}$ are plane-wave propagators between reference points in each successive layer with the form

$$P_{g'}^{\pm(i)} = \delta_{gg'} e^{ik_g^{\pm} \cdot r}. \qquad (2.18)$$

29

These equations are solved iteratively with $a_{(i)g}^{new}$ overwriting $a_{(i)g}$ as each new layer is reached. The reflectivity and transmission matrices are those that were calculated previously for each layer.

Typically RFS uses 12-15 layers and requires three to four orders to achieve convergence [2.9]. RFS requires the interlayer spacing to be greater than ~1.0Å or the method does not converge well because too many plane waves are needed.

2.4.3. Temperature Effects; The Debye-Waller Factor

The temperature of the surface affects the I-V spectra by reducing the intensities, which is the same effect observed in X-ray diffraction. The reason is that the thermal motion of the ion-cores about their equilibrium positions causes a random phase shift which means that not all the waves scattered in a specific direction will all be in phase. Some destructive interference will occur and reduce the intensity that would otherwise be observed for a rigid lattice. The larger the amplitudes of the vibrating ion-cores, which correspond to higher temperatures, the greater the reduction in intensity. In X-ray diffraction the calculated intensities are multiplied by a Debye-Waller factor, exp(-2M), i.e. $I=I_o$exp(-2M). The Debye-Waller factor has the form

$$\exp(-2M) = \exp\left[-|s|^2 \left\langle (\Delta r)^2 \right\rangle\right], \tag{2.19}$$

where $\left\langle (\Delta r)^2 \right\rangle$ is the mean-square deviation and s is the momentum transfer. Equation (2.19) assumes that the vibrational amplitudes are small and that the vibrations are uncorrelated with those of neighboring atoms. Of course collective vibrational modes, phonons, exist in solids but at the present time no one has developed a more sophisticated formalism to account for this. If the Debye model of thermal vibrations is employed, equation (2.19) becomes

$$\exp(-2M) = \exp\left[\frac{-3\hbar^2 |s|^2 T}{m_a k_B \Theta_D^2}\right], \tag{2.20}$$

30

where k_B is the Boltzmann constant, T is the temperature, Θ_D is the Debye temperature, and m_a is the mass of the surface atoms. In the LEED calculations a Debye-Waller factor is used but since multiple scattering occurs the Debye-Waller factor is used to generate temperature-dependent phase shifts, $\delta_\ell(T)$, for each surface atom.

2.4.4. R-Factor Analysis

In the early 1970's surface structure determinations by LEED were done by a trial and error method in which the theoretical I-V curves for a model geometry were calculated and then compared visually with the experimental I-V curves. For clean substrates and substrates with atomic adsorbates this was acceptable, but obviously a less subjective method was desirable and necessary to make small refinements of the geometry. In X-ray diffraction R-factors or reliability factors are used for this purpose; unfortunately, the R-factors which are suitable for X-ray diffraction are less suitable for LEED. The main problem with constructing an R-factor is that no consensus exists as to what features in the I-V curves are most sensitive to geometrical parameters. The position of the peaks in the I-V curves are sensitive to the geometry but some debate exists as to the importance of relative intensities. Many R-factors exist and it seems more a matter of preference as to which one or combination of R-factors are used. The Pendry R-factor was used almost exclusively in this work.

Pendry [2.10] designed an R-factor to treat all maxima and minima in the I-V curves equally, i.e. all portions of the I-V curve yield structural information - absences of peaks are structurally as meaningful as a peak. This is done by using a logarithmic derivative of the intensities with respect to energy which has the form

$$L = I'/I .\tag{2.21}$$

To avoid singularities when I=0 a Y-function is defined as

$$Y = L/\left(1 + V_{0i}^2 L^2\right) ,\tag{2.22}$$

31

where V_{oi} may be taken as the average peak width of a single peak. With these definitions the Pendry R-factor is defined as

$$R_P = \int (Y_e - Y_t)^2 \, dE \Big/ \int \left(Y_e^2 + Y_t^2 \right) dE \; . \qquad (2.23)$$

The Pendry R-factor can have values which range from zero to two where $R_P = 0$ indicates that the two curves are identical and $R_P = 2$ means that the two curves are anticorrelated. A value of one indicates no correlation between the two curves. From this discussion it is obvious that the R-factor optimization is a minimization. Although no strict criteria exist for deciding what value of the Pendry R-factor indicates an acceptable fit, we can make some generalizations based on the many surface structure determinations made using the Pendry R-factor. In general, a Pendry R-factor in the range of 0.1-0.2 is obtained for clean unreconstructed metals and for simple atomic adsorbate systems a value in the range of 0.2-0.3 is obtained. These values are rough and must be used with caution. R-factors are intended only to serve as guides and not as the final say in a structure determination. Ultimately, the solved structure should be physically realistic, for instance bond lengths which deviate largely from known bond lengths are suspect although not necessarily incorrect.

2.5. Tensor LEED Calculations

Tensor LEED is a newer advance in surface structure theory. Combined with an automated search algorithm, tensor LEED makes possible accurate and fast structure determinations. It also allows the user to probe regions of geometric parameter space that before were not possible. Perhaps the most promising aspect of tensor LEED is that coupled with an automated search algorithm finally the experimentalist has the opportunity to analyze his or her own data.

If an atom in a reference structure is displaced by some value, δr, how does it affect the intensity of a diffraction beam? Displacing an atom by δr causes a change in the

surface potential which can be thought of as causing a change in the atomic scattering t-matrix. Using first order perturbation theory the change in amplitude of an outgoing diffraction beam, with parallel momentum $k'_{\parallel}$, can be related to the reference structure by

$$\delta A = \sum_{j} \left\langle \Psi^{+}\left(k'_{\parallel}\right) \middle| \delta t^{j}_{\ell} \middle| \Psi^{+}\left(k_{\parallel}\right) \right\rangle , \qquad (2.24)$$

where $\left| \Psi^{+}\left(k_{\parallel}\right) \right\rangle$ is the wave function of a LEED electron incident on the reference structure and $\left\langle \Psi^{+}\left(k'_{\parallel}\right) \right|$ is the wave function of a LEED electron leaving the reference structure. The intensity of the diffraction beam from the distorted surface is given by

$$I_{g} = \left| A_{g} + \delta A_{g} \right|^{2} , \qquad (2.25)$$

where A_{g} is the amplitude of the electrons diffracted from the undistorted surface.

The atomic t-matrix for the jth atom in the distorted surface can be expanded to first order as

$$\tilde{t}^{j}_{\ell} = t^{j}_{\ell} + \delta t^{j}_{\ell}\left(\delta r\right) , \qquad (2.26)$$

where

$$t^{j}_{\ell} = ie^{i\delta_{\ell}} \sin \delta_{\ell} , \qquad (2.27)$$

in atomic units ($\hbar^{2} = m = 1$). The t-matrix for the undistorted surface, t^{j}_{ℓ}, is diagonal but the t-matrix for the distorted surface, $\tilde{t}^{j}_{\ell}$, has off-diagonal elements since the perturbation is a non-spherical distortion.

The change in amplitude may be put into an angular momentum basis and has the final form [2.11]

$$\delta A_{g} = \frac{1}{N} \sum_{j} \sum_{\ell m, \ell'm'} F^{j}_{\ell m, \ell'm'} S^{j}_{\ell m, \ell'm'} - F^{j}_{00,00} / 4\pi , \qquad (2.28)$$

where N is the number of atoms in the surface unit cell. $F^{j}_{\ell m, \ell'm'}$ is analogous to a form factor and has the form

$$F^{j}_{\ell m, \ell'm'} = \left(1/2i\Gamma\kappa k^{\pm}_{gz}\right) \sum_{\ell''m''} f^{j-}_{\ell m, \ell''m''} t^{j}_{\ell''} f^{j+}_{\ell''m'', \ell'm'} , \qquad (2.29)$$

where Γ is the area of the reference unit cell and κ is the wavevector of the electron in the surface given by

$$\kappa = \left[2\left(E - V_{or}\right)\right]^{\frac{1}{2}} , \qquad (2.30)$$

33

in atomic units ($\hbar^2 = m = 1$).

The partial form factors, $f^{j-}_{\ell m, \ell'' m''}$ and $f^{j+}_{\ell m, \ell'' m''}$, are defined as:

$$f^{j-}_{\ell m, \ell' m'} = \sum_{\ell'' m''} i^{\ell''} C_{\ell'' m'', \ell m, \ell' - m'} A^j_{\ell'' - m''}(-\mathbf{k}_{\|} - \mathbf{g}) , \qquad (2.31)$$

$$f^{j+}_{\ell m, \ell' m'} = \sum_{\ell'' m''} i^{\ell''} C_{\ell m, \ell' m', \ell'' - m''} A^j_{\ell'' - m''}(\mathbf{k}_{\|}) , \qquad (2.32)$$

where $C_{lm, l'm', l''m''}$ are Gaunt coefficients defined as

$$C_{\ell m, \ell' m', \ell'' m''} = \int Y_{\ell m}(\Omega) Y_{\ell' m'}(\Omega) Y_{\ell'' m''}(\Omega) d\Omega . \qquad (2.33)$$

where $Y_{\ell m}$ are spherical harmonics. $A^j_{\ell'' - m''}(\mathbf{k}_{\|})$ is the amplitude of a spherical partial wave incident on the atom located at $\mathbf{r}_j$ which is produced by exciting the reference structure with a LEED beam with parallel momentum $\mathbf{k}_{\|}$. $A^j_{\ell'' - m''}(-\mathbf{k}_{\|} - \mathbf{g})$ is the amplitude of a spherical partial wave of a time-reversed LEED state with parallel momentum $-\mathbf{k}_{\|} - \mathbf{g}$. $S^j_{\ell m, \ell' m'}$ is analogous to a structure factor and has the form

$$S^j_{\ell m, \ell' m'} = i^{-(\ell + \ell')} j_\ell(\kappa |\delta \mathbf{r}_j|) Y_{\ell - m}(\delta \mathbf{r}_j) j_{\ell'}(\kappa |\delta \mathbf{r}_j|) Y_{\ell' - m'}(\delta \mathbf{r}_j) \exp(i \mathbf{g} \cdot \mathbf{r}_j) , \qquad (2.34)$$

where j_ℓ is a spherical Bessel function. The form factor only depends on the scattering properties of the reference structure and only needs to be computed once. The structure factor depends on the distorted structure; therefore, only the structure factor needs to be reevaluated each time the surface is perturbed.

The structure factor is summed over angular momentum, ℓm. In principle this would require summing from $\ell = 0$ to $2\ell_{max}$ since the t-matrix has values up to ℓ_{max}. However, the spherical Bessel function decreases with increasing ℓ, so

$$S^j_{\ell m, \ell' m'} \approx 0 \qquad \text{for } \ell \text{ or } \ell' \geq \kappa \delta r .$$

In addition, since two Bessel functions are multiplied together in the structure factor then terms for which

$$\ell + \ell' \geq \kappa \delta r ,$$

can be neglected. This allows the tensor or form factor to be truncated and this leads to a considerable reduction in computational time relative to other methods.

34

The tensor LEED calculation is essentially split into two parts. In the first part a full dynamical LEED calculation is performed on a reference structure. As the program calculates the scattering amplitudes of the exiting beams the elements of the tensor are calculated and stored in an output file. The second part of the tensor LEED calculation involves perturbing the reference structure geometry and calculating the change in the scattering amplitude, δA. The diffraction intensities from the perturbed surface, which we call a trial structure, are compared with the set of experimental intensities. Since the second part of the tensor LEED calculation is very fast at calculating how a displacement of an atom affects the change in the scattering amplitude, this method is very amenable to being combined with an automated search algorithm. The difficulty is finding a good method for searching through a multidimensional parameter space.

One important question that we have not mentioned is how far can an atom be displaced before the tensor LEED approximation breaks down. Previous work by Rous [2.12] suggested a radius of convergence, outside of this radius the tensor LEED approximation does not yield reliable results, of 0.4Å. We adopted a more conservative estimate of 0.2-0.25Å. We cannot emphasize enough that the result of a tensor LEED calculation should always be checked by doing a full dynamical LEED calculation on that geometry!

References

2.1 M.A Van Hove, W.H. Weinberg, and C.-M. Chan, **Low-Energy Electron Diffraction** (Springer-Verlag, 1986), p. 119.

2.2 M.A Van Hove, W.H. Weinberg, and C.-M. Chan, **Low-Energy Electron Diffraction** (Springer-Verlag, 1986), p. 121.

2.3 V.L. Moruzzi, J.F. Janak, A.R. Williams, **Calculated Electronic Properties of Metals** (Pergamon, New York 1978).

2.4 J.L. Beeby, J. Phys. C **1,** (1968) 82.

2.5 S.Y. Tong and M.A. Van Hove, Phys. Rev. B **16** (1977) 1459.

2.6 M.A. Van Hove and S.Y. Tong, **Surface Crystallography by LEED** (Springer-Verlag Berlin Heidleberg, 1979) p. 49.

2.7 S.Y. Tong, Prog. Surf. Sci. **7,** (1975) 1.

2.8 J.B. Pendry, **Low Energy Electron Diffraction** (Academic, London 1974).

2.9 M.A Van Hove, W.H. Weinberg, and C.-M. Chan, **Low-Energy Electron Diffraction** (Springer-Verlag, 1986), p. 174.

2.10 J.B. Pendry, J. Phys. C **13,** (1980) 937.

2.11 P.J. Rous and J.B. Pendry, Surf. Science **219,** (1989) 355.

2.12 P.J. Rous, Prog. Surf. Sci. **39,** (1992) 3.

Chapter 3.   Video LEED Techniques

3.1.   Introduction

Various techniques have been used to obtain experimental I-V curves over the past 20 years. The Faraday cup assembly [3.1, 2] and spot photometer [3.3] were the most common methods used in the 1970's. A less common photographic method was developed and used by this group during the mid-1970's [3.4]. With the advent of video cameras sensitive at low-light levels, particularly vidicon cameras, and computer data acquisition boards which operate at video rates, typically 10-20 MHz, I-V curves are now typically acquired with video/computer-based acquisition systems. This procedure was first used by Heilmann et al [3.5] to measure diffraction spot profiles; the system was based on a vidicon camera, a TV monitor, a computer, and a time base. Later, Lang et al [3.6] modified this system with the addition of a video tape recorder (VTR) to decrease the data-acquisition times. Shorter acquisition times allowed I-V data collection for electron-beam sensitive adsorbate systems and substrate/adsorbate systems which are sensitive to residual gas adsorption (e.g. clean transition metals). A similar video LEED system was assembled and used in this group in the 1980's [3.7]. One drawback with this system was that the video signal was degraded by storing the video images on magnetic tape. With the large magnetic hard drives, 40-200 MB, available today the video images can be quickly and easily transferred from the frame buffer of the video processor to the hard disk without degrading the integrity of the video signal.
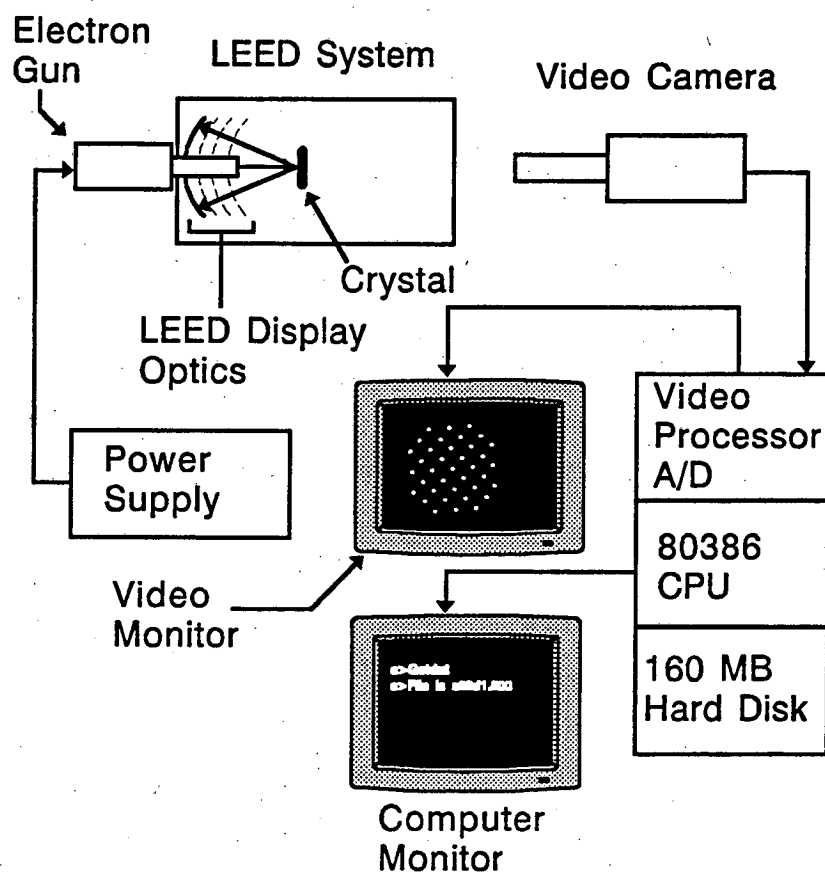
Figure 3.1   Block diagram of video LEED apparatus

The video LEED data acquisition system that was assembled and used in this work consisted of a video camera, a computer, and a TV monitor. A block diagram of the system is illustrated in Figure 3.1. The video camera and the video processor board are discussed below in detail.

3.2. Camera Overview

Video cameras are used for a broad spectrum of purposes, ranging from night surveillance to camcorders for recreational use. The same technology which is used in applications for night surveillance and astronomy is useful for the measurement of LEED intensities from a phosphor screen. This requires a camera which is sensitive under low-

light level conditions. Closed circuit video cameras used for night surveillance are good for low-light level situations but have the drawback that they are not fast to respond to moving objects in the scene. However, these cameras are excellent for video LEED applications where this drawback is not a concern.

A video camera is composed of 1) a taking lens which focuses light from a scene onto 2) a video transducer which converts the light from the scene into an electrical current which is proportional to the brightness of the scene, 3) a video amplifier which amplifies the output signal from the video transducer and 4) a signal processor which shapes the video signal to yield the video output signal. The video output signal is the analog signal which is sent to the video processor board.

3.2.1. Optical Elements

The optical element of a video camera is the taking lens which is available in a number of focal lengths and sizes. The aperture diameter of the lens is adjusted with a mechanical iris, which operates much like the iris of the human eye, and can only be changed in increments. The aperture diameter settings on the iris ring are calibrated in f-stops. An f-stop is defined as $F=f/D$ where f is the focal length and D is the diameter of the aperture. Clearly, larger f-stops correspond to smaller apertures and consequently allow less light to enter the camera. Typically the smallest f-stop is desirable for acquiring video LEED data with the constraint that the diffraction intensities do not saturate the camera.

The depth of field and field of view are other characteristics of the camera which are partly determined by the lens. The depth of field is the range of distances over which objects remain in focus. It increases as the aperture decreases, higher f-stop settings, but is also affected by the focal length and the distance away from the camera. In addition, the depth of field increases with increasing distance. In the specific case of video LEED data acquisition the depth of field is not really an important consideration in adjusting the f-

stop setting even though the LEED screen is hemispherical and diffraction beams near the detector edge are closer to the camera than beams near the center of the detector (the depth of the detector is only ~0.8cm for a Varian LEED screen). This was determined empirically by observing that the entire LEED pattern could be focused at once. Therefore, we concluded that the f-stop setting should be adjusted to provide the maximum signal.

The field of view is defined as the angle of acceptance of the camera and can be written mathematically as

$$\theta = 2\tan^{-1}\frac{h}{2f} \,,$$ (3.1)

where f is the focal length of the lens and h is the height of the image sensor for a solid-state device or the height which is rastered for a video tube. This is illustrated in Figure 3.2. Since the LEED screen is circular we are interested in the field of view in the vertical direction. From equation (3.1) we can see that the field of view increases as the focal length decreases. The field of view is an important consideration when choosing a taking lens. A lens which captures the entire LEED screen and provides the largest image possible on the video monitor is desirable because the user-interactive analysis is easier if the diffraction spots are separated as much as possible in the image. This is particularly true for LEED patterns with a high density of diffraction beams.

Simple spherical lenses are not used for TV lenses because of chromatic and spherical aberrations. Chromatic aberrations occur because different wavelengths of light are refracted by different amounts, for instance blue light is bent more than red light. This is called dispersion and is the same phenomenon that occurs in a prism. Therefore, light composed of different wavelengths will not come to a common focal point (e.g. blue light will be focused at a point nearer to the lens than red light). Spherical distortion occurs

40
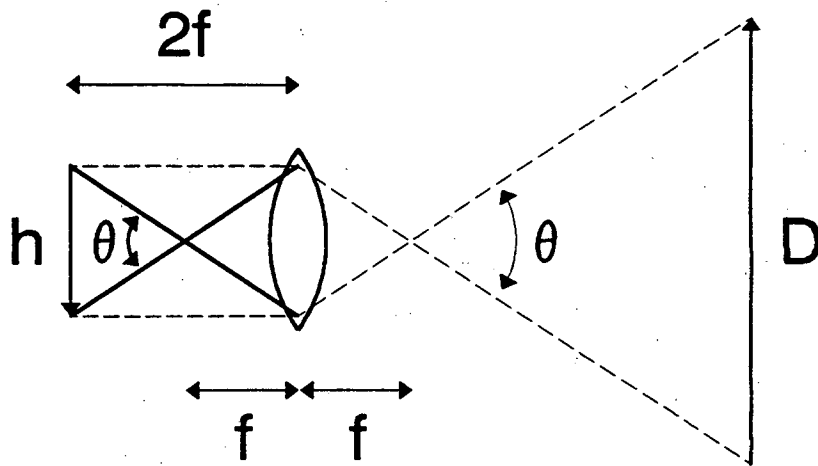
Figure 3.2 Field of view. D is the diamter of the LEED screen, h is the height of the image sensor, f is the focal length of the lens, and θ is the field of view.
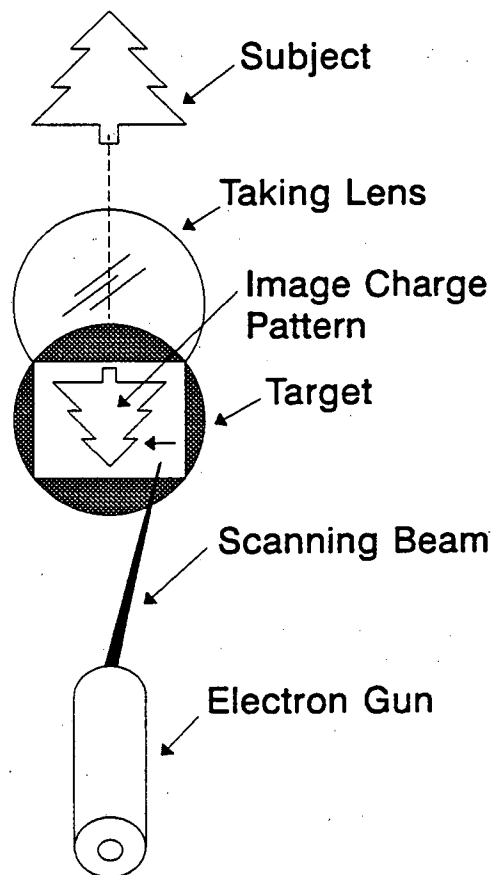
Figure 3.3 Illustration of the video camera imaging process. The electron gun and target are components of the video tube.

41

because a truly spherical lens does not have one focal point. Both spherical and chromatic aberrations are corrected with a convex-concave compound lens which combines a convex lens made of crown glass with low dispersion and a concave lens made of flint glass with a higher dispersion [3.8].

3.2.2. Video Transducer

Video transducers are devices which convert electromagnetic waves into an electrical signal. This is accomplished with video tubes (e.g. vidicons) or solid-state devices [e.g. charge-coupled devices (CCD) or charge injection devices (CID)]

Video tubes are vacuum tubes composed of 1) a storage target which stores a image charge pattern and 2) an electron gun which produces an electron beam which scans the target. In Figure 3.3 the imaging process of a camera with a video tube is illustrated. Many types of video tubes are commercially available but only those that were used in this work will be discussed in detail.

In Figure 3.4 the elements of the electronics for a video tube camera are illustrated. The sync generator produces the vertical (V) and horizontal (H) sync which drives the magnetic deflection of the scanning electron beam. The signal from the video tube enters a preamp where it is amplified prior to being sent to the signal processor. The signal processor shapes the video signal and makes various corrections. The signal from the signal processor is combined with the composite sync, both horizontal and vertical, to form the video output. Notice in Figure 3.4 that the output has a 75Ω characteristic impedance. All short distance connections to other devices (e.g. video monitor and video processor) should be made with coaxial cable with a 75Ω characteristic impedance to prevent energy from being reflected back to the source [3.9].
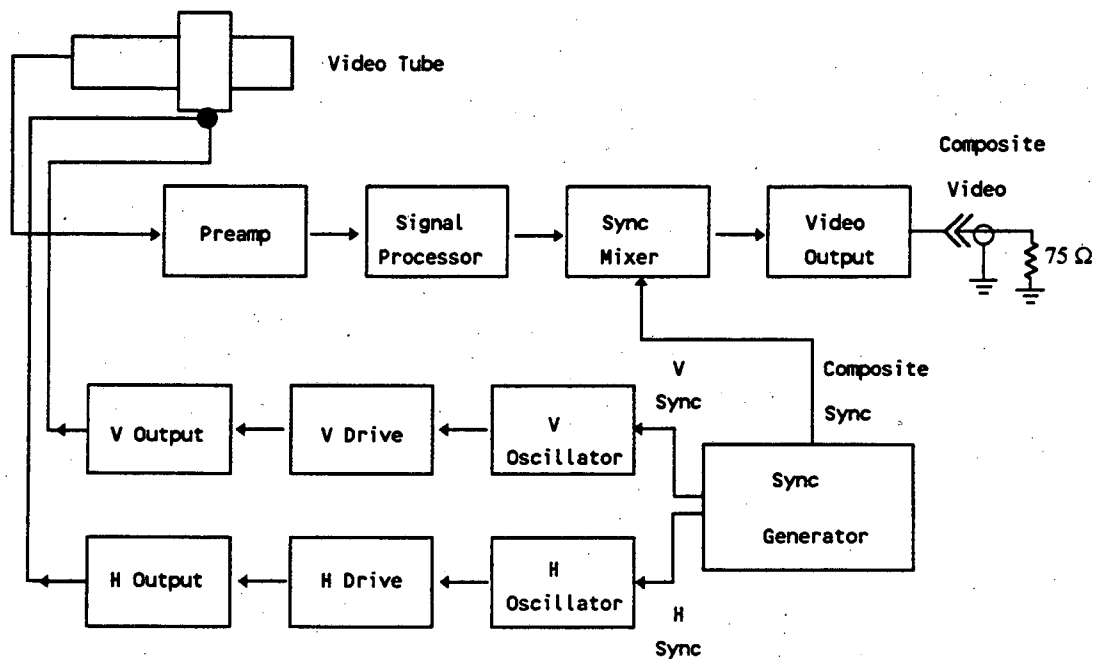
Figure 3.4   Video camera block diagram

Although video tubes were used exclusively in this work, solid-state image sensors are also available. Solid-state image sensors (e.g. CCD) are not vacuum tubes but are large-scale integrated circuits with an array of individual microscopic "photo sites". The resolution of these devices is determined by the density of photo sites.

3.2.3. Video Amplifier

The video output is a signal composed of the video signal corresponding to the brightness of the scene plus the synchronization pulses. The composite signal is $1V_{pp}$ (1 Volt peak-to-peak) of which 714mv corresponds to the video signal and 286mV to the synchronization pulses. The synchronization pulses are negative with respect to blanking. Blanking is the turning off of the electron beam at the end of a horizontal or vertical scan. The black level is set at 54mV above blanking. The composite video signal is illustrated in
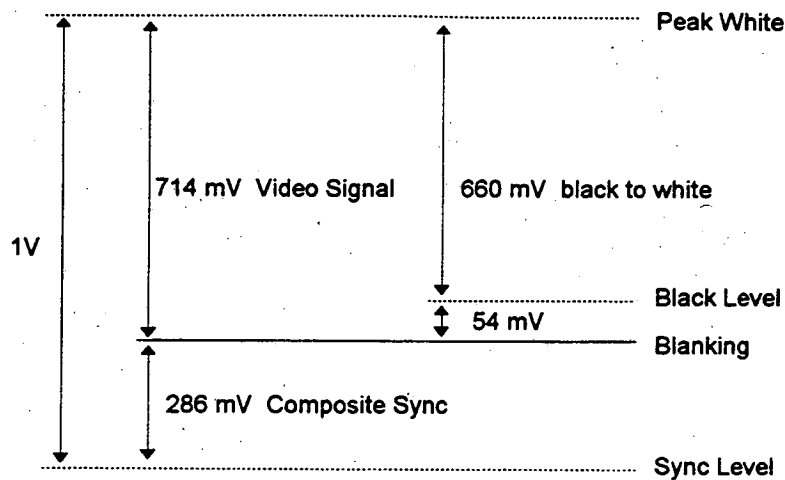
Figure 3.5   Schematic of composite video output signal

Figure 3.5. For instrumentation cameras such as those used in this work the black level is under external control so that the user may optimize the contrast of the image. More important than this is that for accurate photometric work the camera black level and gain must be kept constant once they have been optimized. In commercial video cameras the black level and gain are adjusted internally to provide the best picture.

The amplifier bandwidth is determined by the desired resolution of the video image. In 1/30 s 525 horizontal lines are scanned, 42 of them are for vertical blanking, which means that one horizontal scan takes 63.5 μs. The video processor digitizes one video line into 512 pixels. One active scan takes 63.5 μs - 11 μs (horizontal blanking) or 52.5 μs. This corresponds to 512/52.5 = 9.8 MHz. According to the Nyquist sampling theorem, the sampling frequency must be twice the highest frequency component in the signal [3.10]. So approximately a 20 MHz bandwidth is needed to obtain the desired 512 pixel resolution. The video amplifier for the intensified silicon intensified target (ISIT) camera has an adjustable bandwidth of 6-18 MHz in 6 MHz increments and an 18 MHz bandwidth for the vidicon camera. For the ISIT camera a 6 MHz bandwidth is typically

used because the signal-to-noise ratio for the intensities is better at lower spatial resolution.

3.3. Video Tubes

This section is a detailed discussion of the video transducers, more specifically the video tubes, that were used in this work. The two types of video tubes, vidicon and ISIT, are discussed first, with an emphasis on the differences between the two. Next the components which the two tubes have in common are discussed. Finally, the characteristics of the video tubes and their relevance to video LEED data acquisition are discussed.

3.3.1. Types of Video Tubes

3.3.1.1. Vidicon

A vidicon tube consists of a photosensitive silicon target for producing and storing an image charge pattern and an electron gun which generates an electron beam which rasters across the image charge pattern. First, light passes through a transparent conducting film and then impinges on the target generating electron-hole pairs in proportion to the intensity of the light. The holes migrate to the back of the target because a positive bias is applied to the front of the target and the back of the target is essentially at the cathode, usually ground, potential. The electron beam rasters across the back of the target and neutralizes the holes that constitute the image charge pattern. Excess electrons are turned back toward the electron gun. The exact number of electrons needed to neutralize the holes constitute a flow of current between the electron gun cathode and the target. This signal current generates the output signal voltage of the pickup tube which is sent to the preamplifier and the signal processor. A vidicon tube is illustrated in Figure 3.6.
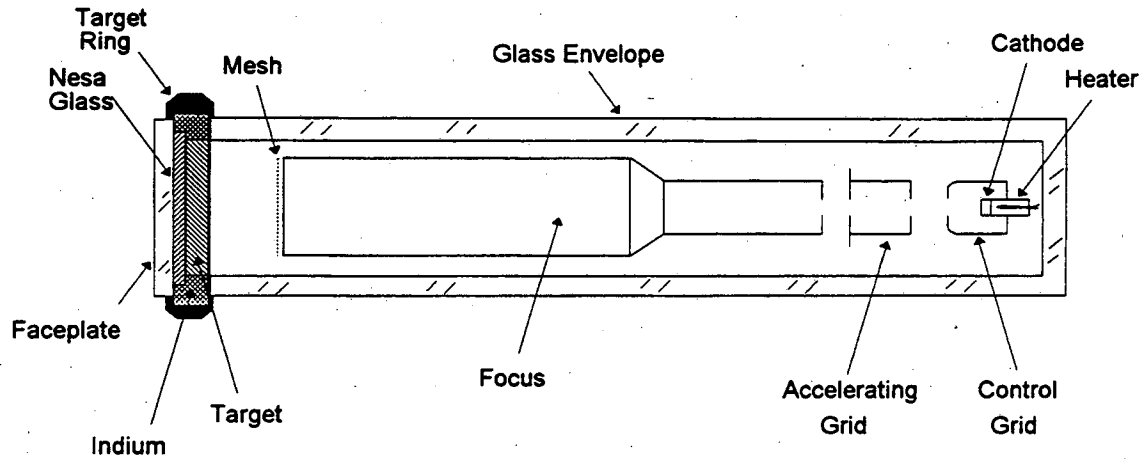
Figure 3.6   Schematic of a vidicon tube

3.3.1.2.   Intensified Silicon Intensified Target (ISIT)

Silicon intensified target (SIT) and intensified silicon intensified target (ISIT) camera tubes are very good for low-light level applications and are even better than vidicon cameras because both have intensification stages. SIT and ISIT tubes use a photoemissive cathode as a light sensitive detector and a silicon-diode array, which contains 1800 diodes per square inch, to store the image charge pattern. The gain of the SIT and ISIT arises from the large number of electron-hole pairs that are generated when the photoelectrons from the cathode bombard the silicon target, for example a SIT tube with 9kV across the intensifier section will have a gain of about 1600 [3.11].

The ISIT tube is illustrated in Figure 3.7. The two image sections provide the intensification. In the SIT tube only one image section is used, i.e. the phosphor screen and the photoemissive coating are absent. The photoelectrons from the photocathode and photoemissive coating are focused by means of electrostatic lenses which are not shown in the diagram.
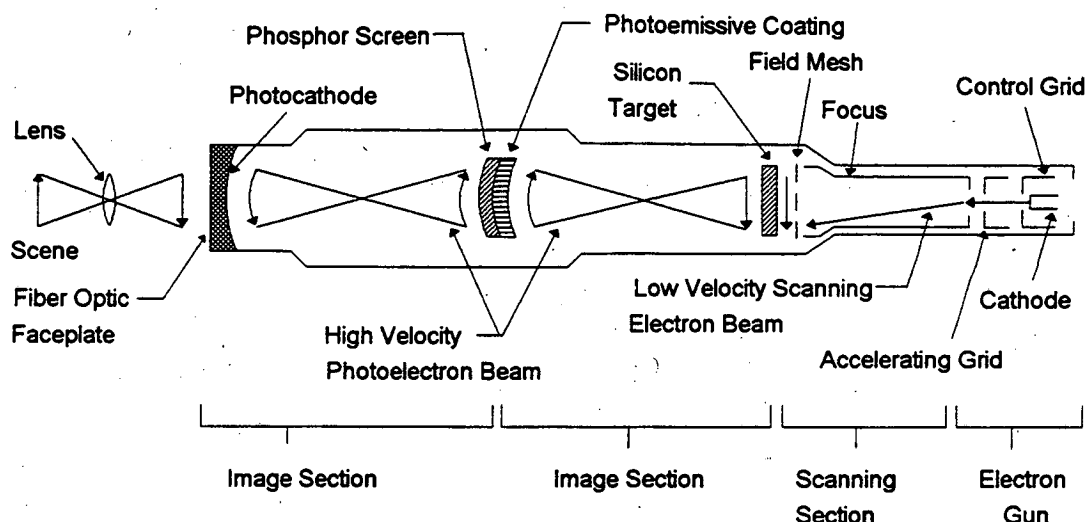
Figure 3.7   Schematic of ISIT tube: The light from a scene enters the ISIT tube through a fiber optic faceplate which transfers the flat-scene image onto the curved photocathode. The photocathode emits photoelectrons which are focused onto a phosphor screen which has a photoemissive coating which emits photoelectrons which are focused onto the silicon diode-array target. An image charge pattern is formed on the back of the target and is scanned by an electron beam.

The photocathode is a S-20 multi alkali compound (Na-K-Cs-Sb) and is coated onto a curved fiber-optic faceplate. The fiber-optic has poor UV transmission and limits the tubes response in the UV region (340nm cut off). The near-IR region is also not accessible since the silicon target is bombarded with electrons. This is in contrast to the silicon target vidicon which is sensitive to the near-IR. The phosphor screen is coated with a P-20 phosphor.

The ISIT tube has greater sensitivity than the SIT tube but the ISIT tube has a lower signal-to-noise ratio. The SIT tube is sufficiently sensitive for collecting I-V data from ordered LEED patterns and is less expensive than the ISIT tube. The ISIT camera may be a good choice for diffuse LEED intensity measurements, where the background intensity of a LEED pattern is measured, but the intensified CCD may be a better choice. No comparisons were made between ISIT and intensified CCD cameras. The ISIT camera used in this work was loaned by Dage-MTI as a demonstration model. A SIT camera was later purchased with the intention of using it for recording LEED I-V data from LEED patterns of well ordered surfaces.

47

3.3.2. Basic Components of Video Tubes

3.3.2.1. Target

The target of the video tube is circular and comes in a few common sizes: 25mm (1 inch), 18mm (2/3 inch), and 13mm (1/2 inch) diameters. Only a small rectangular area, with an aspect ratio of 4:3, in the middle of the target is actually scanned by the electron beam. For a 18mm target, which was the size of the targets used in this work, the diagonal measurement of the usable portion of the target is 11mm [3.12]. This implies that only 23% of the target area is actually used.

The spectral sensitivity of the target depends on its chemical composition. Many of the vidicons use doped silicon targets to tailor the spectral sensitivity for a broad range of applications. For video LEED purposes the spectral sensitivity of the target should be matched to the spectral characteristics of the phosphor of the LEED screen.

3.3.2.2. Electron Gun and Video Scanning

The electron beam scanning is accomplished by magnetic deflection of the electron beam. The coils which produce the magnetic fields fit over the video tube. The electrons are accelerated at high voltages, hundreds of volts in this context, towards the target to reduce the effects of space charge, thereby obtaining a sharp spot on the target. The electrons are typically decelerated prior to colliding with the target to reduce damage and heating of the target. The scan is typically interlaced which means that two scans are used to produce one frame of video. The first scan rasters only the even horizontal lines and the second scan rasters the odd horizontal lines. Interlacing reduces flicker on a television monitor and is the standard format for television applications. Since each part of an interlaced scan takes 1/60 s, one frame requires 1/30 s. Therefore, 30 images/s are acquired in the RS170A video format. Alternatively, the European standard operates at 50 Hz and 25 images/s are acquired.

A scan is divided into an active scan and blanking. Blanking occurs when the

electron beam is cut off. Horizontal blanking occurs at the end of a horizontal trace and vertical blanking occurs at the end of the scan. In the RS170A format there are 480 active lines of scan and 42 lines of vertical blanking.

3.3.3. Characteristics of Video Tubes

3.3.3.1. Dark Current

The dark current, the target current which occurs when no light impinges on the target, is produced by the thermal generation of electron-hole pairs. Therefore, the dark current is a function of target temperature which results from two sources: 1) the ambient temperature and 2) heating of the target by the electrons bombarding the back of the target. This second effect means that the target temperature depends on the target voltage which is the bias applied between the target and the electron gun cathode. The dark current limits the ultimate sensitivity of the camera.

3.3.3.2. Blooming

Blooming is a condition which occurs when an area on the silicon target becomes saturated. Saturation occurs when the photon flux incident on the target exceeds a certain limit and a large number of electron-hole pairs are generated. Normally the holes do not migrate parallel to the target because the target is almost an insulator and the target bias is applied perpendicular to the target. Blooming is exhibited in the image of a LEED pattern by a "comet tail" effect, i.e. the circular spots become elongated in the direction of the electron gun raster. Blooming is an indication that a diffraction beam has saturated the video camera. The integrated intensity from a diffraction spot that exhibits blooming is not very reliable. Although the integration does to some extent offset the effects of blooming because the integration window is always made larger than the diffraction spot.

3.3.3.3.   Image Lag

Image lag is the persistence or slow decay of an image after an object in the scene has changed position or has been removed entirely. Image lag time is a measure of how quickly the video tube responds to changes in the scene. Image lag is sometimes due to the capacitance between the electron gun side of the target and the Nesa glass terminal. However, for targets thinner than 2.5 μm, as is normally the case, the capacitance is very small and does not contribute very much to lag. In this case, lag occurs because the carrier mobility is reduced by 1) trapping by defects and impurities and 2) collisions with atoms in the target. Therefore, lag becomes worse at higher current densities when more carriers are present. Image lag was not an important consideration in this work because the LEED incident electron beam energy was increased manually. Even in the case of computer control of the electron gun, the power supply must be allowed to stabilize before recording data. The Varian LEED power supply used in this work stabilizes on the order of milliseconds and even then image lag would probably still be insignificant.

3.3.3.4.   Gamma

The response of the video tube to the faceplate illumination is called the gamma of the tube. If the faceplate illumination (lux) is plotted versus target current (nA) an almost linear curve will be the result. The curve can be fit by a function with the form $y=x^\gamma$, with gamma being equal to one for a linear response. In general, video tubes will have gammas less than one which means that the illumination scale is compressed at higher faceplate illumination. A tube with a linear response, $\gamma=1$, is necessary for accurate intensity measurements. The cameras used in this work had gammas equal to one.

3.3.3.5.   Camera Resolution

Camera resolution refers to the smallest picture element that can be resolved. The major factor which determines resolution in video tubes is the diameter of the electron beam striking the target. Therefore, if more spatial resolution is desired a larger target is

used. This is the physical limit of camera resolution but as mentioned earlier the bandwidth of the video amplifier determines if this limit is actually realized. Additionally, the taking lens also contributes to the resolution of the camera.

3.4. Video Processor

To acquire the video data in a format that can be stored and manipulated by the computer requires an A/D (analog/digital) computer board. To obtain the data in real time the board must be capable of operating at video rates, 10-20 MHz, and have enough memory to store a video image, 1 MB. Many such boards are commercially available today. The video processor used in this work was a Matrox MVP-AT Video Digitizer. The accompanying software used to operate the video digitizer was the Imager-AT MS-DOS Software Library. This is a library of functions which can be used in programs written in Microsoft C or FORTRAN. The library functions are used to control input and output operations of the video board and for image processing.

The board can be divided into seven functional sections.

1) The Input Section selects the video source. Additionally, it contains logic to adjust the gain and offset, lookup tables, and analog to digital converters which digitize the analog video signal.

2) The Memory Section consists of 1 MB of video RAM which stores the video information. The Memory Section is accessible by all the other MVP-AT sections and the host computer.

51

3) The Statistical Section is composed of a STAT processor and STAT RAM which performs intensity histograms and profiles. This section was not used by the computer programs in this work.

4) The Graphics Section is composed of a Hitachi ACRTC and provides many drawing primitives, e.g. lines, circles, rectangles, etc. This section provided the cursor for the LEED analysis programs.

5) The Display Section converts the contents of the video memory into video which is sent to the display, a video monitor in the case of this work. This section contains output lookup tables and user-programmable display features such as overlays (mixing graphics with video), windows, and keying (mixing video memory contents with an input signal).

6) The Arithmetic Section consists of an ALU, Arithmetic Logic Unit, which performs all arithmetic and logical functions on one frame buffer, between one frame buffer and a constant, or between two frame buffers. The ALU functions in real time which allows arithmetic and logical operations with a camera input. This allowed the successive video frames to be averaged in real time during the data acquisition.

7) The Processor Section consists of an on-board microprocessor.

When an image is grabbed by the MVP-AT board the intensity level of each pixel in the image is measured and assigned a value that is proportional to the intensity. For monochrome, black and white, an 8-bit value is assigned to the pixel intensity. This

52

effectively provides a gray-scale with 256 levels, 0 for completely black and 255 for completely white.

The pixel values are sent to an Input Lookup Table (ILUT) which uses the pixel intensity as an address. At each address in the ILUT a value is stored. The value in the ILUT becomes the new intensity of the pixel which is subsequently stored in the frame buffer. This allows the user to modify the incoming image in a known way. The default ILUT used in this work did not alter the pixel intensities.

The 1 MB of video RAM is partitioned into frame buffers. The computer programs in this work used four basic frame buffers which were four 512x512x8-bit frame buffers. In the American video format only 480 lines of the 512 are displayed and processed. A frame buffer contains a set of addresses which correspond to each pixel in the video image. At each pixel address an 8-bit intensity value is stored. The contents of these frame buffers may be displayed on the video monitor or may be manipulated by the host computer.

The video data acquired in this work was averaged by grabbing a frame and storing it in a 512x512x8-bit source buffer. Then the contents of the source buffer were added to a 512x512x16-bit accumulator buffer. After 128 video frames had been grabbed and the contents of each had been added to the accumulator buffer, the contents of the accumulator buffer were divided by 128 and stored in a 512x512x8-bit destination buffer. This procedure averaged 128 frames of video in real time which required a little more than 4 seconds since 30 frames per second is the acquisition rate.

The contents of the destination buffer were stored on the hard drive before the frame buffers were reset to zero and another image was acquired. After all the images were acquired and stored on the hard drive, the images could be analyzed. The analysis required loading the image from the hard drive into a frame buffer in the video processor.

All the data processing and input/output control was done with the library of functions provided with the video board.

The contents of the frame buffers were displayed on the video monitor. Prior to being displayed the contents of the frame buffer are sent to an output lookup table (OLUT) which functions much like an ILUT except that the OLUT does not affect the contents of the frame buffer. The OLUT can be used to provide a contrast function which will enhance the features of interest in the image. The OLUT used in this work did not alter the contents of the frame buffer before displaying it on the video monitor.

References

3.1   C.J. Davisson and L.H. Germer, Phys. Rev. **30** (1927) 705.

3.2   H.E. Farnsworth, Phys. Rev. **34** (1929) 679.

3.3   F. Jona, Discss. Faraday Soc. **60** (1975) 210.

3.4   P.C. Stair, T.J. Kaminska, L.L. Kesmodel, G.A. Somorjai, Phys. Rev. B **11** (1975) 623.

3.5   P. Heilmann, E. Lang, K. Heinz, K. Muller, Appl. Phys. **9** (1976) 247.

3.6   E. Lang, P. Heilmann, K. Heinz, K. Muller, Appl. Phys. **19** (1979) 287.

3.7   D.F. Ogletree, Ph.D. Thesis, Berkeley, 1986.

3.8   Saville Bradbury, **An Introduction to the Optical Microscope** (Oxford University Press, 1984) p. 34.

3.9   Gerald P. McGinty, **Video Cameras: Operation and Services** (Howard W. Sams & Company 1984) p. 253.

3.10 H.V. Malmstadt, C.G. Enke, and S.R. Crouch, **Electronics and Instrumentation for Scientists** (Benjamin/Cummings Publishing Company, Inc. 1981) p.406.

3.11 G.A. Robinson, RCA Engineer **22** (1977) 47.

3.12 Gerald P. McGinty, **Video Cameras: Operation and Services** (Howard W. Sams & Company 1984) p. 70.

II. Specific Experimental Procedures

Chapter 4. Experimental Procedures

4.1. Introduction

Accurate surface structure determinations require well characterized surfaces prepared under known conditions. These surfaces are typically well-oriented single crystals which are free of contaminants and atomically flat with well ordered adsorbates. Ultra-high vacuum (UHV), $\leq 1 \times 10^{-9}$ Torr, conditions are necessary to obtain and maintain a clean surface for the duration of a typical surface science experiment, 20-60 minutes. Residual gases in a well-baked UHV system, e.g. CO and H_2, may adsorb onto the surface, particularly a clean metal, during an experiment and alter the surface structure.

4.2. The UHV System

4.2.1. Pumps

The UHV system used in these studies was a stainless steel UHV chamber which was pumped by a 240 l/s diode ion pump and a 60 l/s triode ion pump. A schematic of the UHV system is given in Figure 4.1. The triode ion pump, which is not shown in the figure, had a higher pumping speed for noble gases and was intended to be used as an auxiliary pump during Ar^+ ion sputtering; however, the base pressure of the system was lowest when both ion pumps were used. This is most likely because of the poor conductance caused by the Mu metal shielding inside the main chamber which had holes for the mass spectrometer, manipulator, sulfur source, glancing angle electron gun, and ion sputter gun.

Manipulator

Sulfur Source

Quadrupole Mass
Spectrometer

LEED/AugerOptics
(Retarding Field Analyzer)

Variable Leak
Valve

Single Crystal

Gate Valve

Ion Pump
200l/s

Gas Manifold
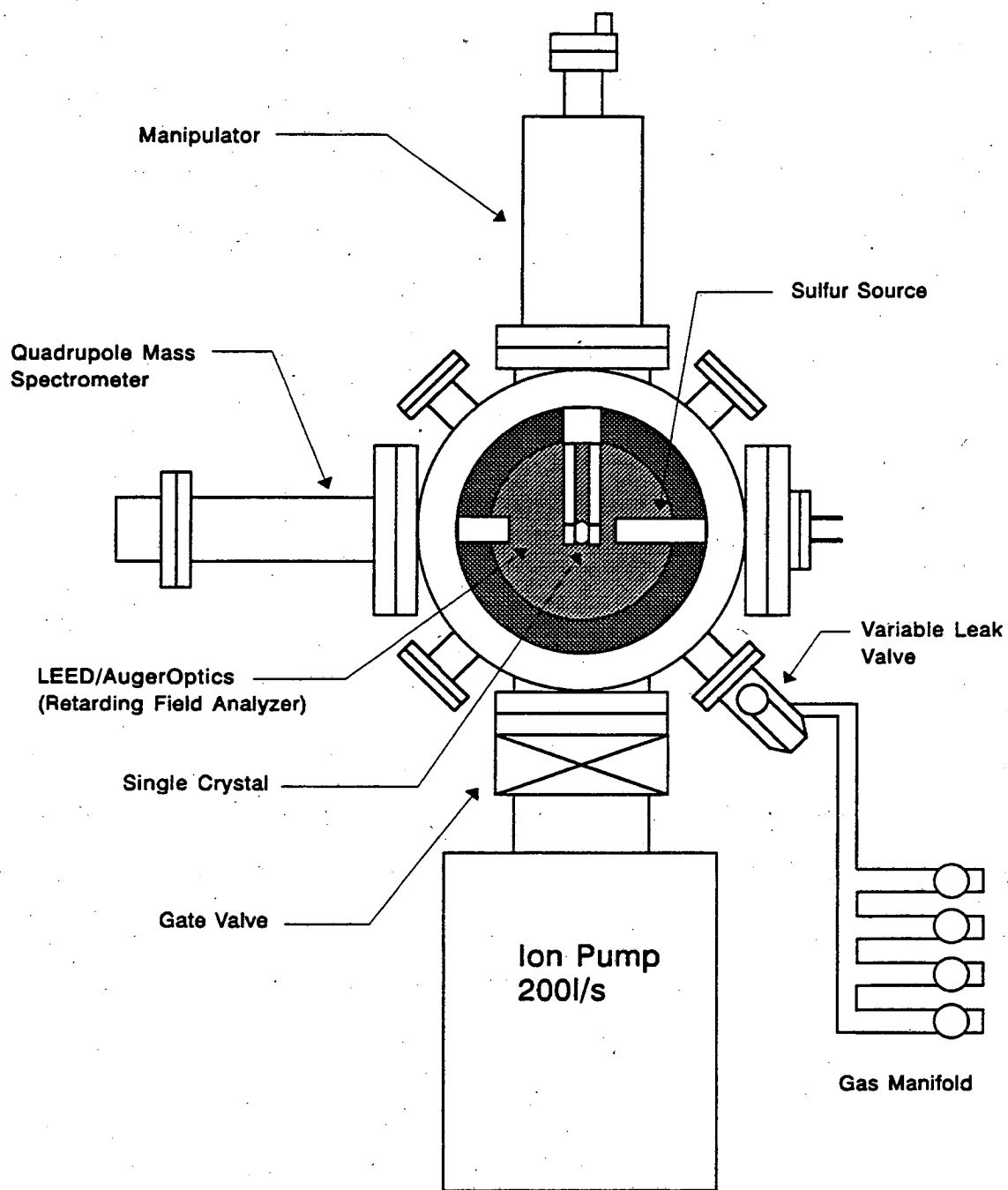
Figure 4.1   Schematic of Video LEED apparatus

4.2.2. Ion gauge

All pressures reported are uncorrected for ion gauge sensitivities, conductance, and other restrictions. The only calibration that was made was adjusting the emission current to 4 mA and all reported pressures are for N_2 calibration. A 1.5 mm diameter doser attached to a Varian leak valve was used to admit gases into the chamber.

4.2.3. Bake-out

A UHV system after first being pumped down has a large amount of water adsorbed strongly to the stainless steel walls of the chamber and it slowly desorbs from the walls, thereby limiting the lowest base pressure. To obtain pressures $\leq 1 \times 10^{-9}$ Torr in a reasonable time the entire chamber must be heated uniformly above 150°C for 1-3 days depending on the size of the UHV system and the pumping speed of the pumps. Ion pumps must be baked-out under the same conditions as the chamber.

A bake-out oven, which was constructed of 1/16" Al sheet metal on the outside with a layer of fiberglass insulation followed by heating elements, covered the upper portion of the UHV system. It could be disassembled and stored when not in use. The lower portion of the chamber, the two ion pumps, was surrounded by a similarly constructed enclosure. During a bake-out, the system was heated between 160-185° C for approximately three days. After the bake-out the filaments were outgassed and the titanium sublimation pump (TSP) filaments were heated numerous times which gave an ultimate base pressure of $\sim 2 \times 10^{-10}$ Torr.

4.2.4. Manipulator

The manipulator used in these experiments was on-axis and had 5 degrees of freedom, x, y, z translation, polar rotation, θ, in a plane perpendicular to the manipulator axis, and a tilt. In Figure 4.2 a schematic of the manipulator is provided. A Vespel block, which provided thermal and electrical isolation, was attached to the center rod. Two 3/8" Cu rods were attached to the Vespel block and an 1/8" Ta rod was inserted at the end of each Cu rod. A 0.030" sheet of Ta was spot welded to each Ta rod and to each sheet was spot welded a 0.0015" Ta tab to which the sample was spot welded. This arrangement allowed the sample to be heated to 2000-2100K and for the sample to be oriented at normal incidence with respect to the LEED electron gun. This design also minimized the amount of the LEED screen that was obscured by the manipulator, which is an important consideration when I-V measurements are made with a front view LEED optics.
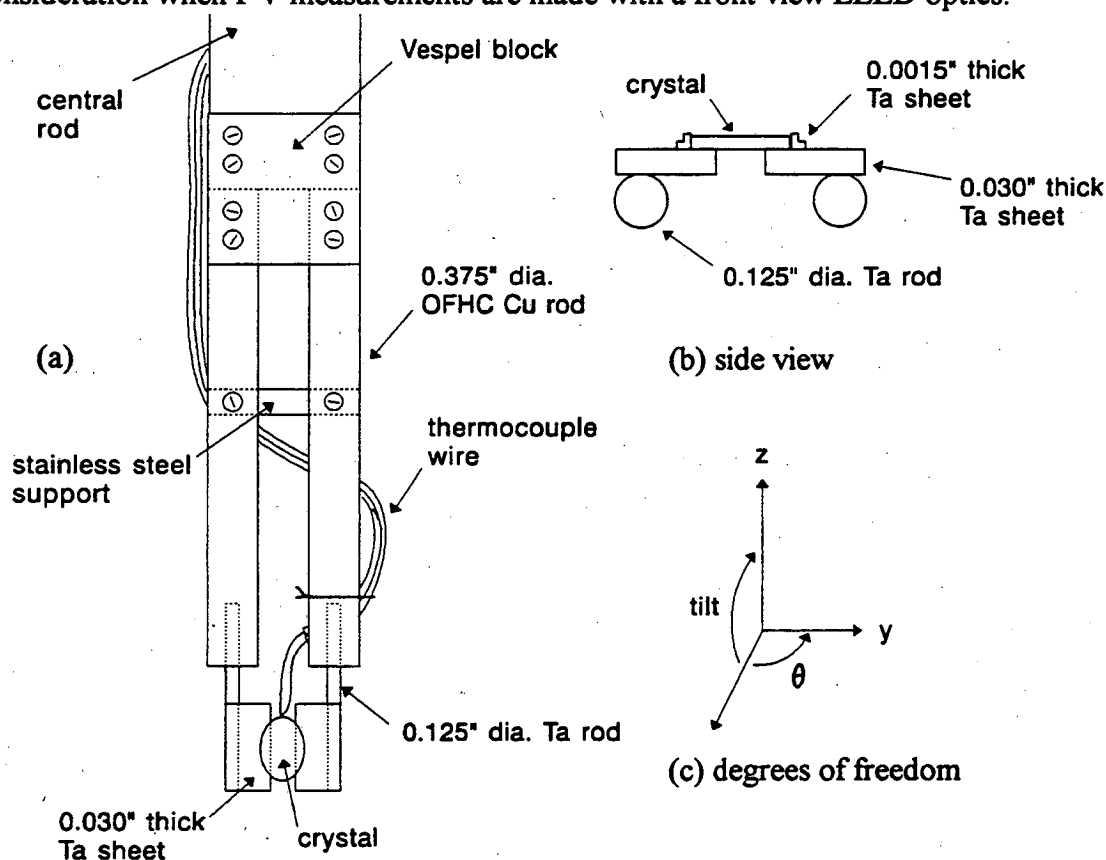
Figure 4.2   (a) Schematic of manipulator, (b) side view of mounted sample and (c) degrees of freedom of manipulator shown in (a)

60

4.2.4.1. Sample Heating

Heating of the sample was accomplished by resistive heating with a power supply capable of delivering 100A. Resistive heating is accomplished by passing AC or DC electrical current through the sample. The electrical resistance of the sample gives rise to I^2R heat loss. Typically, the spot welds are the highest resistance points in the electrical circuit and thermal conductivity is poor through the small cross sectional area spot welds; therefore, the sample heats at an appreciable rate. The optimal sample mounting consisted of spot welding the Re or Mo sample to 0.0015" Ta tabs which were each spot welded to a 0.030" Ta plate (see Figure 4.2b). The Ta tabs were much hotter than the sample while the sample was being heated. The Re sample required in excess of 100A of current to heat the crystal to 2000-2100K, because of its large thermal mass. After many cleaning cycles the sample became hot, 60-100°C, and water cooling was necessary to reduce the temperature of the manipulator and sample.

4.2.4.2. Sample Cooling

Cooling with liquid nitrogen (LN_2) would have been desirable but when this was attempted the thermally induced stress caused the spot welds between the sample, both the Re(0001) and Mo(100), and supports to break; therefore, water cooling was used instead. LN_2 feedthroughs were connected to the two 3/8" Cu rods of the manipulator by copper braids. The braids were connected to the Cu rods about 3" away from the sample which did not provide the best thermal conduction; however, with a Rh(311) sample spot welded in the same configuration the sample was cooled to ~170K with LN_2 cooling.

4.2.4.3. Temperature Measurement

Sample temperature was measured with a W-5%Re/W-26%Re thermocouple. Since Mo is very difficult to spot weld to W, the thermocouple was spot welded to the back of the sample with a 0.0015" Ta foil sandwiched between the thermocouple and the

61

Mo sample. This was not necessary in the case of the Re sample since Re is relatively easy to spot weld to W.

4.3. Surface Analytical Techniques and Instrumentation

4.3.1. Low-Energy Electron Diffraction

The LEED apparatus consisted of a Varian four-grid LEED optics and an "off-axis" electron gun which was described in Chapter 1. The LEED screen was coated at Lawrence Berkeley Laboratory (LBL) with P-11 phosphor, which has a fluorescence peak at λ_{max} = 460nm with a FWHM (full width at half maximum) of 62nm (Sylvania Technical Information Bulletin), in a potassium silicate binder. A bias between 5-7 kV was applied to the LEED screen to obtain diffraction spot intensities that were measurable with the video camera.

4.3.2. Auger Electron Spectroscopy

Auger electron spectroscopy (AES) was used to determine the cleanliness of the sample and the chemical composition of the adsorbate-substrate systems. The LEED electron gun was used at approximately normal incidence with a beam energy of 1.5 keV to induce core-level excitations and the four-grid LEED optics was used as a retarding field analyzer to energy analyze the secondary electrons.

The first derivative of the N(E) spectrum was taken electronically by superimposing an AC modulation, $V_{pp} \approx 7V$ and $\nu \approx 2.7$ kHz, onto a DC voltage ramp. The first and fourth grids of the four-grid LEED optics were at ground potential. The second and third grids had the DC ramp with the AC modulation superimposed on them. The

second harmonic which is proportional to the first derivative of the N(E) spectrum was detected with a phase-sensitive lock-in amplifier.

4.3.3. Residual Gas Analysis

A UTI 100c quadrupole mass spectrometer was used for residual gas analysis and helium leak checking of the chamber. It was located in a port exactly opposite to the sulfur source (see Figure 4.1).

4.4. Sample Preparation

4.4.1. Single Crystals

The Mo(100) sample used in these experiments was oriented with Laue X-ray back-reflection, cut with an electric discharge machine (EDM), and polished according to standard metallurgical procedures. The sample was oriented within 1° of the [100] direction. The Mo(100) sample was a ~7x5x0.5mm oval disk.

The Re(0001) sample used in these experiments was loaned by Atomergic Chemicals Corporation (NY). The Re(0001) sample was a circular disk with a 7mm diameter and was ~1mm thick.

4.4.2. Sample Cleaning

The cleaning procedures for Re and Mo are very similar since both are refractory metals. Refractory metals have high melting points, are brittle, and difficult to machine. Often they are used as heat shields because they oxidize at higher temperatures than other metals. The carbon and sulfur are removed from the surface of both metals with an
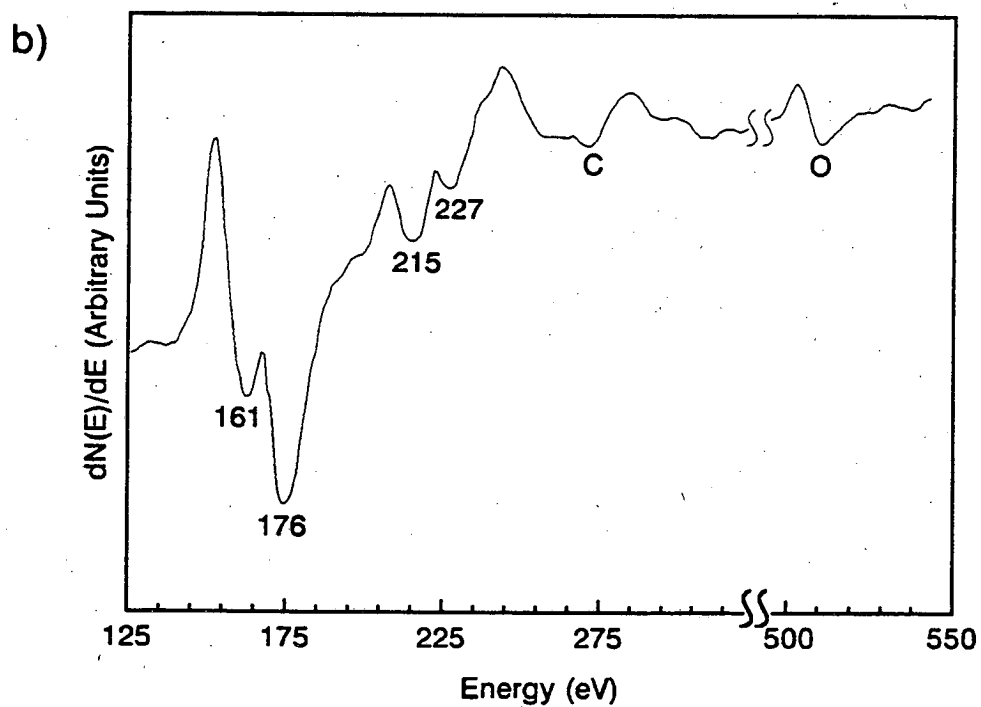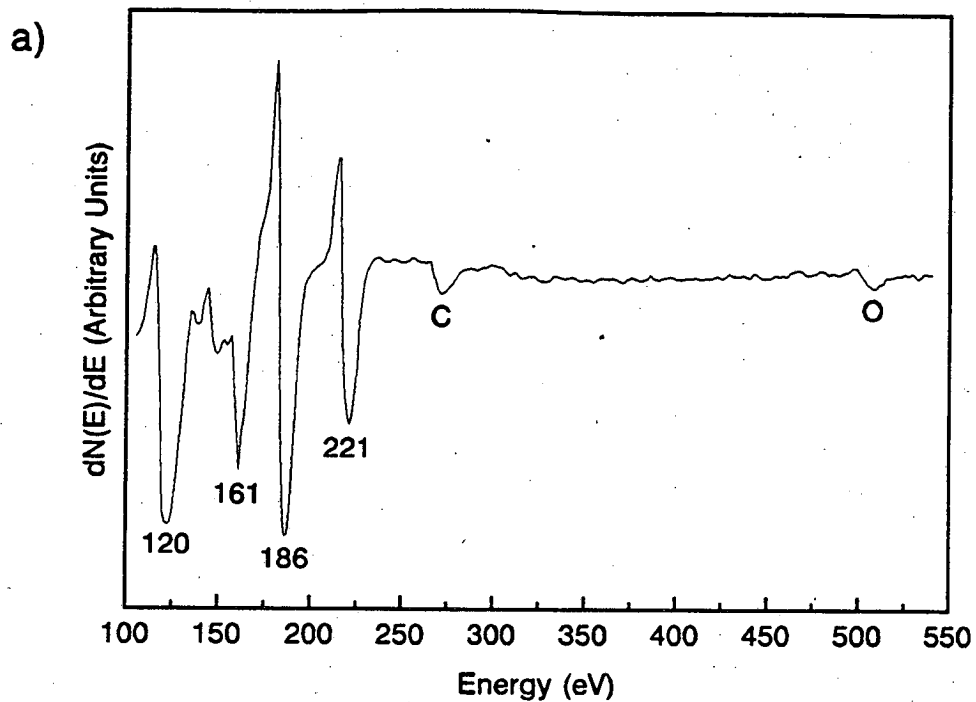
Figure 4.3   Auger spectra of a) Mo(100) and b) Re(0001) contaminated with carbon and oxygen. The numbered peaks in a) and b) refer to the Auger transitions of Mo and Re respectively.

64
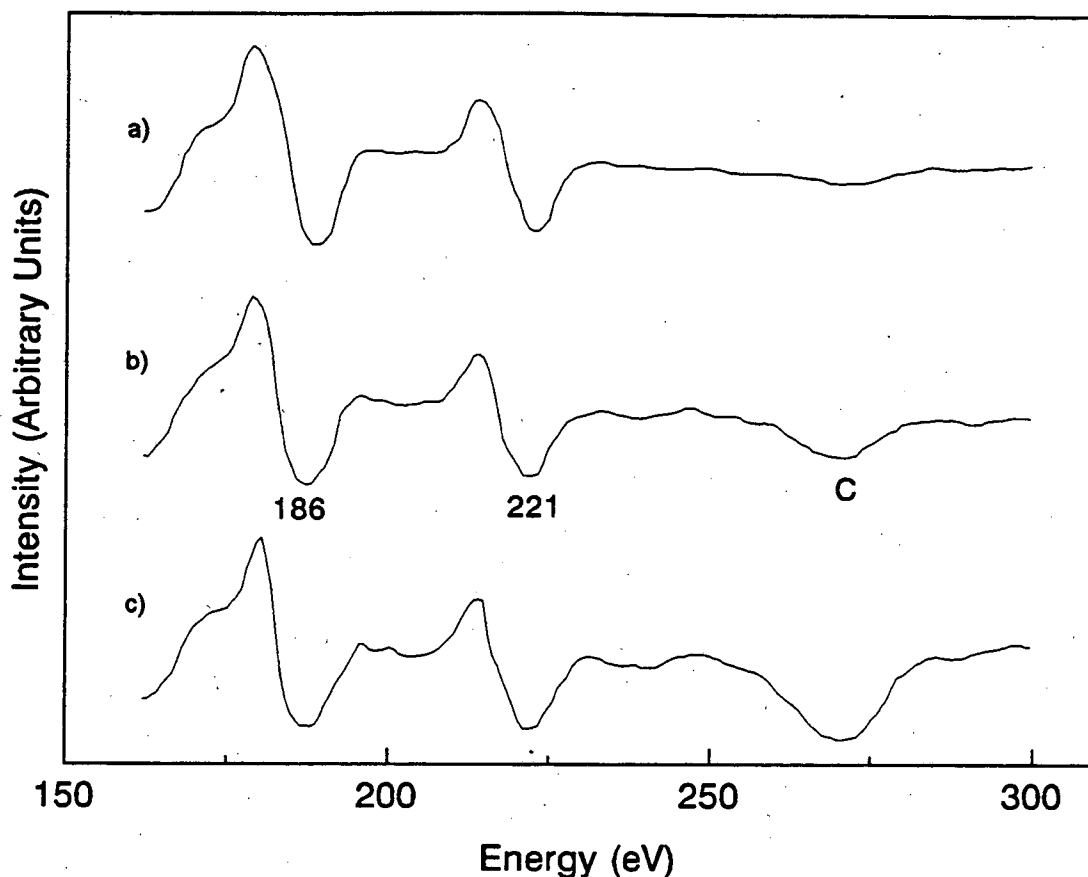
Figure 4.4 Auger spectra of Mo(100) a) immediately after an oxygen treatment b) 30 minutes after a) was taken and c) 1 hour after a) was taken.

oxidation treatment which consists of heating the metal in O_2 and then rapidly heating the crystal to a temperature at which the metal oxide desorbs. Carbon is the most difficult contaminant to remove. In Figure 4.3 Auger spectra of contaminated Mo and Re are presented. Carbon could never be completely removed from the Mo or Re surface according to AES. The working pressure in the chamber was $8\text{-}9\text{x}10^{-10}$ Torr and CO readily adsorbs onto the surface and dissociates at room temperature in the case of Mo. This made it difficult to maintain a clean surface. In Figure 4.4 a series of Auger spectra are shown for different times after an oxidation treatment. The difficulty in maintaining a clean surface prevented us from taking I-V curves of the clean Re(0001) and Mo(100)

surfaces since a typical experiment took 30-45 minutes because we had to manually increment the electron incident beam energy.

Rhenium required numerous cleaning cycles which consisted of heating the sample in 1×10^{-6} Torr O_2 at 1620K for 90s followed by flashing the sample to 2130K for 15-30s.

Molybdenum also required numerous cleaning cycles (on the order of 100) which consisted of heating the sample in 5×10^{-7} Torr O_2 at 1700K for 30s followed by flashing the sample to 2000 - 2100K.

4.4.3. Preparation of Sulfur Overlayer

4.4.3.1.   Electrochemical Sulfur Source

The sulfur source used in these experiments was a solid-state electrochemical cell: Pt/Ag$_2$S/AgI/Ag which has been described in detail elsewhere [4.1]. The source was heated between 150-180°C and a constant current supply was used to generate currents on the order of 40μA. A variety of sulfur clusters are emitted by the source with S_2 being the predominant species as verified by the mass spectrometer. If a voltage was applied across the cell an increase in the mass 64 peak was observed. If the voltage was removed then the mass 64 peak decreased. The sulfur source extended from the flange such that it obscured part of the LEED optics, see Figure 4.1, but allowed the sample to be positioned within 1mm of the source nozzle. Auger spectra of the Mo(100) surface prior to depositing sulfur and after depositing sulfur are shown in Figure 4.5.

4.4.3.2.   H$_2$S

Sulfur deposition was also accomplished by adsorption of H_2S from a leak valve attached to a gas manifold and subsequent dissociation to sulfur and H_2 by heating the sample. Two methods were used to deposit sulfur with H_2S. In the first method, H_2S was adsorbed onto the crystal by backfilling the chamber with 5×10^{-8} Torr of H_2S at room temperature. Then the crystal was heated to the temperature necessary to obtain the
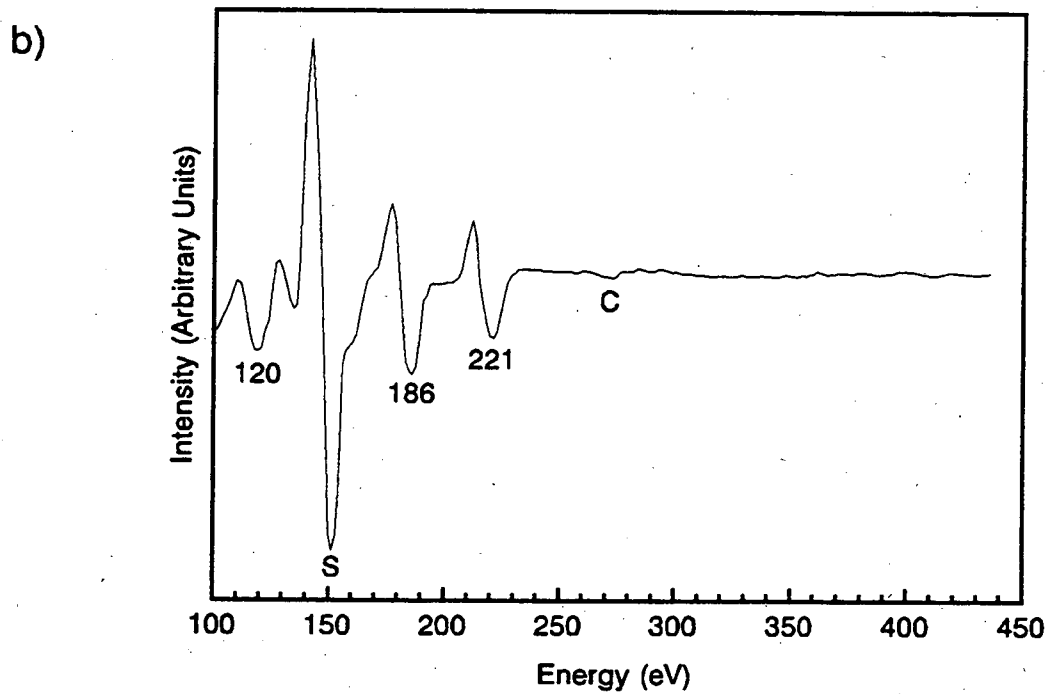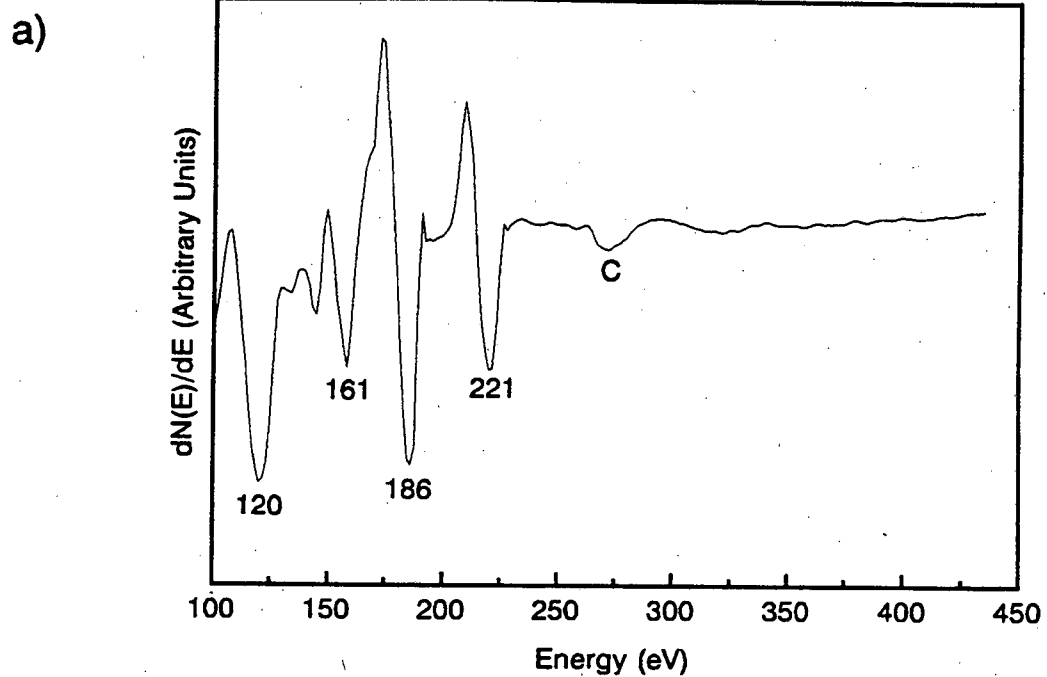
Figure 4.5 Auger spectra of a) Mo(100) prior to depositing sulfur and b) Mo(100) after sulfur was deposited. The numbered peaks are the Auger transitions of Mo.
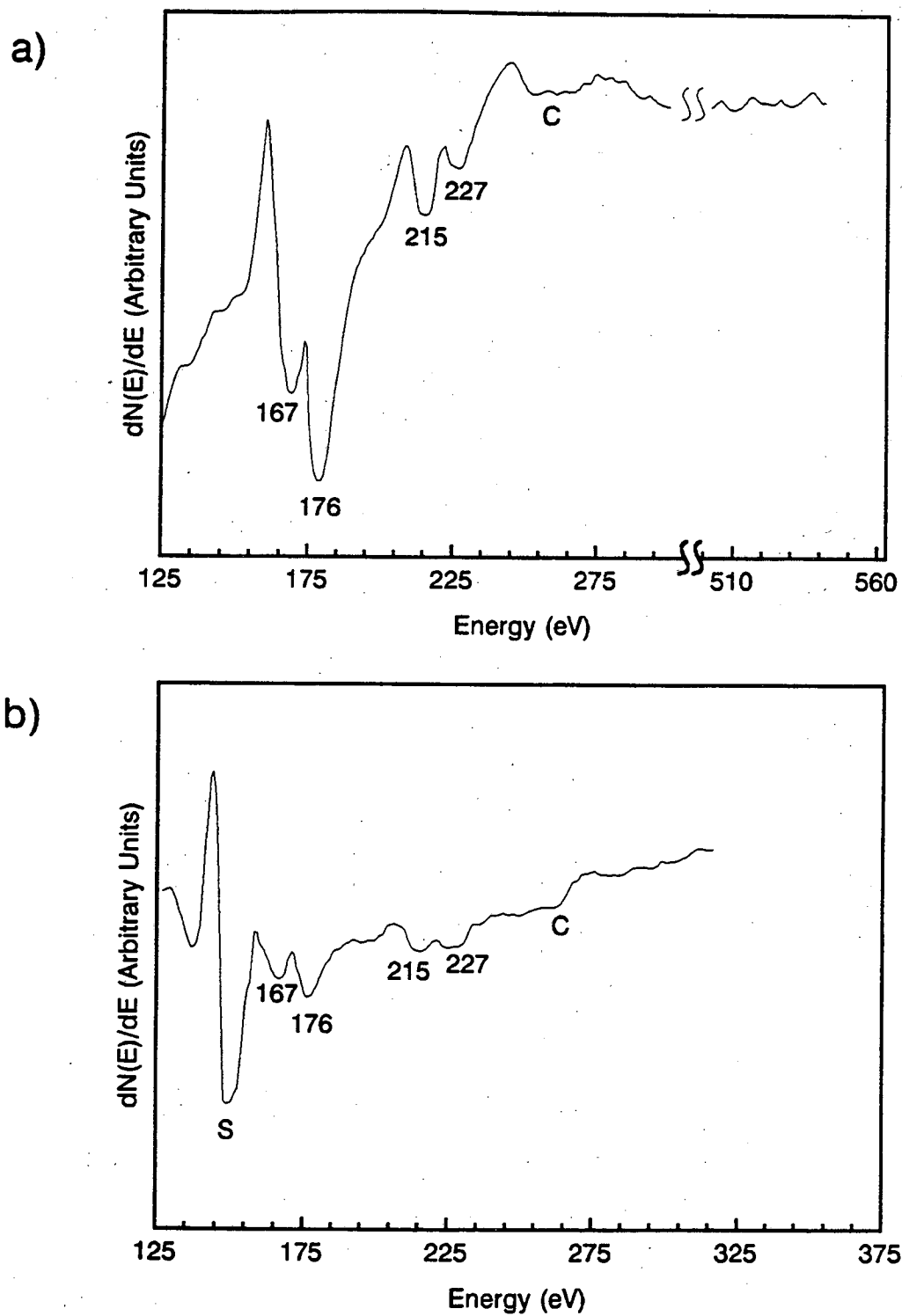
Figure 4.6   Auger spectra of Re(0001) **a)** prior to depositing sulfur and **b)** after sulfur was deposited. The numbered peaks are the Auger transitions of Re.

desired coverage. In the second method, the crystal was heated to the required temperature as H_2S was introduced into the chamber. Both procedures worked equally well. The H_2S was purchased from Matheson and had a minimum purity of 99.5%. The gas manifold was pumped down with a mechanical pump then H_2S was admitted into the gas manifold. Auger spectra of the Re(0001) surface prior to depositing sulfur and after depositing sulfur are shown in Figure 4.6.

Both methods of deposition, the sulfur source and H_2S, caused the base pressure of the chamber to rise to ~1×10^{-9} Torr after repeated deposition and subsequent desorption of sulfur. Using the TSP reduced the base pressure by a marginal amount, but a 2-3 day bake-out restored the chamber pressure to 4 - 5 $\times 10^{-10}$ Torr.

4.5. LEED I-V Measurements

4.5.1. Sample Alignment

The effect of a misaligned crystal on the observed LEED pattern and the measured integrated intensities was a concern in this work. The following discussion addresses these issues. In Figure 4.7 the misalignment of the crystal is illustrated for two different cases: a) the crystal is positioned too far away from the LEED optics and b) the crystal is positioned too close to the LEED optics. The ideal position of the crystal is at the focal point. When this occurs the LEED pattern displayed on the fluorescent screen is undistorted.

If the crystal is not at the focal point then a diffracted electron beam with exit angle θ will have a trajectory that is not radial with respect to the LEED optics. In this case the electron velocity, v, will have a radial, v_r, and a tangential, v_t, component. This is

69

shown in the enlarged portions of Figure 4.7. If the angle between v and v_r is φ then the following relationships exist

$$v_r = v\cos\varphi , \qquad (4.1)$$

$$v_t = v\sin\varphi . \qquad (4.2)$$

If the Law of Sines is used for the geometry depicted in Figure 4.7a the following relationship is obtained relating φ and θ

$$\frac{r}{\sin\theta} = \frac{d}{\sin\varphi} . \qquad (4.3)$$

With a simple rearrangement equation (4.3) can be put into the form

$$\sin\varphi = k \, \sin\theta ,$$

where k=d/r. If the Law of Sines is applied to the geometry depicted in Figure 4.7b the following relationship is obtained

$$\frac{r}{\sin\theta} = \frac{d}{\sin(\pi - \varphi)} . \qquad (4.4)$$

Since $\sin(\pi-\varphi) = \sin\varphi$, then equation (4.4) is equivalent to equation (4.3); therefore, equation (4.3) can be applied to both cases illustrated in Figure 4.7. If d, r, and θ are known then φ, v_r, and v_t can be determined. In Tables 4.1 and 4.2 the values of the radial and tangential velocity components and the angle φ are tabulated for θ=15° and θ =50° respectively. The angle φ indicates the amount by which the beam position on grid 2 deviates from the true value of θ. In Figure 4.7a a dotted line is drawn from the focal point to grid 2 which has an angle θ between it and the center line. This is the position that the

Table 4.1   The radial and tangential velocity components and the angle φ are tabulated for θ=15°.

k	1/12	1/6	1/3	1/2
v_r/v	0.9998	0.999	0.996	0.992
v_t/v	0.02	0.04	0.09	0.13
φ	1.24°	2.47°	5.0°	7.4°

70

Figure 4.7 In both diagrams the radius of curvature is r, the distance between the focal point and crystal is d, and θ is the exit angle of the diffracted electron beam. The electron gun is perfectly aligned; therefore, the incident electron beam is radial. The grids have 120° of arc or π Steradians of solid angle. In a) the crystal is positioned too far from the LEED optics and in b) the crystal is positioned too close to the LEED optics.

Table 4.2   The radial and tangential velocity components and the angle φ are tabulated for θ=50°.

k	1/12	1/6	1/3	1/2
v_r/v	0.998	0.992	0.966	0.92
v_t/v	0.064	0.13	0.26	0.38
φ	3.7°	7.3°	15.1°	22.5°

diffracted electron beam would have if the crystal were located at the focal point. The actual angle is θ+φ when the crystal is displaced some distance, d, behind the focal point. In Figure 4.7b the angle is θ-φ when the crystal is displaced some distance, d, in front of the focal point. From equation (4.3) one can see that φ is directly proportional to θ so that the distortion of reciprocal space becomes worse at larger values of θ. Beams exiting close to the surface normal, assuming normal incidence, strike the grid close to their ideal position; however, those beams with large exit angles will strike grid 2 relatively far from their ideal positions. This leads to a distortion of the LEED pattern known as the pin-cushion effect. In Figure 4.8 this is illustrated for the two different cases of misalignment. Notice that the distorted LEED pattern in Figure 4.8b, when the crystal is too close to the optics, is smaller than the undistorted LEED pattern in Figure 4.8a. This is in contrast to the situation where the crystal is too far from the optics and the observed LEED pattern is larger than the undistorted pattern. In Figure 4.8b the dotted lines which are straight in Figure 4.8a are bowed in; whereas the opposite effect is depicted in Figure 4.8c where the dotted lines are bowed out. One important note here is that although we have been discussing grid 2 the same geometry and equations apply to the LEED screen since all the grids and screen are concentric. The radius of curvature for a Varian LEED screen is 6.35 cm so the values of k=1/12, 1/6, 1/3, and 1/2 correspond to misalignments d=0.53, 1.06, 2.12, and 3.18 cm respectively in Table 4.1 and Table 4.2.

The polar angle and the tilt angle were the critical parameters to set in order to obtain normal incidence. First the correct distance between the sample and the detector
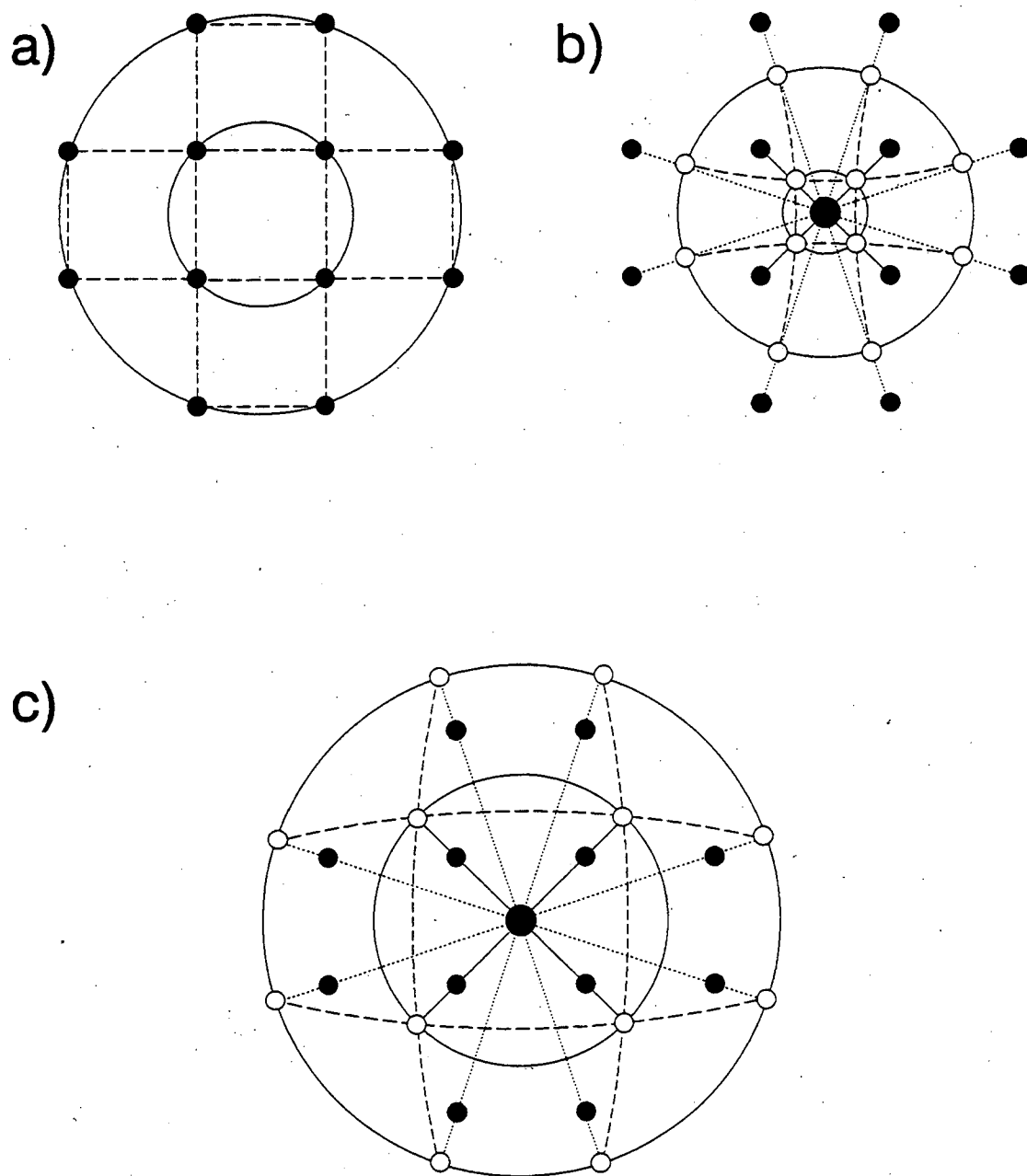
Figure 4.8 In a) a schematic of an undistorted LEED pattern with four-fold symmetry is shown b) the same LEED pattern when the crystal is too close to the LEED optics and c) the same LEED pattern when the crystal is too far from the LEED optics. The symmetry equivalent beams fall on the same circle. The filled spots represent the undistorted LEED pattern and the unfilled spots represent the distorted LEED pattern. The radial solid and dotted lines illustrate the path that the spots are constrained to move along depending upon the amount of misalignment. The dashed lines pass through the observed spots and are straight lines in the case of the undistorted pattern and are curvilinear in the other two cases

73

was determined by placing the sample at the position where the screen darkened homogeneously as the suppressor voltage was decreased. This condition will be satisfied if the sample is at the focal point of the LEED optics. The retarding electric field is radial and only opposes the radial velocity component of the electron trajectory. Additionally, the radial component will be smaller for those trajectories which are farther from the center line connecting the electron gun and the focal point; therefore, the outer portion of the screen will darken first if the sample is not positioned at the focal point of the LEED optics. This will happen for both cases of misalignment shown in Figure 4.7.

Unfortunately, it was very difficult to mount the crystal within the tight tolerances required to both obtain normal incidence and position the sample at the focal point of the LEED optics. This did not change the diffraction spot intensities since we integrate over the entire spot but did distort the diffraction pattern which was apparent from the slight "pin cushion" appearance of the diffraction patterns. The distortion is not easily detected in the LEED photographs unless a straight edge is used. Some distortion may be introduced by the misalignment of the video camera. This is apparent by an oval appearance of the circular edge of the LEED optics. Once again this in not crucial in the measurement of accurate I-V curves since the exact position of the diffraction spots in k-space is not the real concern here.

The sample was initially aligned for the LEED I-V measurements by visually determining that the I-V curves for symmetrically equivalent beams were identical and that these beams reached the detector edge simultaneously as the beam energy was decreased. As was mentioned above, the symmetrically equivalent beams all lie on a circle with its origin at the center of the electron gun if the crystal is at normal incidence. At normal incidence the circle is concentric with the detector edge.

True alignment was determined by recording LEED I-V data and comparing the I-V curves of symmetrically equivalent beams. The quickest method was to first visually

determine if there was a set of symmetrically equivalent beams which were very sensitive to the angle of incidence. This was usually true for a small portion of the I-V spectrum, particularly where there were overlapping peaks. The next step was to measure the I-V spectra of this set of beams and to visually compare the I-V curves. Thus only one set of symmetrically equivalent beams needed to be evaluated over a relatively small energy range (e.g. 25-50 eV) to accurately align the crystal. The alignment was complicated by the fact that no mirror plane of the crystal was parallel to one of the axes of rotation of the manipulator.

4.5.2. Data Acquisition

4.5.2.1.   Camera

All LEED I-V data were acquired with one of two video cameras interfaced to a Matrox MVP-AT video processing board which was installed in one of the expansion slots of an Everex 386/25 personal computer. The raw data were stored on a 160 MB hard disk and subsequently analyzed with a computer program.

The I-V curves for the sulfur/molybdenum structures were obtained with a Dage-MTI Series 68 video camera with an Ultricon III type 4532/U vidicon tube which had a 18mm silicon target. The Ultricon III tube has a broad range of spectral sensitivity from 450 to 900nm. An Apollo 25mm f/0.85 television camera lens was used with this camera.

The I-V curves for the sulfur/rhenium structures were obtained with a Dage-MTI ISIT video camera which was loaned as a demonstration model by Dage-MTI. A Fujinon 35mm f/1.7 lens was used with this camera.

In the case of both cameras the f-stop setting, camera gain, and camera black level were optimized to obtain the largest dynamic range and best contrast.

4.5.2.2. Computer Algorithm for Data Acquisition

The raw data were acquired with a short computer program written in Microsoft C which averaged 128 video frames to generate one image at each energy and stored the image on the hard disk. This averaging procedure increased the signal-to-noise ratio of the experiment. The video image was digitized into 512 x 480 pixels (picture elements) with each pixel intensity digitized to 8 bits of resolution or 256 "gray levels". This procedure produced a two-dimensional intensity map of the entire diffraction pattern at each energy. For all structures two sets of data were taken. Since the substrate beams were often more intense than the superlattice beams, one set of data was taken such that the substrate beams did not saturate the video camera. For the other set the substrate beams were allowed to saturate the video camera so that the weaker superlattice beams could be detected. When a diffraction spot saturates the camera the intensity measurement is no longer reliable for that particular diffraction spot. This procedure in effect increased the dynamic range of the experiment. Since the electron gun power supply was not interfaced with the computer the beam energy was increased manually. After each image was acquired it was transferred from the video frame buffer to the hard disk and the next image was acquired.

4.5.3. Data Analysis

The I-V curves were generated with a computer program also written in Microsoft C. The program follows a diffraction spot as the beam energy is increased and integrates the spot intensity at each energy. This procedure is repeated for every diffraction beam that is included in the analysis.

4.5.3.1. Spot Tracking

Spot tracking refers to centering the integration window around the diffraction spot at each successive energy. Manual tracking of the diffraction spot was used for most

of the analyses. Automated tracking based on finding the largest pixel intensity did not work reliably, although it was later found that looking for the first moment of the intensity worked well. The first moment of the intensity was defined as

$$\bar{I} \cdot \frac{\sqrt{\left(\sum_i I_i \Delta x_i\right)^2 + \left(\sum_i I_i \Delta y_i\right)^2}}{\sum_i I_i} , \qquad (4.5)$$

where $\Delta x_i = x_i - x_c$ and $\Delta y_i = y_i - y_c$ with (x_c, y_c) the coordinates of the center of the integration window and (x_i, y_i) the coordinates of the ith pixel. A user defined window was used for both tracking and integration of diffraction spot intensities. If automated tracking was used it was necessary to monitor the analysis on-line to detect any problems. Some problems included the following:

- the beam is lost when the beam intensity falls below the background intensity level

- the beam disappears behind the manipulator

- the beam moves through some defect on the LEED optics

4.5.3.2. Spot Intensity Integration

The integrated diffraction spot intensities were obtained by positioning the user defined window about either the center of intensity, similar to a center of mass, or the pixel with the largest intensity. The average background intensity around the perimeter of the window was determined first with an equation of the form

$$I_{Bkgd} = \frac{1}{(2n+2m-4)} \sum_j I_j , \qquad (4.6)$$

where I_j is the intensity of the jth pixel on the perimeter of the integration window. For an n pixel by m pixel window there are $2n+2m-4$ pixels on the perimeter. All analyses in this work used n pixel by n pixel windows where n was an odd number. Next the background intensity was subtracted from the intensity of each pixel within the window as the intensities were summed with an equation of the form

$$I_{tot} \cdot \sum_i \left(I_i - I_{Bkgd}\right) . \qquad (4.7)$$

This produced the integrated spot intensity at each energy with the background intensity due to incoherent scattering and electron-phonon scattering subtracted out. This was necessary since the calculated intensities did not account for the background intensity. One important note here is that the integrated intensity is allowed to have a negative value. Although this is not physically realistic, it is possible because the diffraction spot intensity level may be very close to the background intensity level. Oftentimes the I-V curves have negative intensities at the minima of the curves. Since the absolute intensities are not important for the dynamical LEED analysis the I-V curves were shifted upward by adding a constant offset.

The integration window was rectangular in video space because the pixels are rectangular. The video aspect ratio is the American video standard 4:3. Combined with the fact that the video image is digitized to 512 x 480 pixels gives an effective pixel aspect ratio of 5:4. This can be easily understood if we take the image to be 4 inches wide and 3 inches high. Then one pixel is 4/512 inches wide and 3/480 inches high. The ratio of the pixel width to the pixel height is 5:4. This correction was not made to the n pixel by n pixel integration window and its effect is probably minor. Also, a circular window would be more accurate since the spots are typically circular and the one phonon-electron scattering produces a halo around the diffraction spot.

References

4.1   A.J. Gellman, Ph.D. Thesis, Berkeley, 1985.

III. Review of Clean Reconstructed Mo(100) and Adsorption on Mo(100)

Chapter 5.   Review of Clean Mo(100) and Adsorption on Mo(100)

5.1. Review of Clean Mo(100)

5.1.1. The Low Temperature Reconstruction

Since the observation of the reconstruction of clean Mo(100) from (1x1)→ c(2.2x2.2) at temperatures below 200K [5.1], much debate has centered on the exact nature of the reconstruction and the mechanism for the reconstruction. Molybdenum and tungsten are in the same group in the periodic table and both have a body centered cubic (bcc) crystal structure. The reconstruction of the clean W(100) has also been observed by Debe and King [5.2]. They observed that clean W(100) undergoes a phase transformation from the (1x1)→c(2x2) below 370K. The c(2x2) structure is commensurate in contrast to the Mo(100) low-temperature structure, c(2.2x2.2), which is incommensurate. As indicated by Felter et al [5.1], the reconstruction of Mo(100) is due to the periodic displacement of metal atoms and not due to the migration of metal atoms on the surface. The reconstruction in both cases depends only on temperature; however, defects and impurities inhibit the phase transformation.

To explain the reconstruction of W(100), Debe and King [5.2] proposed a zig-zag model which involves a periodic lattice distortion (PLD) with a wavelength of $\sqrt{2}a$, where a is the bulk lattice constant. It is a sinusoidal disturbance in which tungsten atoms in the first layer are displaced along the <11> directions. In Figure 5.1 one domain is illustrated in which the PLD is a longitudinal wave. Another rotational domain with the PLD along $\langle \bar{1}1 \rangle$ is also possible. This type of PLD may explain the reconstruction of Mo(100) except that the wavevector is not a vector sum of the bulk-terminated lattice vectors.
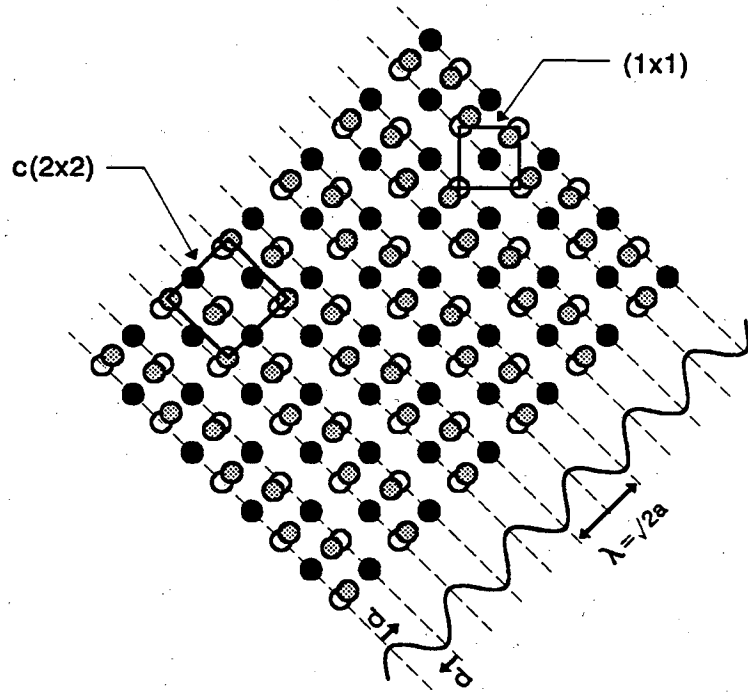
Figure 5.1 Model of reconstructed W(100)-c(2x2) generated by a longitudinal PLD with $\lambda=\sqrt{2}a$ along the <11> direction. The open circles represent the positions of the first layer W atoms in the bulk terminated surface. The shaded circles represent the new positions of the first layer W atoms in the reconstructed surface. The filled circles represent the unreconstructed second layer W atoms. The displacements, **d**, are shown to alternate in direction along the PLD. The displacements are exaggerated.

The model first proposed by Felter et al [5.1] for the low-temperature reconstruction of clean Mo(100) was one in which the sinusoidal variation was perpendicular to the surface such that rows of atoms perpendicular to the <11> directions alternated in height above the second layer. This is a PLD with wavevector, **q**, along the <11> directions and with a wavelength, $\lambda \approx \sqrt{2.2}a$. The magnitude of the vertical displacement is modulated to give the proper wavelength of the PLD.

Later, lateral displacements were suggested to explain the incommensurate reconstruction of Mo(100) [5.3]. The investigation involved a study of the diffraction spot intensities by applying a simple kinematic treatment. The investigators found that perpendicular displacements alone could not explain the diffraction intensities. A kinematic analysis of the diffraction intensities was used to obtain the relation $I \propto J_1^2(\mathbf{k}\cdot\mathbf{d})$, where J_1

is the first order Bessel function, $\mathbf{k} = \mathbf{K} - \mathbf{K_o}$ is the momentum transfer, and $\mathbf{d}$ is the displacement vector. The intensity analysis showed that $d_{\parallel}$ is along the <11> direction. However, the analysis was unable to determine the magnitude of $d_{\perp}$. $\sqrt{2.2}$

A recent analysis reveals that the incommensurate reconstruction of Mo(100) is actually commensurate [5.4]. Apparently, two weak diffraction spots were not observed before. The indexing of this diffraction pattern is a c($7\sqrt{2}$x$\sqrt{2}$)R45°. The investigation used high-energy ion scattering (HEIS) because of its simple real space interpretation and the difficulties in performing a structural determination on a large unit cell by LEED intensity analysis. The HEIS analysis compared the experimental ion yields with the yields calculated from a Monte Carlo simulation of the ion trajectories for a given model structure. An antiphase domain (APD) and the PLD models were used. The vertical displacements were varied as a uniform contraction of the first layer and lateral displacements were varied along the <11> direction. The results were 0.12±0.02Å for the lateral displacements and 7±2% of the bulk interlayer spacing for the vertical displacements. The APD model had a domain wall thickness less than 2 atoms in width. The analysis did not favor one model over the other.

The dynamical LEED analysis for the high-temperature phase, ~300K, of clean Mo(100) was performed by this group [5.5]. The results were lateral displacements of 0.13Å along the <11> direction which were random and produced a disordered "1x1". A uniform contraction of the first layer by 5.4% of the bulk interlayer spacing was obtained. This result differed substantially from the 11% contraction obtained by Ignatiev et al [5.6].

5.1.2. Explanations: Theory and Experiment

A great deal of effort has been expended in attempting to theoretically explain the reconstructions of clean Mo(100) and W(100). Basically, the theories can be divided into two categories (1) those which emphasize collective electronic modes (i.e. the charge-density-wave (CDW) model) and (2) those which use a local bonding description.

5.1.2.1. Charge-Density-Wave (CDW) Model

The charge-density-wave (CDW) model for surface reconstructions was applied by Tosatti and Anderson in 1974 to semiconductor surfaces [5.7]. At that time, they pointed out that Kohn singularities, screening anomalies of the conduction electrons, are greatly enhanced in one and two dimensional systems and may play an important role in the properties of low dimensional systems. The main ingredients of the CDW theory are the following:

1. periodic lattice distortion; a deformation of the lattice which is periodic

2. phonon softening; when the frequency of a phonon mode goes to zero or becomes imaginary

3. charge density wave; a nonuniform periodic distribution of the conduction electrons

A periodic lattice distortion (PLD) will generate a band gap in the electronic bands, which in CDW theory will occur between occupied and unoccupied states. This will result in a lowering of the total electronic energy. If the PLD has a wavevector, q, which spans a nested 2D Fermi surface (a Fermi surface which has large parallel portions) then many occupied electronic states will decrease in energy provided that the energy decrease offsets the increase in elastic energy from the deformation of the lattice. If this occurs then the distorted state becomes the ground state and since the occupied electronic states are nonuniform they form a CDW with wavevector, q.

Another way to think of this is that the electrons distribute themselves nonuniformly in an effort to most effectively screen the Coulombic ion-ion interaction. Because the wavelength of the CDW is the same as that of the soft phonon mode, the formation of the CDW "freezes" in the phonon mode which leads to a periodic lattice distortion (PLD).

The Kohn screening anomaly, which is provided by the surface states, depends on the Fermi distribution of electrons; the Kohn anomaly "sharpens up" as the temperature

84

decreases. This is because only those occupied states on the nested Fermi line contribute to the size of the band gap. A Kohn anomaly, accompanied by nonadiabatic effects which increase electron-phonon coupling, produces a softening of surface phonon modes.

Many of the concepts of CDW theory are not transparent; however, a great deal of insight can be gained by reviewing some of the concepts of screening by conduction electrons.

5.1.2.1.1. Screening by Conduction Electrons

The screening of conduction electrons is central to the CDW model. What follows is a brief summary of the treatment in Ashcroft and Mermin [5.8]. The following model assumes a homogeneous distribution of positive charges representing the ion cores immersed in a free electron gas which represents the conduction electrons. Sometimes this model is referred to as the *jellium model*.

The external charge is the positive charge due to the ion cores. Although the ion cores are physically in the free electron gas, they are considered external to the system of free electrons. Poisson's equation can be applied to $\phi_{ext}(r)$, since the potential is solely due to the positive charges, and yields an equation of the form

$$-\nabla^2 \phi_{ext}(\mathbf{r}) = 4\pi\rho_{ext}(\mathbf{r}) , \qquad (5.1)$$

where $\rho_{ext}(r)$ is the charge density of the ion cores. An analogous equation can be applied to the total potential, $\phi(r)$, due to the positive charges and the screening electrons which has the form

$$-\nabla^2 \phi(\mathbf{r}) = 4\pi\rho(\mathbf{r}) , \qquad (5.2)$$

where
$$\rho(\mathbf{r}) = \rho_{ext}(\mathbf{r}) + \rho_{ind}(\mathbf{r}) , \qquad (5.3)$$

and $\rho_{ind}(r)$ is the charge density of the free electron gas induced by the ion cores. The corresponding Fourier transforms of equations (5.1) and (5.2) have the form

$$\phi_{ext}(\mathbf{q}) = \frac{4\pi}{q^2} \rho_{ext}(\mathbf{q}) , \qquad (5.4)$$

$$\phi(\mathbf{q}) = \frac{4\pi}{q^2} \rho(\mathbf{q}) . \qquad (5.5)$$

Now if $\phi(\mathbf{q})$ is sufficiently weak then $\phi(\mathbf{q})$ and $\rho_{ind}(\mathbf{q})$ can be linearly related. Their Fourier transforms will satisfy an equation of the form

$$\rho_{ind}(\mathbf{q}) = \chi(\mathbf{q})\phi(\mathbf{q}) , \qquad (5.6)$$

where $\chi(\mathbf{q})$ is the general susceptibility which is the quantity which is the most easily calculated. Two elementary theories for calculating $\chi(\mathbf{q})$ exist. The Thomas-Fermi approach makes a semiclassical approximation, requiring ϕ to be a slowly varying function. The other is the Lindhard theory which requires the induced charge of the electron gas to be linearly related to ϕ, the full physical potential. The Thomas-Fermi result is not as accurate at large values of $\mathbf{q}$ as the Lindhard theory. Since we will be interested in large values of $\mathbf{q}$, $q \approx 2 k_F$, we will only consider the Lindhard theory.

We will present only the result of the Lindhard theory of screening which has the form

$$\rho_{ind}(\mathbf{q}) = -e^2 \int \frac{d\mathbf{k}}{4\pi^2} \frac{f_{k-\frac{q}{2}} - f_{k+\frac{q}{2}}}{\hbar^2 (\mathbf{k}\cdot\mathbf{q})\big/m} \phi(\mathbf{q}) , \qquad (5.7)$$

where f_k is the Fermi equilibrium distribution. Equation (5.7) is the Fourier transform of the induced charge to first order in ϕ, the total potential. Using equation (5.6) and integrating at T=0, equation (5.7) becomes

$$\chi(\mathbf{q}) = -e^2 \left(\frac{m k_F}{\hbar^2 \pi^2}\right)\left[\frac{1}{2} + \frac{1-x^2}{4x} \ln\left|\frac{1+x}{1-x}\right|\right] , \qquad (5.8)$$

where $x = \dfrac{q}{2 k_F}$.

Notice that $\chi(\mathbf{q})$ has a singularity at $q = 2 k_F$. From equation (5.7) we can infer from the $\mathbf{k}\cdot\mathbf{q}$ term that the singularity will be greatest for a wavevector, $\mathbf{q}$, which is parallel to $\mathbf{k}$. In addition, the singularity in $\chi(\mathbf{q})$ will be more pronounced when many electronic states have $\mathbf{k}$ parallel to $\mathbf{q}$, since equation (5.7) is integrated over $\mathbf{k}$. This is the

reason that the Fermi surface must have nesting properties, i.e. the Fermi surface must have large parallel segments. The Fermi equilibrium distribution requires that only *occupied* electronic states with k parallel to q contribute to the singularity in $\chi(q)$.

5.1.2.1.2. Soft Phonons

Phonon softening occurs when the frequency, $\omega(q)$, of a phonon mode goes to zero or becomes imaginary. This can occur for values of q that cause the susceptibility, $\chi(q)$, to become singular. From equation (5.8) one can see that as q approaches $2k_F$, $\chi(q)$ diverges logarithmically. For this to occur the Fermi surface must have nesting properties. As mentioned above, nesting refers to large portions of the Fermi surface which are parallel to each other. These parallel sections allow a large number of wavevectors satisfying the relation, $q + G = 2k_F$, to span them. The singularity in $\chi(q)$ exhibits itself in the phonon spectrum by the softening of the phonon mode. These anomalies in the phonon dispersion are known as Kohn anomalies [5.9]. In general, q can be the wavevector of a general disturbance.

In the CDW theory the phonon softening leads to a disturbance in the conduction electrons, known as a charge density wave (CDW). The electrons are scattered by the phonon mode with wavevector, q, from state k to $k + q$, $k + q + G$, etc. where G is a reciprocal lattice vector. This scattering of electrons by the phonon mode sets up a CDW with wavevector, q.

Phonon softening requires relatively strong electron-phonon coupling. This will occur when there is a breakdown in adiabaticity, i.e when the conduction electron velocities are comparable to the velocities of the oscillating ion cores. This will occur when the electronic bands are flat because the group velocity, $d\omega/dk$, is proportional to the slope of the band.

5.1.2.1.3. Applications of the CDW Model

In 1977, Tosatti applied the CDW model to the then recently discovered phase transitions on Mo(100) and W(100) [5.10]. He found that the CDW model did not conflict with the experimental findings for Mo(100) [5.1] or W(100) [5.2]. However, more experiments were necessary to prove or disprove the model's application to these surfaces.

In 1987, Wang, Tosatti, and Fasolino [5.11] performed a molecular dynamics study on the Mo(100) surface. They found that at high temperatures a Σ_1 phonon mode softens signaling an incommensurate transition. Additionally, they found that the low-temperature phase was incommensurate because of a competition between the phonon modes M_1, a vertical distortion, and M_5, an in-plane distortion. The low-temperature result was a structure composed of antiphase domains (APD) of c(2x2) with soliton-like domain misfit walls. Solitons are solitary waves which can collide with other solitary waves and retain their identity. The domains in the APD model are due to the competition between the two phonon modes.

5.1.2.2. Local Bonding Models

Local bonding models have also been used to explain the reconstruction of semiconductor surfaces [5.12]. In the case of semiconductors this seemed reasonable because of the directional covalent bonds that exist in the bulk. For example, on Si(111) the "dangling" bonds may hybridize, from the normally sp^3 hybridized bonds in the bulk, and become more s-like or more p-like, accounting for the (2x1) surface unit cell [5.13].

In 1979, Terakura [5.14] considered a transverse phonon mode with polarization parallel to [100] and a longitudinal mode with polarization parallel to [110]. He used a tight binding method because the d-band energy had been shown to be the most important factor in determining the crystal structure of transition metals [5.15]. He found that the contraction of the first layer enhances electron-phonon interactions to obtain a lower

energy. He concluded that energy lowering from Fermi nesting may be small relative to that obtained from a first-layer contraction. Therefore, the first-layer contraction may stabilize the reconstruction.

McMillan in studying charge density waves in layered-transition metal dichalcogenides suggested a modification to the conventional CDW theory [5.16]. He suggested that the coherence length of the charge density waves is very short and that the phonon entropy is more important than the electronic entropy.

Inglesfield used this modified CDW theory applied to Mo(100) [5.17]. He found that the instability of the surface is the critical factor in the reconstruction. His work showed that surface states are important, but that phonon softening occurs because surface atoms move in an effective temperature-independent anharmonic potential. He also found a uniform surface contraction to be favorable because it increases the interaction of the 4d peak in the density of states with the substrate atoms.

Singh and Krakauer [5.18] performed *ab initio* calculations using a linear augmented plane wave method based on a general potential approximated by local-density to study the energetics of several distortions on the Mo(100) surface. They found that the unreconstructed surface is highly unstable and is not likely to be the high temperature structure. They also found that a surface interlayer relaxation tends to stabilize the ideal surface and is due to short-range interactions resulting from undercoordination of the ideal surface (i.e. dangling bonds need to be satisfied, so to speak). They conclude that the high temperature structure would have correlated displacements comparable to those on the reconstructed surface without long-range order. Roelefs et al indicate that experimental evidence supports this [5.19, 20]. Contrary to the finding of Fasulino, Santoro, and Tosatti [5.21], that short-range repulsive forces are important, Singh and Krakauer found that short-range attractive forces are important.

5.1.2.3. Experiments to Verify or Disprove the CDW Model

The CDW model can be experimentally investigated by mapping out the two dimensional (2D) Fermi surface. For the CDW model to be valid for Mo(100) and W(100) the respective 2D Fermi surface must have nesting properties, that is there must be surface electronic states close to the Fermi level with large parallel segments which can be spanned by a wavevector, q, which has the same magnitude and direction as the PLD observed for the respective surface.

Before discussing the results of the experiments some terms must be defined. The surface Brillouin zone (SBZ) is the projection of the three dimensional Brillouin zone along the crystallographic direction which is perpendicular to the surface. The 2D Fermi surface, however, is not simply the projection of the three dimensional (3D) Fermi surface because there may exist surface states and Rydberg states which modify the projection of the 3D Fermi surface. Two dimensional Fermi surfaces are well approximated as tubular in shape and this geometry leads to more effective coupling of different portions of the Fermi surface [5.22]. This in turn leads to more pronounced instabilities and electronic screening since many occupied states of the Fermi surface can be spanned by a wavevector, q, of a general disturbance.

Smith et al [5.23, 24] used high-resolution angle resolved photoemission spectroscopy to map out the 2D Fermi surfaces of Mo(100) and W(100). They were primarily looking for heavily nested Fermi surfaces to support the CDW model of surface reconstruction on Mo(100) and W(100). If significant nesting does not exist on these surfaces then the CDW model is not valid for these surfaces; but if nesting does exist, it may not be the main factor driving the reconstruction. A previous experimental study found no significant nesting of the 2D Fermi surface of W(100) and the CDW model was discarded [5.25]. However, calculations of phonon dispersions on Mo(100) [5.26] indicate that Fermi surface nesting is important.

Smith et al [5.23] found what they considered to be significant Fermi surface nesting on W(100) and Mo(100). They also found flat, non-dispersive electron bands near the Fermi level, E_F, over significant regions of the SBZ. This is significant because a breakdown in adiabaticity occurs when electron velocities are small relative to ion core vibrations and this occurs when the bands are flat. Additionally, since phonon vibrational energies are generally smaller than electron binding energies, a strong breakdown of adiabaticity will only occur if the flat electron bands are near E_F. Smith et al [5.23] interpret their results to be in agreement with the theoretical results of Wang and Weber [5.27], that an interplay between non-adiabatic effects and Fermi surface phenomena are important in the reconstruction of Mo(100) and W(100).

5.2. Review of Adsorption on Mo(100)

5.2.1. H/Mo(100)

The phase diagram for the H/Mo(100) system is very complex and has received a great deal of attention over the past 15 years because (1) the system provides a good physical model for the study of two dimensional phase transitions, and (2) because the different phases are thought to be due to strong adsorbate-induced reconstruction [5.28]. Two dimensional phase transitions are very interesting from both a theoretical and experimental viewpoint. One common, yet simplistic, model for studying two-dimensional phase transitions is the lattice gas model. This model assumes that the substrate primarily provides an array of sites on which the adsorbate binds. Additionally, the model assumes that adsorbate-substrate interactions are more important than adsorbate-adsorbate interactions. A major shortcoming of this model is that it does not include substrate reconstruction which is relevant for Mo(100) and W(100) since they both reconstruct.

Phase transitions may be categorized into two types: first order and second and higher order. First-order phase transitions are those in which an abrupt rearrangement of

the crystal lattice occurs and the thermodynamic state changes discontinuously. In other words, the thermodynamic function has a discontinuity, its first derivative does not exist, at some critical temperature, T_c. Second or higher order phase transitions display a continuous change of thermodynamic state from one phase to the other.

As early as 1978, Barnes and Willis [5.29] concluded from an HREELS study that hydrogen on W(100) at room temperature sits in a two-fold bridge site and that the W(100) surface is reconstructed in a manner similar to the low-temperature reconstruction of the clean W(100). Barker and Estrup [5.30] concluded that the H/Mo(100) structures are like the low-temperature H/W(100) structures, due to adsorbate-induced reconstruction because a simple relationship between coverage and structure did not exist.

Although tungsten and molybdenum are very similar, the [100] face, clean and hydrogen covered, of each behaves differently with regards to structural transitions [5.31, 32]. In 1987, Prybyla et al [5.32] found that phase transitions on the H/W(100) system are second order, whereas those on the H/Mo(100) system are predominantly first order. They concluded that the effective H-H interactions are very different for the two substrates. The H-H interactions lead to island formation on Mo(100) and to a uniform hydrogen layer on W(100). They explained the difference by a phonon-mediated interaction mechanism. The H adatoms induce substrate distortions which couple with surface phonon modes, but the surface phonon modes on the two surfaces are thought to be different. They suggested that a rigid-substrate model be abandoned for one which includes surface phonon modes.

In 1991, Prybyla et al [5.28] combined LEED studies with surface infrared spectroscopy (SIRS) studies of the H/Mo(100) system and found that the H sit in two-fold bridge sites for all coverages and temperatures. They concluded that the complexity of the phase diagram is due to the tendency of Mo(100) to reconstruct. Additionally, they found

that the IR frequency of the Mo-H-Mo symmetric stretch could be correlated to the magnitude of the Mo displacements in each of the reconstructed phases.

As regards a domain-wall model, Prybyla et al [5.28] found that the Mo-Mo distance for the bridge site must be constant over the surface so a domain-wall structure would be consistent with the LEED and SIRS results. They found that the Mo-Mo distance at the bridge sites is smallest at low H coverages where the surface is reconstructed the most and that the Mo-Mo distance slowly relaxes back to the bulk value with increasing coverage.

In 1980, Barker et al [5.3] used a simplified kinematic treatment of the intensity of the LEED patterns for the clean and H covered Mo(100). As already mentioned they found that the displacements were along the <11> direction for the clean Mo(100) and that the Mo displacements were along the <10> direction for the H/Mo(100) structures. They suggested that the Mo displacements are along the <11> direction for the clean Mo(100) and that the hydrogen adsorption induces displacements along the <10> direction. This phenomenom appears to occur on W(100) also [5.33, 34].

5.2.2. O/Mo(100)

Oxygen and sulfur are similar in that both are in the same group in the periodic table; however, important differences exist - oxygen is more electronegative than sulfur (3.5 for O and 2.4 for S), sulfur's covalent radius, 1.40Å, is larger than oxygen's, 0.66Å, and sulfur can form more highly coordinated compounds than oxygen can, for example SF_6 where the sulfur is the central atom to which all the fluorine are attached. From the fact that sulfur and oxygen are both chalcogens one might expect them to have similar adsorption behavior on Mo(100); however, this is not the case.

Two main studies of the O/Mo(100) system have been performed for low coverages, one by Bauer and Poppa [5.35] in 1979 and another by Ko and Maddix [5.36] in 1981. Both studies investigated oxygen adsorption on Mo(100) at basically two

temperatures, 300K and 1050K [5.36] and 1100K [5.35]. For the most part their LEED results and coverages agree fairly well. Figure 5.2 shows a summary of their results.

Bauer and Poppa [5.35] studied the O/Mo(100) system using AES, LEED, electron stimulated desorption (ESD), and thermal desorption (TD). They found that Mo and W differ at low coverages and/or at room temperature. Mo is already reconstructed at room temperature and seemed to re-reconstruct at higher coverages while W remained unreconstructed up to saturation coverage at room temperature. This difference disappeared with increasing coverage when lateral repulsion created a distorted hexagonal array of oxygen atoms, but still W and Mo differed. They proposed that the large differences between the O/Mo(100) and O/W(100) systems were due to: (1) weaker interatomic bonding of Mo compared to W and (2) to the nearly equal strength of the metal-oxygen interactions. They formulated three stages which characterize oxygen adsorption on the [100] face of bcc refractory metals

1. oxygen is incorporated into the topmost layer up to a maximum coverage, θ_1, at a given temperature

2. oxygen adsorbs on top up to a temperature-dependent maximum coverage, θ_2

3. this becomes unstable above θ_2 and again oxygen is incorporated into the first two metal layers

Ko and Maddix [5.36] found that heating any oxygen structure, that was obtained from room temperature adsorption, above 1000K irreversibly transformed into the high temperature structure at that given coverage.

The work function measurements of Bauer and Poppa [5.35] showed that at certain oxygen coverages there is a work function decrease. This was interpreted as surface reconstruction involving the incorporation of oxygen from on top of the first Mo layer to in between the first two Mo layers. This exchange of adsorbed oxygen from on
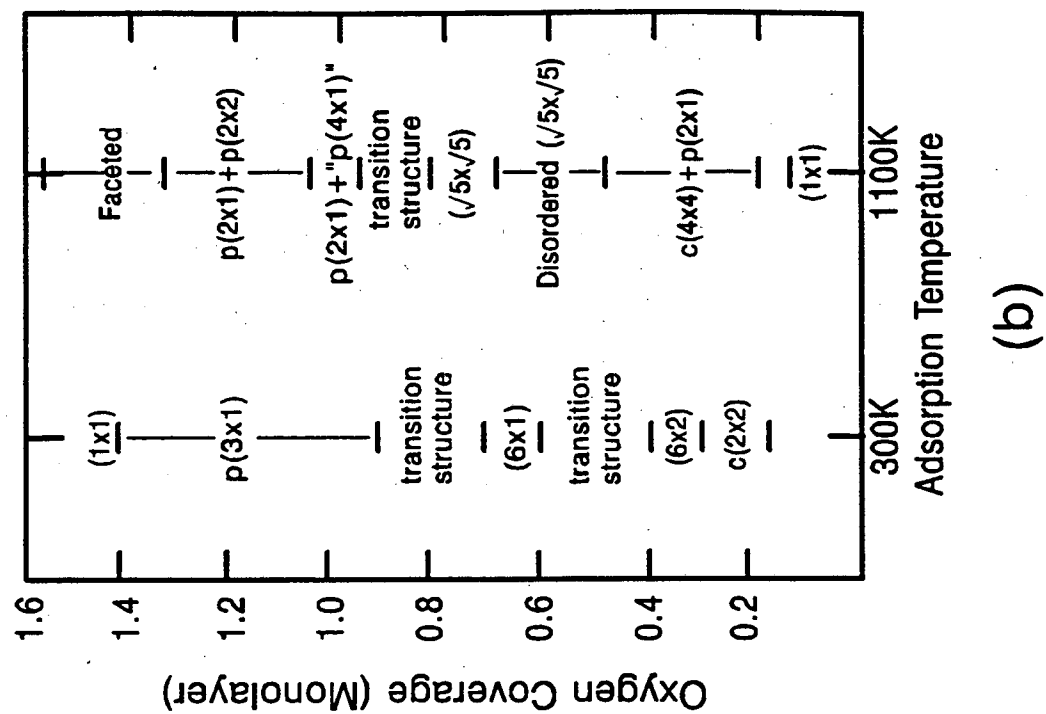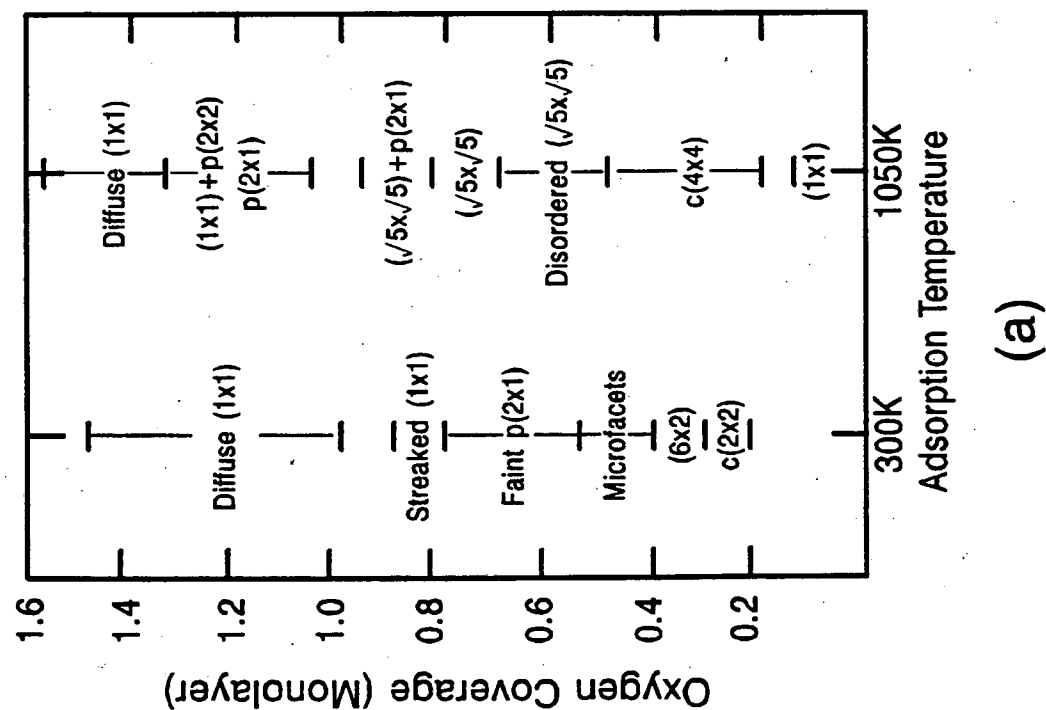
Figure 5.2   Phase diagrams for O/Mo(100) system compiled by (a) Ko and Maddix [5.36] and (b) Bauer and Poppa [5.35]

top of the topmost Mo layer to directly below it had been suggested previously for the O/W(100) system [5.37, 38].

5.2.3. S/Mo(100)

The plethora of investigations of the S/Mo(100) system, consisting primarily of LEED, AES, work function measurements, and thermal desorption studies, have done very little to resolve the controversies regarding the differences in the results of these studies.

Table 5.1   LEED patterns as a function of sulfur coverage on Mo(100) [5.40]

coverage range (monolayers)	LEED pattern
0.0-0.3	1x1
0.3-0.5	c(2x2)
0.65-0.70	$\begin{pmatrix} 2 & -1 \\ 1 & 1 \end{pmatrix}$
0.75-0.9	c(4x2)
0.9-1.1	p(2x1)

Salmeron et al [5.39] noted that some of the LEED patterns that they and others had observed might be due to oxygen contamination which is primarily due to the oxygen cleaning treatments and subsequent flashes. They proposed that as the crystal cools oxygen that had diffused into the bulk during the cleaning treatment segregates to the surface. Farias et al [5.40] also suggested that some of the discrepancies among their work and that of other investigations might be due to contamination by small amounts of

oxygen. This seems entirely reasonable given the fact that the Auger cross section for oxygen is small, so small amounts of oxygen would be difficult to detect. Additionally, an added overlayer of sulfur may cause the oxygen to be virtually undetectable especially if the oxygen is beneath the first Mo layer as suggested by the work of Bauer and Poppa [5.35]. Salmeron et al [5.39] made the observation that only the c(2x2), $\begin{pmatrix} 2 & -1 \\ 1 & 1 \end{pmatrix}$, and the c(4x2) structures were observed by all investigations [5.39]. Interestingly, all the other structures were observed for the O/Mo(100) system. Since Farias et al [5.40] published their results the accepted ordered structures of sulfur on Mo(100) are given in Table 5.1.

Many investigations have claimed that the p(2x1) was often streaked in the [10] and [01] directions [5.39, 41]. In our work this streakiness was observed to sharpen into (m/4, n/2) spots of the c(4x2) LEED pattern. Salmeron et al [5.39] suggested that the p(2x1) might be a disordered version of the c(4x2) with sulfur vacancies in the compact rows of their proposed real space model which would give domains shorter along the <10> directions. Clarke [5.41] interpreted the streakiness to indicate a degree of disorder in the bridge site rows of his proposed structure.

A scanning tunneling microscopy (STM) study performed by Marchon et al [5.42] imaged the p(2x1)S-Mo(100) structure at atmospheric pressure. The sample had been prepared in UHV prior to being placed in the STM. Within the error of the calibration of the piezoelectrics the sulfur heights were equivalent so the 1/4 1/4 model was implicated. The 1/4 1/4 model places the sulfur adatoms in equivalent asymmetric hollow sites. This model can be generated from a (1x1) unit cell with one sulfur per cell. The sulfur is located at the center of the unit cell, i.e. a four-fold hollow site. The sulfur atoms are displaced by $a/4$, where a is the bulk lattice constant of Mo, in the direction parallel to the shorter side of the p(2x1) unit cell. Every other sulfur is displaced in the same direction such that the sulfur atoms form zig-zagged rows along the direction of the long side of the

p(2x1) unit cell. Clarke [5.41] had earlier proposed a bridge-hollow model to explain the coverage and unit cell dimensions.

Wang and Louie [5.43] performed electronic structure and total energy calculations using an *ab initio* pseudopotential local density functional approach to investigate the various models for the c(2x2) and p(2x1) structures. This study did not consider substrate reconstruction because it is generally of minor importance, a few hundredths of an eV, relative to different adsorption sites, tenths of an eV. For the c(2x2) structure they only considered sulfur in a four-fold hollow site since Clarke's dynamical LEED analysis [5.41] had indicated that this site was the best of the three possible high-symmetry sites (atop, two-fold bridge, and four-fold hollow). They varied the distance of the sulfur above the first Mo layer; their optimum value, $d_{\perp}=0.95\text{Å}$, compared well with the LEED [5.41] and ion scattering results [5.44]. For the p(2x1) structure they considered models with various distortions from hollow-hollow, where both sulfurs occupy four-fold hollow sites, to bridge-bridge sites, where both sulfurs occupy two-fold bridge sites. This effectively amounts to displacing the sulfur overlayer by $a/2$, where a is the bulk lattice constant of Mo. The hollow-hollow model was lower in energy than the bridge-bridge model which implied that the hollow site is energetically more favorable. The bridge-hollow model was lowest in total energy and the 1/4 1/4 model was the highest in total energy.

References

5.1   T.E. Felter, R.A. Barker, and P.J. Estrup, Phys. Rev. Let. **38** (1977) 1138.

5.2   M.K. Debe and D.A. King, Surface Sci. **81** (1979) 193.

5.3   R.A. Barker, S. Semancik, and P.J. Estrup, Surface Sci. **94** (1980) L162.

5.4   M.L. Hildner, R.S. Daley, T.E. Felter and P.J. Estrup, J. of Vacuum Sci. and Tech. A **9** (1991) 1604.

5.5   D.G. Kelly, R.F. Lin, M.A. Van Hove, and G.A. Somorjai, Surface Sci. **224** (1989) 97.

5.6   A. Ignatiev, F. Jona, H.D. Shih, D.W. Jepsen, and P.M. Marcus, Phys. Rev. B **11** (1975) 4787.

5.7   E. Tosatti and P.W. Anderson, Solid State Comm. **14** (1974) 773.

5.8   Neil W. Ashcroft and N.David Mermin, **Solid State Physics** (W.B. Saunders 1976).

5.9   W. Kohn, Phys. Rev. Let. **2** (1959) 393.

5.10   E. Tosatti, Solid State Comm. **25** (1978) 637.

5.11   C.Z. Wang, E. Tosatti, and A. Fasolino, Phys, Rev. Let. **60** (1988) 2661.

5.12   S.E. Trullinger and S.L. Cunningham, Phys, Rev. Let. **30** (1973) 913.

5.13   D. Haneman, Phys. Rev. **119** (1960) 563 and **121** (1961) 1093; N.R. Hansen and D. Haneman, Surface Sci. **2** (1964) 566. D. Haneman and D.L. Heron, in **The Structure and Chemistry of Solid Surfaces**, edited by G.A. Somorjai (Wiley, New York, 1969).

5.14   K. Terakura, I. Terakura, Y. Teroaka, Surface Sci. **86** (1979) 535.

5.15   D.G. Pettifor, in: **Metallurgical Chemistry**, Ed. O. Kubaschewski (HMSO, London, 1972) p.191.

5.16   W.L. McMillan, Phys. Rev. Let. **16** (1977) 643.

5.17   J.E. Inglesfield, J. Phys. C **12** (1979) 149.

5.18   D. Singh and H. Krakauer, Phys. Rev. B **37** (1988) 3999.

5.19   L.D. Roelofs and J.F. Wendelken, Phys. Rev. B 34 (1986) 3319.

5.20   L.D. Roelofs, G.H. Hu, and S.C. Ying, Phys. Rev B **28** (1984) 6369.

5.21   A. Fasolino, G. Santoro, and E. Tosatti, Phys. Rev. Let. **44** (1980) 1684.

5.22   K. Jeong, R.H. Gaylord, and S.D. Kevan, Phys. Rev. B **39** (1989) 2973.

5.23   K.E. Smith, G.S. Elliot, and S.D. Kevan, Applied Surface Sci. **48/49** (1990) 135.

5.24   K.E. Smith and S.D. Kevan, Phys. Rev. B **43** (1991) 3986.

5.25   J.C. Campuzano, J.E. Inglesfield, D.A. King, and C. Somberton, J. Phys. C **14** (1981) 3099.

5.26   X.W. Wang, C.T. Chang, K.M. Ho, and W. Weber, Phys. Rev. Lett. **60** (1988) 2066.

5.27   X.W. Wang and W. Weber, Phys. Rev. Lett. **58** (1987) 1452.

5.28   J.A. Prybyla, P.J. Estrup, and Y.J. Chabal, J Chem. Phys. **94** (1991) 6274.

5.29   M.R. Barnes and R.F. Willis, Phys. Rev. Let. **41** (1978) 1729.

5.30   R.A. Barker and P.J. Estrup, Phys. Rev. Let. **41** (1978) 1307.

5.31   Y.J. Chabal, S.B. Christman, J.J. Arrecis, J.A. Prybyla, and P.J. Estrup, J. of Elec. Spec. and Rel. Phenom. **44** (1987) 17.

5.32   J.A. Prybyla, P.J. Estrup, S.C. Ying, Y.J. Chabal, and S.B. Christman, Phys. Rev. Let. **58** (1987) 1877.

5.33   M.K. Debe and D.A. King, J. Phys. C **10** (1977) L303; Phys, Rev Let. **39** (1977) 708.

5.34   D.A. King and G. Thomas, Surface Sci. **92** (1980) 201.

5.35   E. Bauer and H. Poppa, Surface Sci. **88** (1979) 31.

5.36   I. Ko and R.J. Madix, Surface Sci. **109** (1981) 221.

5.37   V.Y. Kolot, V.I. Tatus, V.F. Rybalko, V.V. Vodolazhchenko, and Eyseev, Soviet Phys.-Solid State **17** (1973) 1876.

5.38   A. Benninghoven, Phys. Letters **32A** (1970) 427; Chem. Phys. Letters **6** (1970) 626.

5.39   M. Salmeron, G.A. Somorjai, R.R. Chianelli, Surface Sci. **127** (1983) 526.

5.40   M.H. Farias, A.J. Gellman, and G.A. Somorjai, Surface Sci. **140** (1984) 181.

5.41   L.J. Clarke, Surface Sci. **102** (1981) 331.

5.42   B. Marchon, P. Bernhardt, M.E. Bussell, G.A. Somorjai, M. Salmeron, and W. Siekhaus, Phys. Rev. Let. **60** (1988) 1166.

5.43   X.W. Wang and S.G. Louie, Surface Sci. **226** (1990) 257.

5.44   B.M. DeKoven, S.H. Overbury, and P.C. Stair, J. Vac. Sci. Technol. A **3** (1985) 1640.

IV. Results and Discussion

Chapter 6.   Ordered Sulfur Overlayers on Mo(100)

6.1.   Specific Procedures Used for Structure Determination

The experimental I-V curves for each diffraction beam were generated from the video images of the LEED pattern at each energy using the analysis program described in Chapter 4. The experimental I-V curves were acquired on a 2eV energy grid. Once the I-V curves were generated they were normalized with respect to the incident electron beam current. In the experiment the incident electron beam current increases almost linearly with increasing electron beam energy; therefore, the intensities of the diffraction beams at a given energy cannot be compared to the intensity of the same diffraction beam at another energy. Although we used the Pendry R-factor which is most sensitive to the peak position in the I-V curves and not the relative intensities of the peaks, the peaks can be skewed if the I-V curves are not normalized with respect to the incident-electron beam current. All the experimental I-V curves and averaged experimental I-V curves which are presented in the figures in Chapters 6 and 7 have been normalized with respect to the incident electron beam current and have not been smoothed. After normalizing the I-V curves, an experimental file which contained all of the individual I-V curves was generated. This file was used as an input file for the tensor LEED programs for comparison with the calculated beam intensities.

In the tensor LEED programs the experimental I-V curves were averaged, then smoothed once with a three point smoothing algorithm, and finally interpolated onto a 0.25eV energy grid prior to being compared with the theoretical I-V curves, i.e. the R-factor analysis. The theoretical I-V curves were generated on a 4eV energy grid and were also interpolated onto a 0.25eV energy grid.

The atomic scattering of Mo and S was described by 8 phase shifts; therefore, the spherical wave expansion was truncated at $\ell_{max}=7$. The phase shifts were calculated previously [6.1] for a cluster of 67 sulfur and molybdenum atoms which had approximately the structure that was expected for the Mo(100)-c(2x2)-S. The imaginary part of the potential, i.e. the damping term, was energy independent and was held constant at 5eV. The thermal vibrations of the surface atoms were included with the bulk Debye temperatures of 450K for Mo and 686K for S.

The atomic scattering of Re and S was described by 9 phase shifts; therefore, the spherical wave expansion was truncated at $\ell_{max}=8$. The phase shifts were calculated for a semi-infinite slab, composed of one layer of sulfur atoms and three layers of rhenium atoms, which had approximately the expected structure of the Re(0001)-p(2x2)-S. The imaginary part of the potential was 5eV and the Debye temperatures of Re and S were 360K and 850K respectively.

For all the surface structure analyses presented in this work, the Pendry R-factor was used for the R-factor analysis. The procedure that we followed for the surface structure determinations was to use structural models based on the known unit cell dimensions and the sulfur coverage. In general we placed the sulfur in high symmetry sites with the greatest coordination with the substrate atoms. If experimental or theoretical evidence suggested variations from this then we tried those models also. In general, only a few structural models were likely candidates and these were used as reference structures for the tensor LEED analysis. The optimum structure found by the tensor LEED analysis was always checked by performing a full dynamical LEED calculation, i.e. a conventional LEED calculation. A best fit structure was not always obtained from the tensor LEED analysis because, presumably, our models were not close enough to the correct structure. If we could not generate more models within the restrictions of the unit cell dimensions

and sulfur coverage then we said that the LEED analysis failed to produce a best fit structure.

In the following discussion of our results we give the value of the muffin-tin constant, which we loosely refer to as the inner potential, V_{or}. The muffin-tin constant is the difference in potential energy between the vacuum level and the regions of constant potential in the interstitial regions of the muffin-tin model. This value is an adjustable parameter in the LEED calculations and amounts to a rigid shift of the energy scale of the theoretical I-V curves. Typical values of the muffin-tin constant range from 5-15 eV.

A left-handed coordinate system was used to define the geometry of the models with the positive x direction into the surface. All the figures have the positive z-axis pointing vertically upward, the positive y-axis pointing horizontally to the right, and the positive x-axis pointing into the paper. The Δx, Δy, and Δz values correspond to the change in the respective coordinate relative to the reference geometry. The x' values are the new x values normalized so that the origin corresponds to the center of an atom, which is usually the sulfur, which is farthest from the substrate surface. Therefore, the x' values are the coordinates of the structure found by the tensor LEED analysis.

6.2. Mo(100)-c(2x2)-S

The LEED pattern for the Mo(100)-c(2x2)-S is shown in Figure 6.1. The corresponding schematic which shows the symmetry of the diffraction beams is illustrated in Figure 6.2. The I-V curves for the individual beams are shown in Figure 6.3. The structure was prepared by depositing sulfur from a sulfur source and subsequently annealing the surface at 1600-1700K for 30s. This formed a structure which produced a sharp c(2x2) LEED pattern. As was mentioned before, the Mo(100)-c(2x2)-S structure occurs at a sulfur coverage equal to 0.5 ML which is defined as one sulfur atom for every two molybdenum atoms. Previous investigations of the structure [6.1, 2] found the
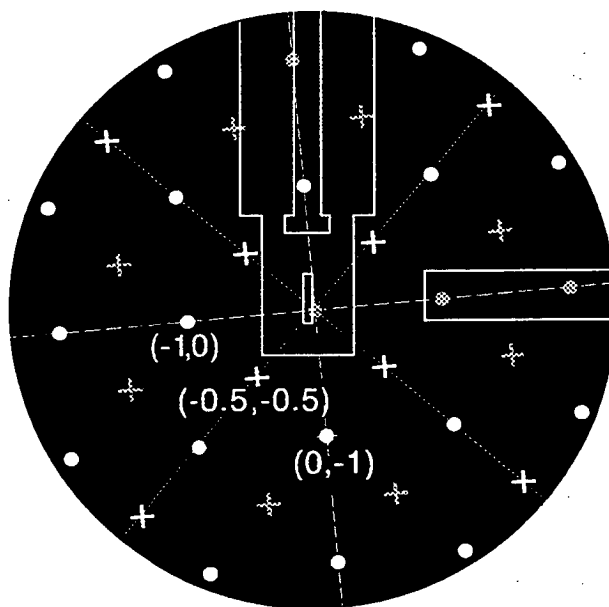
a)

b)

(-1,0)

(-0.5,-0.5)

(0,-1)
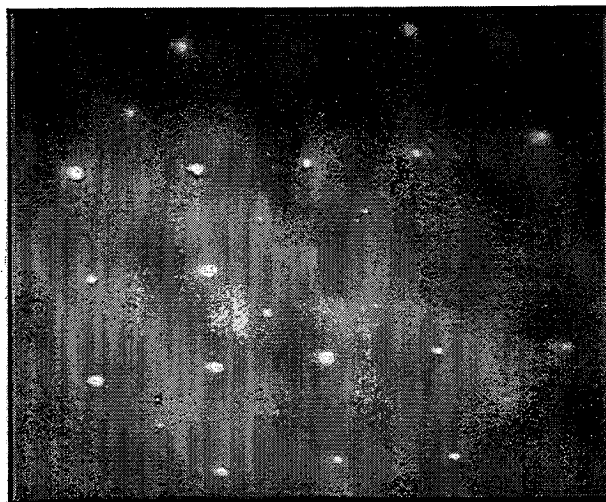
Figure 6.1 a) diffraction pattern of Mo(100)-c(2x2)-S at 114 eV as displayed on video monitor and b) schematic of c(2x2) diffraction pattern with the crosses represent the fractional order beams and the filled circles represent the integral order beams. The (hk) labels of the beams are directly beneath the beam. The dotted and dashed lines represent the four mirror planes. The shaded crosses and circles are the beams that are not seen in the photograph.

Integral Order Beams

⬡ (hexagon)	(1.0, 0.0)
⬠ (pentagon)	(1.0, 1.0)
■ (square)	(2.0, 0.0)
● (circle)	(2.0, 1.0)
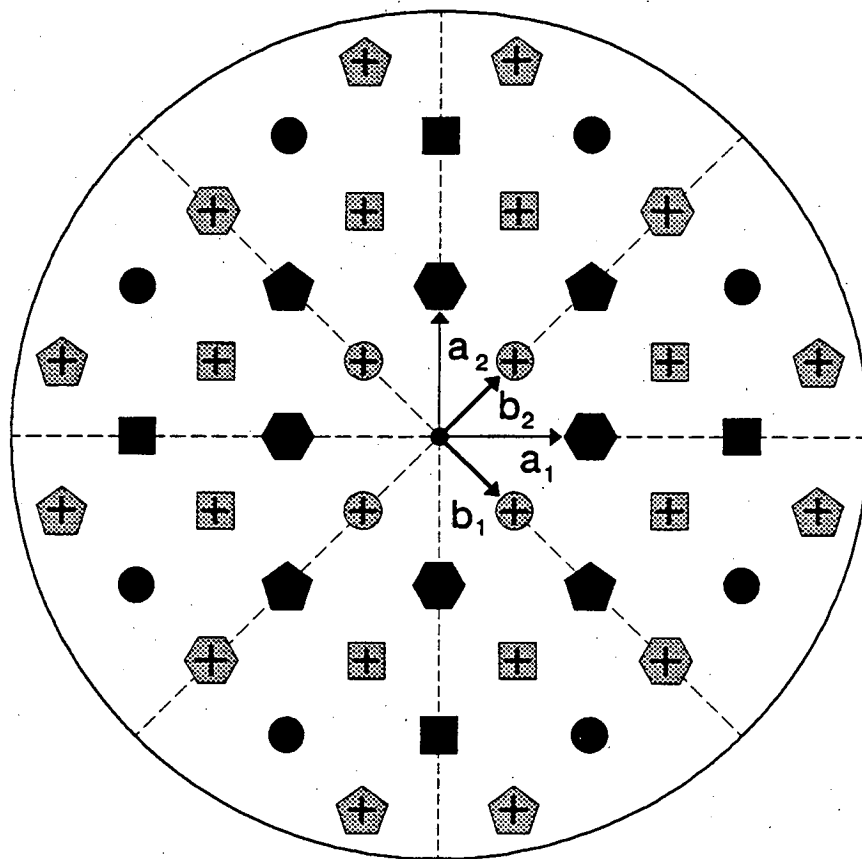
Fractional Order Beams

⊕ (circle)	(0.5, 0.5)
⊞ (square)	(1.5, 0.5)
⬡⊕ (hexagon)	(1.5, 1.5)
⬠⊕ (pentagon)	(2.5, 0.5)

Figure 6.2   Schematic of c(2x2) LEED pattern illustrating the symmetry of the diffraction beams at normal incidence.

Figure 6.3   Experimental I-V Curves of Mo(100)-c(2x2)-S
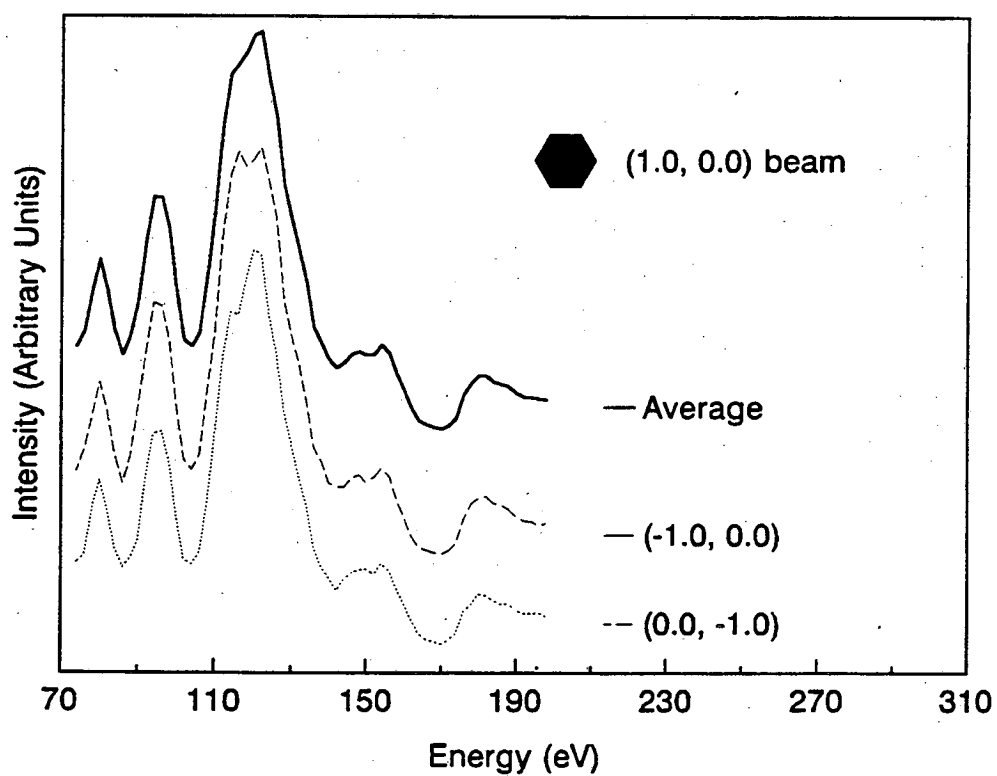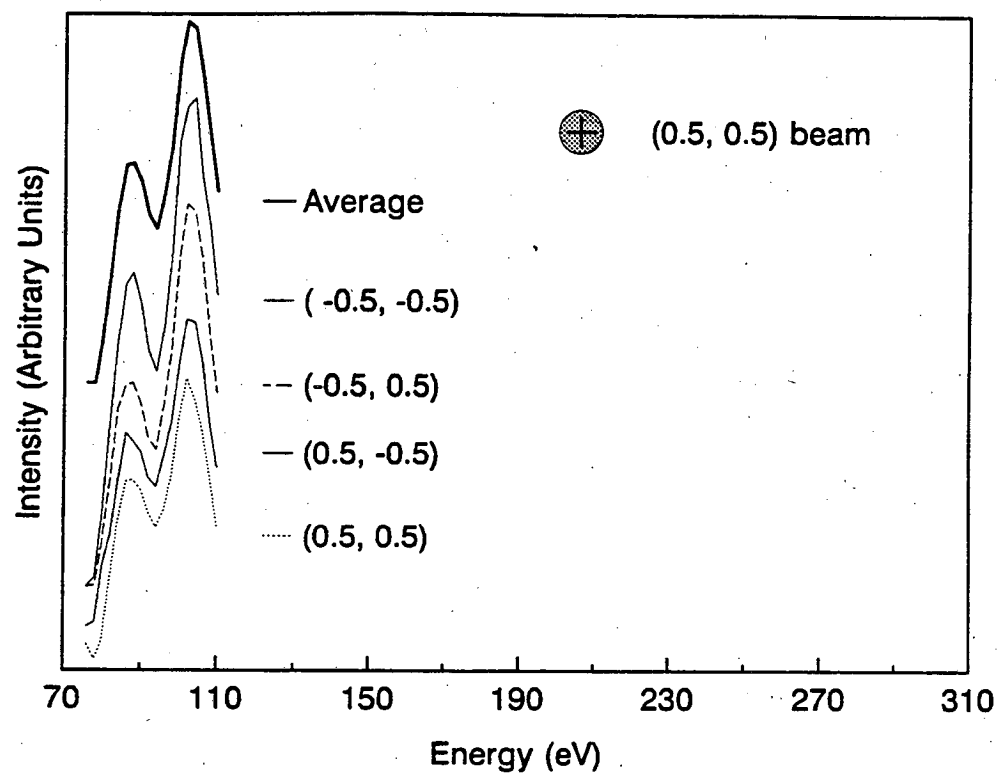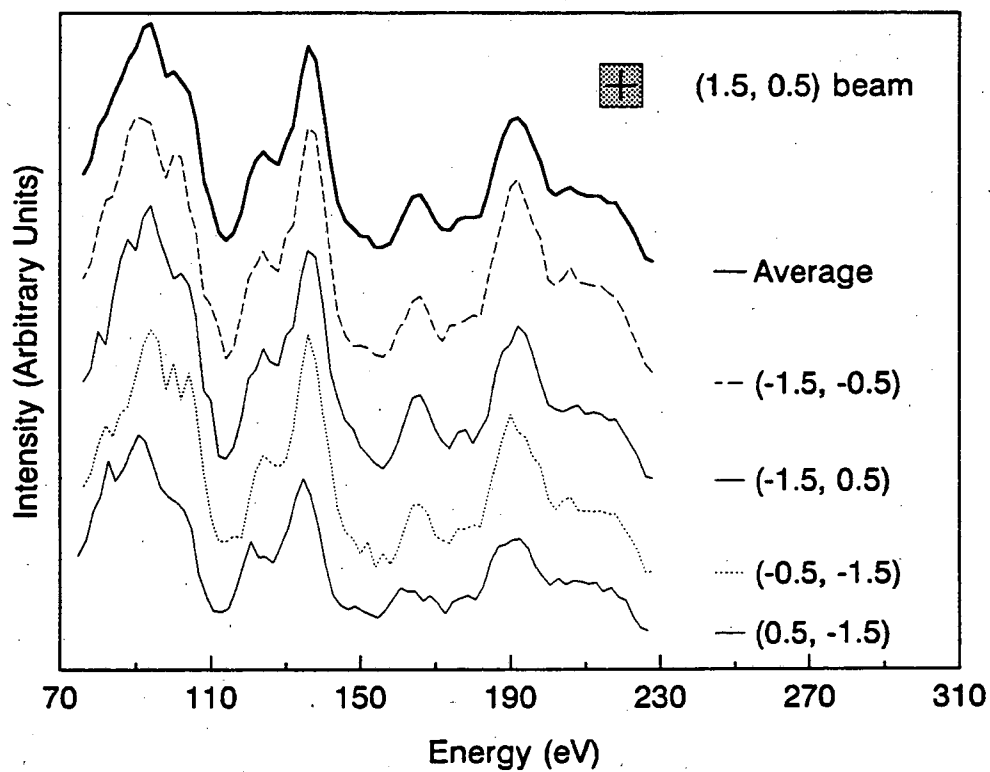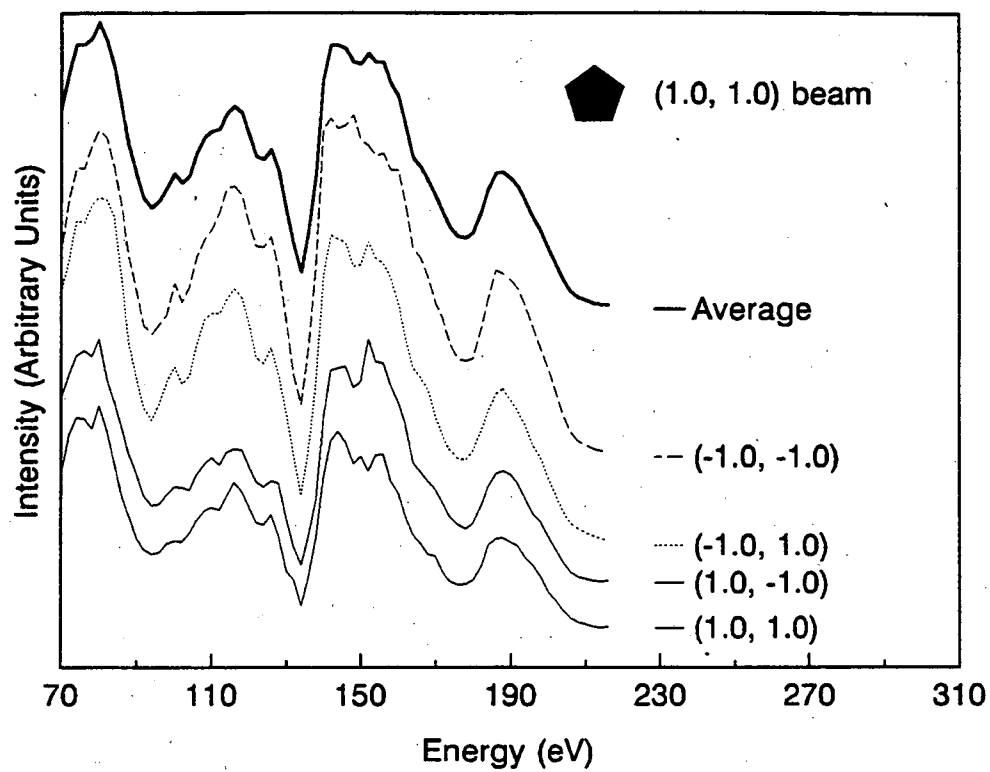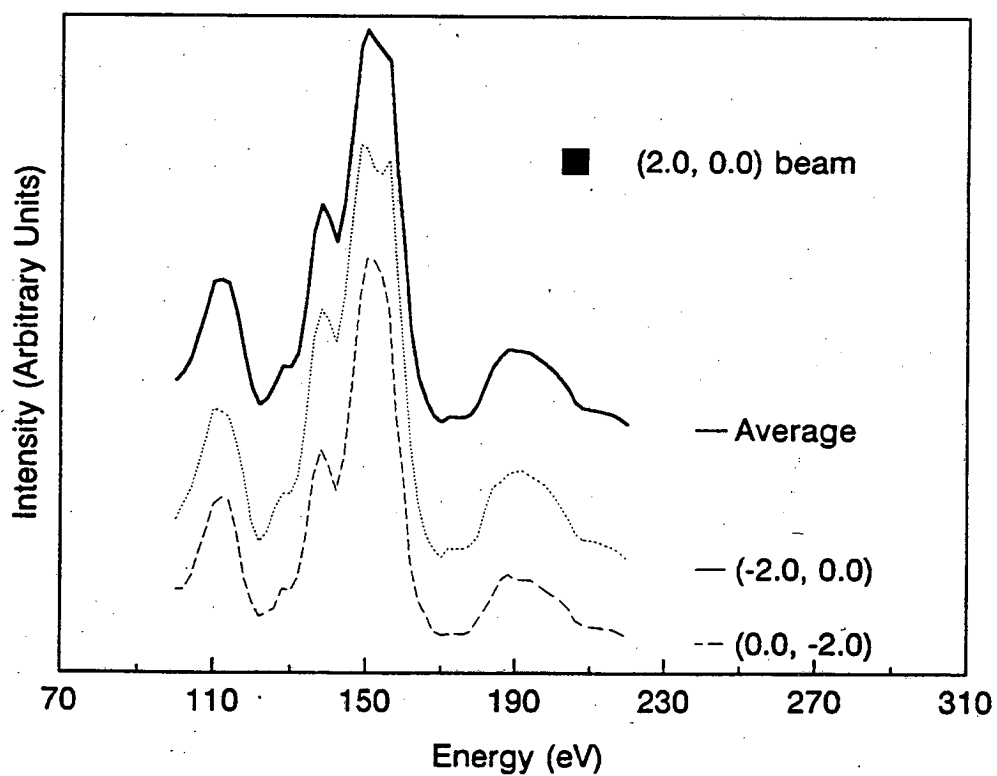
108

Figure 6.3 Continued   Experimental I-V Curves of Mo(100)-c(2x2)-S

Figure 6.3 Continued   Experimental I-V Curves of Mo(100)-c(2x2)-S
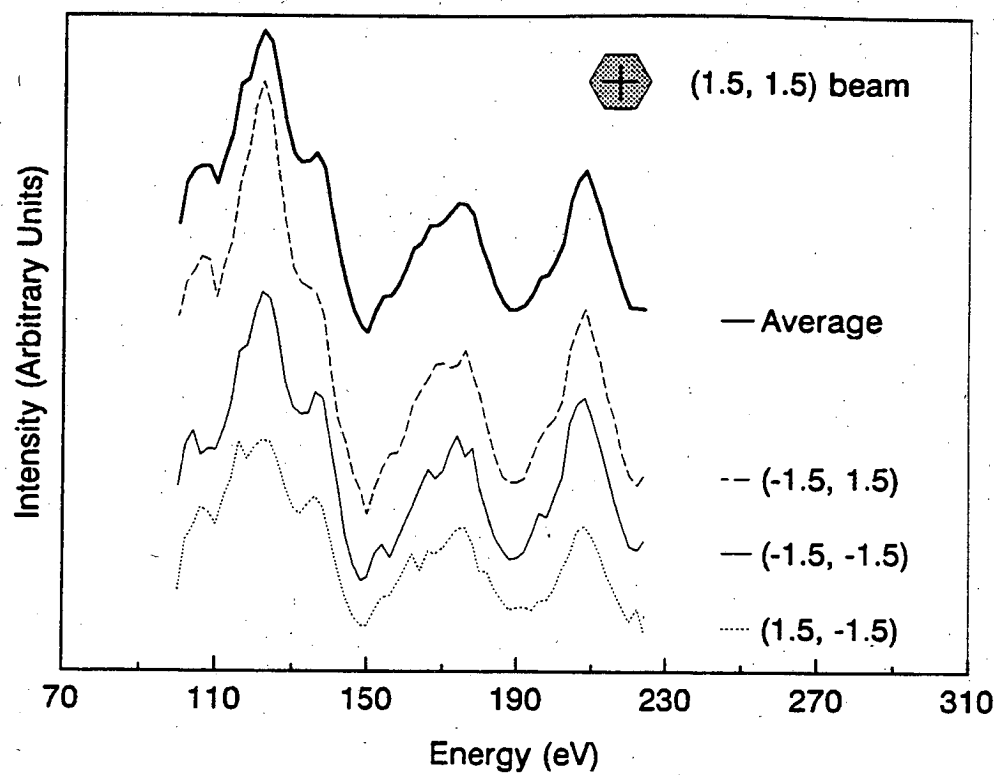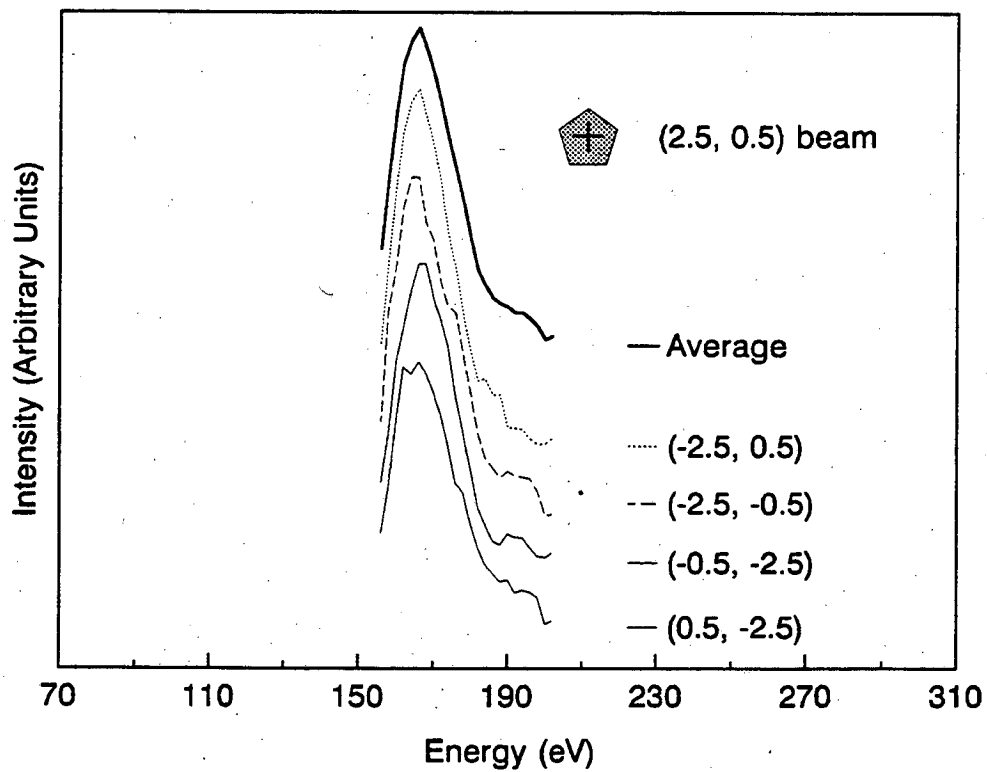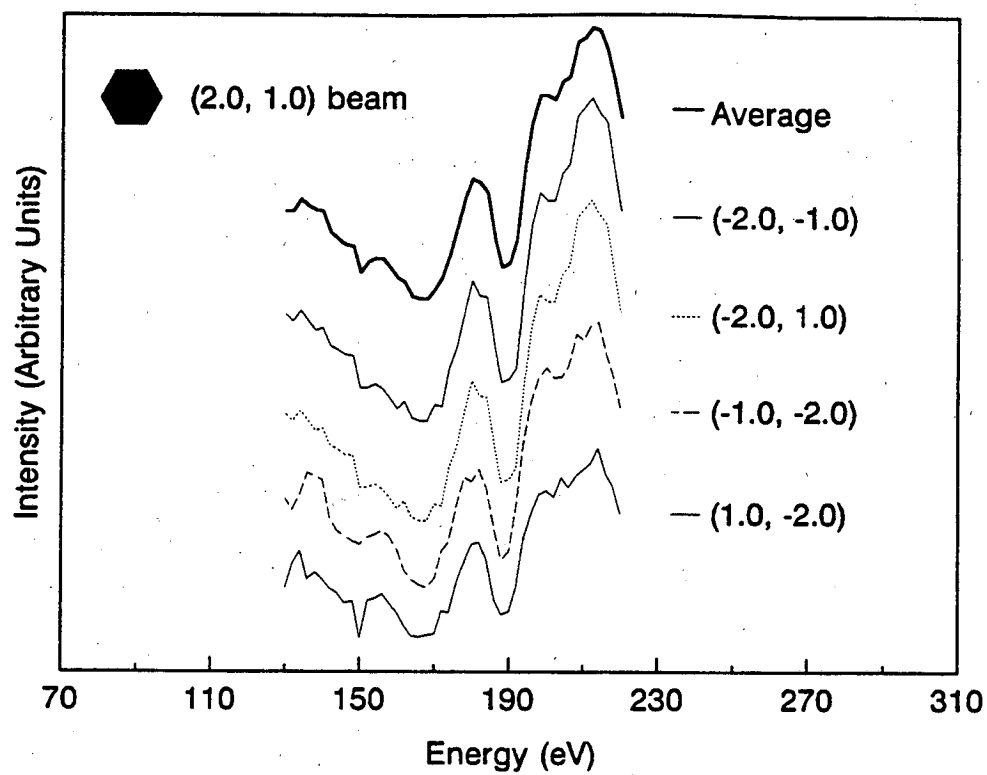
110

Figure 6.3 Continued   Experimental I-V Curves of Mo(100)-c(2x2)-S

111

four-fold hollow site to be the best site among the possible high symmetry sites, atop, two-fold bridge, and four-fold hollow. Therefore, the two other high symmetry sites were not considered in our structural analysis. In Figure 6.4 a top view and side view of the real-space model are depicted. The smaller unit cell is the c(2x2) and the larger unit cell is a p(2x2) unit cell. In Figure 6.4b a side view is shown where the shaded circles represent the second- and fourth-layer Mo atoms which are behind the plane of the paper as are the sulfur atoms. Our first tensor LEED analysis [6.3] of our data found a best fit geometry in which the second-layer Mo atom, atom 5 in Figure 6.4, buckled upward. This resulted in a sulfur bonded to 5 molybdenum atoms, four in the first layer and one in the second layer. Each of the five bonds was approximately the sum of the covalent radii. These results seemed reasonable and a good fit was indicated by a Pendry R-factor of 0.24. The bcc(100) surface is more open than other low-Miller index surfaces and the relatively large sulfur atom is able to fit deep into the hollow sites. The second-layer buckling was relatively large, ~0.16Å; however, the R-factor was fairly insensitive to the magnitude of the buckling.
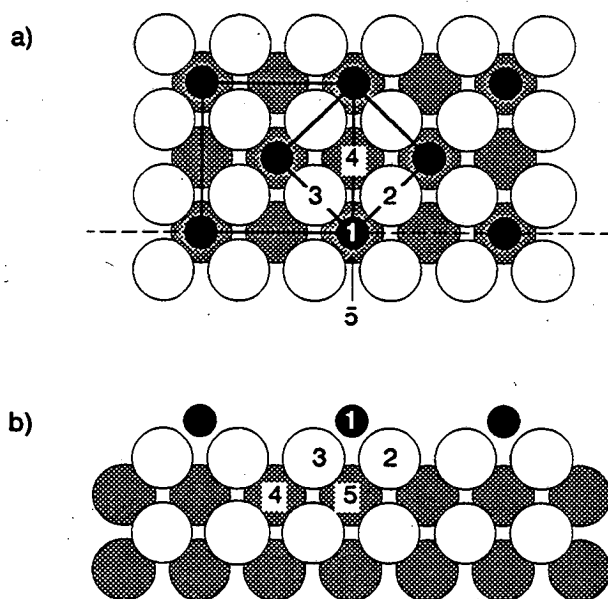

Figure 6.4   Real space model of Mo(100)-c(2x2)-S a) top view and b) side view which is a cut along the dotted line in a). The numbers label the atoms which were allowed to vary in the tensor LEED calculation. These atoms make up the composite layer. The numbers refer to the geometry given in Table 6.1 where atoms 4 and 5 have been reversed.

112

A reanalysis of this structure was undertaken with an improved version of the tensor LEED code. The reference structure that we initially used assumed bulk interlayer spacings and used the S-Mo interlayer spacing that we had determined in our earlier calculation [6.3]. The sulfur overlayer and first two Mo layers were allowed to vary in the tensor LEED analysis. No reconstruction was taken into account, since the displacements of the Mo atoms on the clean or H covered Mo(100) surface are on the order of 0.1Å [6.1, 4]. If the Mo(100) substrate is reconstructed with displacements on the order of 0.1Å then the tensor LEED analysis may be able to determine whether this is the case. However, determining whether the substrate is reconstructed may not be possible since the uncertainty in the lateral positions of the atoms is on the order of 0.1Å also. Additional off-normal incidence I-V data would be needed to reduce this uncertainty. The input geometry is given in Table 6.1.

Table 6.1 Input geometry of the reference structure where the interlayer spacings have the bulk value and the Mo-S interlayer spacing is the result from our previous calculation [6.3].

	x	y	z
S(1)	0.000	0.000	0.000
Mo(2)	1.003	1.575	1.575
Mo(3)	1.003	-1.575	1.575
Mo(4)	2.578	0.000	0.000
Mo(5)	2.578	0.000	3.150

The result of the tensor LEED search is summarized in Table 6.2. The atoms were constrained to move only in the x-direction. The result of the tensor LEED analysis revealed a second layer buckling as we had found previously [6.3], but the buckling was in the opposite direction, that is the second layer Mo, atom 5 in Figure 6.4, moved deeper down. The results are similar whether the first-layer Mo atoms were allowed to move independently or constrained to move together since they are equivalent by symmetry.

113

Table 6.2 Results of tensor LEED search perpendicular to the surface. The two first-layer Mo atoms are moved together. The Pendry R-factor was 0.206 and the inner potential was 9.0 eV.

	Δx	x'
S(1)	0.0357	0.0000
Mo(2)	0.0536	1.0209
Mo(3)	0.0536	1.0209
Mo(4)	0.0687	2.6110
Mo(5)	-0.0191	2.5232

This can be seen by comparing the results in Table 6.2, for the case where the two first layer Mo atoms were constrained to move together, with the results in Table 6.3, for the case where they were allowed to move independently.

Since the result of this new calculation contradicted our previous study [6.3], the optimal geometry of the previous study was used as the reference structure and a conventional dynamical calculation and subsequent tensor LEED calculation were performed. The input geometry is given in Table 6.4. We will refer to this structure as

Table 6.3 Results of tensor LEED search perpendicular to the surface. The two first layer Mo atoms are allowed to move independently. The Pendry R-factor was 0.214 and the inner potential was 8.68 eV.

	Δx	x'
S(1)	0.0127	0.0000
Mo(2)	0.0233	1.0136
Mo(3)	0.0152	1.0055
Mo(4)	0.0328	2.5981
Mo(5)	-0.0188	2.5465

Table 6.4   Input geometry of the reference structure, Buckled Structure A.

	x	y	z
S(1)	0.000	0.000	0.000
Mo(2)	1.000	1.575	1.575
Mo(3)	1.000	-1.575	1.575
Mo(4)	2.380	0.000	0.000
Mo(5)	2.540	0.000	3.150

Buckled Structure A. The results of the tensor LEED calculation are given in Table 6.5. The surface unbuckled and started to buckle in the opposite direction. The sulfur-molybdenum bond distance did not differ much between the two calculations. If only the inner potential, V_{or}, was varied the R-factor for the input geometry was obtained. In Table 6.6 the Pendry R-factor for each reference structure is listed.

Table 6.5 Results of tensor LEED search perpendicular to the surface. Buckled Structure A was the reference structure. The Pendry R-factor was 0.262 and the inner potential was 9.3 eV.

	Δx	x'
S(1)	-0.0103	0.0000
Mo(2)	0.0064	1.017
Mo(3)	0.0064	1.017
Mo(4)	0.1584	2.549
Mo(5)	-0.0044	2.534

Table 6.6   Pendry R-factor for three reference structures. Only a conventional dynamical LEED calculation has been performed.

	Buckled Structure A	unbuckled structure	Buckled Structure B
R_p	0.651	0.265	0.216

115

The input geometry for the buckled reference structure is given in Table 6.7. The R-factor for this structure is given in Table 6.6. Clearly, it is the better of the three. Using the results of the tensor LEED analysis of the unbuckled reference structure in Table 6.2 for the x coordinates (i.e. use x') and the y and z coordinates given in Table 6.1 as the input geometry of another tensor LEED calculation provides a check of the validity of the first calculation. We will refer to this structure as Buckled Structure B. Table 6.8 shows the results of the tensor LEED analysis. The changes are extremely small, on the order of

Table 6.7   Input geometry of reference structure, Buckled Structure B.

	x	y	z
S(1)	0.000	0.000	0.000
Mo(2)	1.0209	1.575	1.575
Mo(3)	1.0209	-1.575	1.575
Mo(4)	2.5232	0.000	3.150
Mo(5)	2.6110	0.000	0.000

$0.01\,\text{Å}$, which is within the error of the calculation. Smoothing the experimental I-V curves did not make a significant difference in the optimum geometry.

Table 6.8   Results of tensor LEED analysis. The Buckled Structure B was the reference structure.

	Δx
S(1)	-0.0069
Mo(2)	-0.0070
Mo(3)	-0.0070
Mo(4)	0.0045
Mo(5)	-0.0089

If all the atoms are allowed to move in all three directions independently, that is no constraints are imposed, then the first layer buckles. This can be seen in Table 6.9. The parallel displacements are small, <0.1Å, and their significance is not obvious.

Table 6.9 Results of allowing all atoms to move independently in all three directions for Buckled Structure B as the reference structure. R_p=0.1868 and V_{or}= 8.49 eV.

	Δx	Δy	Δz
S(1)	-0.0154	0.1395	0.0531
Mo(2)	0.0219	0.0499	0.0060
Mo(3)	-0.0445	0.0718	-0.0912
Mo(4)	0.0059	-0.0096	0.0007
Mo(5)	-0.0169	0.0313	-0.0077

To check the significance of the first layer buckling a reference calculation and subsequent tensor LEED analysis was done. The calculation was slightly more difficult because the symmetry of the surface was reduced by buckling the first molybdenum layer. The lower symmetry required more beams to be considered in the calculation. The input geometry is given in Table 6.10. We will refer to this structure as Buckled Structure C.

Table 6.10 Input geometry of reference structure, Buckled Structure C. The results from Table 6.9 were used for the x coordinates.

	x	y	z
S(1)	0.000	0.000	0.000
Mo(2)	0.9918	-1.575	1.575
Mo(3)	1.0582	1.575	1.575
Mo(4)	2.5445	0.000	3.150
Mo(5)	2.6095	0.000	0.000

The R-factor for this structure (i.e. only varying the inner potential) was 0.216 which is essentially the same as that obtained for the reference structure with second-layer

buckling only, Buckled Structure B. The results of the tensor LEED analysis are given in Table 6.11.

Since the R-factors are essentially the same for the reference structure with second-layer buckling alone, Buckled Structure B, and the reference structure with both first- and second-layer buckling, Buckled Structure C, the R-factor is insensitive to the first-layer buckling. If buckling of the first layer exists, it is too small to reliably determine with this technique.

Table 6.11 Results of tensor LEED analysis for the direction perpendicular to the surface. R_p=0.212 and V_{or}=8.75 eV.

	Δx
S(1)	0.0142
Mo(2)	0.0108
Mo(3)	0.0080
Mo(4)	-0.0046
Mo(5)	0.0084

When all coordinates were varied independently for each of the five atoms in the composite layer the sulfur atom and the top-most buckled first-layer Mo atom, atom 3 in Figure 6.4, had displacements on the order of 0.1Å parallel to the surface. All the other Mo atoms had lateral displacements <0.05Å. Notice in Table 6.9 that the sulfur Δy displacement, along the <10> direction, is relatively large. As mentioned earlier, the first-layer Mo atoms in the H/Mo(100) system have displacements on the order of 0.1Å along the <10> direction. However, in the case of S/Mo(100) one might suspect that the sulfur atoms bond strongly to the Mo substrate and possibly remove the reconstruction. This may be very probable but from the tensor LEED analysis this is difficult to say with complete certainty. A tensor LEED analysis using off-normal incidence data would be required to try to resolve these issues. This would also seem to be required to accurately

determine the low-temperature reconstruction of clean Mo(100) since the displacements are thought to be on the order of 0.1Å.

In conclusion, the proposed structure for Mo(100)-c(2x2)-S exhibits second-layer buckling, has a Mo-S bond length of 2.45Å which is roughly the sum of the covalent radii of S and Mo (2.40Å), and the sulfur adatoms sit in four-fold hollow sites. The structure is shown in Figure 6.5. A comparison between the experimental and theoretical I-V curves is
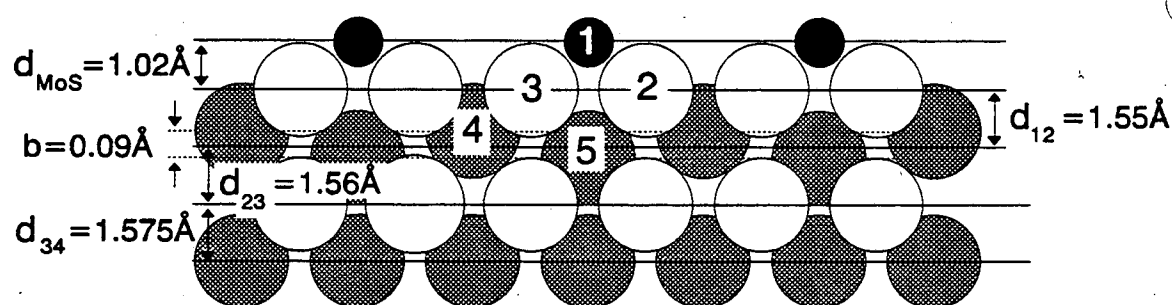

Figure 6.5   Side view of the best fit geometry for the Mo(100)-c(2x2)-S structure.

shown in Figure 6.6. Three sets of theoretical I-V curves are compared to the set of 8 experimental I-V curves. The theoretical curves, labeled Vo, correspond to the input geometry given in Table 6.7. The theoretical curves, labeled "x", correspond to a geometry with the x coordinates given in Table 6.8 and the y and z coordinates given in Table 6.7. These I-V curves are the result of the tensor LEED calculation where the atoms were only allowed to move perpendicular to the surface and the coordinates of the reference structure are given in Table 6.7. The other theoretical curves, labeled "xyz", are the results of the tensor LEED calculation where the atoms were allowed to move along all three coordinates. Notice that the theoretical curves look very similar and that not much improvement is made by displacing the atoms from the reference structure geometry. This strongly suggests that we are in a minimum.
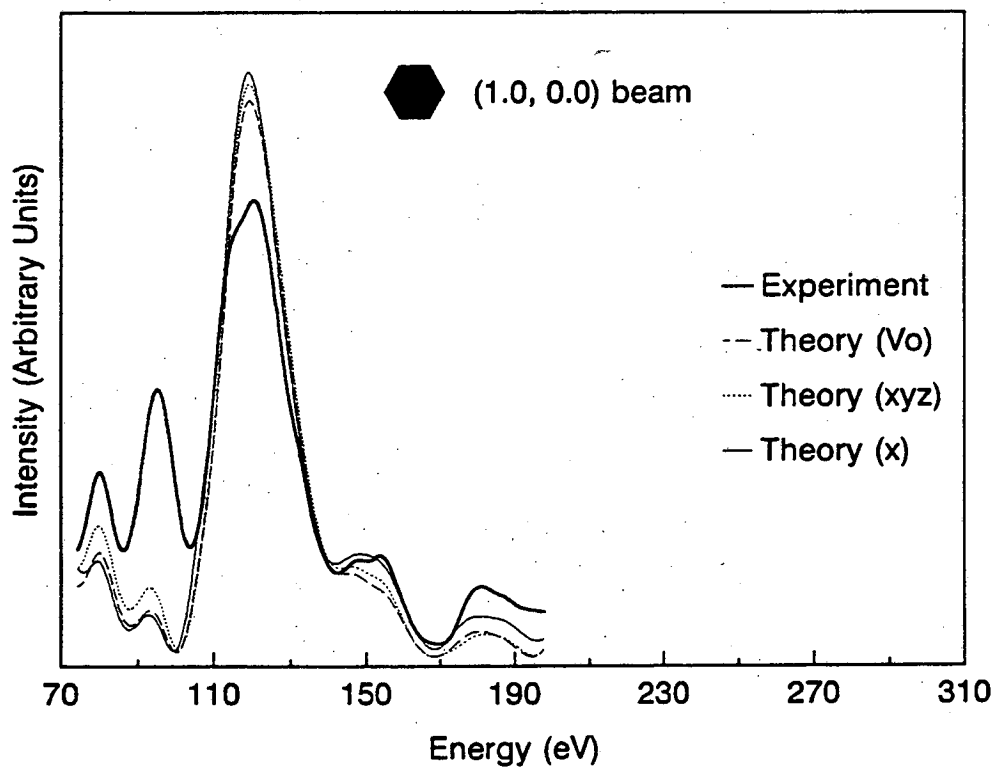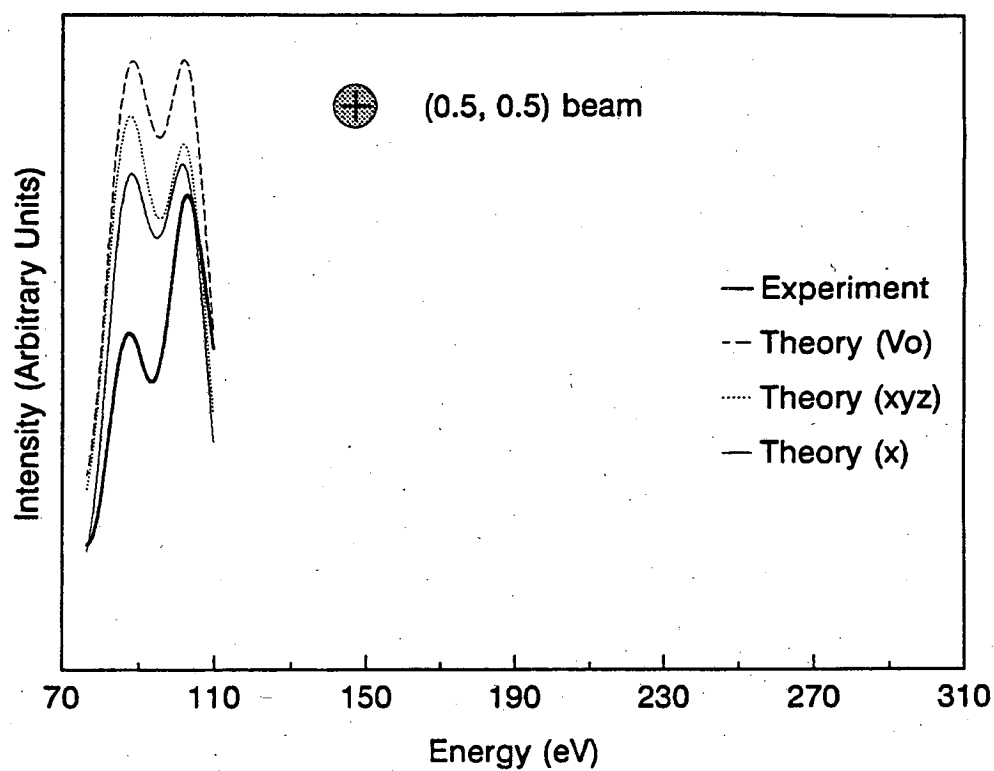
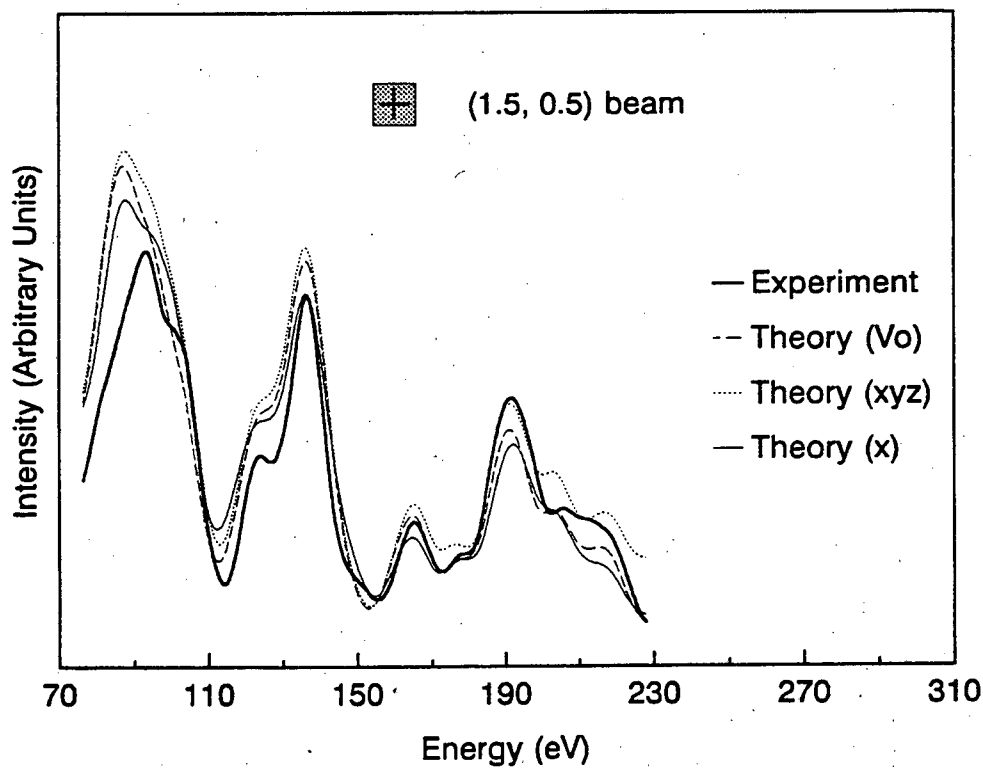**Figure 6.6** I-V Curves of Mo(100)-c(2x2)-S: Comparison between theory and experiment
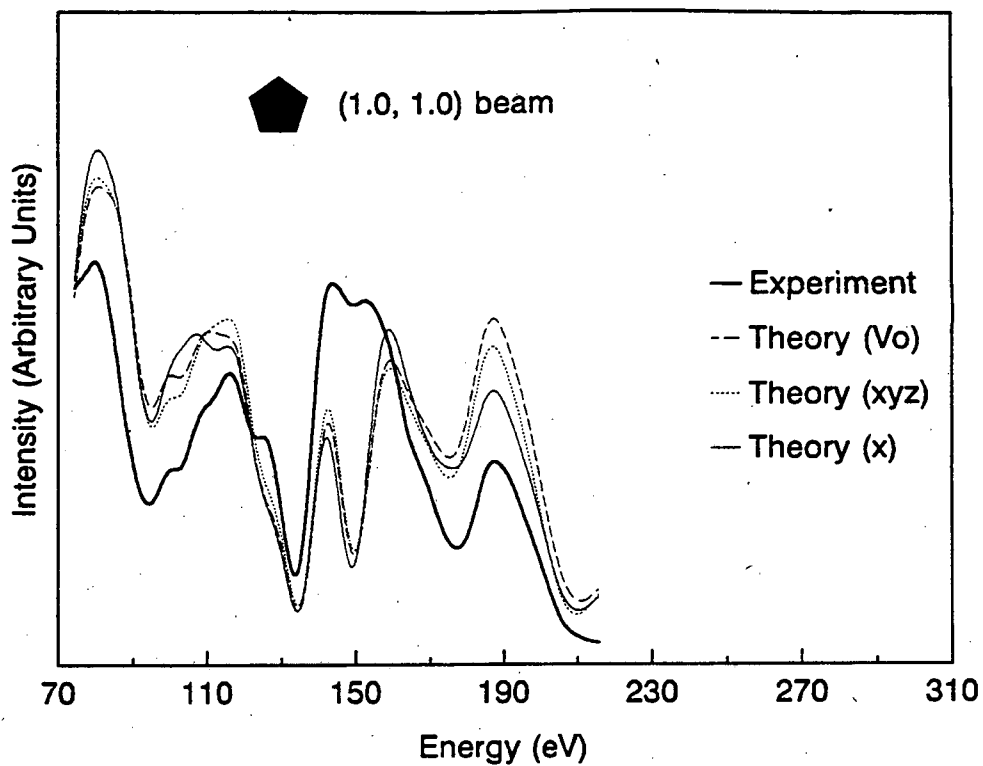
120

Figure 6.6 Continued   I-V Curves of Mo(100)-c(2x2)-S: Comparison between theory and experiment

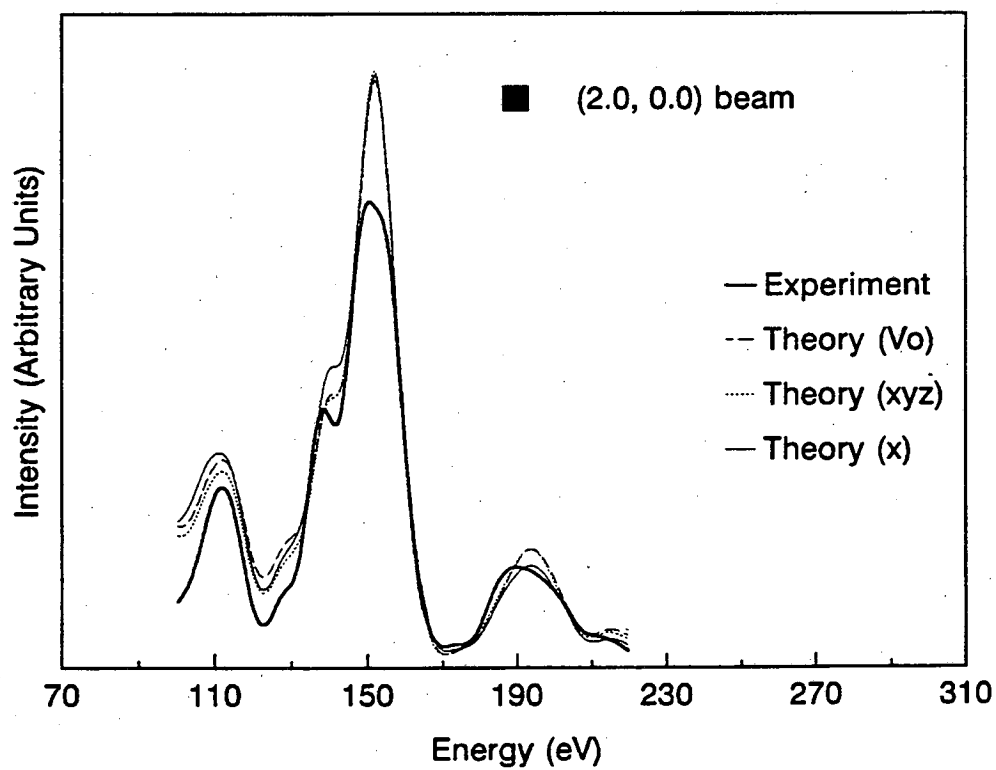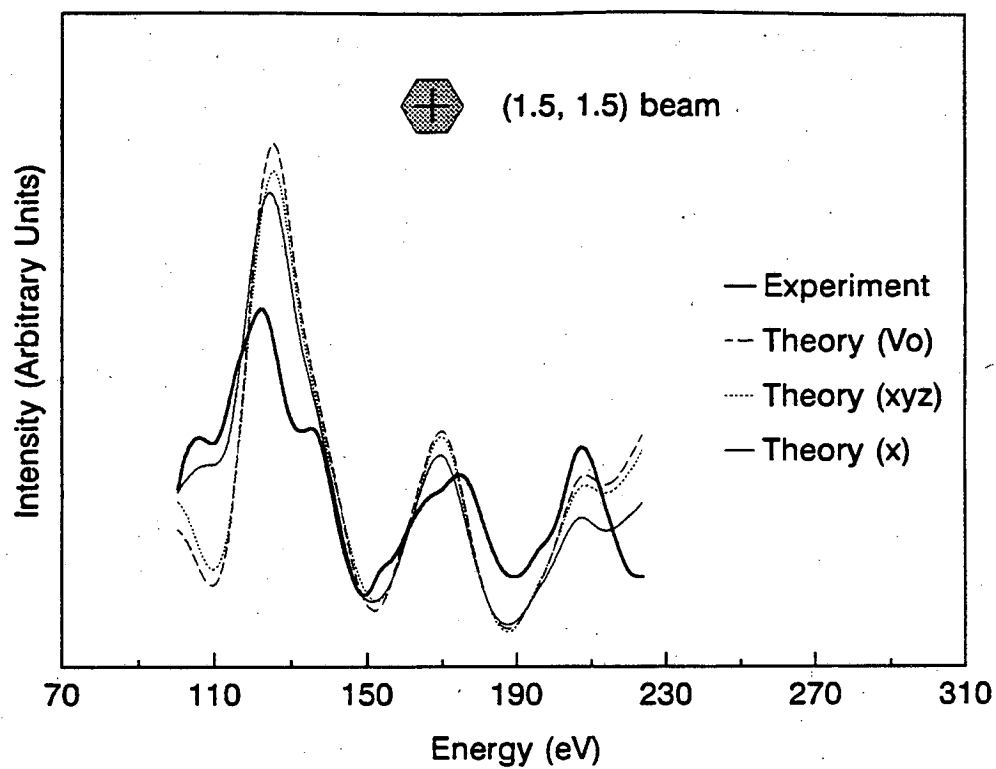**Figure 6.6 Continued**   I-V Curves of Mo(100)-c(2x2)-S: Comparison between theory and experiment
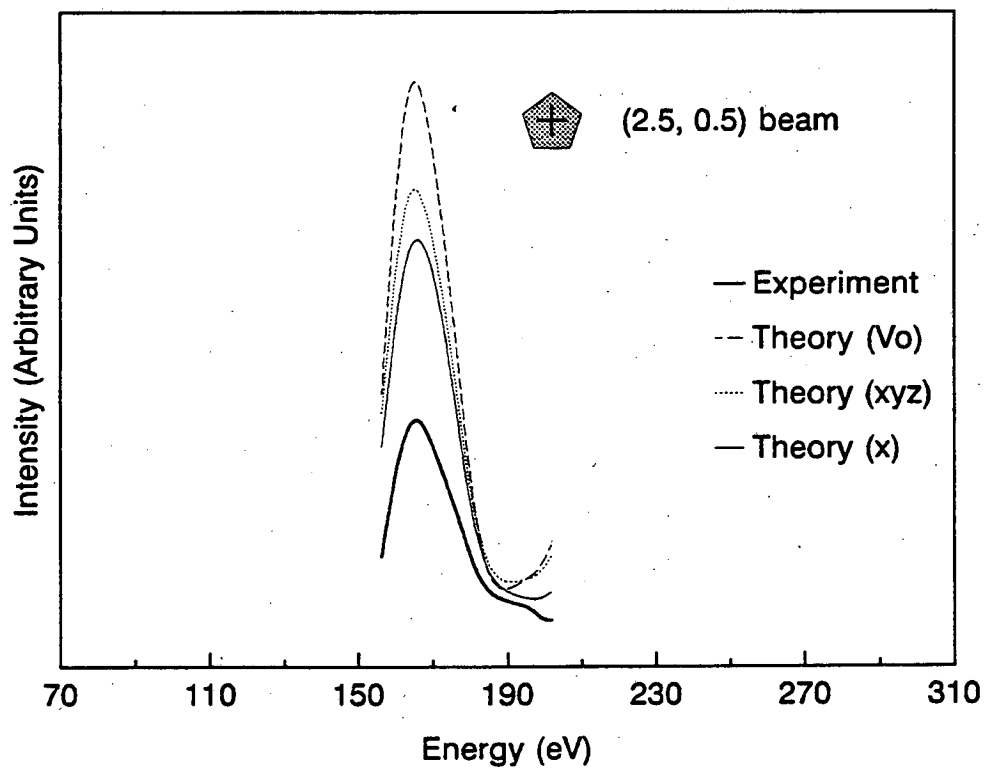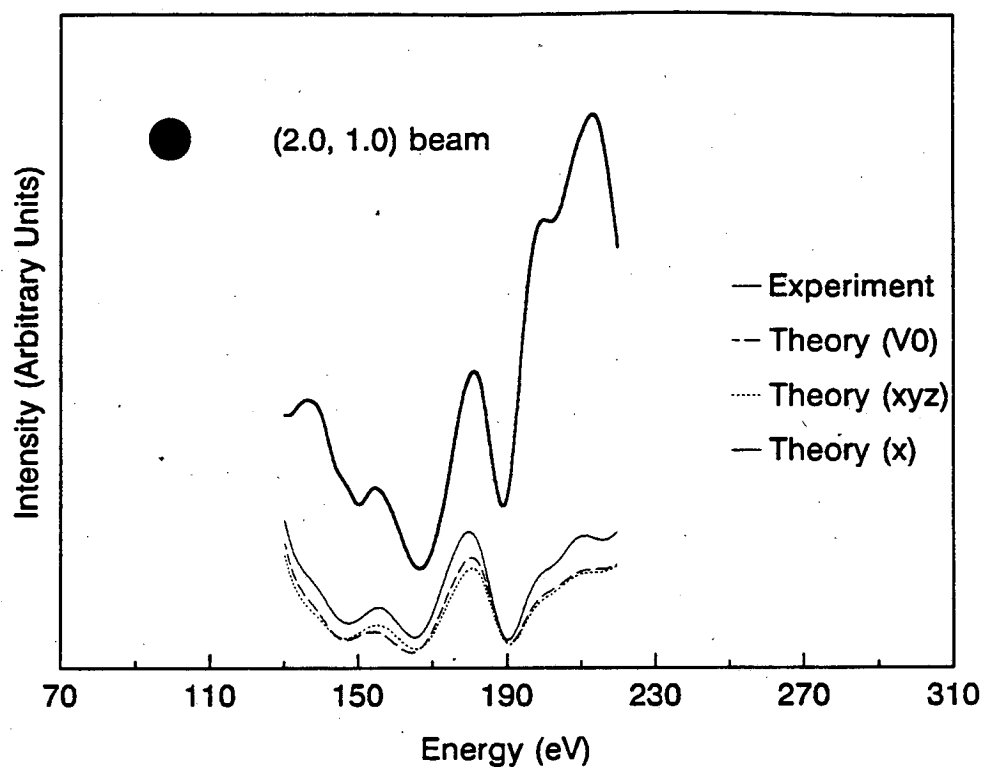
122

Figure 6.6 Continued   I-V Curves of Mo(100)-c(2x2)-S: Comparison between theory and experiment

123

6.2.1. Comparison with Other Studies

A recent scanning tunneling microscopy (STM) study of Mo(100)-c(2x2)-S system compared the STM data with the results of calculations[6.5]. The calculations model the structure of both the surface and the STM tip and calculate what the theoretical STM image would look like. The preliminary results have indicated that both geometries proposed by the two different LEED calculations give a minimum in the STM calculation. Our first result with the second-layer Mo beneath the sulfur buckled upward is the best structure if the STM tip is a Re tip. A Re wire tip was used in the actual experiment. Our second result with the second-layer Mo beneath the sulfur buckled downward is the best structure if the STM tip is covered with sulfur atoms. The second result seems likely since the STM tip may very likely be picking up sulfur atoms as it scans across the surface. However, the STM calculations are unable to determine which tip is actually doing the imaging in the experiment.

The result of our second tensor LEED calculation compares qualitatively well with a conventional LEED study of Ni(100)-c(2x2)-O [6.6]. The best fit results are for a four-fold symmetric hollow adsorption site with buckling in the Ni second layer. The buckling consisted of the second-layer nickel beneath the unoccupied site moving upward. The magnitude of the buckling is 0.035Å. This is smaller than the buckling obtained in our calculations for Mo(100)-c(2x2)-S. However, no *a priori* reason exists to suspect that the two systems should be similar in spite of the fact that oxygen and sulfur are both chalcogens. Oxygen and sulfur have been observed to behave differently on surfaces, for example Mo(100) as indicated earlier. Additionally, the Ni(100) substrate is an fcc(100) surface, whereas the Mo(100) is a bcc(100) surface. The major difference is that the fcc(100) surface is more close packed, that is each first-layer atom has four nearest neighbors in the first layer which touch it. In the bcc(100) each first-layer atom also has four nearest neighbors in the first layer but the difference is that they do not touch each

other. The qualitatively similar result for the Ni(100)-c(2x2)-O structure and the Mo(100)-c(2x2)-S is interesting, but more results of chalcogens on other four-fold surfaces are needed to determine if some trend actually exists.

6.3. Mo(100)-c(4x2)-3S

The Mo(100)-c(4x2)-3S structure occurs at a sulfur coverage of 0.75 ML which is equivalent to three sulfur atoms for every four Mo atoms. The structure was obtained by depositing sulfur from a sulfur source and subsequently annealing the surface to 1000K for 30 seconds. This preparation produced a sharp c(4x2) LEED pattern. The corresponding LEED pattern and schematic are shown in Figure 6.7. In Figure 6.8 a more detailed schematic illustrates the symmetry of the beams at normal incidence. The I-V curves for all the 22 inequivalent beams that were measured and used in the analysis are shown in Figure 6.9. Some beams, which are not presented here, were measured but were not included in the analysis because the signal-to-noise for these beams was very low. Some of the beams, especially the "quarter" order beams (i.e one of the hk indices has the form, $n/4$ with n odd) are very noisy.

For this structure, models which had a mixture of both occupied two-fold symmetric bridge sites and four-fold symmetric hollow sites were considered. Previous investigations of this structure suggested the existence of more than one adsorption site occupied by the sulfur adatoms [6.7]. In all three models the sulfur occupy more hollow sites than bridge sites. This is because the hollow site is believed to be the site which is energetically favored and this is the site which is occupied in the Mo(100)-c(2x2)-S structure. However, these reasons alone should not necessarily exclude other possibilities. Three models were considered in the tensor LEED analysis. In Figure 6.10 two unit cells are shown, the larger unit cell is the p(4x2) and the smaller unit cell is the c(4x2) or primitive unit cell. Since the sulfur overlayer and the first two Mo layers were relaxed in the tensor LEED calculation, 11 atoms needed to be included in the composite layer which meant that a maximum of 33 geometrical degrees of freedom was possible.
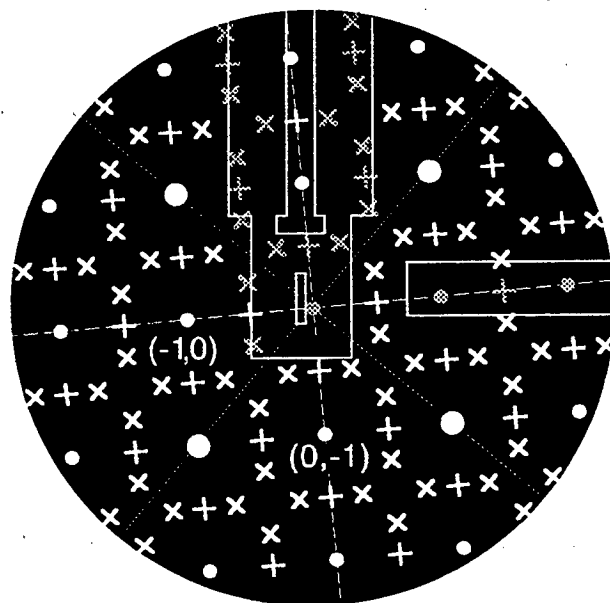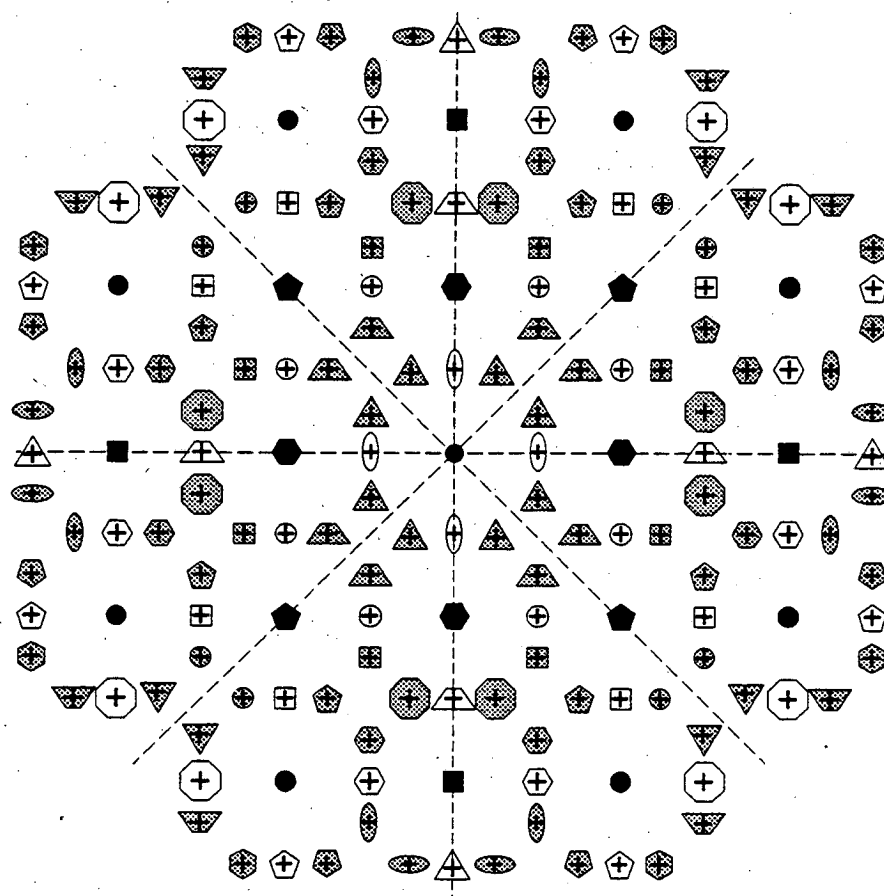
a)

b)

Figure 6.7 a) diffraction pattern of Mo(100)-c(4x2)-3S at 114 eV as displayed on video monitor and b) schematic of c(4x2) diffraction pattern where the crosses represent the fractional order beams (n/2,m) and (m,n/2) and the x's represent the fractional order beams (m/4,n/2) and (n/2,m/4). The filled circles represent the integral order beams. The (hk) labels of the beams are directly beneath the beam. The dotted and dashed lines represent the four mirror planes. The shaded crosses, x's, and circles are the beams that are not seen in the photograph. The outline of the manipulator is in the center of the schematic and the outline of the sulfur source is on the right hand side of the schematic.

127

Integral Order Beams

Symbol	Value	Symbol	Value
⬢	(1.0, 0.0)	⊞	(1.0, 1.5)
⬟	(1.0, 1.0)	⊕	(2.0, 0.5)
●	(2.0, 1.0)	⊕	(2.0, 1.5)
■	(2.0, 0.0)	⊕	(1.0, 2.5)

Fractional Order Beams

Symbol	Value
⊕	(0.0, 0.5)
⟁	(0.0, 1.5)
⊕	(1.0, 0.5)

Additional legend entries:

- △ (0.0, 2.5)
- ▲ (0.5, 0.25)
- ▲ (0.5, 0.75)
- ▦ (0.5, 1.25)
- ⊕ (1.5, 0.25)
- ⊛ (1.5, 1.25)
- ⊛ (1.5, 0.75)
- ▽ (1.5, 1.75)
- ⊛ (0.5, 1.75)
- ⊘ (0.5, 2.25)
- ▽ (1.5, 2.25)
- ⬬ (2.5, 0.25)
- ⊛ (2.5, 0.75)
- ⊛ (2.5, 1.25)

Figure 6.8   Schematic of LEED pattern of Mo(100)-c(4x2)-3S showing symmetry of beams at normal incidence.

Figure 6.9   Experimental I-V Curves of Mo(100)-c(4x2)-3S

129

Figure 6.9 Continued   Experimental I-V Curves of Mo(100)-c(4x2)-3S

130

Figure 6.9 Continued   Experimental I-V Curves of Mo(100)-c(4x2)-3S

131

Figure 6.9 Continued   Experimental I-V Curves of Mo(100)-c(4x2)-3S
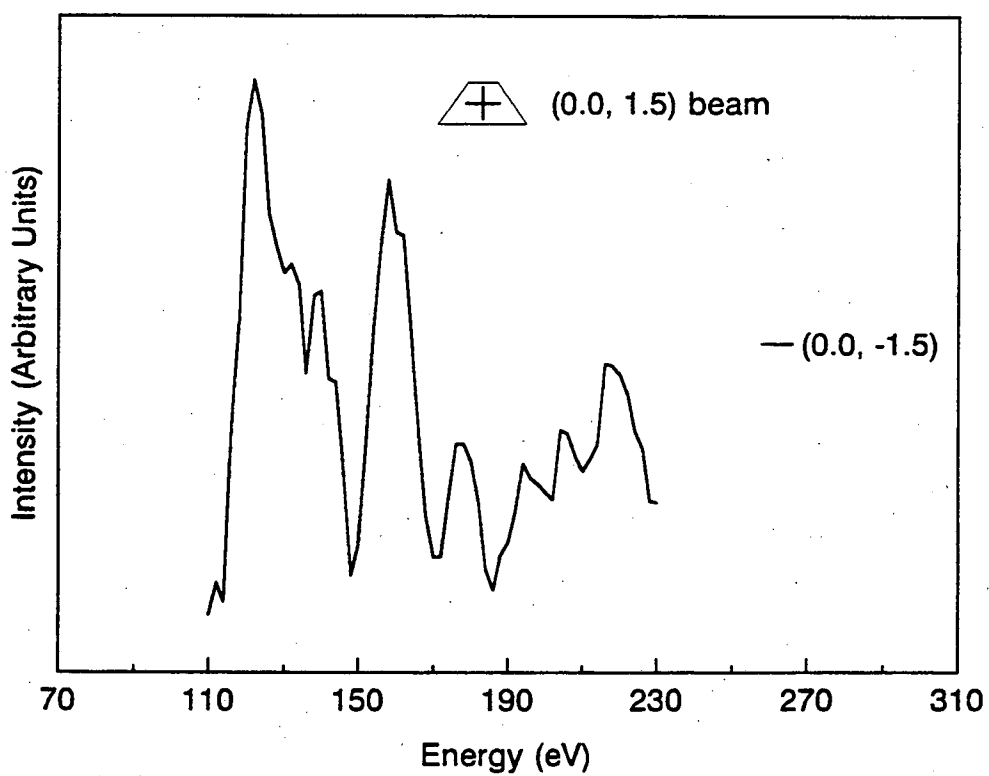
132

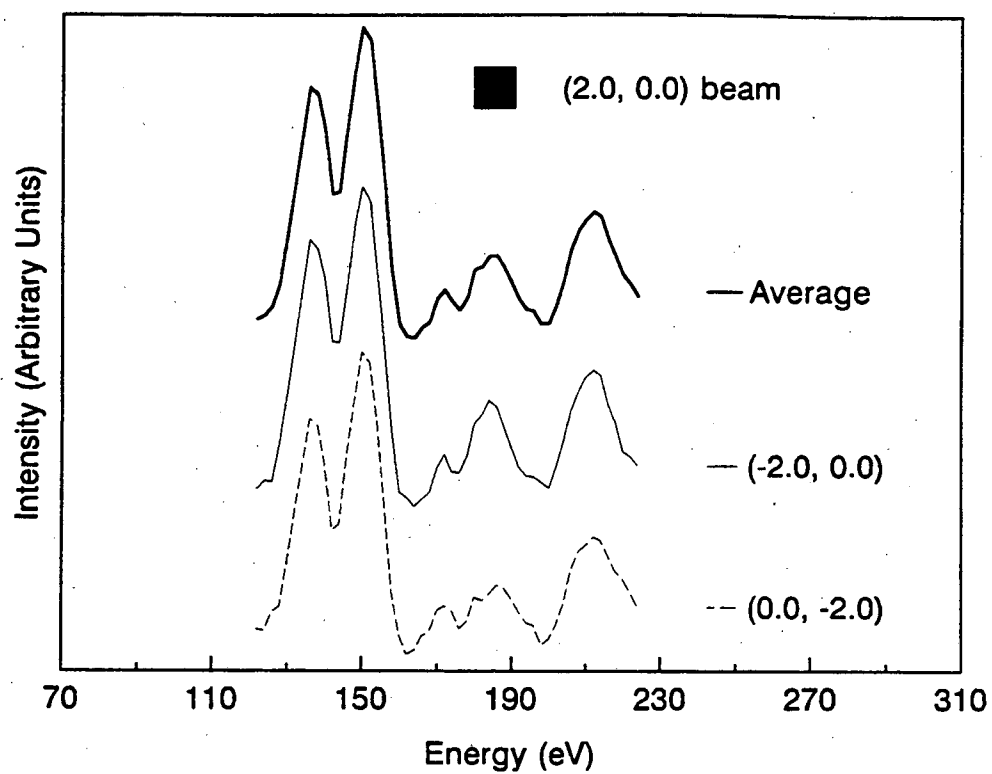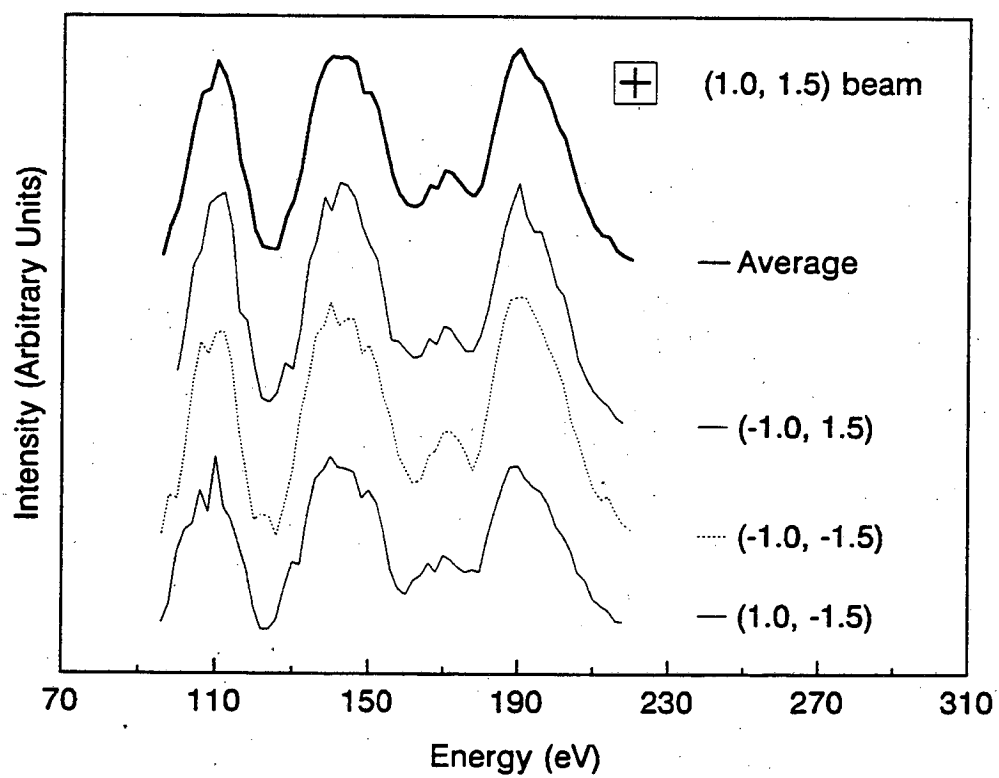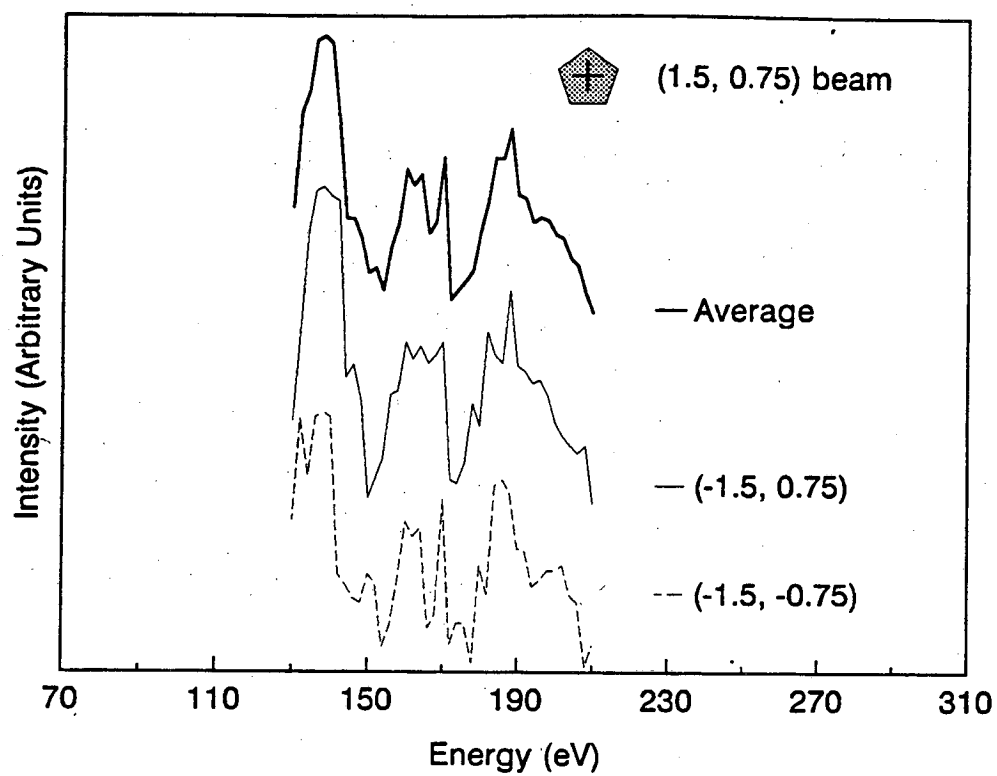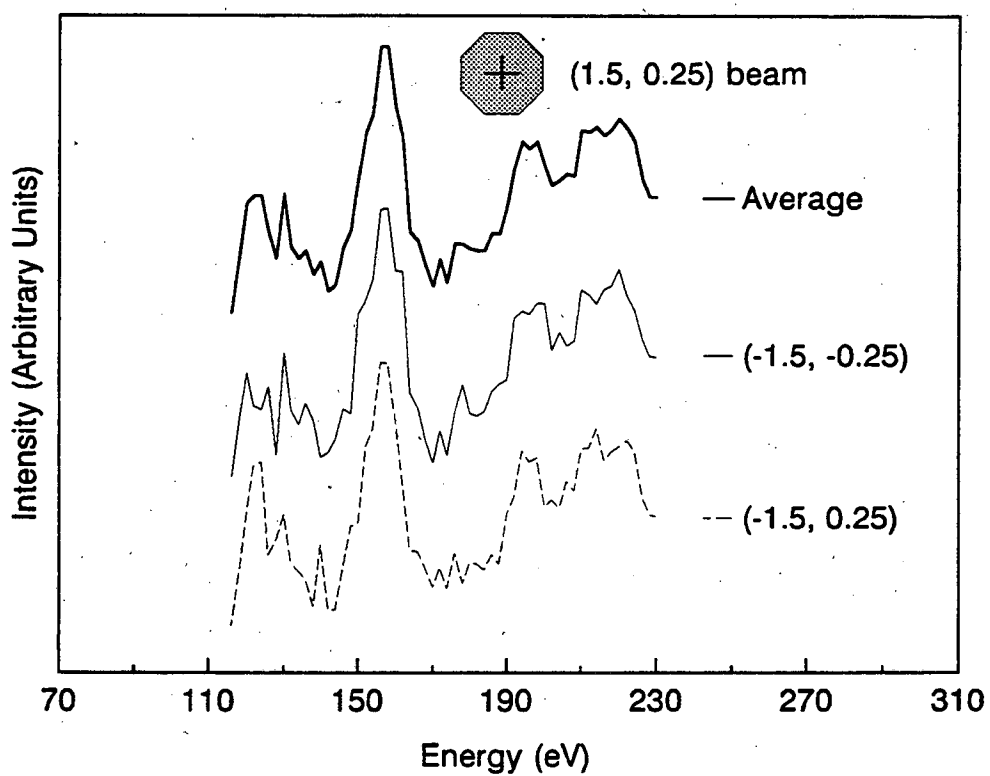Figure 6.9 Continued   Experimental I-V Curves of Mo(100)-c(4x2)-3S

Figure 6.9 Continued   Experimental I-V Curves of Mo(100)-c(4x2)-3S

Figure 6.9 Continued   Experimental I-V Curves of Mo(100)-c(4x2)-3S

135

Figure 6.9 Continued   Experimental I-V Curves of Mo(100)-c(4x2)-3S

136

Figure 6.9 Continued Experimental I-V Curves of Mo(100)-c(4x2)-3S

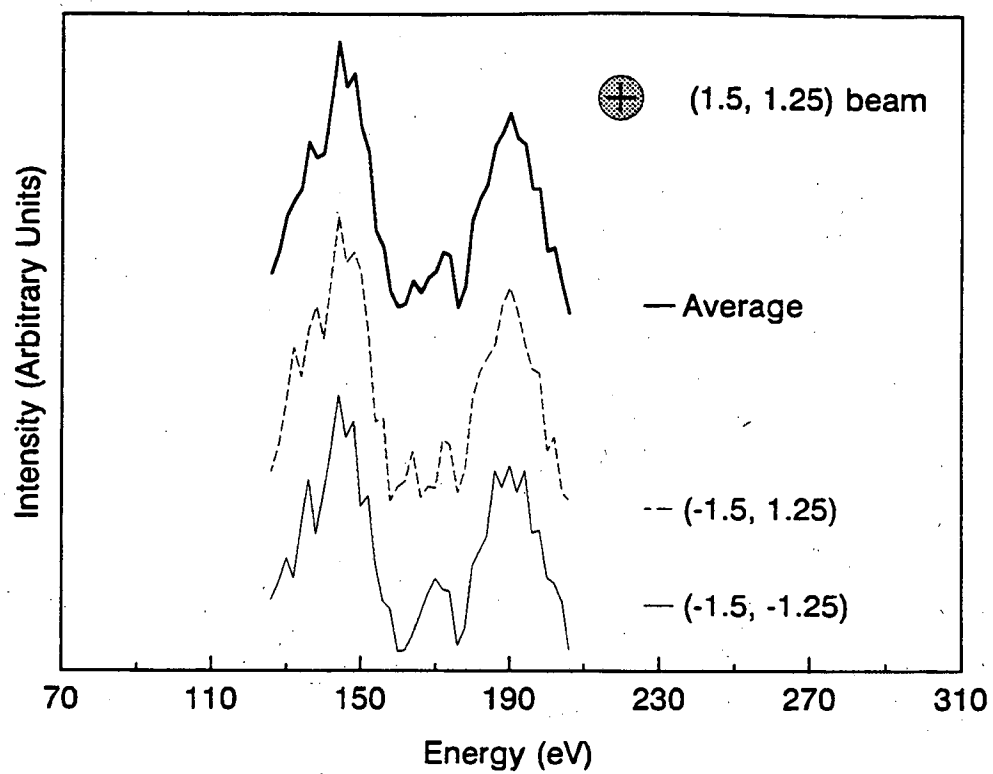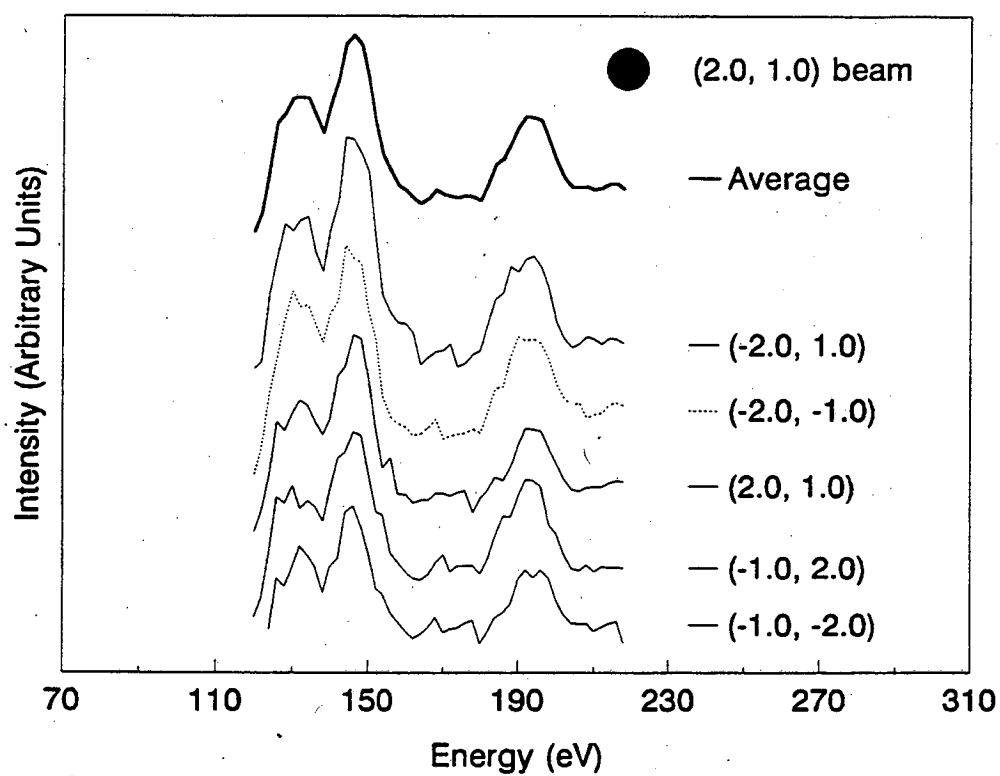**Figure 6.9 Continued** Experimental I-V Curves of Mo(100)-c(4x2)-3S

Figure 6.9 Continued   Experimental I-V Curves of Mo(100)-c(4x2)-3S

(A)

(B)

(C)
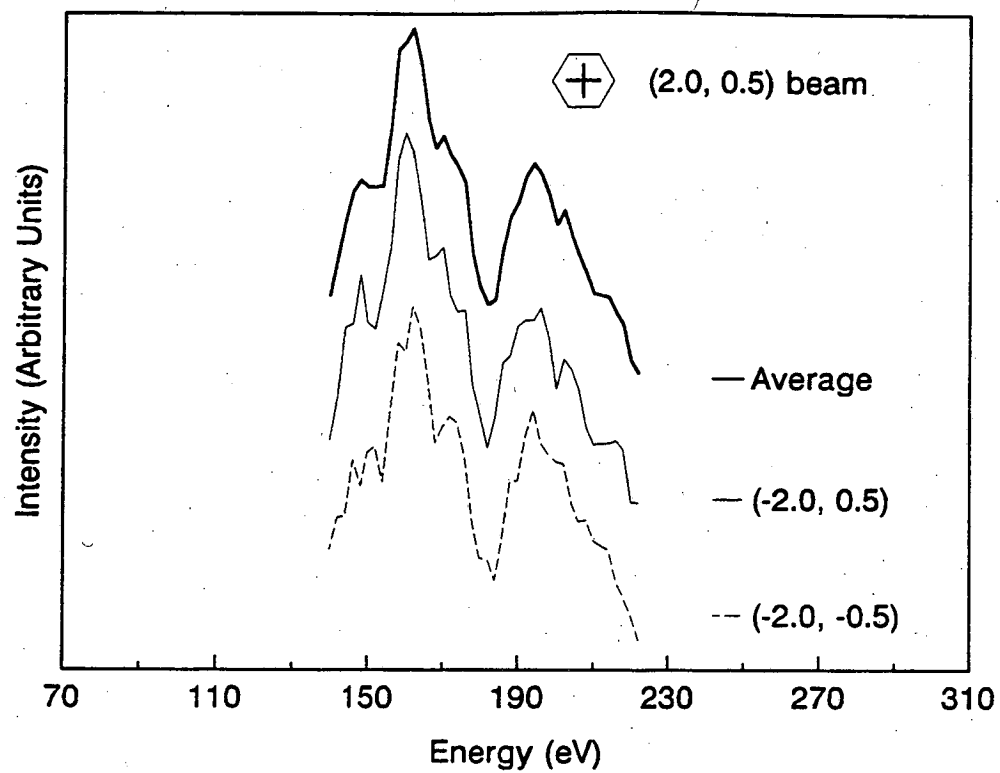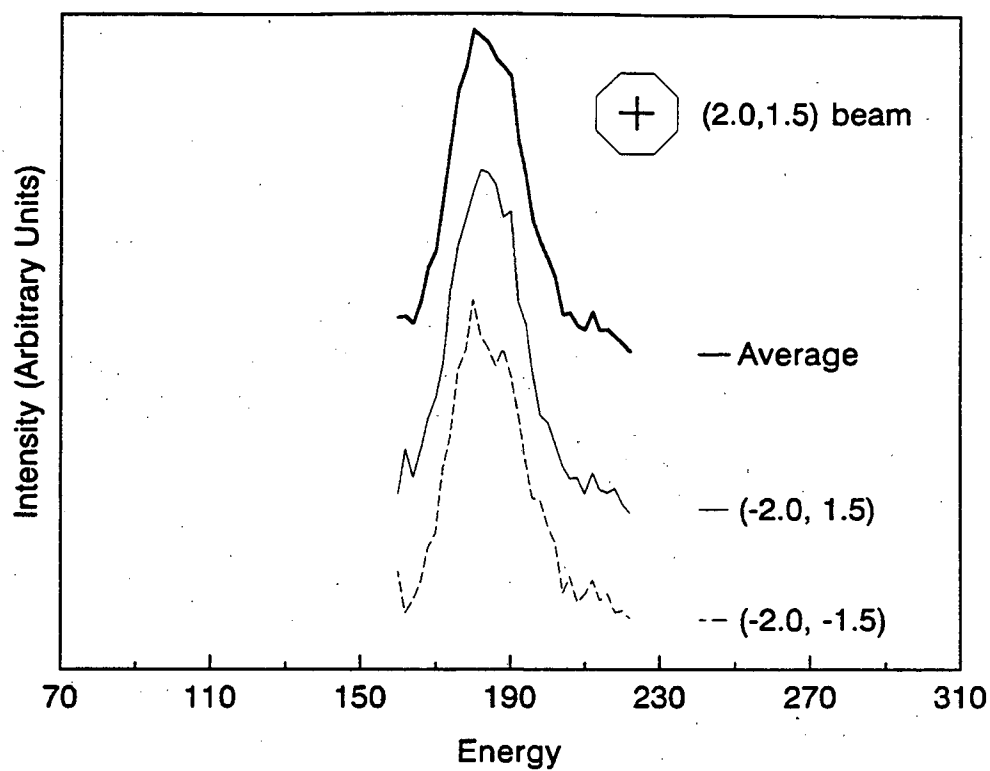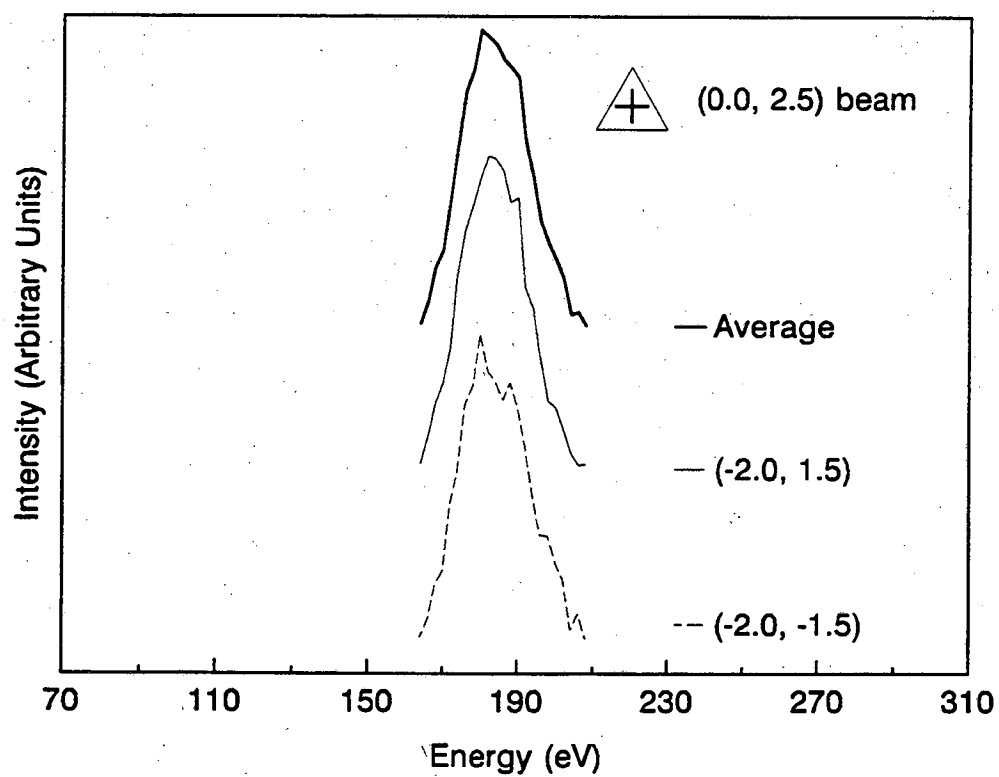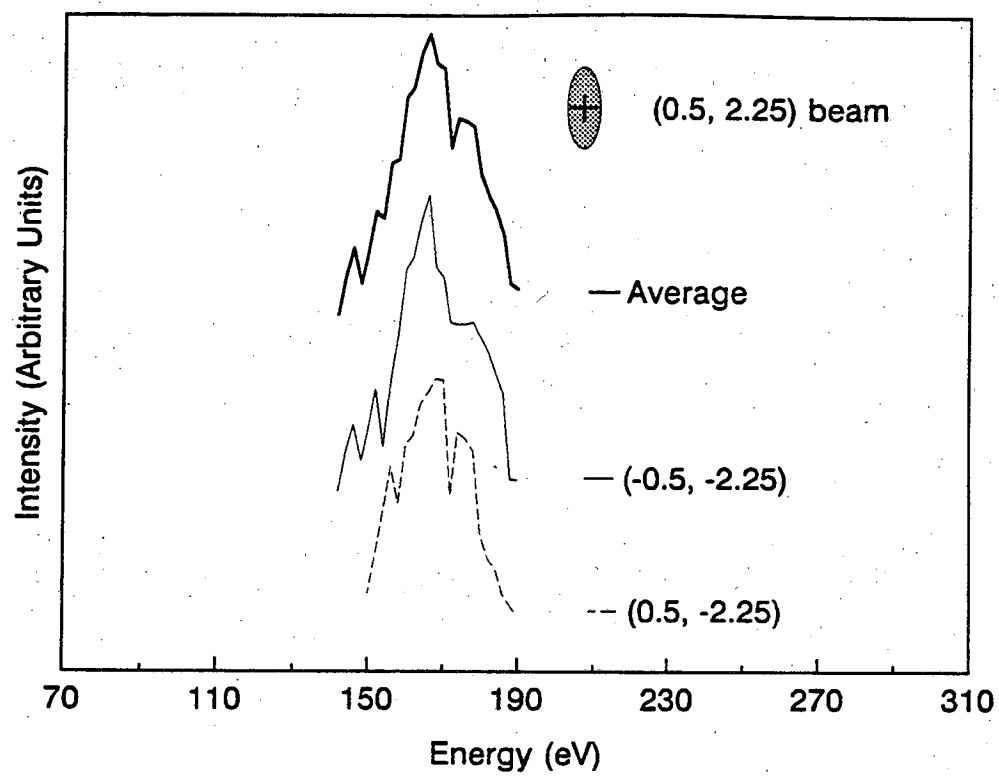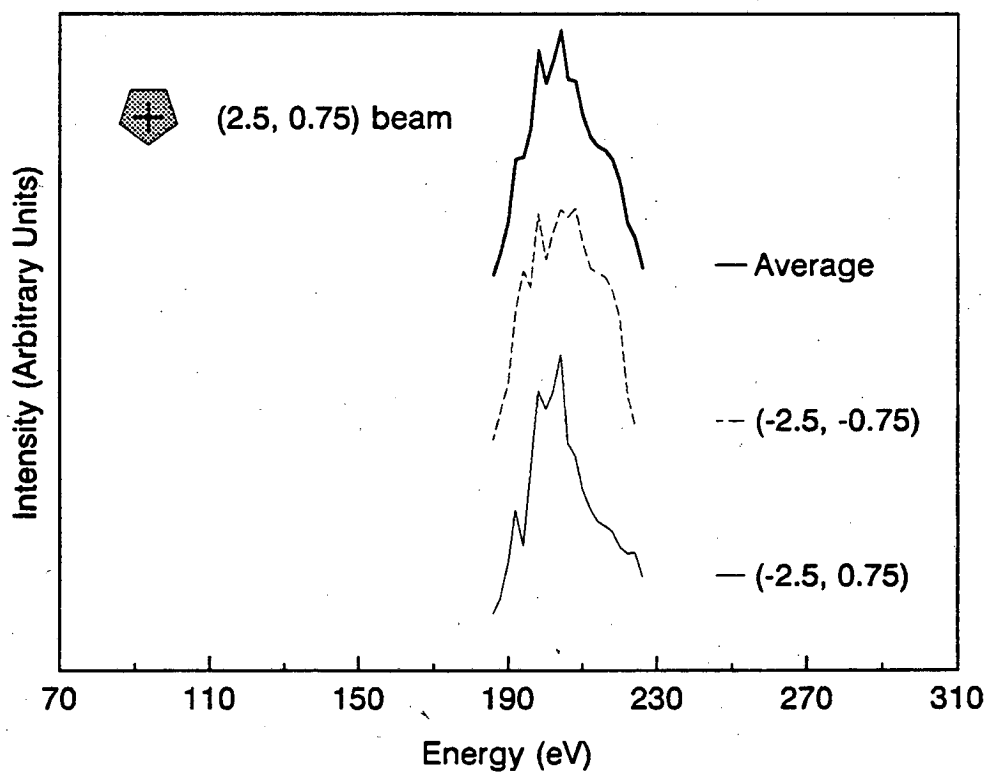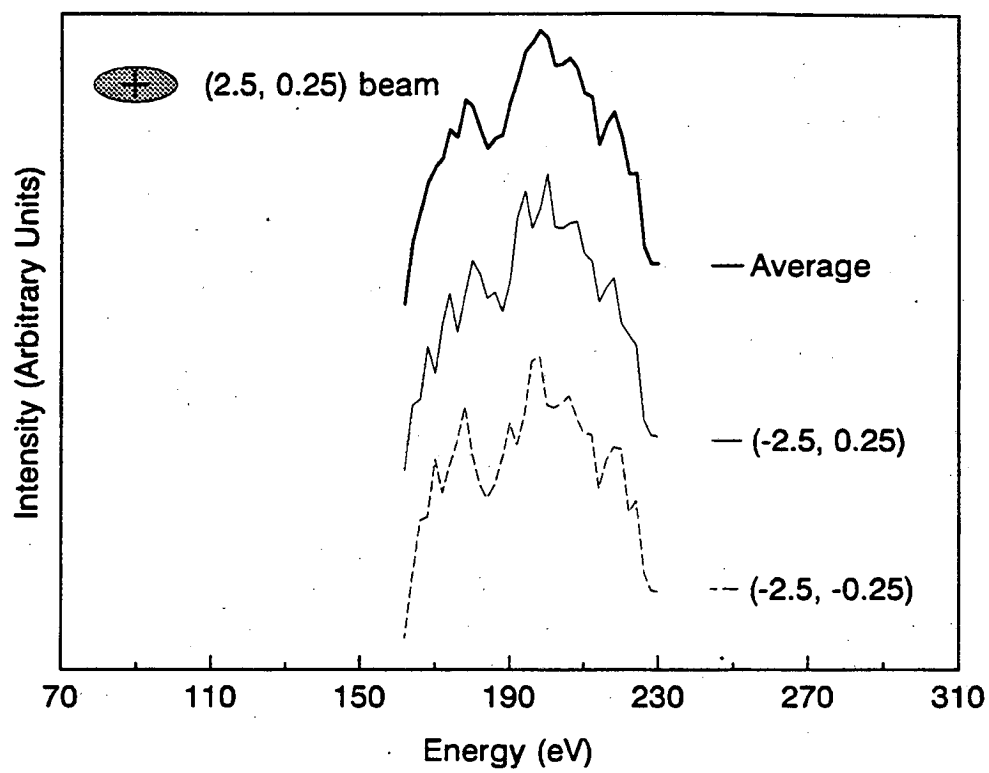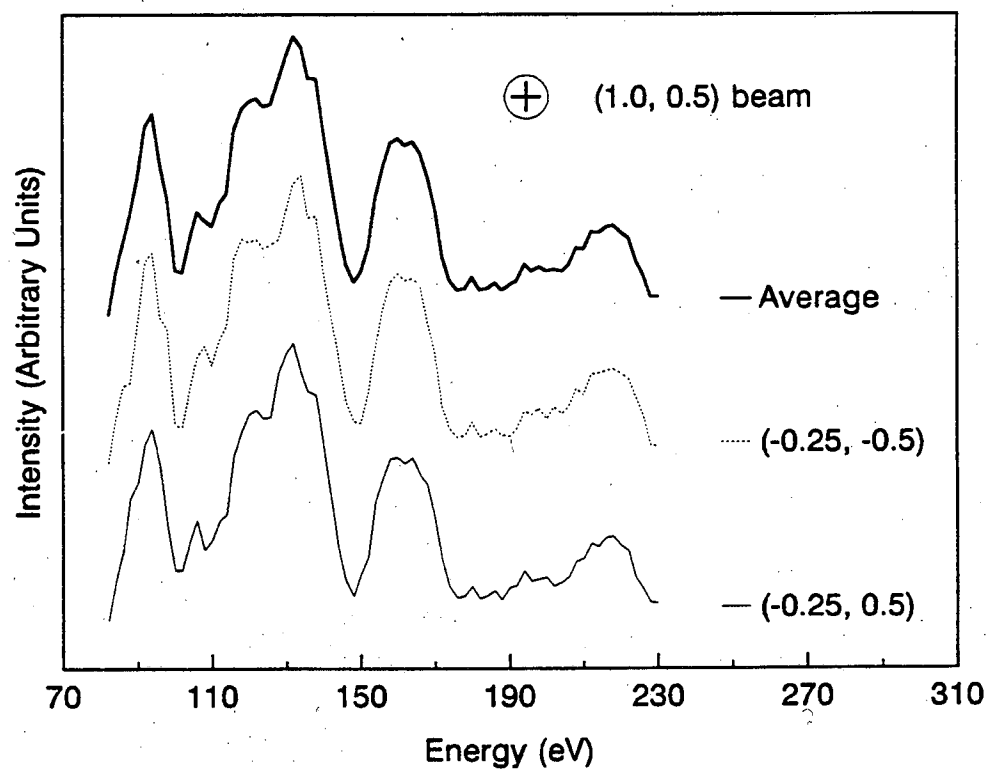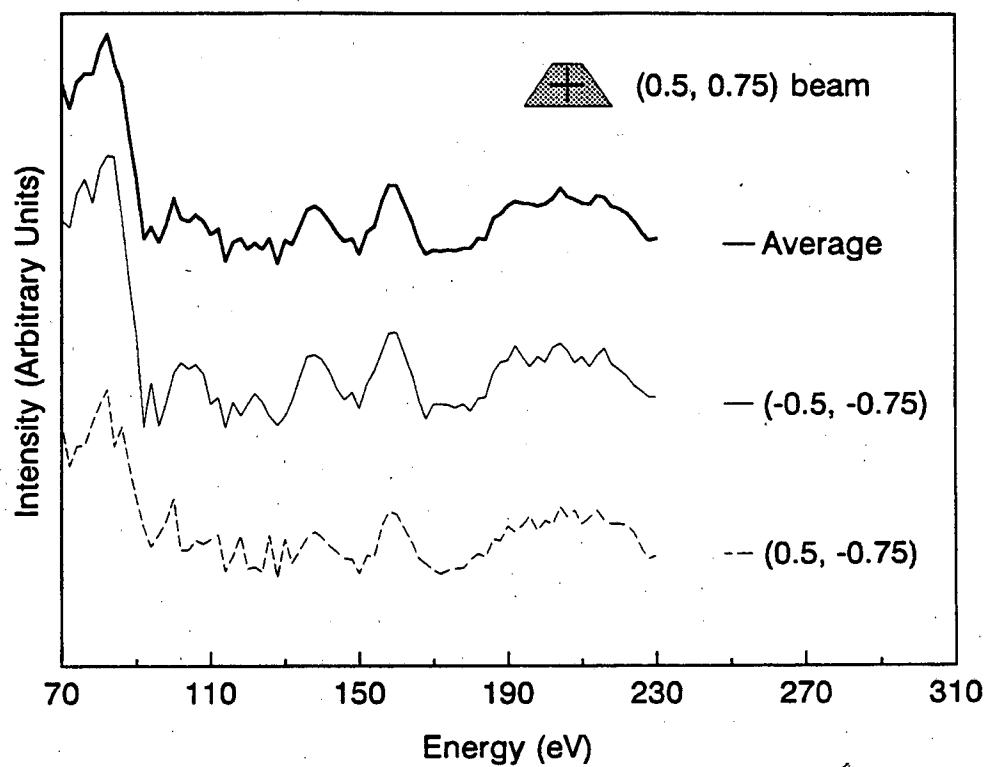
Figure 6.10   Real-space models of Mo(100)-c(4x2)-3S **(a)** All-Hollow Model, **(b)** Bridge-Hollow Model 1, and **(c)** Bridge-Hollow Model 2. The open circles are the first-layer Mo atoms; the dark circles are the sulfur adatoms, and the hatched circles are the second-layer Mo atoms.

140

Table 6.12   Input geometry for All-Hollow Model.

	x	y	z
S(1)	0.000	0.000	0.000
S(2)	0.000	0.000	3.150
S(3)	0.000	3.150	3.150
Mo(4)	0.805	-1.575	-1.575
Mo(5)	0.805	-1.575	1.575
Mo(6)	0.805	1.575	1.575
Mo(7)	0.805	1.575	4.725
Mo(8)	2.380	0.000	0.000
Mo(9)	2.380	0.000	3.150
Mo(10)	2.380	3.150	3.150
Mo(11)	2.380	3.150	6.300

In the first model, all the sulfur atoms occupy hollow sites. This is illustrated in Figure 6.10a. The input geometry of this model is given in Table 6.12. The conventional LEED calculation yielded a Pendry R-factor equal to 0.8932. The tensor LEED analysis was unable to lower the R-factor significantly when all 11 atoms were allowed to move independently in the direction perpendicular to the surface, i.e. in the x direction. The lowest R-factor was on the order of 0.6. If the true structure were composed of all sulfur adatoms occupying four-fold hollow sites then it was not within the radius of convergence of the tensor LEED analysis. The difficulty here was that with so many atoms to consider it was very difficult to decide which parameters to adjust. In all of our analyses, we have assumed that the I-V curves are most sensitive to small changes in the perpendicular direction once the adsorption sites have been determined.

Table 6.13   Input geometry for Bridge-Hollow Model 1.

	x	y	z
S(1)	0.0000	0.0000	0.0000
S(2)	0.9458	1.5750	3.1500
S(3)	0.9458	4.7250	6.3000
Mo(4)	1.7843	0.0000	-1.5750
Mo(5)	1.7843	0.0000	1.5750
Mo(6)	1.7843	3.1500	1.5750
Mo(7)	1.7843	3.1500	4.7250
Mo(8)	3.3593	1.5750	0.0000
Mo(9)	3.3593	1.5750	3.1500
Mo(10)	3.3593	4.7250	3.1500
Mo(11)	3.3593	4.7250	6.3000

The other models considered had a mixture of two-fold bridge sites and four-fold hollow sites. For both models one two-fold bridge site and two four-fold hollow sites are occupied by sulfur in the primitive unit cell. The model that was considered next was the Bridge-Hollow Model 1 which is depicted in Figure 6.10b. The input geometry is given in Table 6.13. The Pendry R-factor for the conventional LEED calculation was 0.949 and the inner potential was 13.3 eV. The tensor LEED calculation varied the sulfur atoms independently and each of the four Mo atoms in the first layer were moved together as were the second-layer Mo atoms. The atoms, given the constraints just mentioned, were allowed to move in the x direction only. The Pendry R-factor was 0.811 and the inner potential was 10.0 eV. The results were not very promising.

The next model was called the Bridge-Hollow Model 2 which differed from Bridge-Hollow Model 1 only in the arrangement of the sulfurs. The sulfur adatoms occupy 1/3 of the bridge sites and 2/3 of the hollow sites. The geometry is shown in Figure 6.10c.

Table 6.14   Input geometry for Bridge-Hollow Model 2.

	x	y	z
S(1)	0.0000	0.0000	0.0000
S(2)	0.9458	3.1500	1.5750
S(3)	0.9458	3.1500	4.7250
Mo(4)	1.7843	-1.5750	-3.1500
Mo(5)	1.7843	-1.5750	0.0000
Mo(6)	1.7843	1.5750	0.0000
Mo(7)	1.7843	1.5750	3.1500
Mo(8)	3.3593	0.0000	-1.5750
Mo(9)	3.3593	0.0000	1.5750
Mo(10)	3.3593	3.1500	1.5750
Mo(11)	3.3593	3.1500	4.7250

The input geometry is given in Table 6.14. The Pendry R-factor was 0.917 and the inner potential was 22.0 for the conventional LEED calculation. The inner potential is outside the range of inner potentials that are usually found. Aside from this, the poor R-factor makes this structure seem unlikely.

Since none of the three models seemed very promising the hollow model was reexamined to see what the effects of smoothing the I-V curves would have and what the effect of using a smaller set of beams would be. Ideally one would like to use all the available data and especially the I-V curves for the superstructure beams. The problem here is that, as mentioned before, the signal-to-noise ratio of some of the beams was very poor. Smoothing had little effect on the results; however, excluding the weaker "quarter" order beams gave a Pendry R-factor of 0.621 and an inner potential of 9.8 eV when all the atoms were allowed to move independently in the x direction. The results are given in Table 6.15.

None of the three models yielded a reasonable fit. The large number of geometrical parameters used in the calculation require a large amount of geometrical parameter space to be sampled. Although we have constrained the 11 atoms in the composite layer to only move perpendicular to the surface, the lowest R-factor after a search was 0.62 for the All-Hollow Model with a restricted set of experimental beams. These results indicate that some problems exist. We have not excluded with complete certainty that the experimental I-V curves are not the problem, i.e the signal-to-noise of the I-V curves of some of the beams is very low. Of course the other possibility is that the models we tried are incorrect. Incorrect could simply mean that the sulfur heights are much different from those that we used, i.e. are beyond the radius of convergence of the tensor LEED analysis (0.25 Å). Further work needs to be done to say with confidence that the three models that were tried are not correct.

Table 6.15   Results of tensor LEED calculation for the All-Hollow Model.

	Δx
S(1)	-0.2365
S(2)	-0.0275
S(3)	0.0484
Mo(4)	0.0108
Mo(5)	-0.0051
Mo(6)	-0.0607
Mo(7)	-0.0029
Mo(8)	0.1521
Mo(9)	0.0304
Mo(10)	-0.0068
Mo(11)	-0.0286

6.4. Mo(100)-p(2x1)-2S

The Mo(100)-p(2x1)-2S structure purportedly occurs at a sulfur coverage of 1.0 ML which is equivalent to one sulfur atom for one molybdenum atom. If each sulfur occupied the same type of site a (1x1) structure would be formed at 1.0 ML; therefore, the sulfur atoms must occupy two different sites or the two sulfurs may occupy the same type of site but must be translationally inequivalent.

Experimentally, this structure was very problematic. As mentioned earlier, this is one of the structures that was not consistently reported in the literature. Oftentimes it was reported as giving a streaked LEED pattern and different investigators suggested various modifications of their models to account for this. This "streaked" p(2x1) was always encountered in this work. Originally we dismissed it as a poorly ordered c(4x2). After considerable effort had been expended to produce a sharp p(2x1) LEED pattern we decided that the "streaked" p(2x1) LEED pattern corresponded to a surface with coexisting domains of p(2x1) and c(4x2). Since the sulfur coverage, as determined by Auger peak ratios, was larger than that for the well-ordered c(4x2) we concluded that the c(4x2) existed in small domains relative to the p(2x1) and would not contribute much to the I-V curves.

In Figure 6.11a a photograph of a streaked c(4x2) or p(2x1) is shown. In Figure 6.11b a LEED pattern of a fairly well-ordered c(4x2) is shown. Notice that the streaks in Figure 6.11a sharpen up in Figure 6.11b into the "quarter" order beams of the c(4x2) LEED pattern.

The LEED pattern and schematic of the p(2x1) are shown in Figure 6.12. In Figure 6.13 a detailed schematic depicts the symmetry of the LEED pattern at normal incidence. The LEED pattern has two rotational domains which are rotated 90° relative to each other. In Figure 6.13a-b the schematics of the two LEED patterns due to the two different domains are illustrated. The observed LEED pattern is the superposition of both

a)
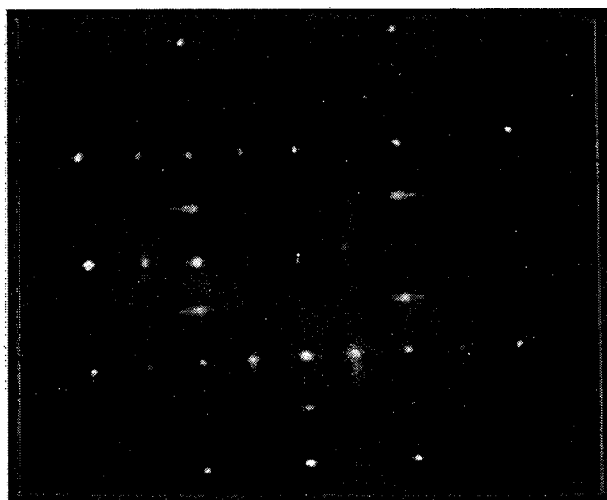
b)
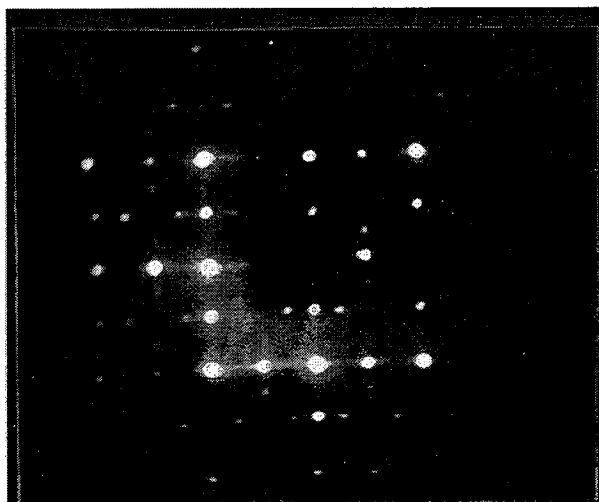
Figure 6.11 Photographs of a) a diffraction pattern of a not very well-ordered Mo(100)-c(4x2)-3S at 133 eV and b) a diffraction pattern of a well-annealed Mo(100)-c(4x2)-3S at 122 eV. Both photographs were taken with a Polaroid camera and Polaroid 57 black and white film was used.

146

a)

b)
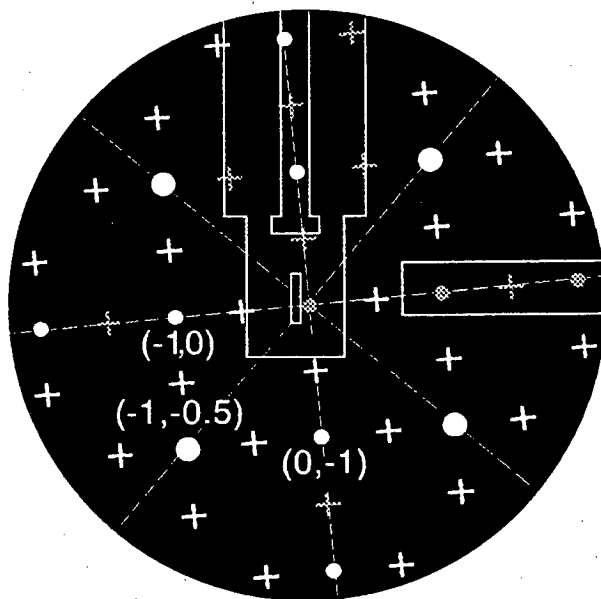
Figure 6.12 a) diffraction pattern of Mo(100)-p(2x1)-2S at 114eV as displayed on the video monitor and **b)** schematic of a p(2x1) diffraction pattern where the crosses represent the fractional order beams and the filled circles represent the integral order beams. The (hk) labels of the beams are directly beneath the beams. The dotted and dashed lines represent the four mirror planes. The shaded crosses and circles are the beams that are not seen in the photograph and the larger circles correspond to the more intense beams. The outline of the manipulator is in the center of the schematic and the outline of the sulfur source is on the right hand side of the schematic.

147

(a)

(b)

Integral Order Beams

(1.0, 0.0)

(1.0, 1.0)

(2.0, 0.0)

(2.0, 1.0)

Fractional Order Beams

(0.5, 1.0)

(1.5, 1.0)

(0.5, 2.0)

(2.5, 1.0)

(1.5, 2.0)

(0.5, 0.0)

(1.5, 0.0)

(2.5, 0.0)

(c)
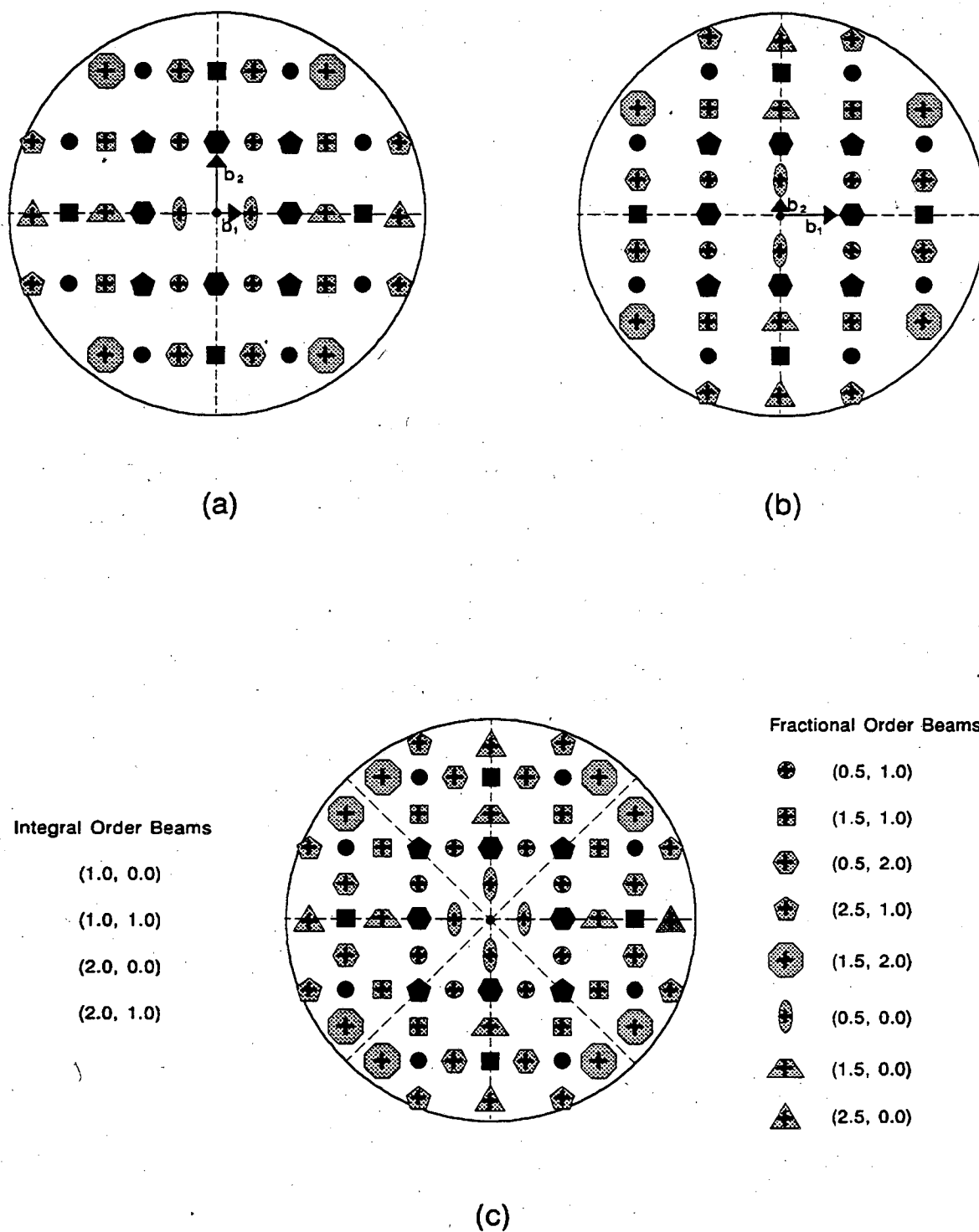
Figure 6.13   Schematic of **a)** a p(2x1) LEED pattern, **b)** a p(1x2)LEED pattern, and **c)** the LEED pattern which results from the superposition of both p(2x1) and p(1x2) LEED patterns.
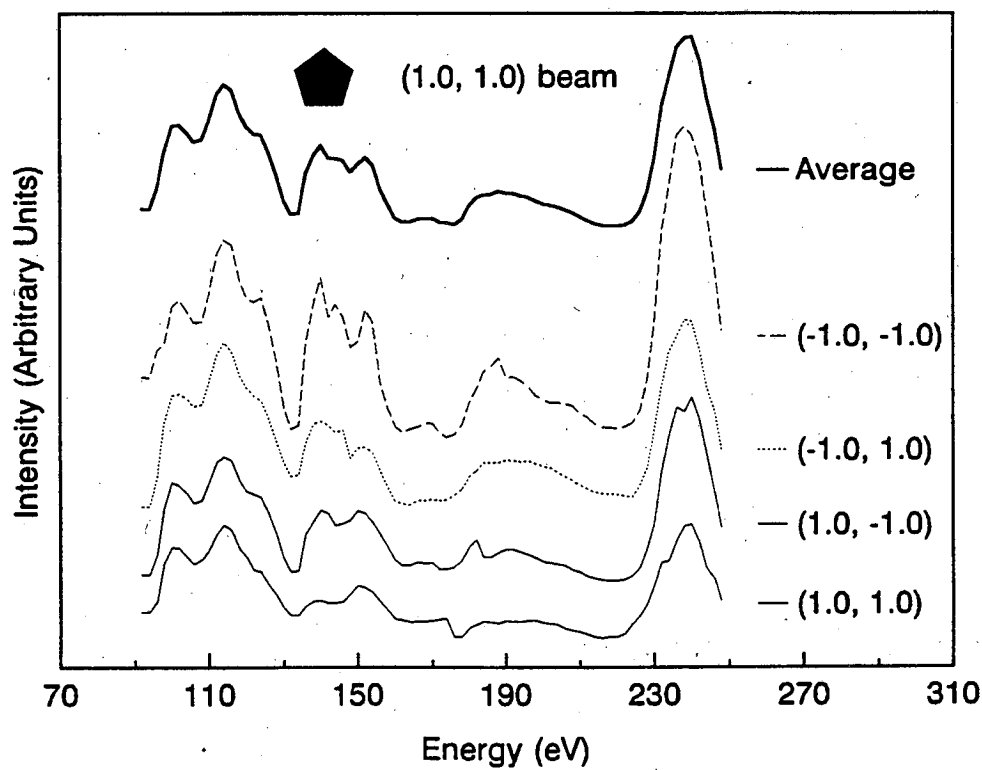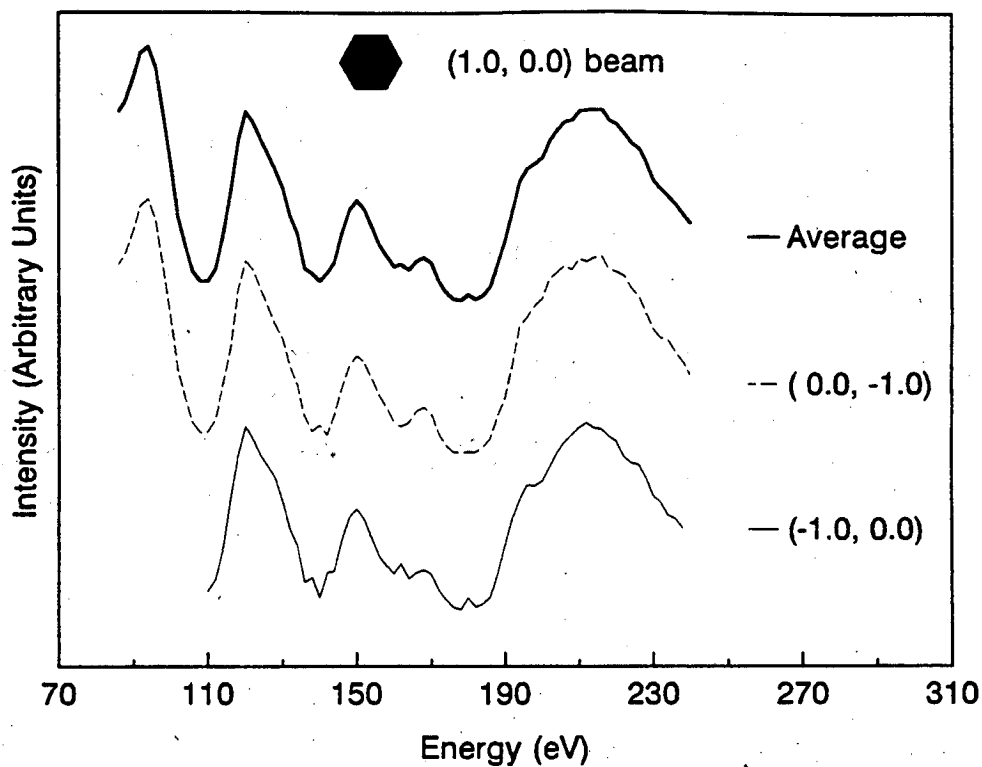
Figure 6.14 Experimental I-V curves of Mo(100)-p(2x1)-2S
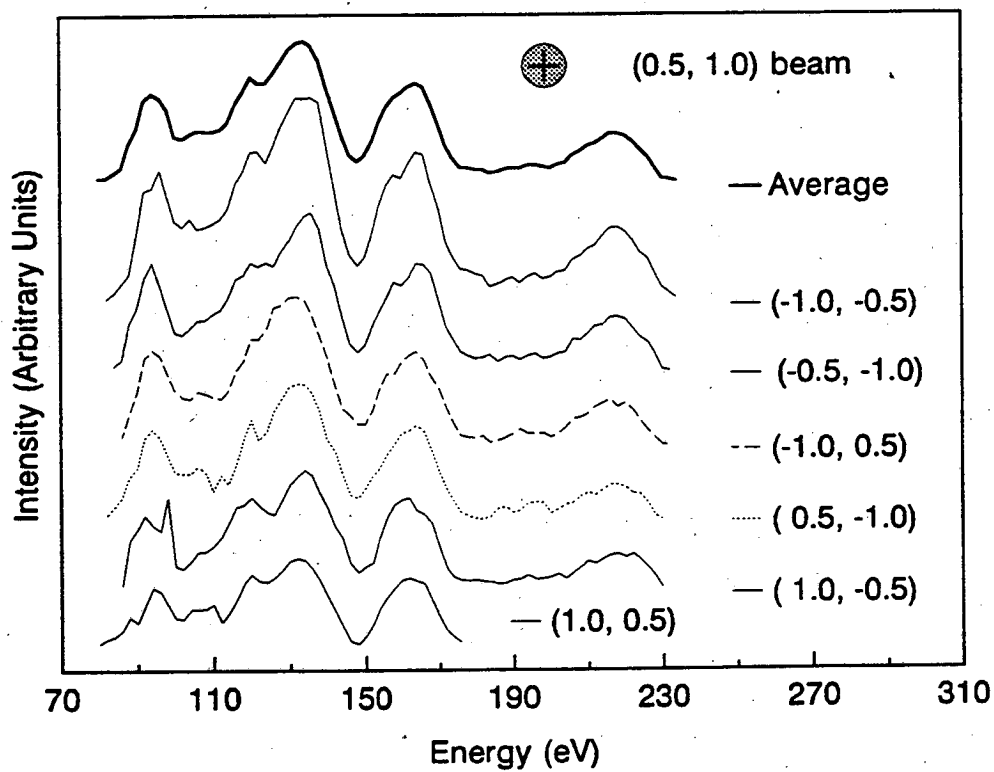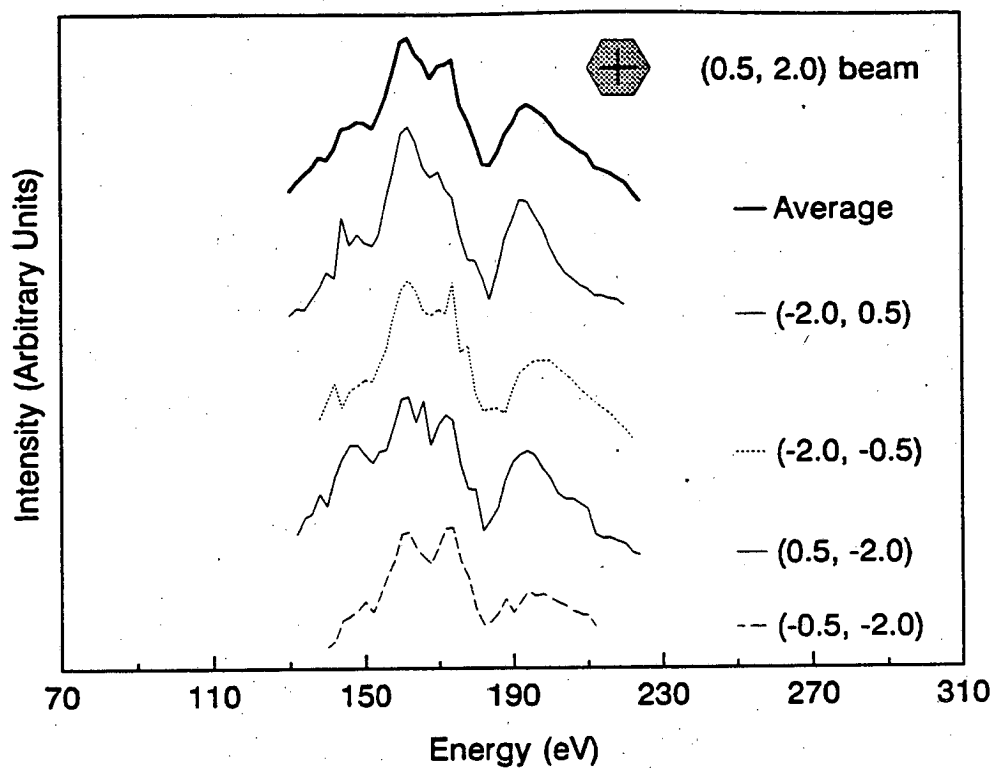
149

Figure 6.14 Experimental I-V curves of Mo(100)-p(2x1)-2S

150

Figure 6.14 Experimental I-V curves of Mo(100)-p(2x1)-2S

151

Figure 6.14 Experimental I-V curves of Mo(100)-p(2x1)-2S

152
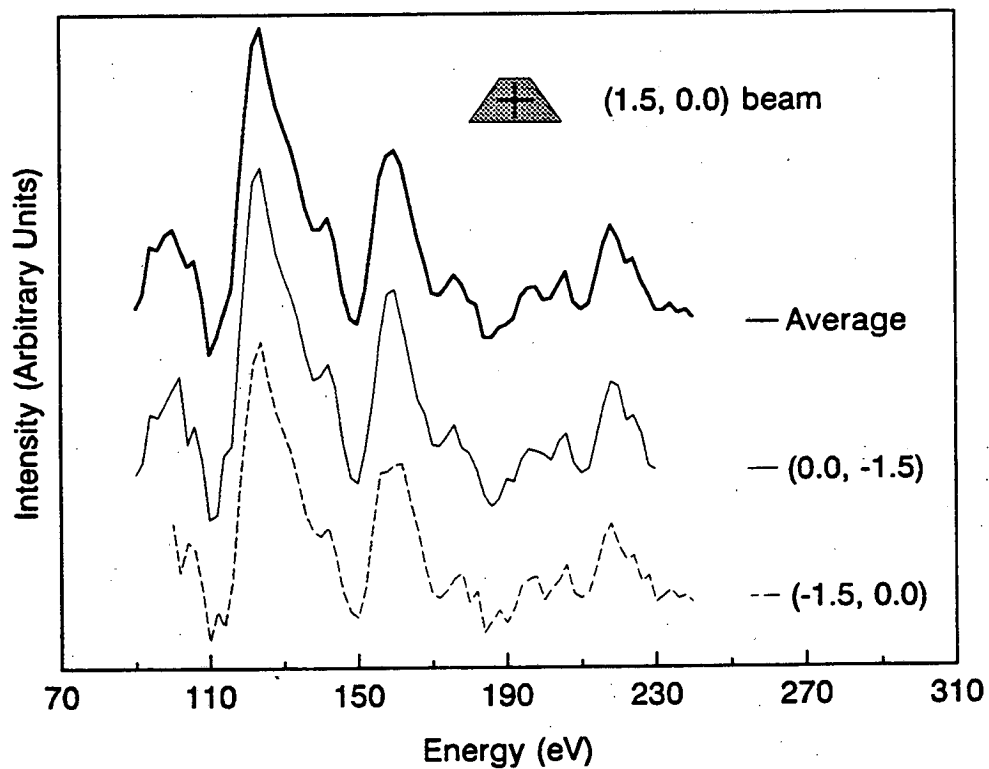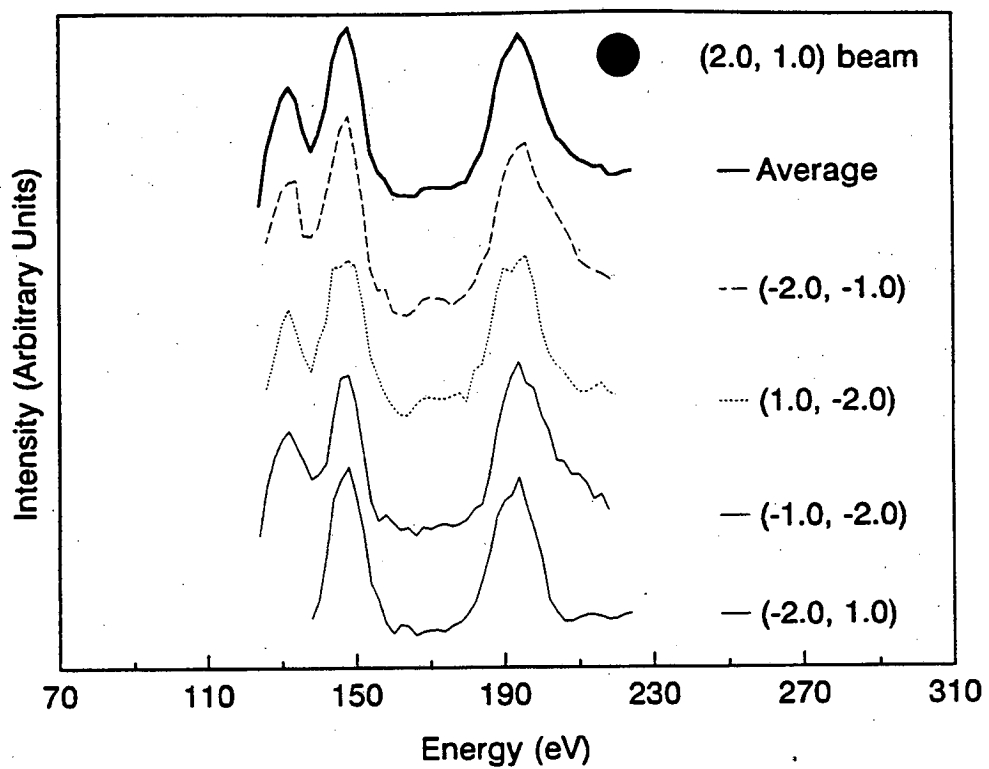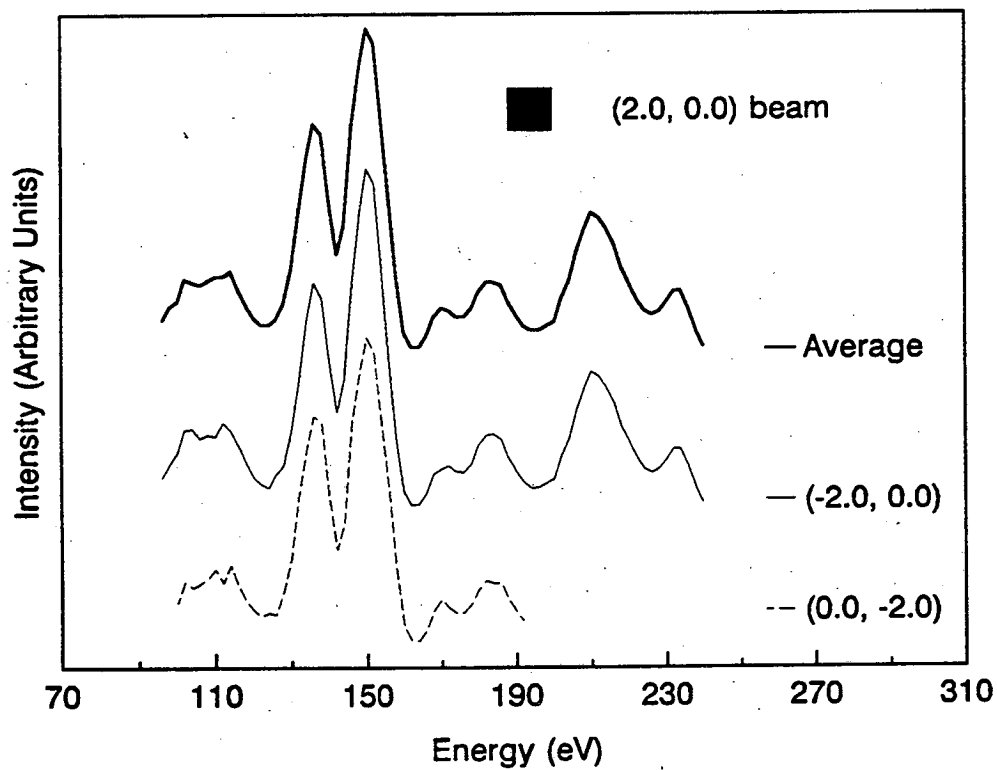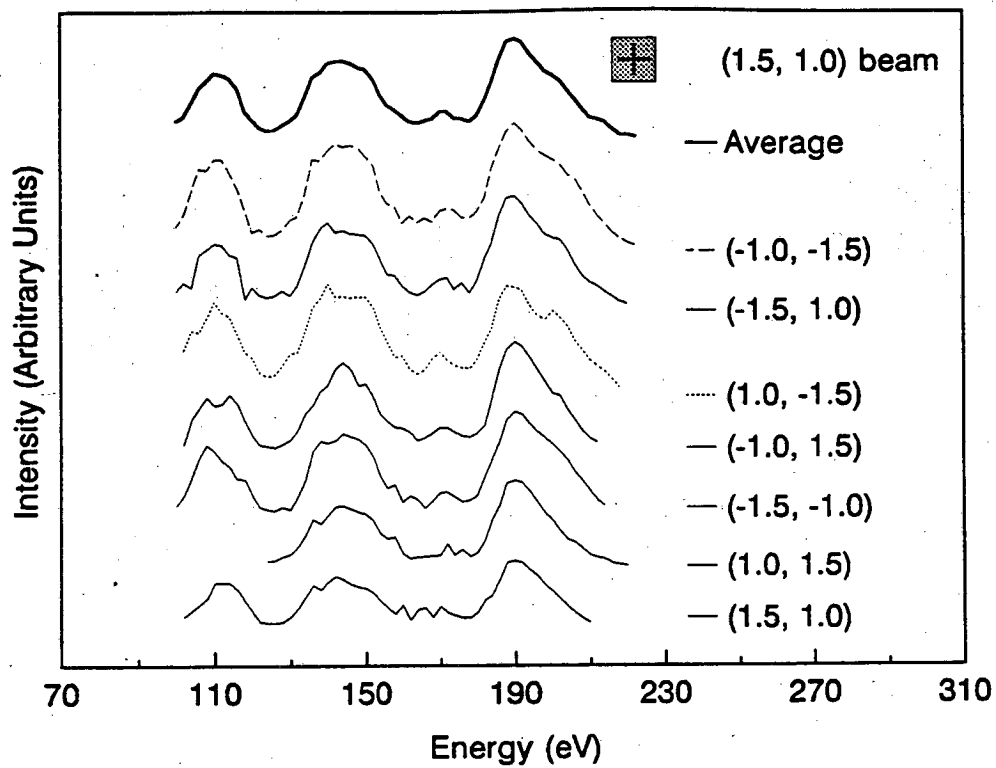
LEED patterns. This is illustrated in Figure 6.13c. Notice that each domain has two mirror planes but the superposition has four mirror planes just as the substrate does. Thus, the observed LEED pattern at normal incidence has the full symmetry of the substrate. The experimental I-V curves of the Mo(100)-p(2x1)-2S are presented in Figure 6.14.

Many models were used in the tensor LEED analysis of the Mo(100)-p(2x1)-2S structure. The first model which was considered is illustrated in Figure 6.15. The two sulfur atoms in the unit cell occupy one bridge site and one hollow site. This model will be referred to as the Bridge-Hollow Model. For the LEED analysis the sulfur overlayer and first two Mo layers were relaxed. This meant that 6 atoms, 2 sulfur atoms and 4 molybdenum atoms, were included in the composite layer. The input geometry for this model is given in Table 6.16. The tensor LEED results for this model were a Pendry R-factor of 0.521 and an inner potential of 7.75 eV. This was for a search over all coordinates for all 6 atoms.

a)

b)
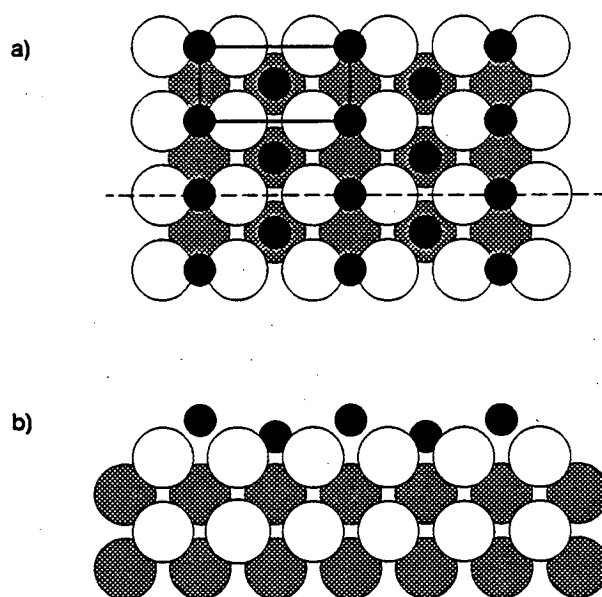
Figure 6.15 Bridge-Hollow Model of Mo(100)-p(2x1)-2S with bridge and hollow positions occupied by the sulfur atoms a) top view and b) side view which is a cut along the dotted line in a).

Table 6.16 Input geometry for Bridge-Hollow Model.

	x	y	z
S(1)	0.0000	0.0000	0.0000
S(2)	0.9172	3.1500	1.5750
Mo(3)	1.8109	1.5750	0.0000
Mo(4)	1.8109	4.7250	0.0000
Mo(5)	3.3860	0.0000	1.5750
Mo(6)	3.3860	3.1500	1.5750

The second model considered is illustrated in Figure 6.16. This model is the 1/4 1/4 model that was proposed by the STM study [6.8]. This model can be thought of as a (1x1) where the sulfur atoms have been displaced towards the bridge sites by $a/4$, where a is the lattice constant. The rows of sulfur are staggered with respect to each other. Notice that this model has a glide plane. The glide plane is the one symmetry element that will cause spot extinctions in the LEED pattern if the incident electron beam is parallel to the glide plane. For the case of a p(2x1) LEED pattern, those spots with indices (0, n/2) or

a)

b)
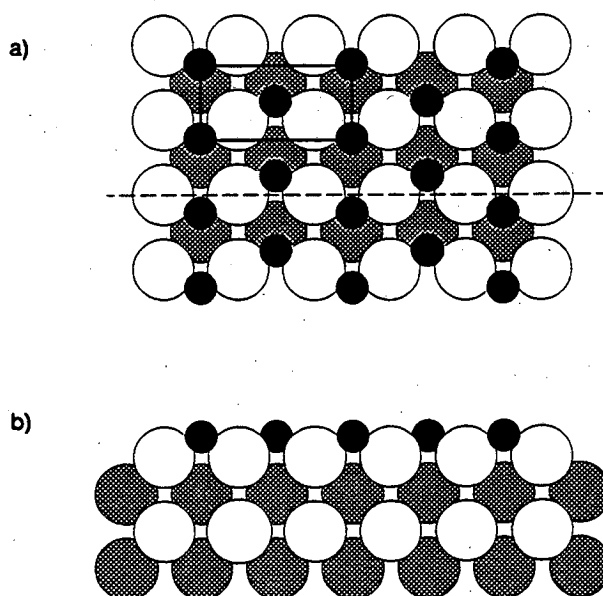
Figure 6.16   Asymmetric-Hollow Model of Mo(100)-p(2x1)-2S with 1/4 1/4 positions occupied by the sulfur atoms a) top view and b) side view which is a cut along the dotted line (i.e. the glide plane) in a).

(n/2, 0) where n is odd will be extinguished. This was not observed in the experiment as can be seen in Figure 6.12 which is one of the video images used to generate the I-V curves shown in Figure 6.14. This fact makes this model questionable but we were not certain how accurate the angle of incidence must be in order to satisfy the condition for spot extinctions, so the model was not excluded.

The input geometry is given in Table 6.17. The tensor LEED calculation gave a Pendry R-factor of 0.609 and an inner potential of 5.05 eV. At the start of the tensor LEED calculation the reference structure needed to be perturbed slightly to remove the glide plane symmetry. Otherwise the theoretical beams that had nearly zero intensity, within the accuracy of the computer, could not be compared to the experimental beams which had measurable intensities.

Other models were considered in the LEED analysis. A total of 13 models were considered, that is conventional LEED calculations were performed for 13 reference structures. Some of these structures are slight variations on each other but they are all beyond the reach of the radius of convergence of the tensor LEED calculation, that is one reference structure can not be reached by starting with another reference structure. The results of the 5 types of models are listed in Table 6.18. None of these models which are illustrated in Figures 6.15-19 gave a satisfactory fit.

Table 6.17   Input geometry for Asymmetric-Hollow Model, 1/4
1/4 Model.

	x	y	z
S(1)	0.0000	0.0000	0.0000
S(2)	0.0000	3.1500	1.5750
Mo(3)	1.7403	1.5750	2.3625
Mo(4)	1.7403	4.7250	2.3625
Mo(5)	3.3153	0.0000	0.7875
Mo(6)	3.3153	3.1500	0.7875

155

Table 6.18 Tensor LEED results for five representative models. The Pendry R-factor, Rp, and the inner potential, V_{or}, are given for each model.

Models	Bridge-Hollow	Asymmetric-Hollow	Sulfur-Pairing	Mo-Pairing	Quasi-hexagonal
Rp	0.52	0.61	0.42	0.50	0.56
$V_{or}(eV)$	7.8	5.0	9.0	16.8	3.0

In Figure 6.20 the experimental I-V curves of the beams which are shared in common between the p(2x1) and c(4x2) are plotted for comparison. The energy ranges are slightly different but the curves look extremely similar if not exactly alike. Initially this was disturbing; however, very similar I-V curves for structures with different LEED patterns, long range order, is possible because the I-V curves reflect the local bonding geometry of the atoms comprising the structure. Although the I-V curves themselves are not proof of anything, the failed tensor LEED analysis adds some doubt as to whether the I-V curves are for a Mo(100)-p(2x1)-2S structure. Additionally, the inconsistencies in the
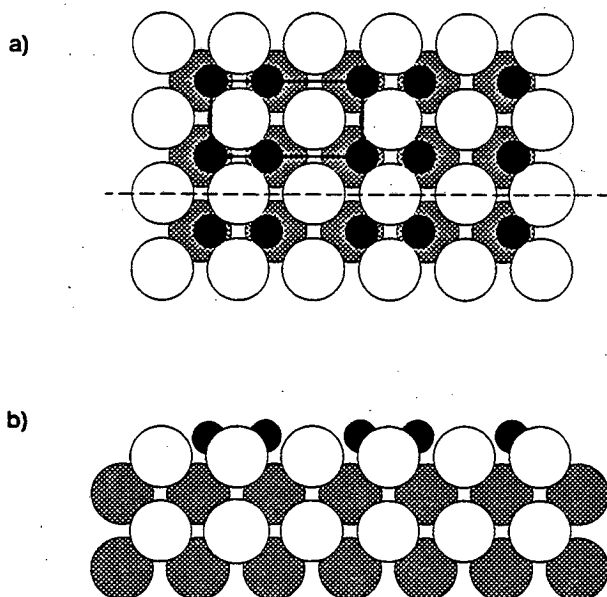
Figure 6.17 Sulfur-Pairing Model of Mo(100)-p(2x1)-2S with off-center hollow sites occupied by the sulfur atoms a) top view and b) side view which is a cut along the dotted line in a).
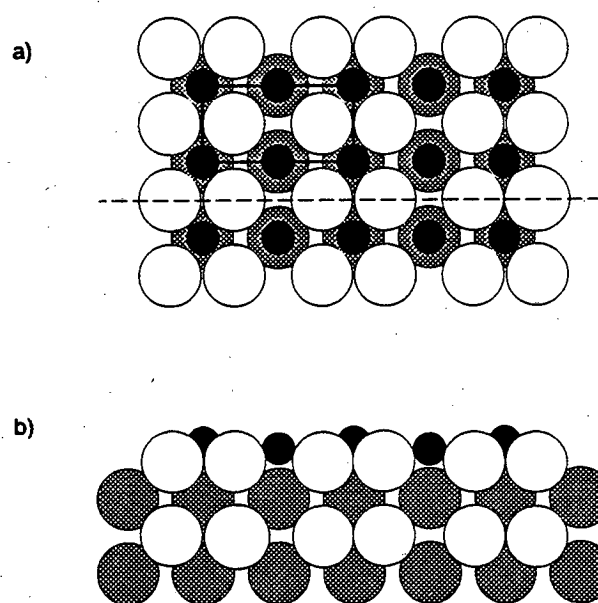
Figure 6.18   Mo-Pairing Model of Mo(100)-p(2x1)-2S with   hollow sites occupied by the sulfur
atoms and the first-layer Mo atoms paired together in rows a) top view and b) side view which is a cut
along the dotted line in a).
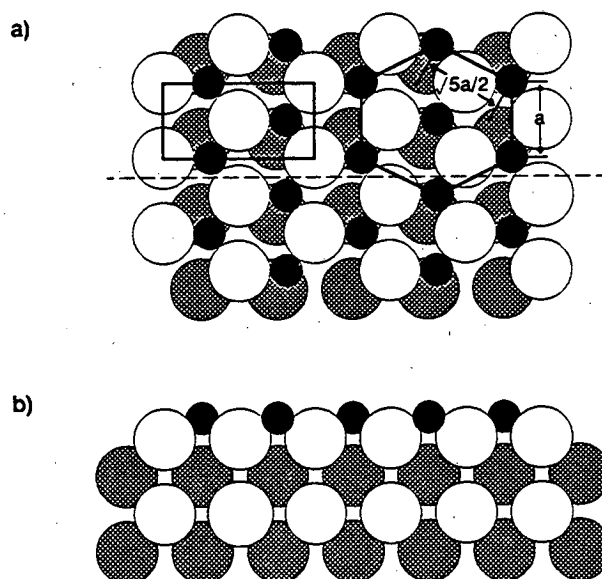
Figure 6.19   Quasihexagonal Model of Mo(100)-p(2x1)-2S with quasi three-fold sites occupied by the
sulfur atoms a) top view and b) side view which is a cut along the dotted line in a).
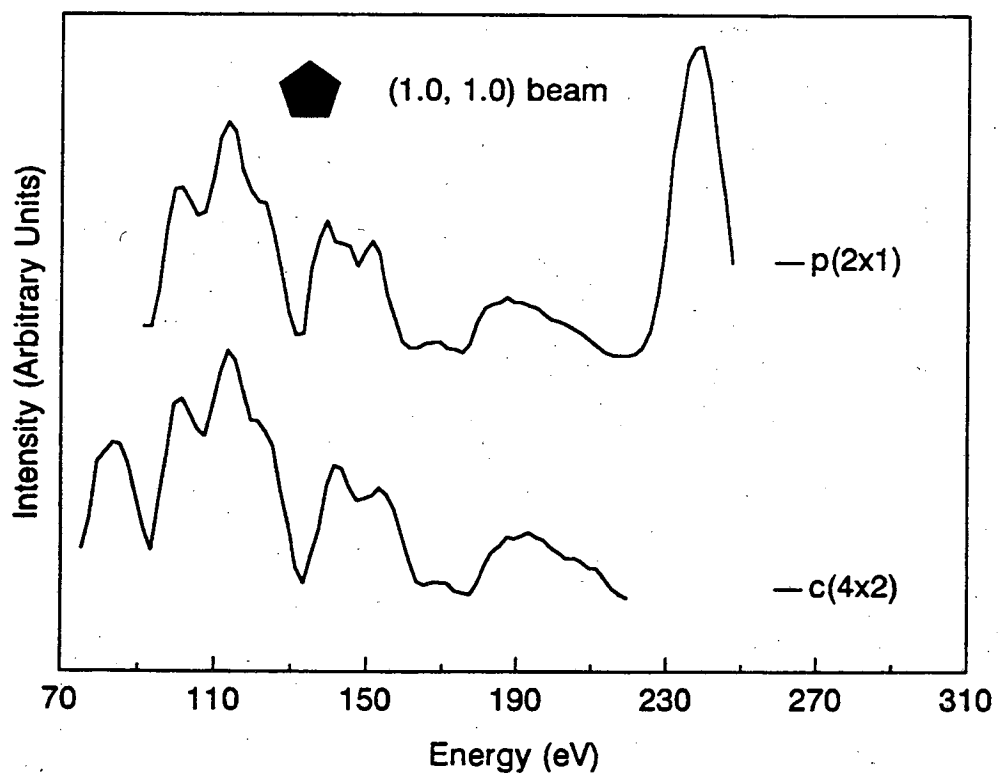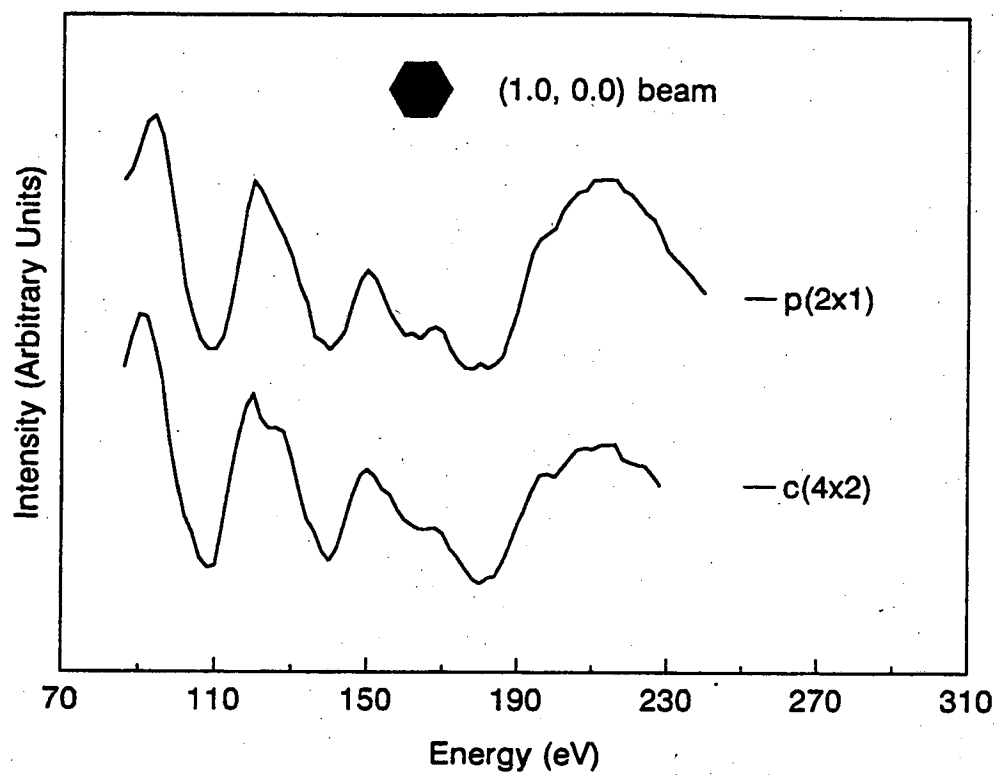
Figure 6.20   Comparison of I-V Curves of Mo(100)-p(2x1)-2S and -c(4x2)-S

(0.5, 2.0) beam

— p(2x1)

— c(4x2)

(2.0, 0.0) beam
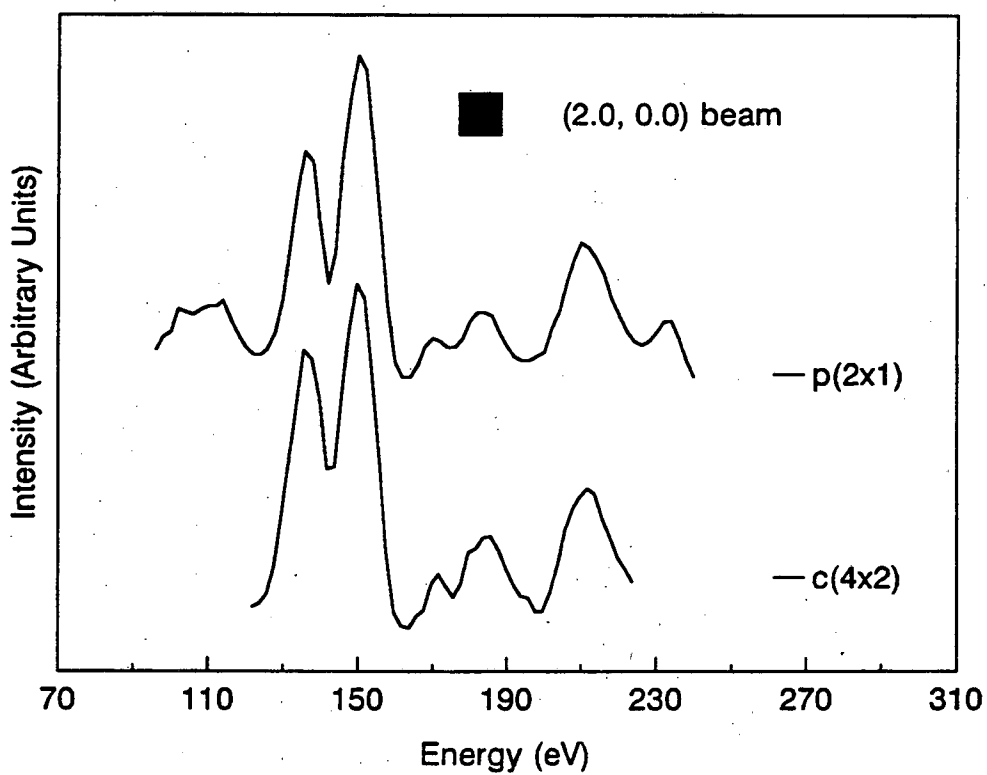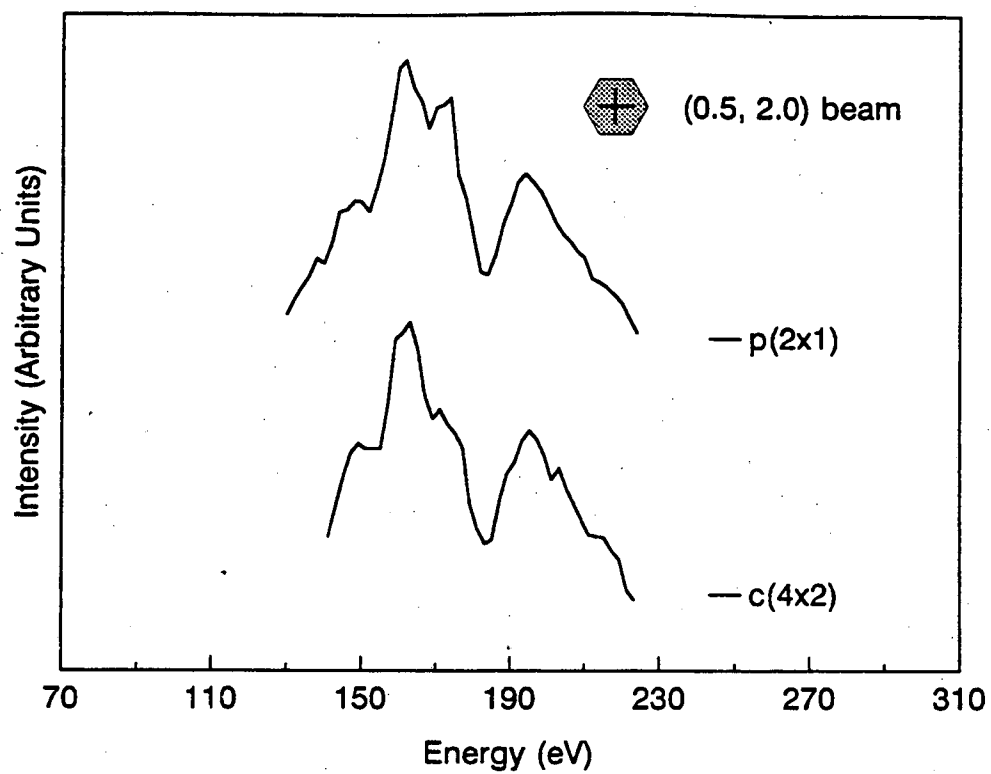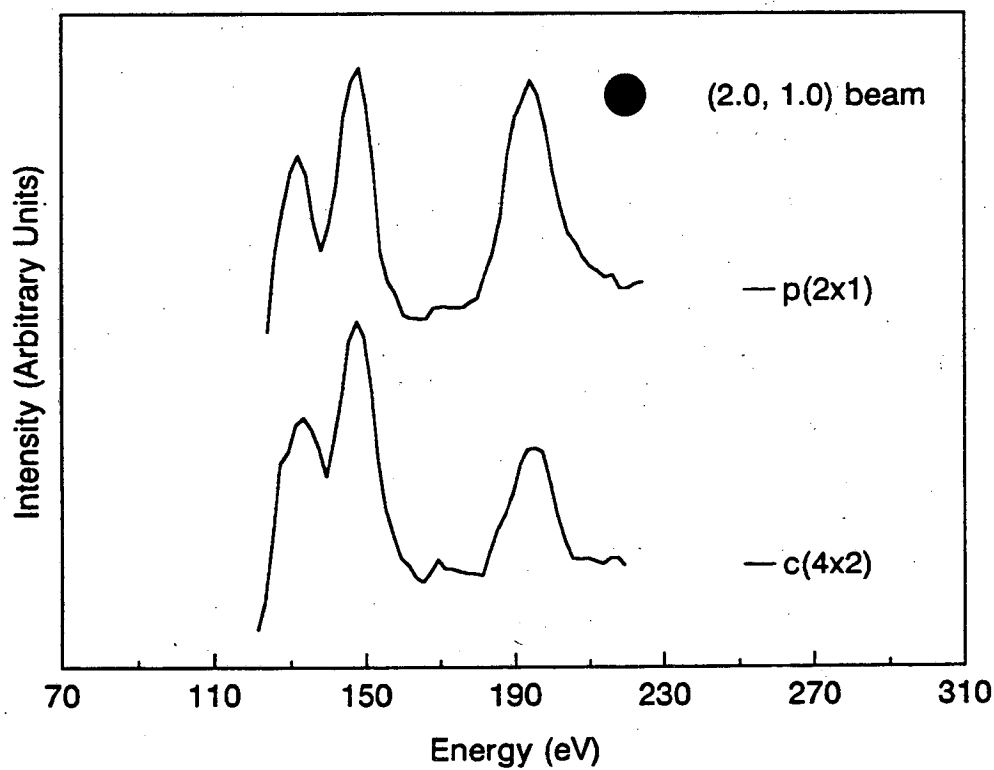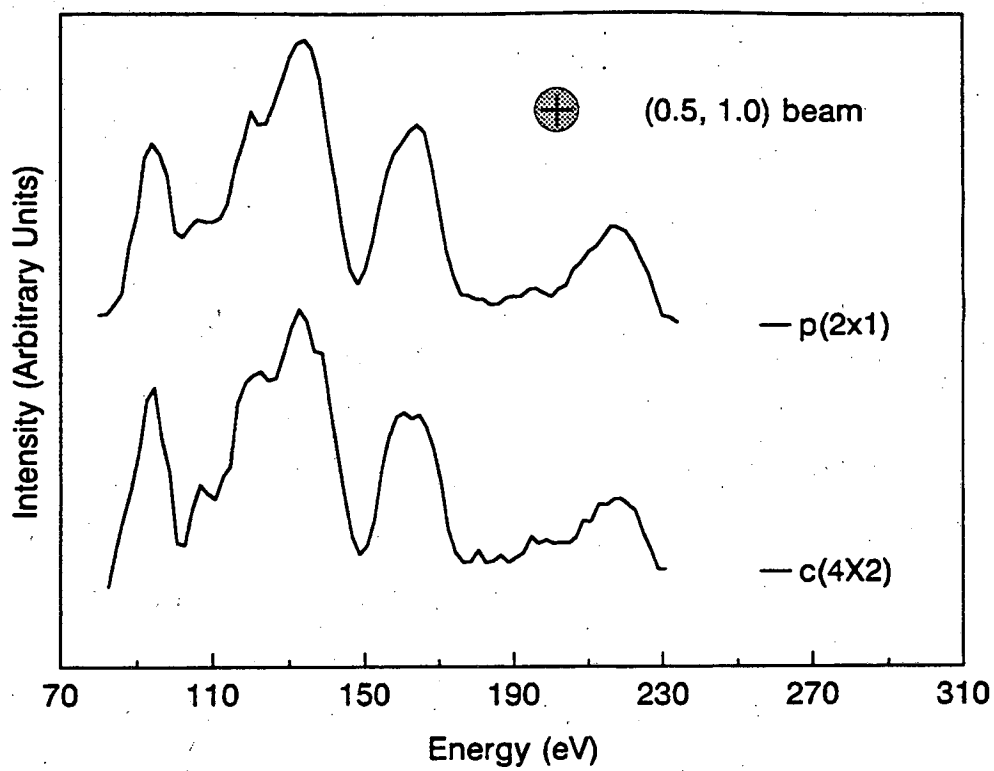
— p(2x1)

— c(4x2)

Figure 6.20 Continued   Comparison of I-V Curves of Mo(100)-p(2x1)-2S and -c(4x2)-3S

Figure 6.20 Continued   Comparison of I-V Curves of Mo(100)-p(2x1)-2S and -c(4x2)-3S

160

(1.5, 0.0) beam

— p(2x1)

— c(4x2)

(1.5, 1.0) beam

— p(2x1)

— c(4x2)

Figure 6.20 Continued   Comparison of I-V Curves of Mo(100)-p(2x1)-2S and -c(4x2)-3S

161
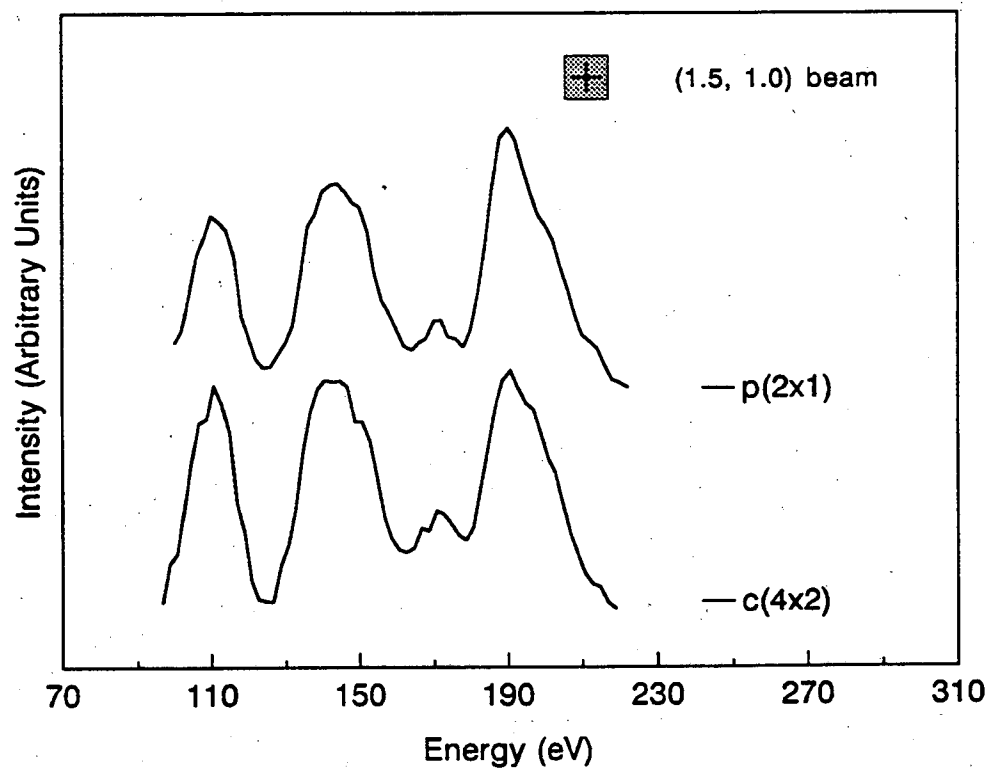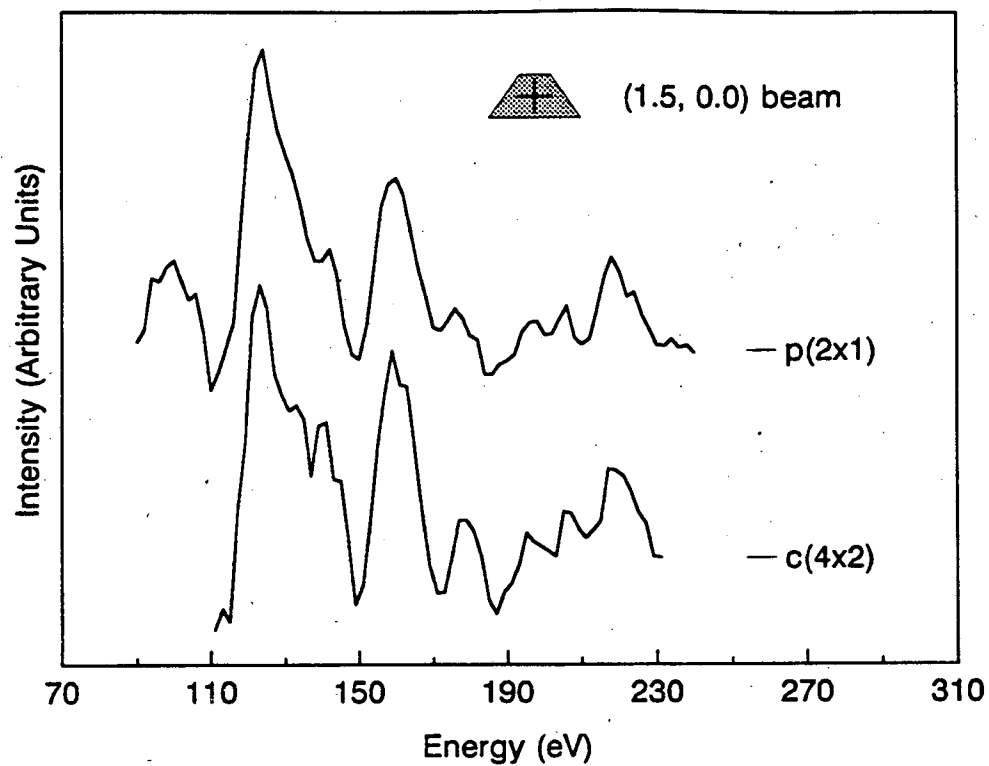
literature regarding this structure create even more doubt. Especially since all the S/Mo(100) structures that were not unanimously reported have a counterpart in the O/Mo(100) system. For instance, a Mo(100)-p(2x1)-O structure exists. In Figure 6.21 a LEED pattern and schematic of this structure is shown. Compare this with the Mo(100)-p(2x1)-2S LEED pattern in Figure 6.12.

A UHV STM study of the S/Mo(100) system was conducted by the Salmeron group recently [6.5]. They attempted to reproduce the previous results of their study of the Mo(100)-p(2x1)-S structure which had used a STM at atmospheric pressure [6.8]. They invariably encountered the same difficulties encountered in our LEED study. They could not produce a true Mo(100)-p(2x1)-2S. The best they could do was obtain a surface which produced a streaked c(4x2) LEED pattern (see Figure 6.11a). The STM image of this surface is shown in Figure 6.22. The STM image for a surface which produced a sharp c(4x2) LEED pattern (see Figure 6.11b) is shown in Figure 6.23. Note that the two images have the same unit cell which has the same dimensions as the primitive unit cell of the Mo(100)-c(4x2)-3S. These results, at the very least, indicate that the LEED I-V data for the streaked p(2x1) LEED pattern is actually for the Mo(100)-c(4x2)-3S structure. Therefore, it is not very surprising that the I-V curves from the two different LEED patterns are virtually identical. The main difference between the two STM images is that the domains are smaller, in the direction parallel to the longer unit cell vector of the p(4x2) unit cell, for the structure which produces the streaked c(4x2) LEED pattern.

In conclusion, we were unable to reproduce the results of previous researchers. From our results and the results of the STM study, the Mo(100)-p(2x1)-2S reported in the literature does not seem to actaully exist. We can fairly confidently say that the streaked p(2x1) LEED pattern is actaully due to a poorly ordered Mo(100)-c(4x2)-3S strucuture and that this is consistent with the LEED patterns and LEED I-V data. The STM images were essential in establishing this.

a)

b)
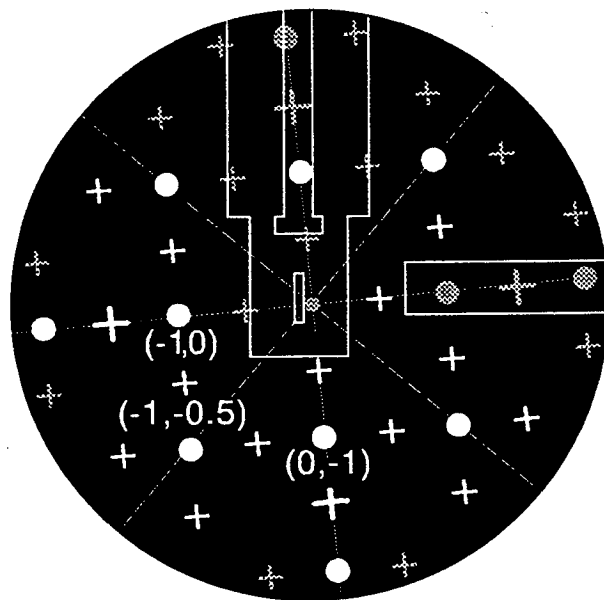
Figure 6.21 a) diffraction pattern of Mo(100)-p(2x1)-O at 114eV as displayed on the video monitor and **b)** schematic of p(2x1) diffraction pattern where the crosses represent the fractional order beams and the filled circles represent the integral order beams. The (hk) labels of the beams are directly beneath the beams. The dotted and dashed lines represent the four mirror planes. The shaded crosses and circles are the beams that are not seen in the photograph. The larger circles and crosses correspond to the more intense beams. The outline of the manipulator is in the center of the schematic and the outline of the sulfur source is on the right hand side of the schematic.
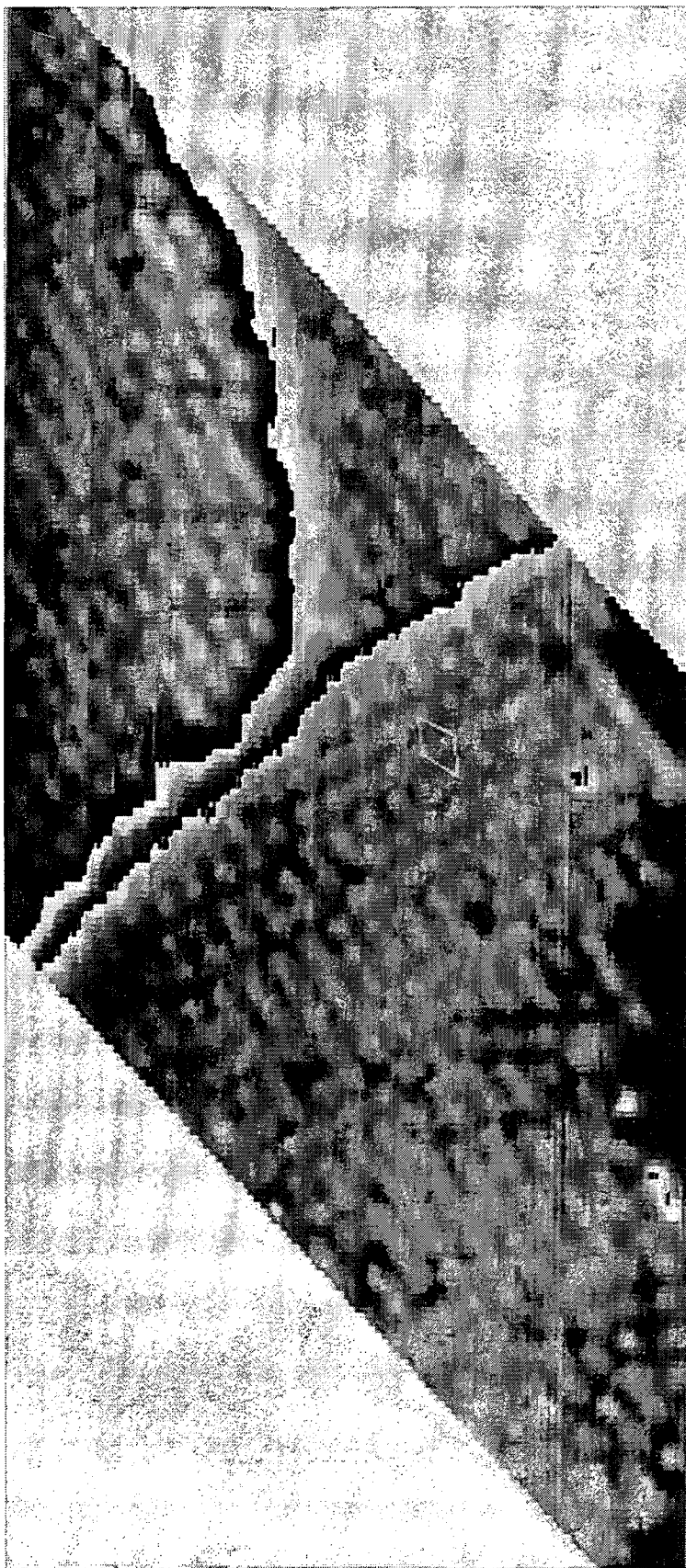
Figure 6.22 STM image of a Mo(100)-c(4x2)-3S structure which produces a streaked LEED pattern. The primitive unit cell is marked on the image in white.
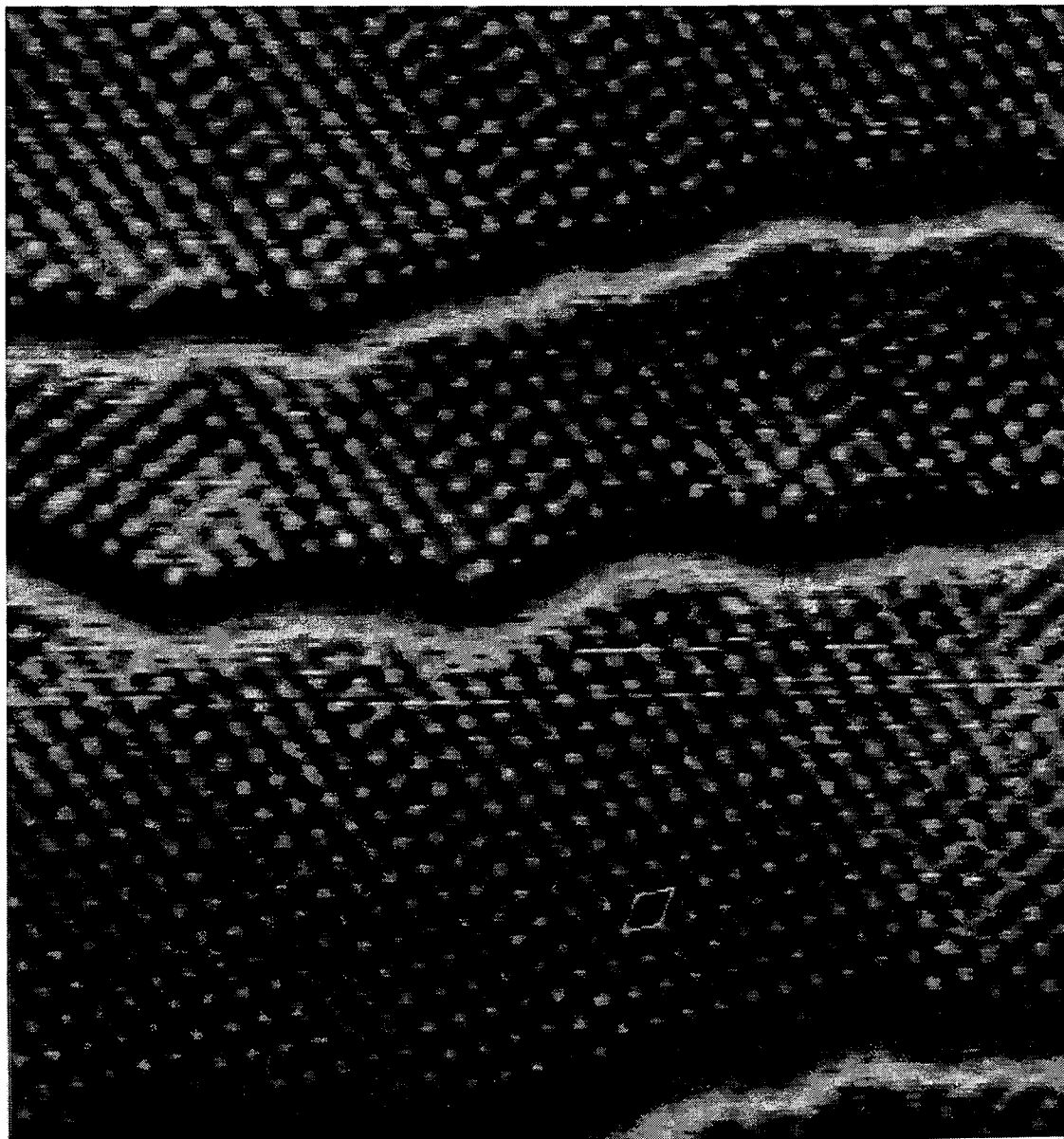
Figure 6.23 STM image of a Mo(100)-c(4x2)-3S strucutre which produces a sharp LEED pattern. The primitive unit cell is marked on the image in white.

165

6.5. MoS$_2$-like Overlayer on Mo(100)

A MoS$_2$-like overlayer forms on Mo(100) at very high sulfur coverages, multilayers. We refer to it as MoS$_2$-like overlayer because the diffraction spots have the correct symmetry and the unit cell dimensions are very similar to those of MoS$_2$. This structure was produced by depositing multilayers of S$_2$ and subsequently annealing the crystal at 800°C. Further annealing at higher temperatures produced a c(4x2) structure. The diffraction pattern that the overlayer produced is shown in Figure 6.24. The diffraction spots due to the MoS$_2$-like overlayer are not sharp and only occur at certain energies which prevented an I-V analysis of the diffraction intensities.

MoS$_2$ is a layered compound which, as in the case of graphite, is a good lubricant. Each sheet is composed of a layer of Mo atoms sandwiched between two layers of sulfur atoms. These sheets are stacked upon one another and the weak interaction between the sulfur atoms in neighboring sheets is responsible for the good lubricating properties of MoS$_2$.

The bulk lattice constant of MoS$_2$ is 3.16Å and the bulk lattice constant of Mo is 3.15Å. Assuming the Mo(100) surface-unit cell to have the bulk lattice constant, we used that value to determine the approximate lattice constant of the MoS$_2$-like overlayer. The value obtained from the distances measured in the photograph is a=3.11Å. Notice in Figure 6.24 that two rotational domains, rotated 30° with respect to each other, are present. The fact that the overlayer spots are streaked indicates that each domain is not locked into a specific orientation. If complete rotational disorder existed only pure rings would be present in the diffraction pattern for the overlayer.

For rotational disorder to exist a weak interaction between the substrate and the overlayer must exist. Sulfur bonds strongly to Mo(100) at submonolayer coverages as indicated by the high temperature of desorption [6.9]. This suggests that, similar to the case of bulk MoS$_2$, two weakly interacting sulfur layers are in contact with each other.

Two possible types of models are apparent. The first has an overlayer of sulfur on the Mo(100) with a second layer of sulfur in a hexagonal array on top of the first sulfur overlayer. The second model involves a sheet of MoS_2 on top of a sulfur covered Mo(100). These models are not rigorous since the exact registries have not been worked out.

The interesting note here is that, as mentioned previously, for the O/Mo(100) system a hexagonal underlayer was proposed for some of the high coverage structures. There may be a possible connection between the two systems. What is not obvious is whether the MoS_2-like structure is structurally related to the Mo(100)-c(4x2)-3S structure.

a)

b)

(-1,0)

(-1,-0.5)

(0,-1)
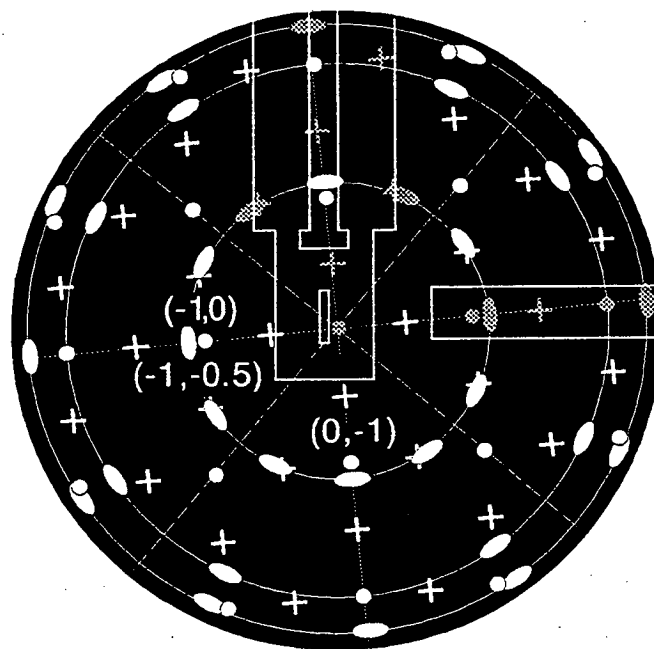
Figure 6.24 Photograph of **a)** a diffraction pattern of a superposition of Mo(100)-p(2x1)-2S and a MoS$_2$-like overlayer at 143eV taken with a Polaroid camera and **b)** schematic of a superposition of a p(2x1) diffraction pattern, where the crosses represent the fractional order beams and the filled circles represent the integral order beams, and a rotationally disordered MoS$_2$-like overlayer, where the filled ovals represent the streaked spots. The (hk) labels of the beams are directly above the beams. The shaded crosses, circles, and ovals are the beams that are not seen in the photograph. The dotted and dashed lines represent the four mirror planes. The outline of the manipulator is in the center of the schematic and the outline of the sulfur source is on the right hand side of the schematic. Compare this with Figure 6.12.

168

References

6.1   D.G. Kelly, R.F. Lin, M.A. Van Hove, and G.A. Somorjai, Surface Sci. **224** (1989) 97.

6.2   L.J. Clarke, Surface Sci. **102** (1981) 331.

6.3   P.J. Rous, D. Jentz, D.G. Kelly, R.Q. Hwang, M.A. Van Hove, and G.A. Somorjai, in **The Structure of Surfaces-III**, Eds. S.Y. Tong, M.A. Van Hove, K. Takayanagi, and X.D. Xie, (Springer-Verlag, Berlin, Heidelberg, New York, 1991) p. 432.

6.4   M.L. Hildner, R.S. Daley, T.E. Felter and P.J. Estrup, J. of Vacuum Sci. and Tech. A **9** (1991) 1604.

6.5   J. Dunphy and P. Sautet, private communication

6.6   W. Oed, H. Lindner, U. Starke, K. Heinz, K. Müller, and J.B. Pendry, Surf. Sci. **224** (1989) 179.

6.7   A.J. Gellman, Ph.D. Thesis, Berkeley, 1985.

6.8   B. Marchon, P. Bernhardt, M.E. Bussel, G.A. Somorjai, M. Salmeron, and W. Siekhaus, Phys. Rev. Lett. **60** (1988) 1166.

6.9   M.H. Farias, A.J. Gellman, G.A. Somorjai, R.R. Chianelli, and K.S. Liang, Surf. Sci., **140** (1984) 181.

Chapter 7.   Ordered Sulfur Overlayers on Re(0001)

7.1.   Introduction

Previous investigations have studied sulfur overlayers on the Re(0001) surface by LEED, TDS, and AES [7.1, 2, 3]. In addition, a thorough STM investigation under UHV conditions has been performed on the S/Re(0001) system by Salmeron et al [7.4, 5]. Four ordered sulfur structures on Re(0001) have been observed in all these studies. The sulfur coverages, annealing temperatures, and corresponding LEED patterns are summarized in Table 7.1 [7 1]. The $(2\sqrt{3}x2\sqrt{3})R30°$ structure occurs at ~0.5 ML which corresponds to saturation coverage. The quotation marks for the "$(3\sqrt{3}x3\sqrt{3})R30°$" structure signify that some of the diffraction spots implied by the notation, $(3\sqrt{3}x3\sqrt{3})R30°$, are missing. Both the p(2x2) and $(2\sqrt{3}x2\sqrt{3})R30°$ structures were studied in this work. The LEED patterns depend on annealing temperature because an excess of S_2 or H_2S is first adsorbed onto the Re surface at room temperature. Then the surface is annealed to dissociate the S_2 or H_2S and desorb excess sulfur. This procedure can be combined into one step by depositing S_2

Table 7.1 Sulfur coverages on Re(0001), corresponding LEED patterns, and annealing temperatures [7.1]

Sulfur Coverage Range(ML)	LEED Pattern	Annealing Temperature (K)
0.0-0.16	(1x1)	1650-1500
0.16-0.29	p(2x2)	1450-1400
0.29-0.32	(1x1)	1380-1350
0.32-0.39	" $(3\sqrt{3}x3\sqrt{3})R30°$ "	1340-1220
0.39-0.44	$\begin{bmatrix} 3 & 1 \\ 1 & 3 \end{bmatrix}$	1210-1100
0.44-0.59	$(2\sqrt{3}x2\sqrt{3})R30°$	1090-600

or H_2S as the Re surface is being heated. Both procedures work equally well.

The STM investigations of these ordered structures obtained images with atomic resolution [7.4, 5]. At low coverages, $\theta < 0.25$, a c($\sqrt{3}$x5)rect structure, which was not observed by LEED, was imaged. The investigators interpreted the STM images of the different S/Re(0001) structures to correspond to sulfur adsorbed in three-fold hollow sites. In addition, it was observed that the sulfur atoms formed aggregates at higher coverages, for example trimers, tetramers, and hexamers. No sulfur clusters were observed for the p(2x2) structure. However, trimers were observed for the "(3$\sqrt{3}$x3$\sqrt{3}$)R30°" and tetramers for the $\begin{bmatrix} 3 & 1 \\ 1 & 3 \end{bmatrix}$. At saturation coverage hexamers, hexagonal rings of six sulfur atoms, were observed for the (2$\sqrt{3}$x2$\sqrt{3}$)R30° structure. These results were somewhat unexpected because typically adsorbate-adsorbate interactions for electronegative elements such as oxygen and sulfur are thought to be repulsive in nature. So one would expect the sulfur to be separated as much as possible, within the constraints of the coverage. The aggregation may not be that unexpected for sulfur since sulfur is known to form open and cyclic S_n species from $n = 2$ to 20 for cycles and higher for chains [7.6]. However, the STM investigation found the S-S distance to be dictated by the substrate and not the sum of the covalent radii. So an interesting interplay between adsorbate-adsorbate interactions and adsorbate-substrate interactions seems to be at work in the S/Re(0001) system.

7.2. Symmetry of the LEED Pattern of hcp(0001) Surfaces

The LEED pattern of a hcp(0001) surface at normal incidence exhibits six-fold symmetry in the diffraction intensities. If the surface were truly atomically flat the LEED intensities would have three-fold symmetry at normal incidence. The reason for the observed six-fold symmetry can be understood if we consider a hcp(0001) surface with monatomic steps. This is illustrated in Figure 7.1. The triangle in the figure represents the orientation of the three-fold hollow sites. On one terrace, the collection of sites are rotated 180° from those on the adjacent terrace. This is because one terrace has ABA stacking and the adjacent terrace has BAB stacking. The notation ABA refers to layers A and B in which the atoms are closest packed in each layer. The difference between layer A and layer B is orientation, i.e the atoms in layer A are directly above the three-fold hollow sites of layer B. If the terraces are larger than the coherence width of the electron beam then sharp diffraction spots will be observed. The diffraction patterns from the two terraces produce LEED patterns which are rotated 180°, or equivalently 60°, relative to each other. The intensities are averaged in the observed LEED pattern, and this leads to a six-
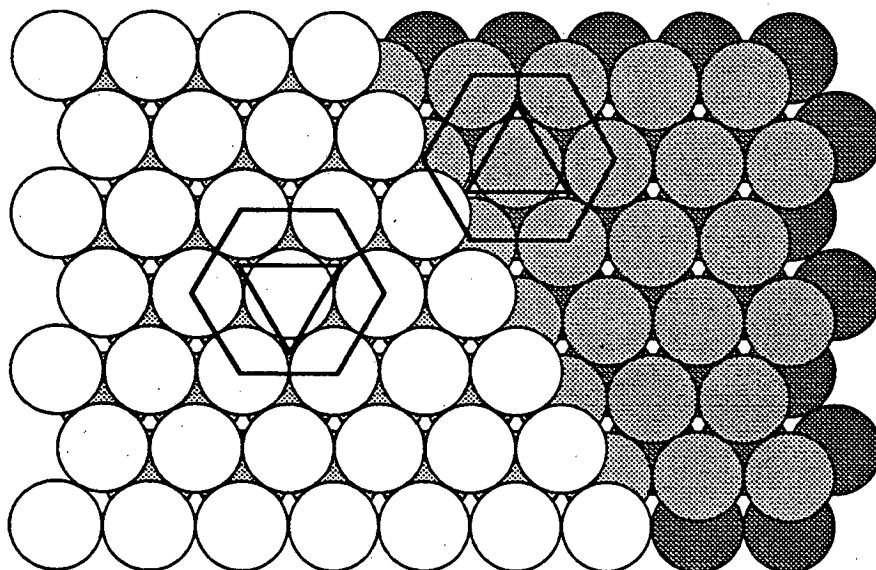
Figure 7.1   A hcp(0001) surface with monatomic steps. The adjacent terraces are rotated 180° relative to each other. The triangles illustrate the rotation.
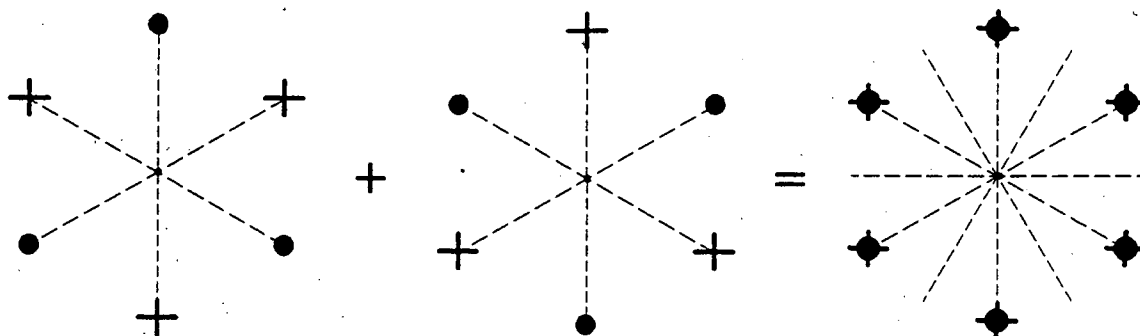
Figure 7.2   Schematic of a LEED pattern of a hcp(0001) surface with monatomic steps. It illustrates that the observed LEED pattern is a superposition of the LEED patterns from two types of terraces. The dotted lines represent the mirror planes.

fold symmetry in the intensities if both terraces have equal areas. This is illustrated in Figure 7.2.

7.3. Re(0001)-p(2x2)-S

The p(2x2) structure forms at an ideal coverage of 0.25 ML (monolayer, where one monolayer is defined as one sulfur atom for one rhenium atom). The LEED pattern and schematic are shown in Figure 7.3. A schematic which illustrates the symmetry of the LEED pattern at normal incidence is shown in Figure 7.4. The experimental I-V curves are shown in Figure 7.5.

Two models were considered: one with the sulfur adsorbed in fcc three-fold hollow sites and the other with the sulfur adsorbed in hcp three-fold hollow sites. A fcc hollow site is a site where a second layer Re atom is not directly beneath it, whereas a hcp hollow site does have a second layer Re atom directly beneath it. The difference in the two sites is illustrated in Figure 7.6.

Using the model with occupied fcc hollow sites as the reference structure, the lowest Pendry R-factor obtained after the tensor LEED analysis was 0.5. The R-factor for the other model after the search was 0.21.

a)

b)

(-1,0)

(-0.5,-0.5)

(0,-1)
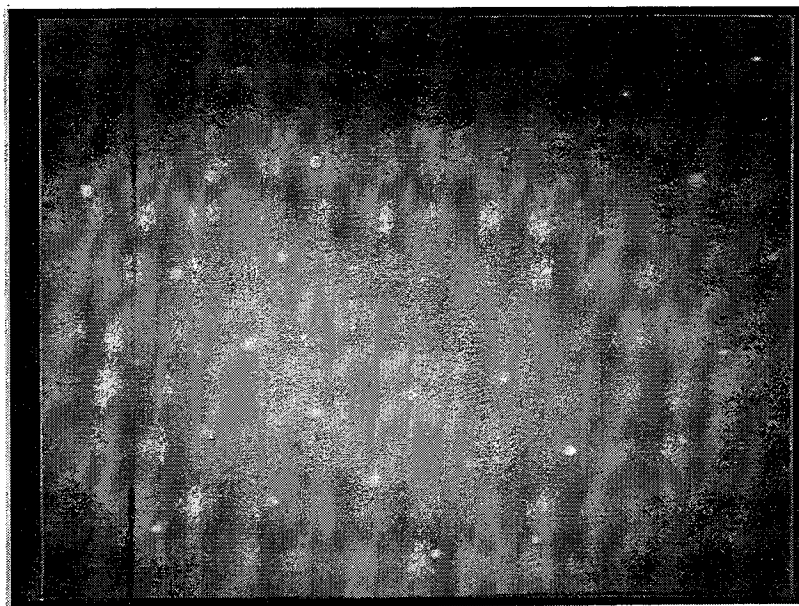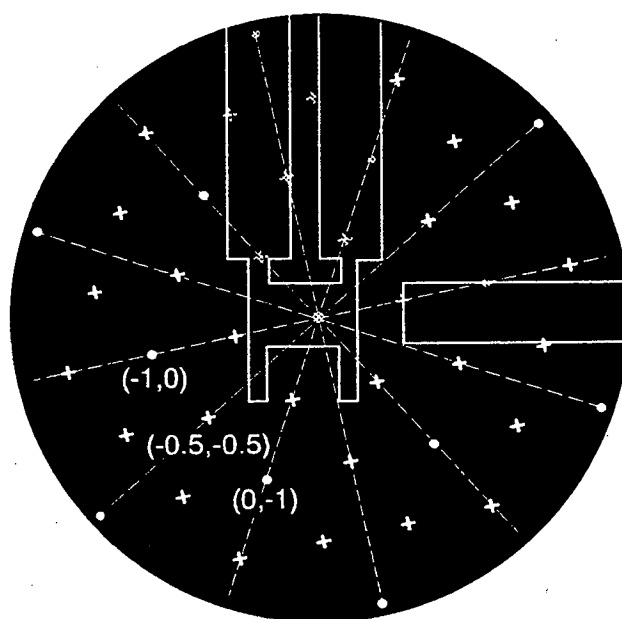
Figure 7.3 a) diffraction pattern of Re(0001)-p(2x2)-S at 134 eV as displayed on the video monitor and **b)** schematic of p(2x2) diffraction pattern where the crosses represent the fractional order beams and the filled circles represent the integral order beams. The (hk) labels of the beams are directly beneath the beams. The dotted and dashed lines represent the six mirror planes. The shaded crosses and circles are the beams that are not seen in the photograph. The outline of the manipulator is in the center of the schematic and the outline of the sulfur source is on the right hand side of the schematic.
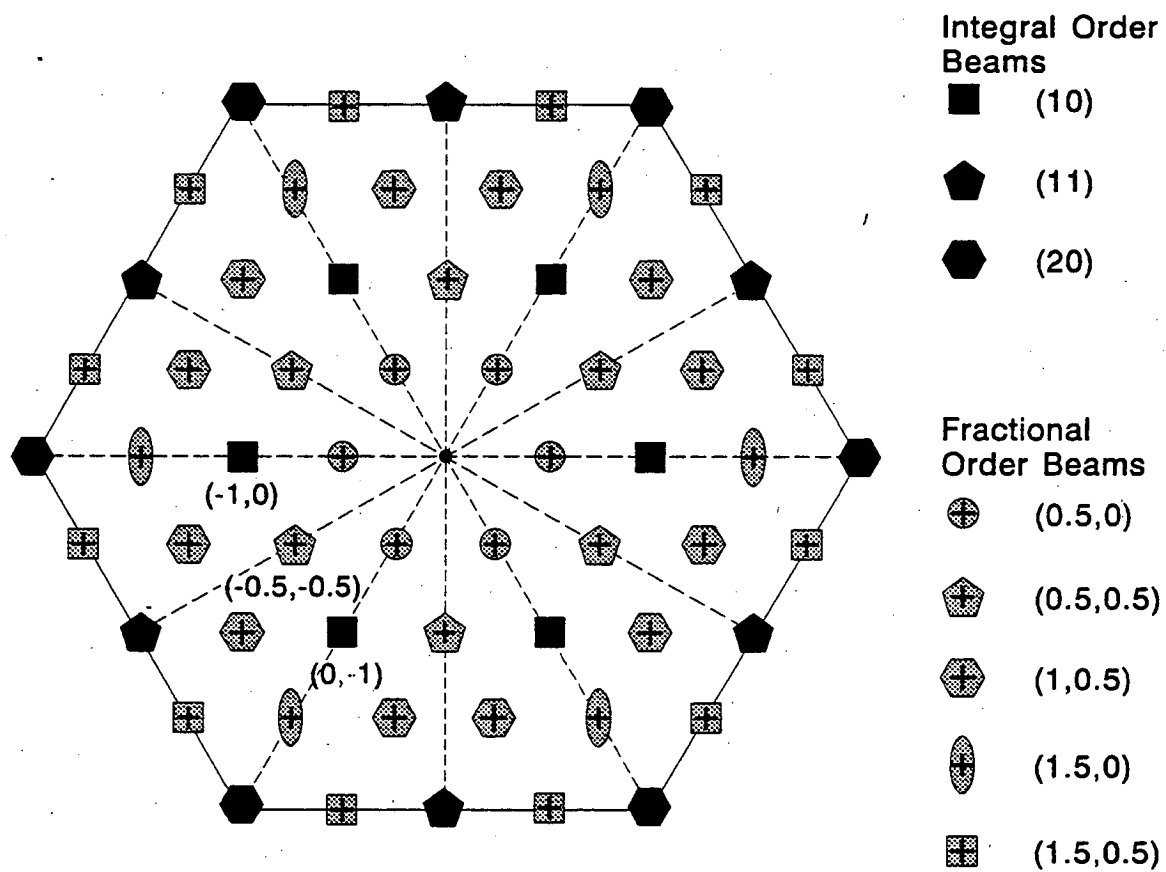
Figure 7.4   Schematic of the LEED pattern for Re(0001)-p(2x2)-S
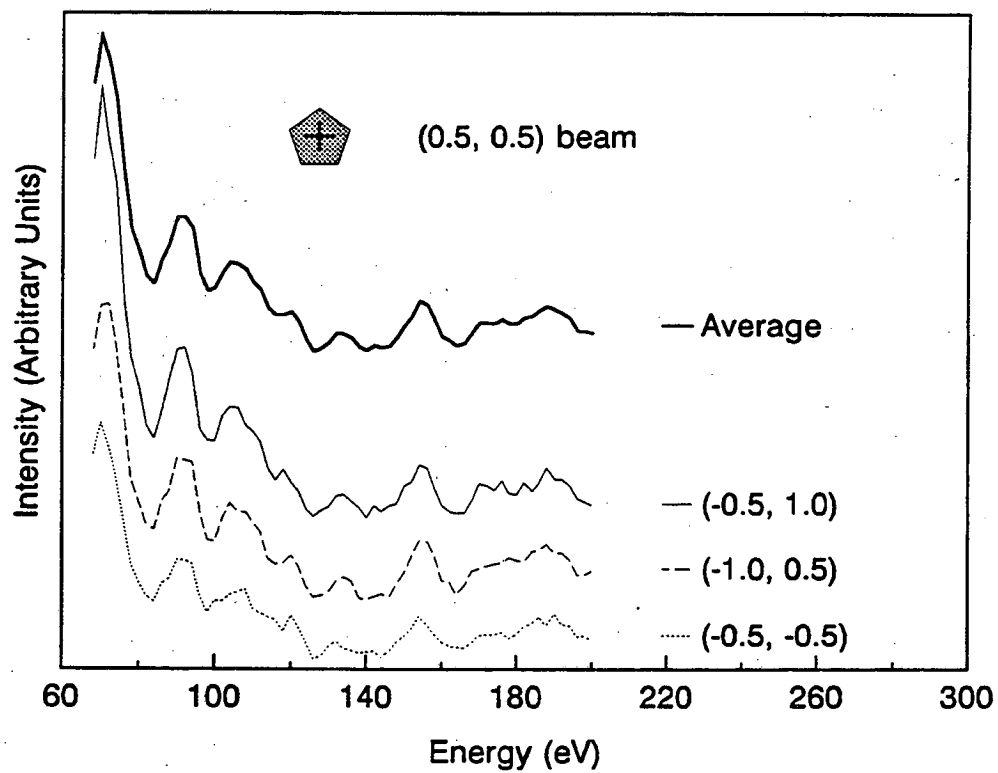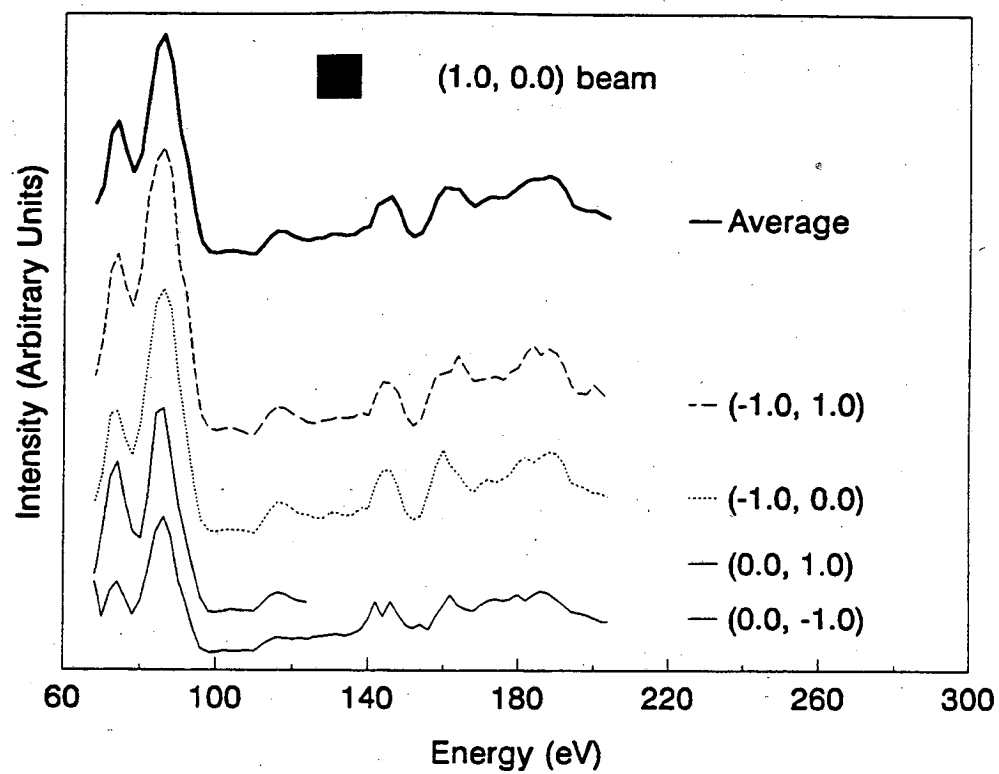
Figure 7.5 Experimental I-V Curves of Re(0001)-p(2x2)-S
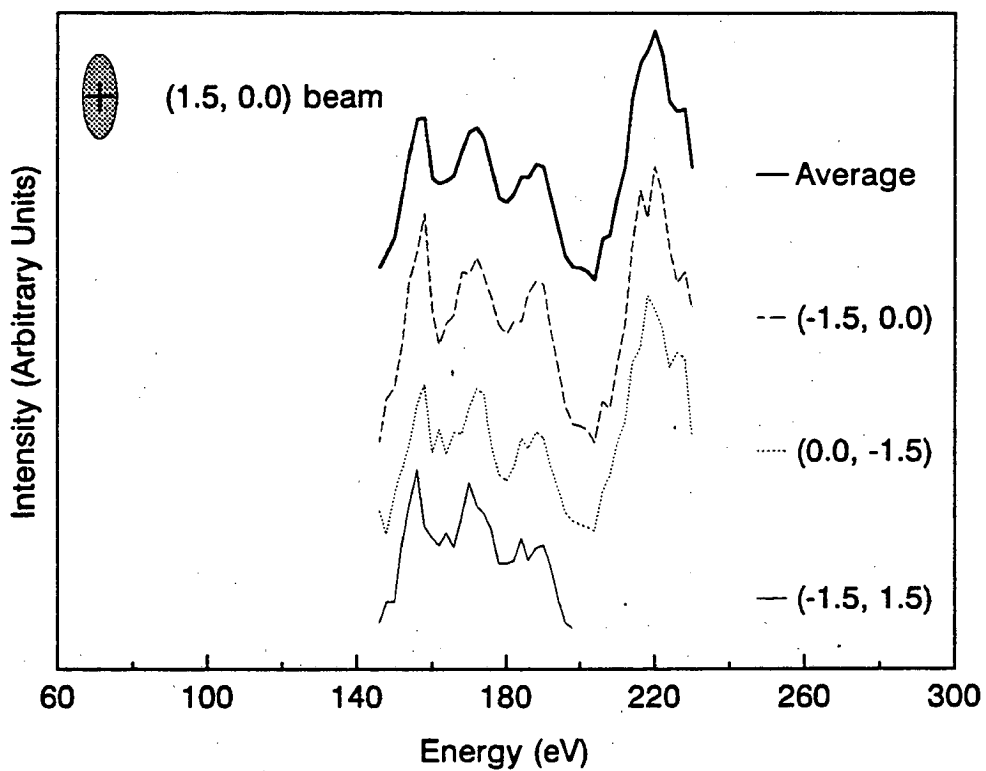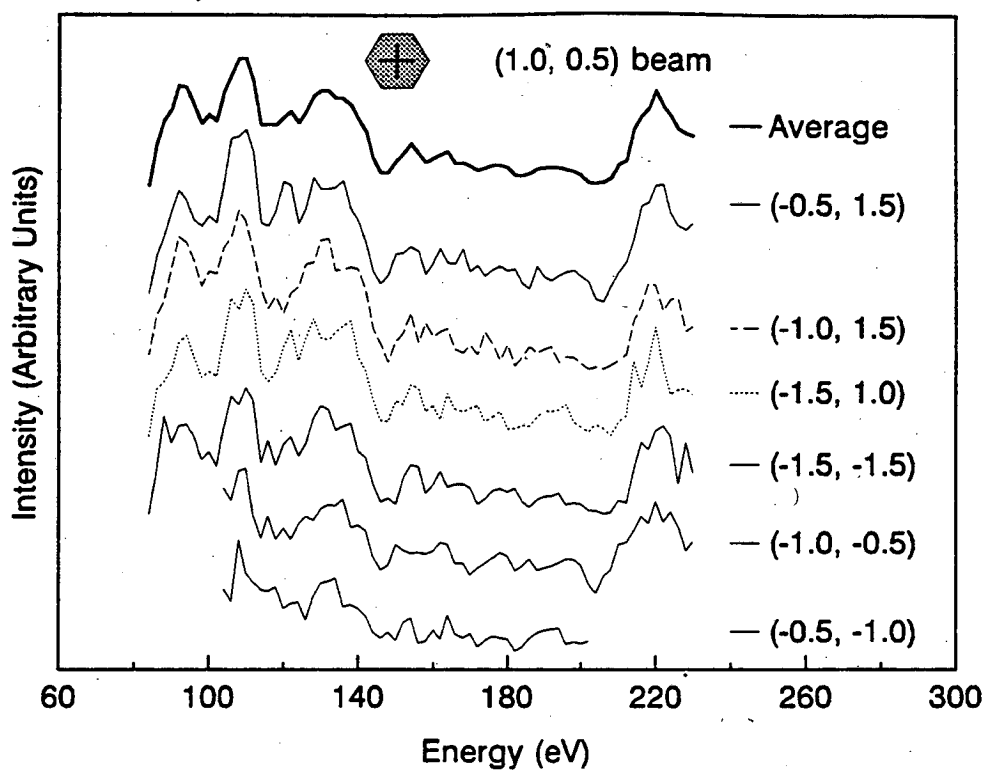
Figure 7.5 Continued Experimental I-V Curves of Re(0001)-p(2x2)-S

177

Figure 7.5 Continued   Experimental I-V Curves of Re(0001)-p(2x2)-S

178
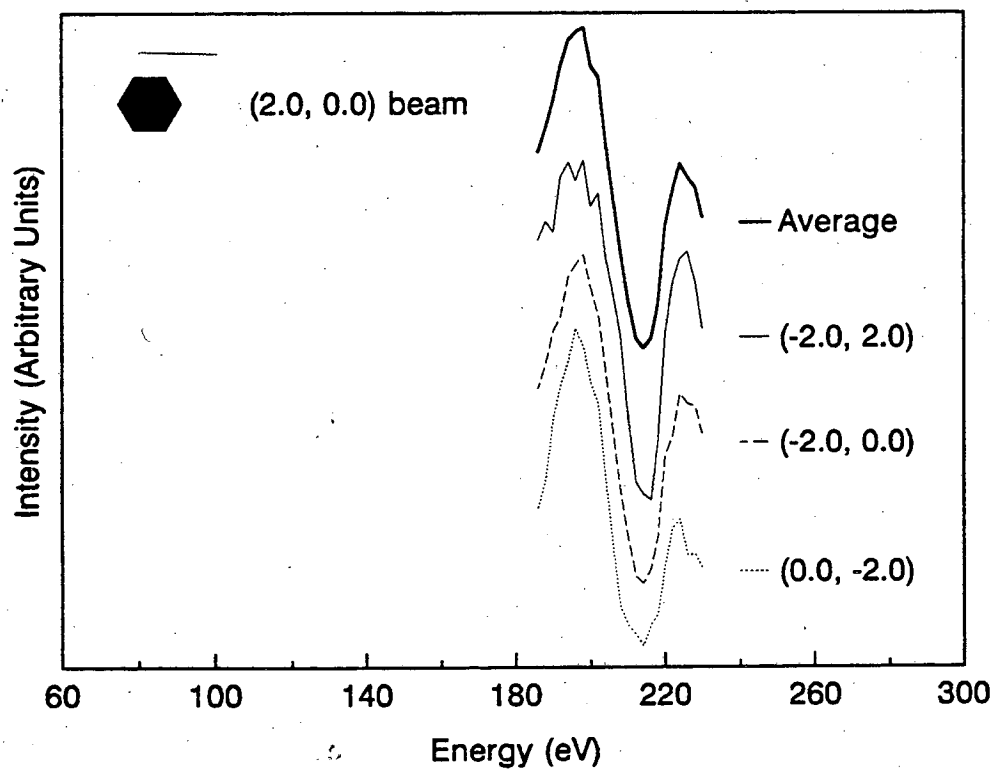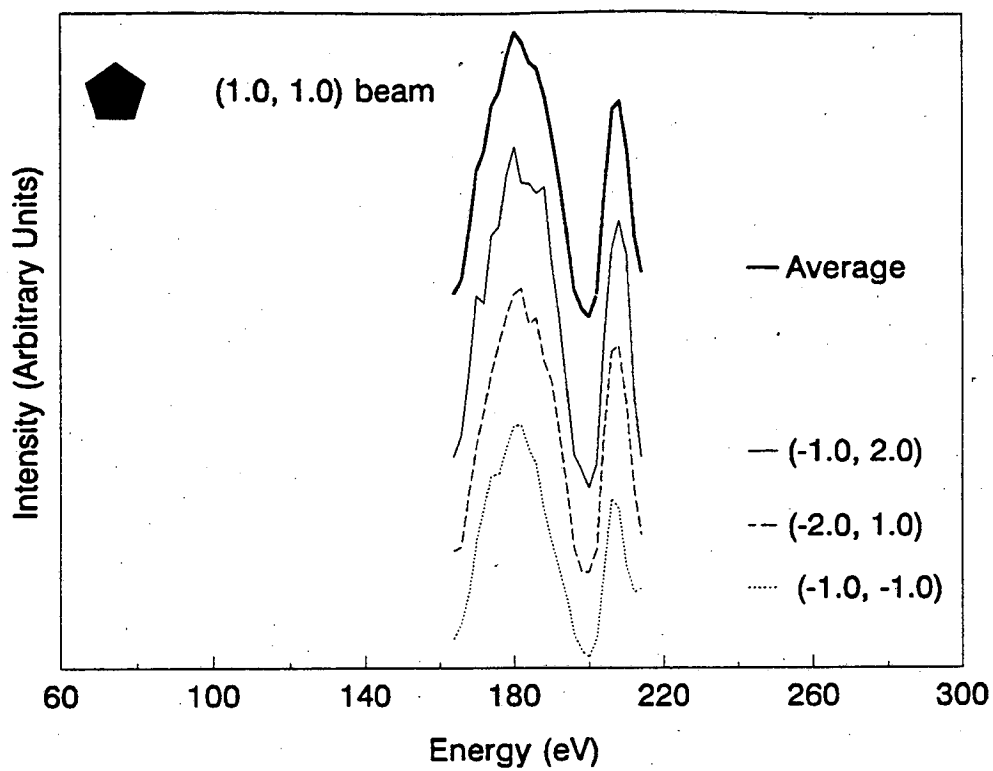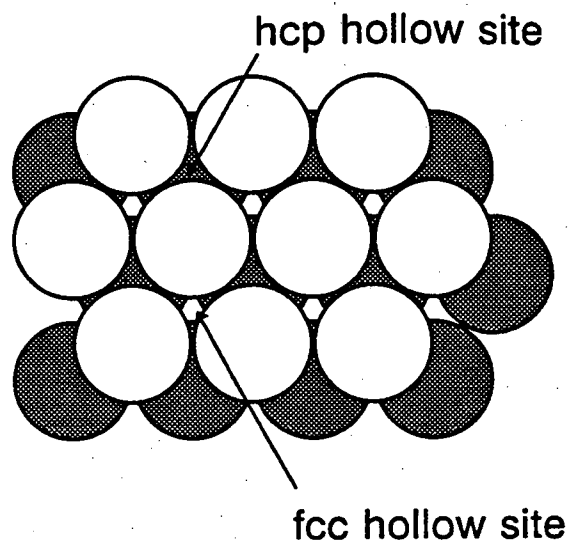
Figure 7.6   Two types of three-fold hollow sites exist on fcc(111) and hcp(0001) surfaces.

The composite-layer unit cell was composed of one sulfur atom, four Re atoms in the first layer, and four Re atoms in the second layer making a total of nine atoms in the composite layer. A real space model of the Re(0001)-p(2x2)-S is illustrated in Figure 7.7. Since the composite layer is composed of 9 atoms 27 degrees of freedom are possible for the geometric parameters. The tensor LEED search was constrained such that the atoms were allowed to move provided they respected a certain symmetry. The symmetry was a three-fold axis and one mirror plane. This constrained the Re atoms, which had equivalent bonding geometries, to move in a way that preserved their equivalence. This constraint reduced the number of geometrical degrees of freedom from the maximum of 27 to 7.

The best fit geometry is illustrated in Figure 7.8. The interlayer spacings are shown for the weighted average of the first and second layers since both are buckled. The S-Re bond length is 2.32Å which compares well with the sum of the covalent radii, 2.41Å. The results are summarized in Table 7.2.

Table 7.2   Summary of the results of the analysis of Re(0001)-p(2x2)-S

d_{SRe}	d_{12}	d_{23}	d_{34}	b_1	b_2
1.68	2.14	2.29	2.23	-0.05	0.06

The bulk interlayer spacing is 2.23Å so the first interlayer spacing is contracted by 4.0% and the second interlayer spacing is expanded by 2.7%. The third interlayer spacing was assumed to be bulk-like.

In the first Re layer the Re atom which is not bonded to the sulfur buckles downward relative to the three other Re atoms in the layer. This is indicated by the negative buckling. In the Re second layer the Re atom directly beneath the sulfur buckles upward relative to the other three Re atoms in the layer. This is indicated by the positive buckling.

The I-V curves for the best fit structure are compared with the experimental I-V curves in Figure 7.9. The Pendry R-factor for each beam is shown.

(a)   (b)
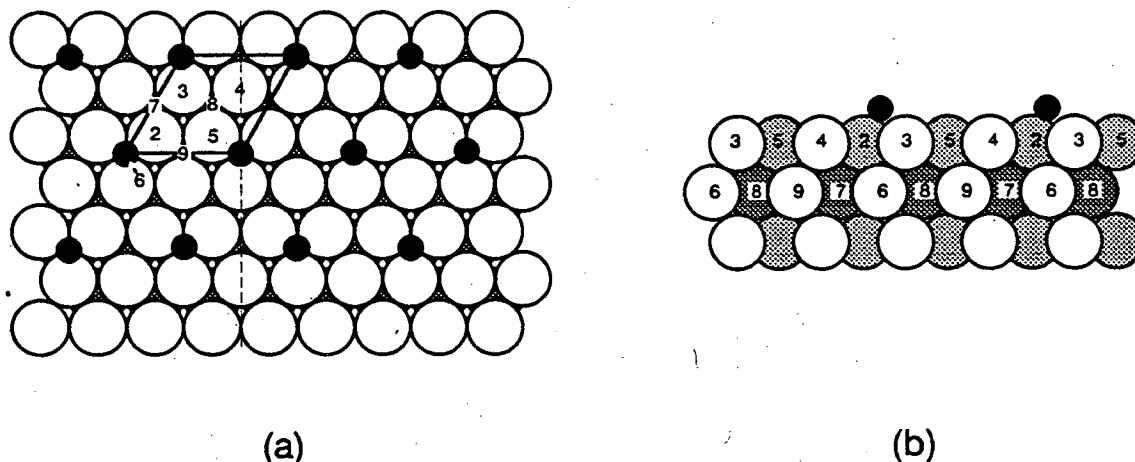
Figure 7.7   Real-space model of Re(0001)-p(2x2)-S. The sulfur atoms are sitting in hcp sites. Two views are presented (a) a top view and (b) a side view along the dotted line in (a). The shading of the Re atoms in (b) indicates the depth behind the plane of the paper. The darkest Re atoms are the farthest behind the plane of the paper.
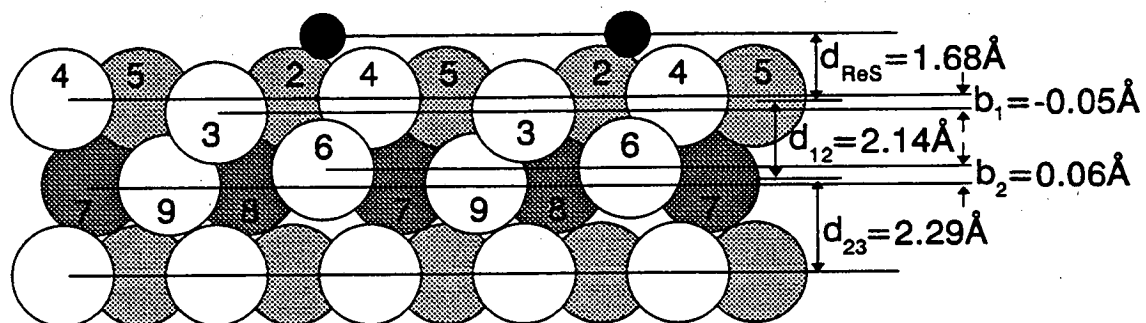
Figure 7.8   Side view of the best fit geometry for Re(0001)-p(2x2)-S
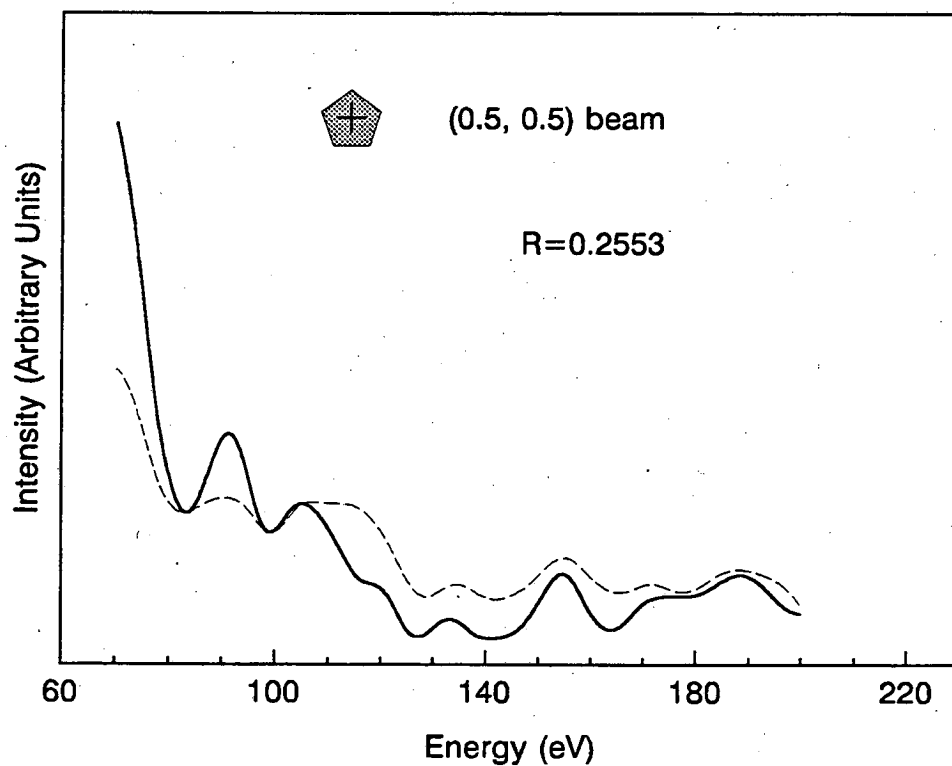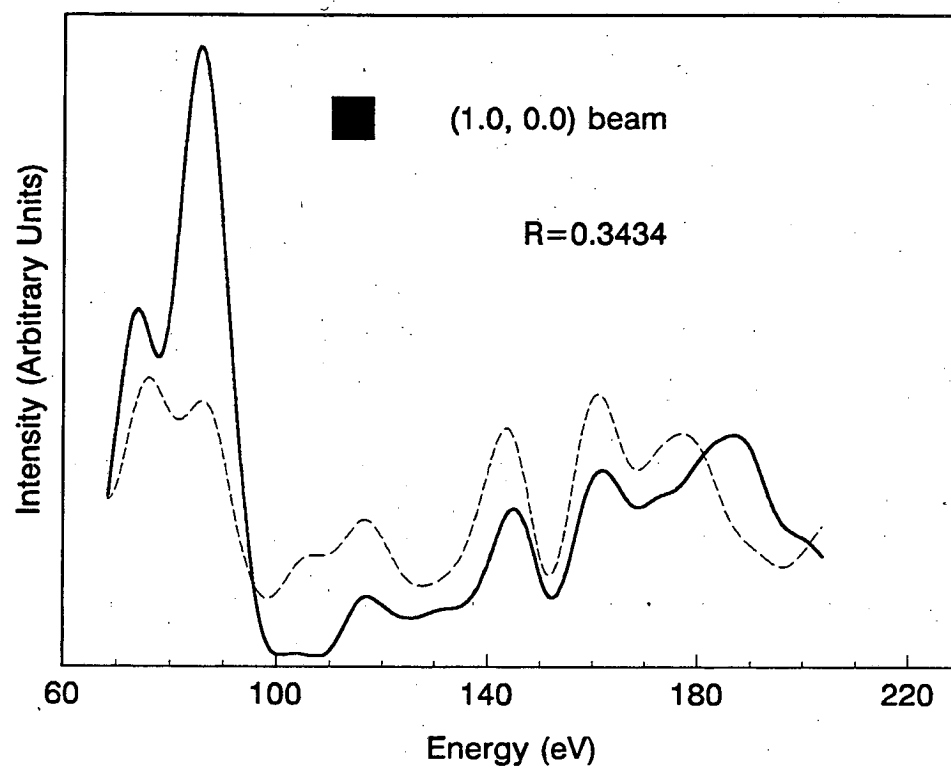
Figure 7.9   I-V Curves of Re(0001)-p(2x2)-S: Theory (dashed line) versus experimental (solid line)
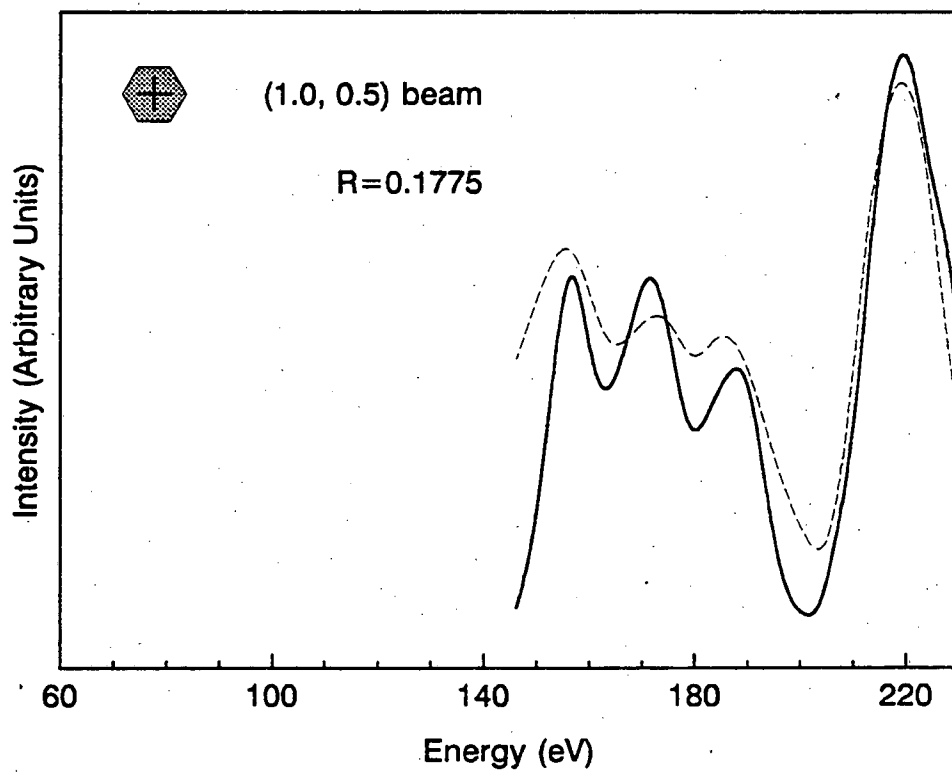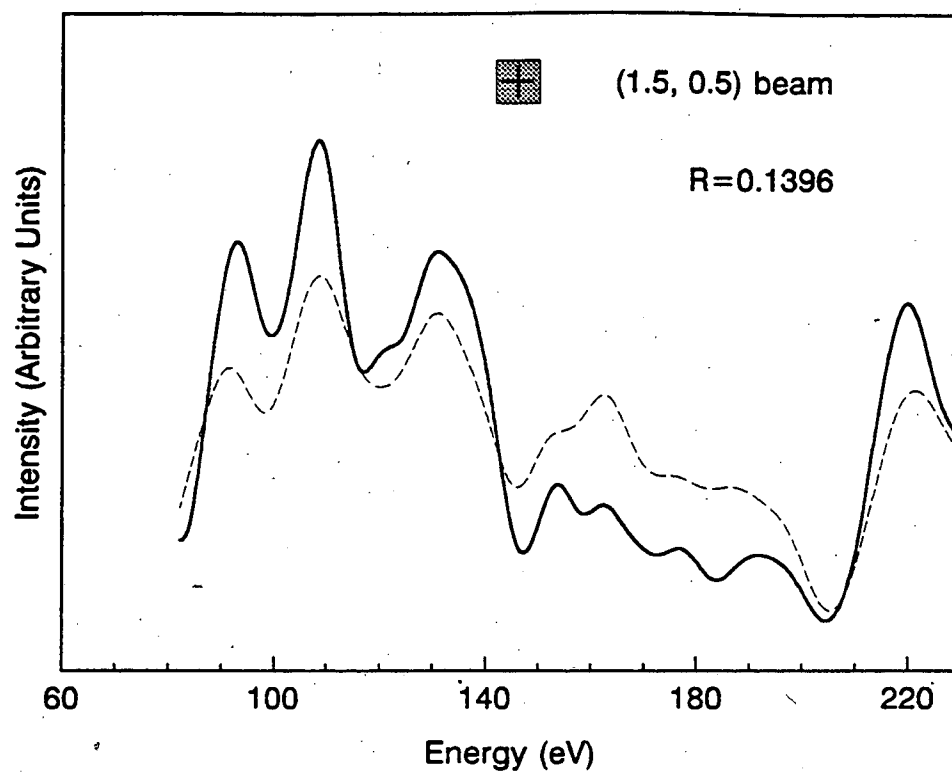
Figure 7.9 Continued   I-V Curves of Re(0001)-p(2x2)-S: Theory (dashed line) versus experimental (solid line)

183
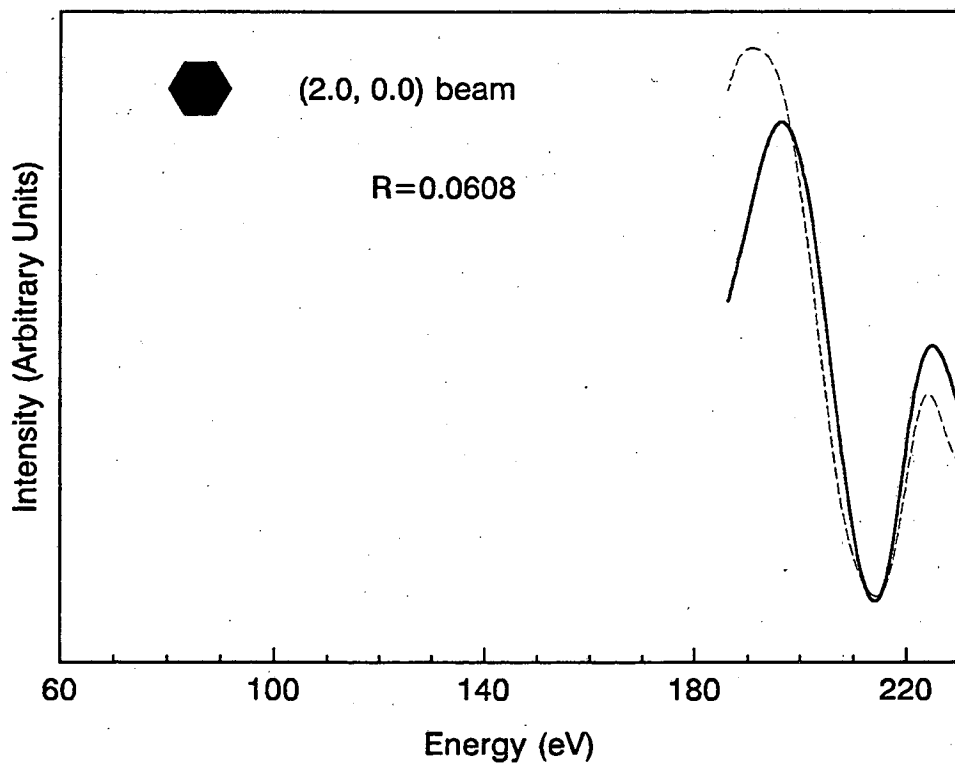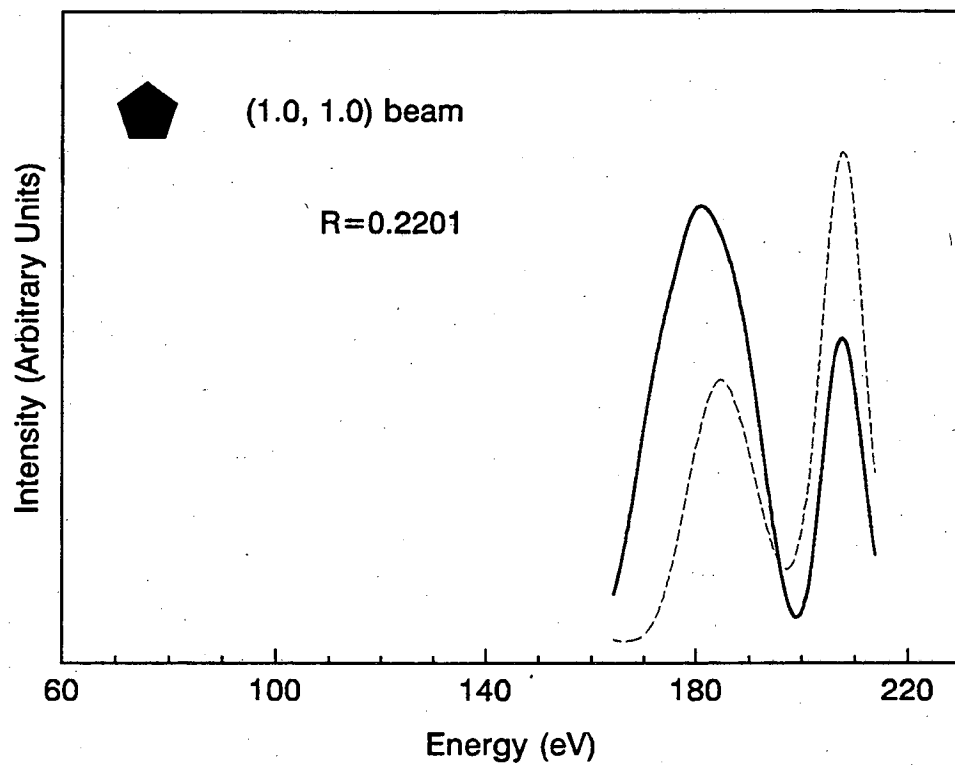
Figure 7.9 Continued   I-V Curves of Re(0001)-p(2x2)-S: Theory (dashed line) versus experimental (solid line)

7.4. Re(0001)-(2√3x2√3)R30°-6S

The sulfur structure which occurs at saturation coverage, $\theta=0.5$, was studied. The LEED pattern and schematic are shown in Figure 7.10. In Figure 7.11 a schematic of the LEED pattern at normal incidence illustrates the symmetry of the beams. The experimental I-V curves are presented in Figure 7.12.

The model which we considered was the hexamer model proposed by the STM study with the sulfur occupying hcp hollow sites like those found for the p(2x2) structure. The model is depicted in Figure 7.13. The preliminary tensor LEED analysis shows that the hexamer model gives a reasonable fit. Further refinements are required to determine the exact geometry.

a)
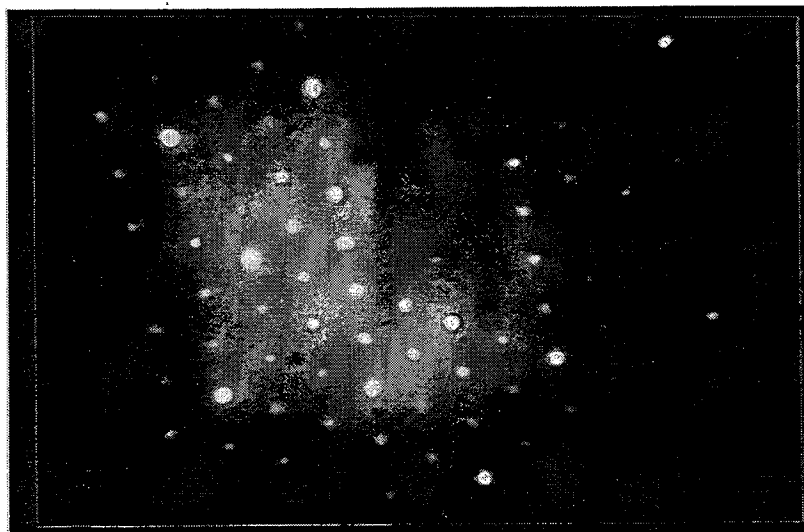
b)
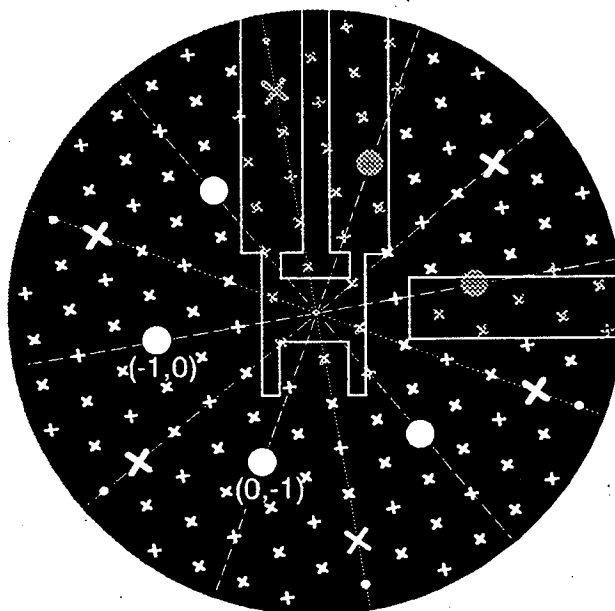
Figure 7.10 a) diffraction pattern of Re(0001)-(2√3x2√3)R30°-6S at 134eV as displayed on video monitor and and **b)** schematic of (2√3x2√3)R30° diffraction pattern where the crosses represent the fractional order beams which also occur in the p(2x2) diffraction pattern and the x's represent the remaining fractional order beams. The filled circles represent the integral order beams. The (hk) labels of the beams are directly beneath the beams. The dotted and dashed lines represent the six mirror planes. The shaded crosses, circles, and x's are the beams which are not seen in the photograph and the larger circles and x's correspond to the more intense beams. The outline of the manipulator is in the center of the schematic and the outline of the sulfur source is on the right hand side of the schematic.
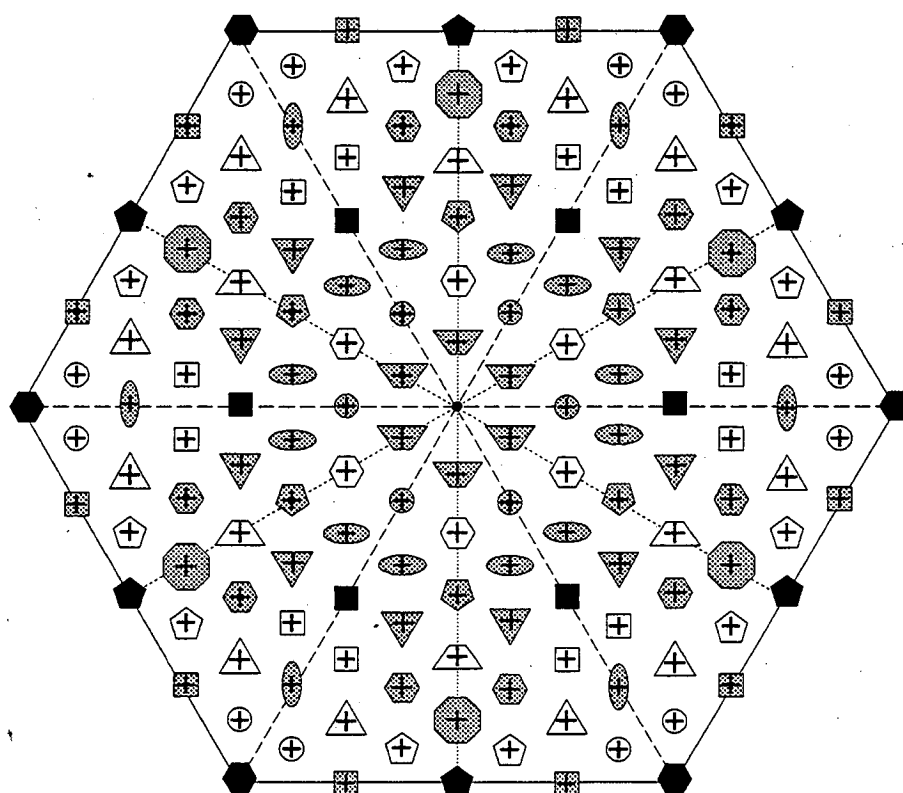
Integral Order Beams

■	(1, 0)
⬟	(1, 1)
⬢	(2, 0)

Fractional Order Beams

(1/2, 0)		(1/6, 1/6)		(7/6, 2/3)	
(1/2, 1/2)		(2/3, 1/6)		(5/3, 1/6)	
(1, 1/2)		(5/6, 1/3)		(1/3, 1/3)	
(3/2, 0)		(5/6, 5/6)		(2/3, 2/3)	
(3/2, 1/2)		(7/6, 1/6)		(4/3, 1/3)	

Figure 7.11   Schematic that illustrates the symmetry of the LEED pattern of Re(0001)-(2√3x2√3)R30 °-6S at normal incidence.
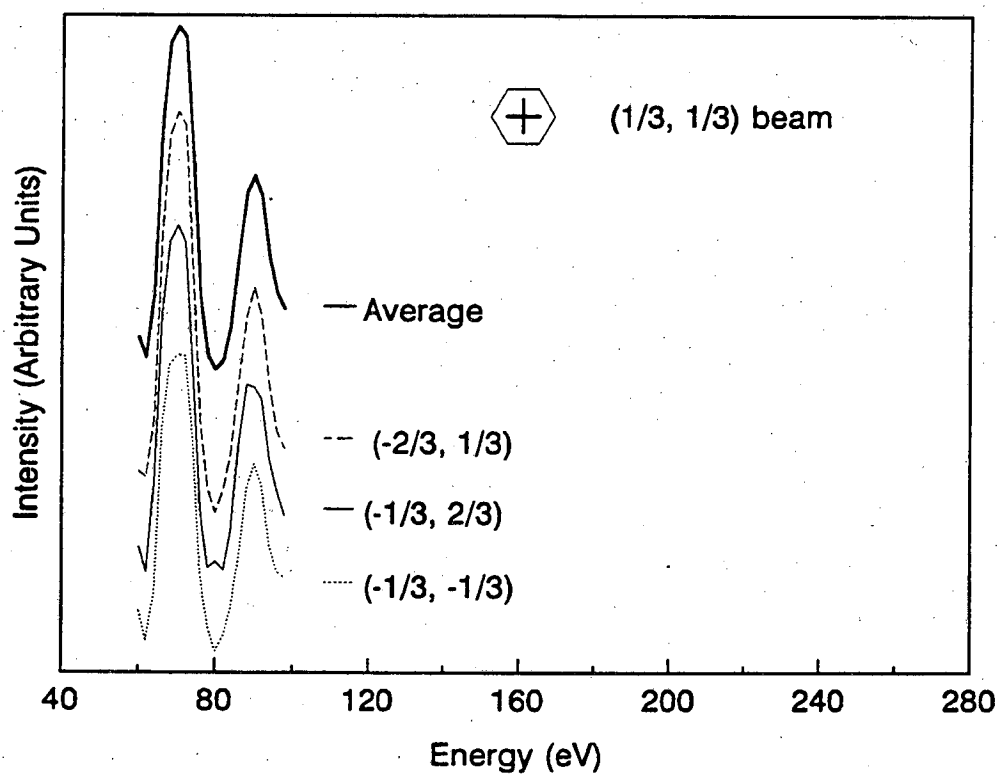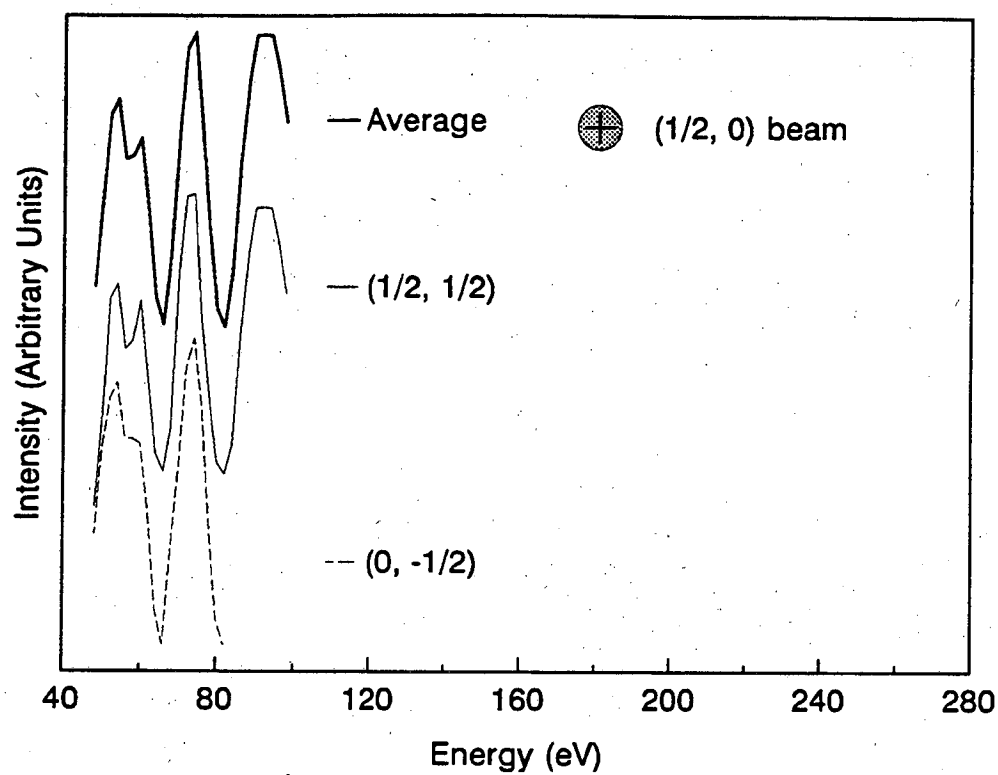
Figure 7.12 Experimental I-V Curves of Re(0001)-(2√3x2√3)R30°-6S
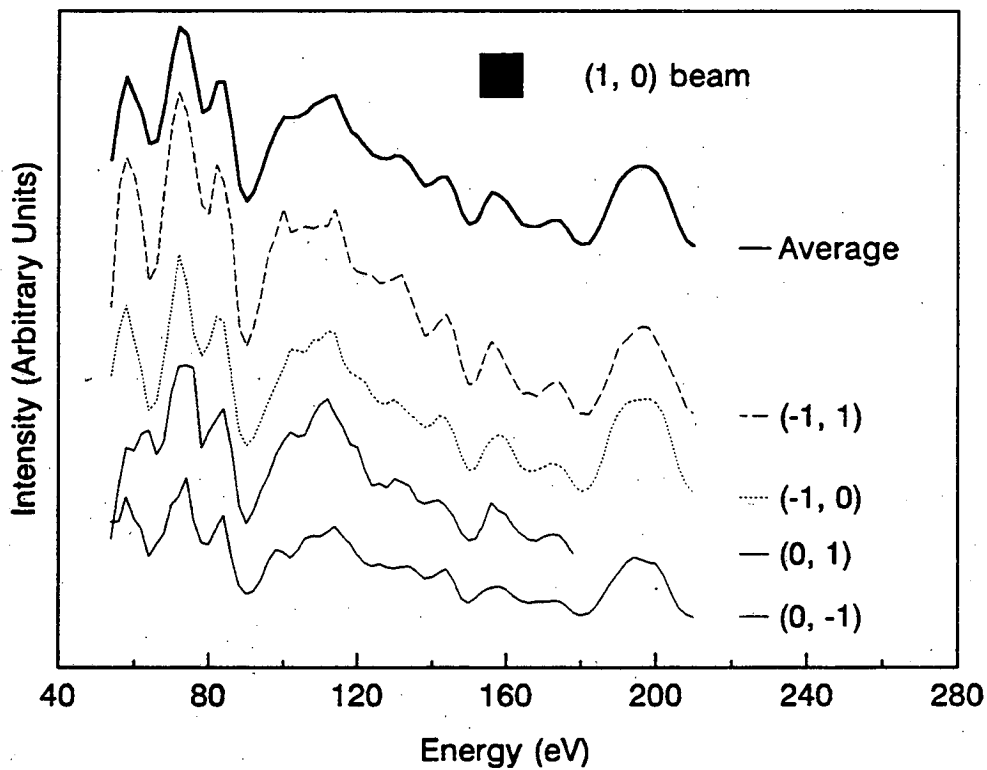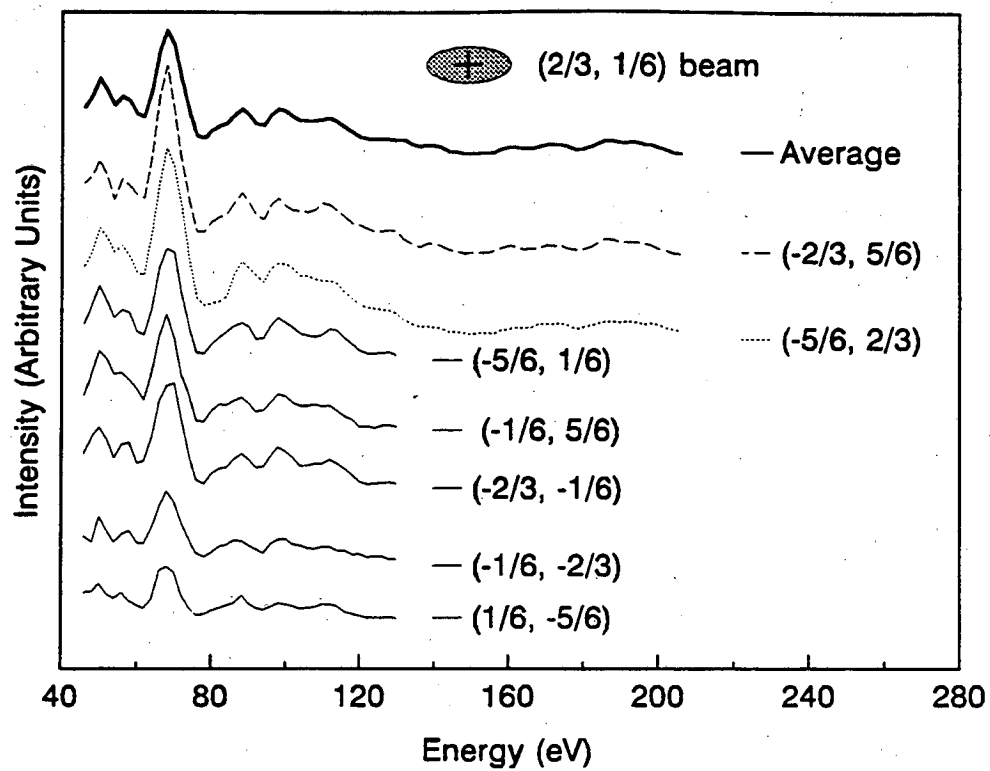
Figure 7.12 Continued   Experimental I-V Curves of Re(0001)-(2√3x2√3)R30°-6S

**Figure 7.12 Continued**   Experimental I-V Curves of Re(0001)-(2√3x2√3)R30°-6S

Figure 7.12 Continued   Experimental I-V Curves of Re(0001)-(2√3x2√3)R30°-6S

191

Figure 7.12 Continued   Experimental I-V Curves of Re(0001)-(2√3x2√3)R30°-6S

192
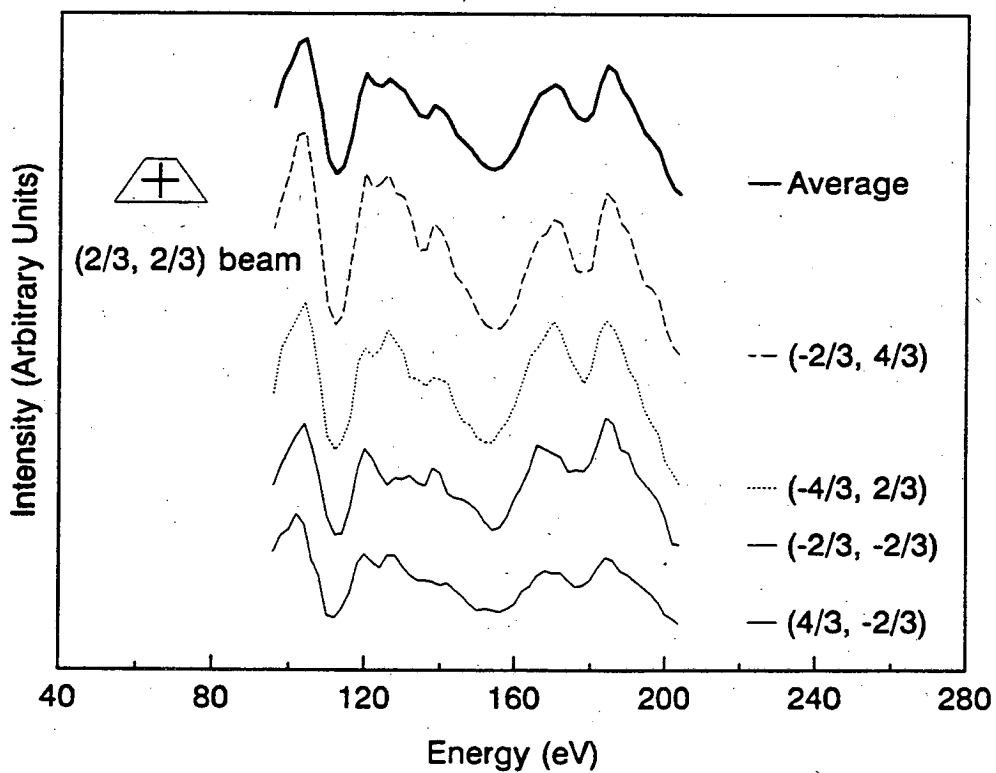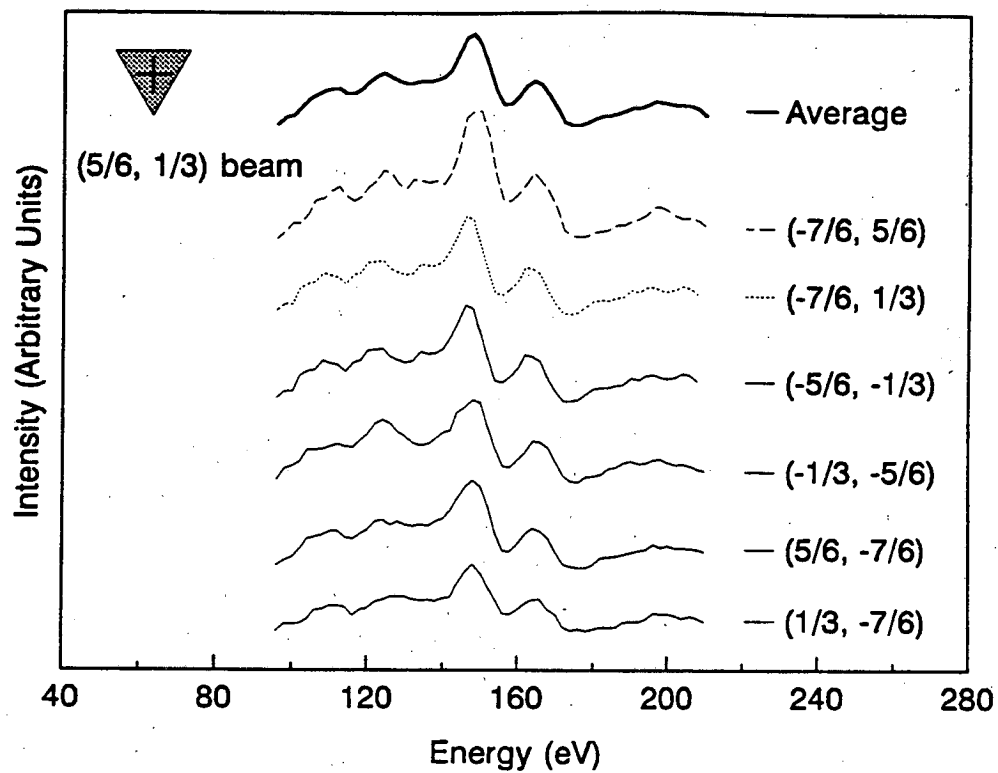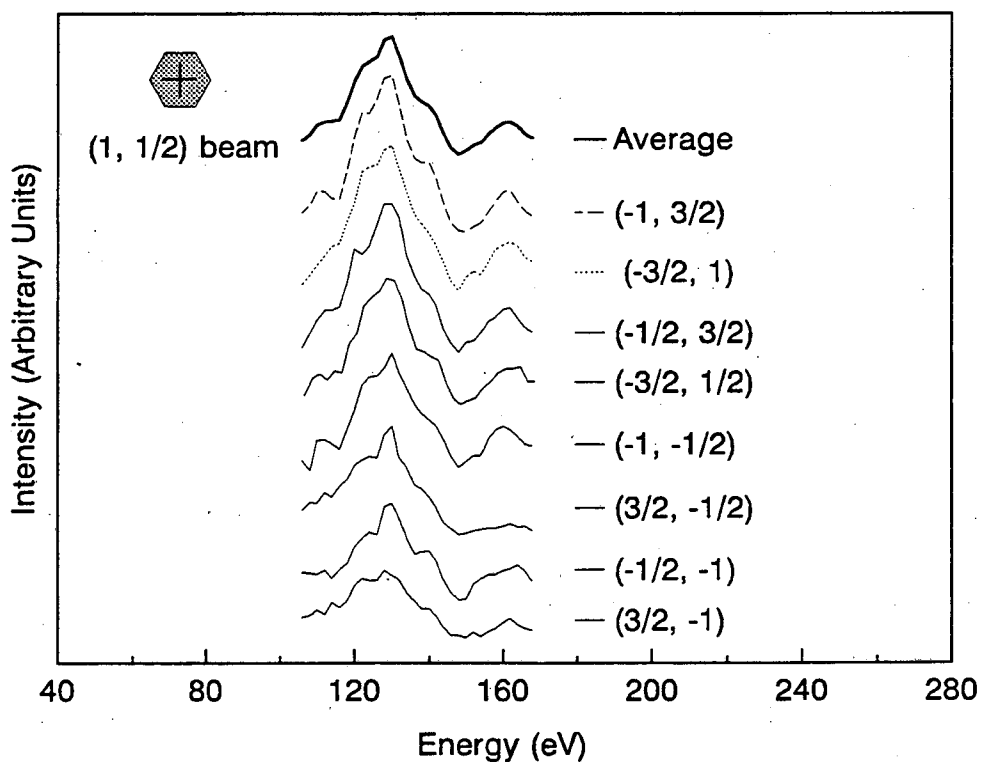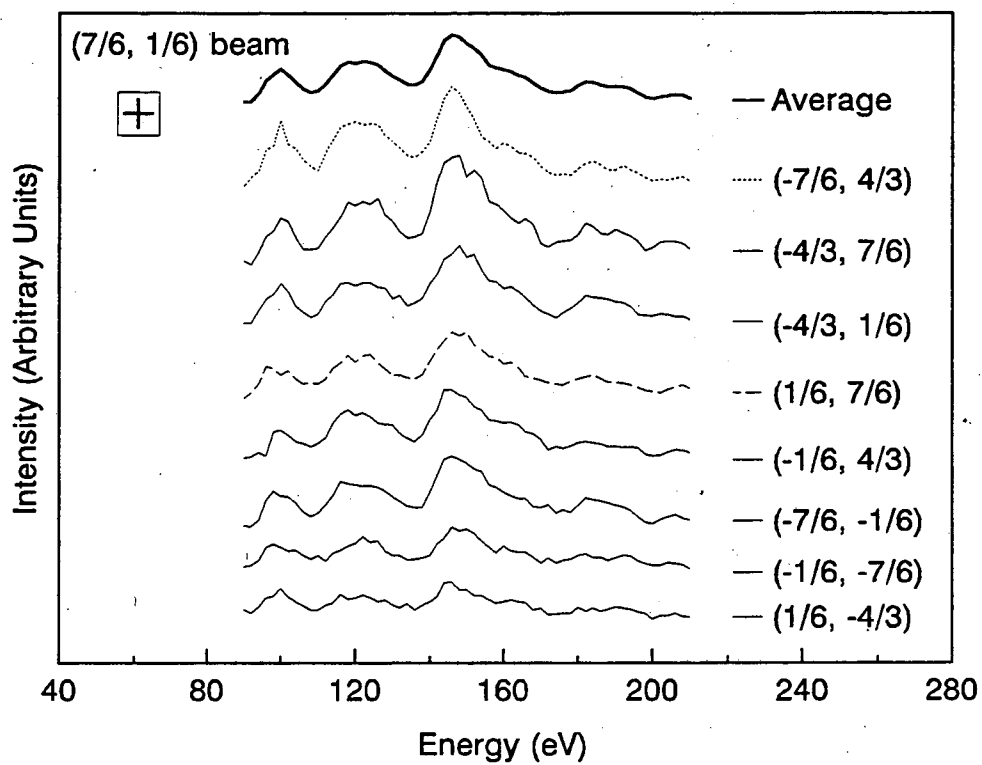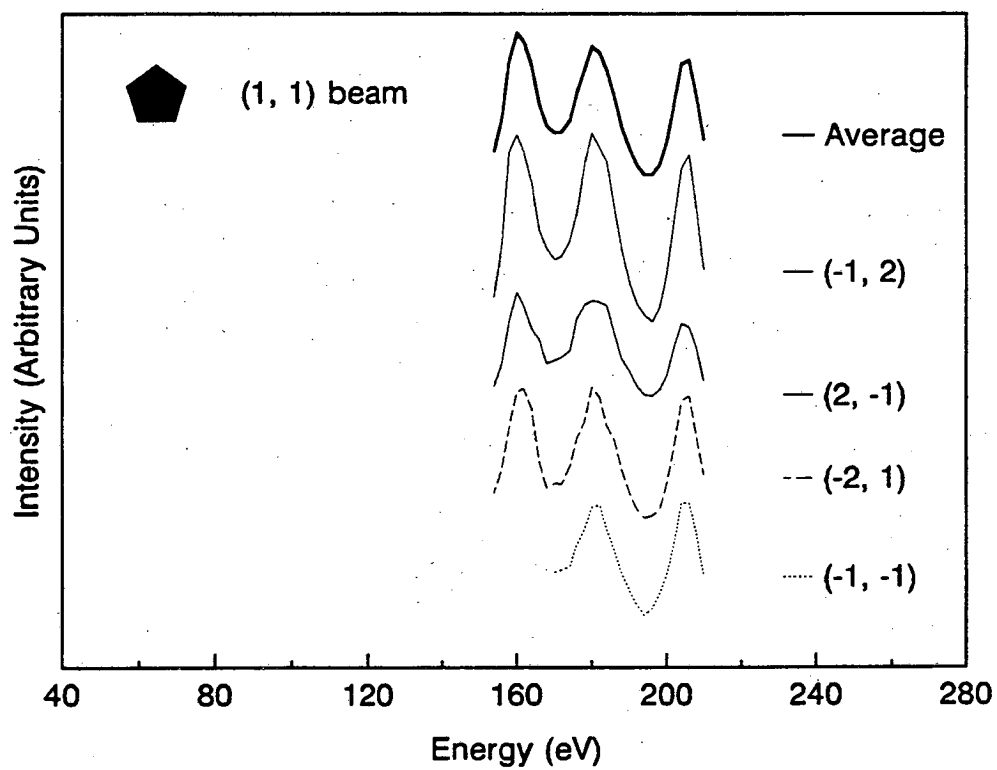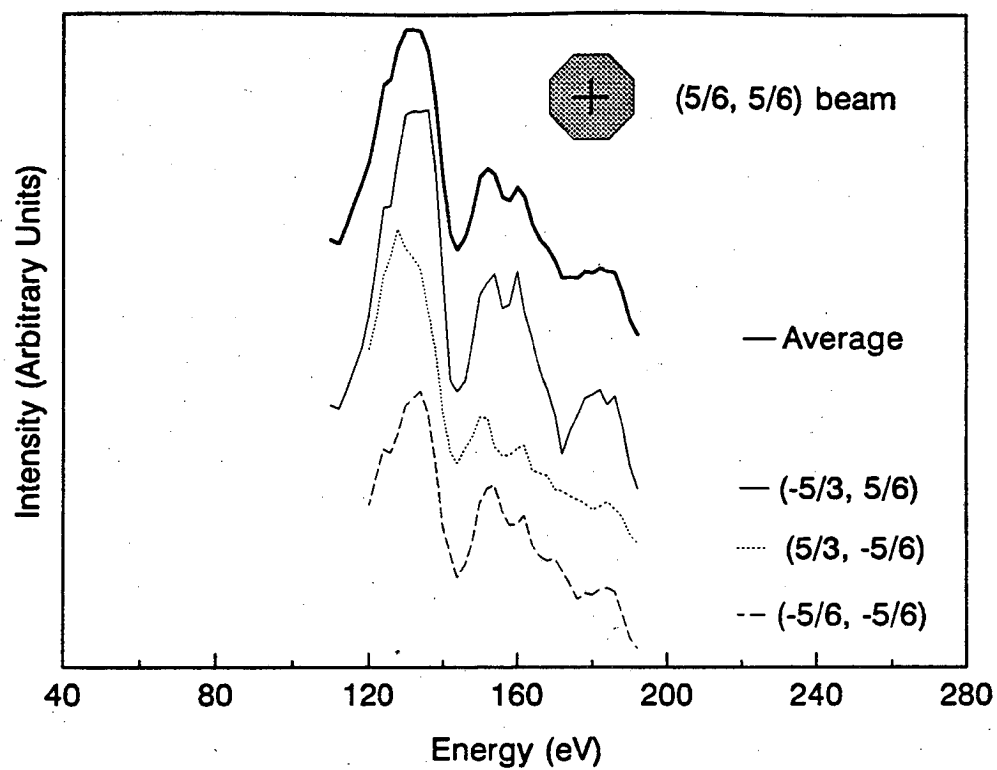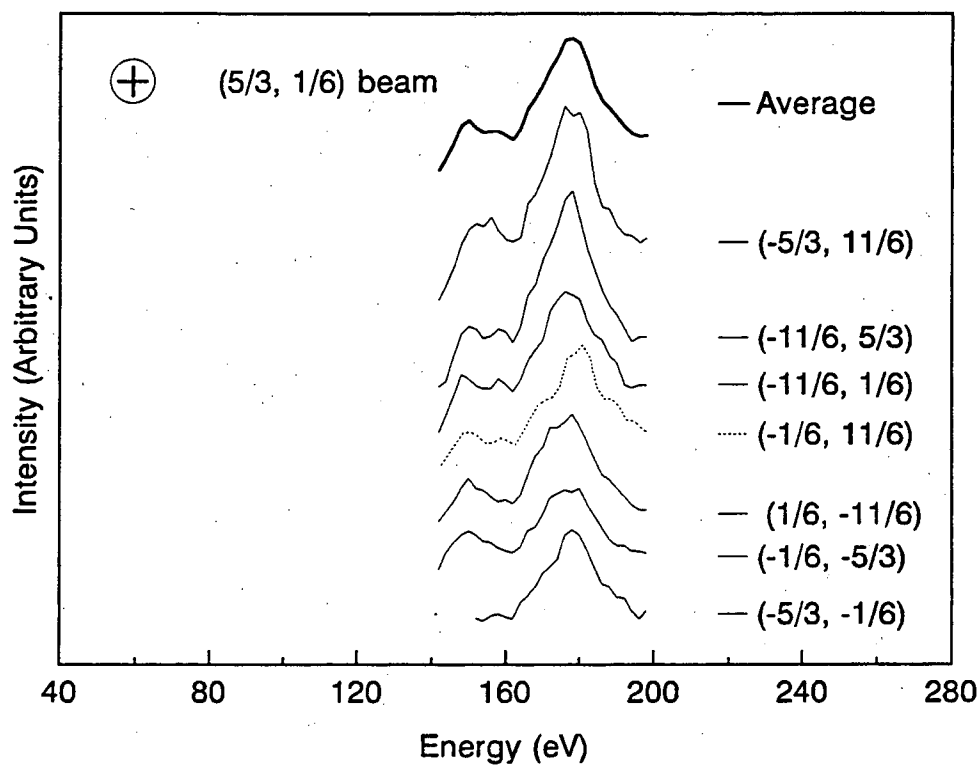
Figure 7.12 Continued   Experimental I-V Curves of Re(0001)-(2√3x2√3)R30°-6S

Figure 7.13 Real-space model of   Re(0001)-(2√3x2√3)R30°-6S

193

References

7.1   D.G. Kelly, Ph.D. Thesis, Berkeley, 1987.

7.2   M.E. Bussell, Ph.D. Thesis, Berkeley, 1988.

7.3   D.G. Kelly, A.J. Gellman, M. Salmeron, G.A. Somorjai, V. Maurice, M. Huber, and J.Oudar, Surf. Sci. **204** (1988) 1.

7.4   D.F. Ogletree, R.Q. Hwang, D.M. Zeglinski, A. Lopez Vasquez-de-Parga, G.A. Somorjai, and M. Salmeron, J. Vac. Sci. Technol. B **9** (1991) 886.

7.5   R.Q. Hwang, D.M. Zeglinski, A. Lopez Vasquez-de-Parga, D.F. Ogletree, G.A. Somorjai, M. Salmeron, and D.R. Denley, Phys. Rev. B **44** (1991) 1941.

7.6   F.A. Cotton and G. Wilkinson, **Advanced Inorganic Chemistry**, 5th ed. (John Wiley and Sons, New York, 1988).

Appendix: Data Acquisition and Analysis Programs

The functions in italics are functions which are supplied by the Imager-AT Software and which control the video board.

Data Acquisition Program

```
/* getdat1.c */
/* acquires video data and stores                              */
/* into files by energy; this program ramps the energy         */
/* from a lower energy to a higher energy                       */

#include <im2to3.h>  /* library of functions to control video board */
char base[6];

main()
{
    int i, energy, ini, final, inc, key, number;

/* initialize video boards */
    init(0xd000,0x300);
    video(1,1);
    clear(1,0);
/* request user to input information */
    printf("Enter initial energy(eV)\n");
    scanf("%d", &ini);
    printf("Enter final energy(eV)\n");
    scanf("%d", &final);
    printf("Enter energy increment (eV)\n");
    scanf("%d", &inc);
    printf("Enter base of filename\n");
    scanf("%s", base);
    printf("Enter offset(0 to 255)\n");
    scanf("%d", &number);

    sync(1,0);
    offset(number);
    gain(0);
/* record background image */

    printf("Hit any key to record background image\n");
    key=getch();
    record(0);
    printf("Hit any key except ""q"" to record the image for the initial energy.\n");
```

195

```
    printf("Hit ""q"" to exit the program. Hit ""r"" to take another image at the same
energy.\n");
    key=getch();

/* record images from initial to final energy */
    for (energy=ini; energy<=final; energy+=inc)
    {
        if(key==113)  /* if "q" is hit exit program */
        {
            break;
        }
            record(energy);
            key=getch();
            if(key==114)    /* if "r" is hit the image is repeated */
            {
                printf("Repeating previous energy\n");
                energy-=inc;
            }
    }
}

/* record() */
/* function to average 128 frames for a given energy and saves the */
/* image in a file whose extension is the energy */
record(energy)
int  energy;
{
    char filename[12];
    opmode(2,0);
    faverage(128,5,0);
    opmode(0,0);
    sprintf(filename, "%s.%d", base, energy);
    todisk(filename);
    printf("filename is %s\n", filename);
}
```

Data Acquisition Program with LEED power Supply Interfaced to Computer

```
/* getdat2.c */
/* acquires video data and writes to      */
/* files. The files are indexed by energy, i.e.  */
/* filename.energy                          */

#include <im2to3.h>
```

196

```c
char base[8];

#define MAXSIZE 11
#define DAC_INTERVAL 200
#define NUMBER_IMAGES 32

void dac_setup(short int);
void dac_out(short int);
void record(int);
void calibrate( int *);
void interpolate( int *, int *, int *, int *);

main()
{
    int i, energy, ini, final, inc, key, number;
    int beam_array[MAXSIZE], DAC_array[MAXSIZE*20];

/* initialize video board */
    init(0xd000,0x300);
    video(1,1);
    clear(1,0);
/* request user to input information */
    printf("Enter initial energy(eV)\n");
    scanf("%d", &ini);
    printf("Enter final energy(eV)\n");
    scanf("%d", &final);
    printf("Enter energy increment (eV)\n");
    scanf("%d", &inc);
    printf("Enter base of filename( 6 characters or less )\n");
    scanf("%s", base);
    printf("Enter offset(0 to 255)\n");
    scanf("%d", &number);

    sync(1,0);
    offset(number);
    gain(0);
/* calibrate LEED power supply */
    printf("ini=%d\n",ini);
    calibrate( &beam_array[0] );
    for(i=0;i<MAXSIZE;i++){
        printf("beam_array[%d]=%d\n", i, beam_array[i]);
    }
/* interpolate between calibration points */
    printf("ini=%d\n", ini);
    interpolate( &beam_array[0], &DAC_array[0], &inc, &ini);
```

197

```c
/* record background image */
    printf("Hit any key except ""q"" to record the image for the initial energy.\n");
    printf("Hit ""q"" to exit the program. Hit ""r"" to take another image at the same
energy.\n");
    key=getch();

/* record images from initial to final energy */
    for (energy=ini; energy<=final; energy+=inc){
        dac_out(DAC_array[(energy - ini)/inc]);
        if(key==113){ /* if "q" is hit exit program */
            break;
        }
        record(energy);
        if(key==114){   /* if "r" is hit the image is repeated */
            energy-=inc;
        }
    }
}

/* calibrate() */
/* function generates an array which correlates DAC(0 to 2047) to beam */
/* energy of LEED power suppply */
void calibrate(int *pointer){
int DAC, beam_energy, init_energy;
    printf("Input initial energy(eV)\n");
    scanf("%d", &init_energy);
    for(DAC=0;DAC<=2000;DAC+=DAC_INTERVAL){
        dac_out(DAC);
        printf("Enter beam energy(%d)\t", DAC/DAC_INTERVAL);
        scanf("%d", &beam_energy);
        printf("\n");
        *(pointer+DAC/DAC_INTERVAL)= beam_energy;
    }
}

/* interpolate() */
/* function interpolates between points obtained from calibration array */
void interpolate(int *beam_array, int *DAC_array, int *increment, int *Einit){

    int    count, j, Einc;
    float   m;

    printf("Einit=%d\n", *Einit);
    Einc=*Einit;
    printf("Einc=%d\n", Einc);
```

198

```
for(j=0;j<(MAXSIZE-1);j++){
        m=(float)DAC_INTERVAL/(*(beam_array+(j+1))-*(beam_array+j));
        printf("m[%d]=%f\n", j, m);
        while(Einc<*(beam_array+(j+1))){
            count=(Einc - *Einit)/(*increment);
            *(DAC_array+count)=DAC_INTERVAL*j + (int)((m*(Einc -
*(beam_array+j)))+0.5);
```

```
/* record() */
/* function to average 128 frames for a given energy and saves the */
/* image in a file whose extension is the energy */
record(energy)
int  energy;
{
    char filename[12];
    opmode(2,0);
    faverage(128,5,0);
    opmode(0,0);
    sprintf(filename, "%s.%d", base, energy);
    todisk(filename);
    printf("filename is %s\n", filename);
}
```

Data Analysis Program Which Uses Manual Tracking

```
/* mantrac.c */
/*.This program generates IV curves by integrating the    */
/* diffraction spot intensity at each energy              */
/* and subtracts the background intensity. The user must  */
/* manually track the spot by centering the cursor around */
/* the spot at each successive energy.                    */

#include <stdio.h>
#include <stdlib.h>
#include <im2to3.h>
#include <math.h>


#define BOUND 10
#define BACKGDBOUND 8
#define INTENSITY_BOUNDS 5
#define CMLIM 1

int identify(int *mx, int *my);
int search(int *dx, int *dy);
void firstmoment(int *,int *);
```

```c
main()
{
    unsigned char ovr[15],transpal[256];
    char base[8],filename[12],outfile[12];
    int i,j,numimage,key1,sum,dx,dy;
    int ini,final,energy,inc;

    FILE *fptr;
    for(i=0;i<15;i++){
         ovr[i]=50;
    }
    for(i=0;i<256;i++){
         transpal[i]=i;
    }
    init(0xd000,0x300);
    video(1,1);
    olutlay(0,ovr,ovr,ovr,transpal,transpal,transpal);
    outpath(0,-1,1,2);
    clear(1,0);

    printf("Enter initial energy (eV)\n");
    scanf("%d",&ini);
    printf("Enter final energy (eV)\n");
    scanf("%d",&final);
    printf("Enter energy increment (eV)\n");
    scanf("%d",&inc);
    printf("Enter base of file name\n");
    scanf("%s",base);
    printf("Hit escape to exit. Hit any other key to continue\n");

while((key1=getch()) != 27 ){          /* "esc" */
  printf("Enter output file name\n\t");
  scanf("%s",outfile);
  fptr=fopen(outfile,"w");
  for (energy=ini; energy<=final;energy+=inc){
       if (key1 == 113){
          break;
       }
       if (energy==ini){
               dx=246;
               dy=250;
               sprintf(filename,"%s.0",base);
               opmode(0,2);                  /* SET I/O MODE; FBUF 2 */
               fromdisk(filename);
       }
```

200

```c
        sprintf(filename,"%s.%d",base,energy);
        printf("%s\n",filename);
        opmode(0,0);           /* SET I/O MODE; FBUF 0 */
        fromdisk(filename);
        opmode(2,0);           /* SET PROCEESSING MODE; FBUF 0 */
        image(0,0,0,2);        /* ADD 2 TO EACH PIXEL INTENSITY */
        interimage(0,2,0,1);   /* SUBTRACT 0 eV BACKGROUND IMAGE */
        clear(1,0);            /* CLEAR FBUF 1, OVERLAY BUF, TO 0 */
        opmode(1,1);           /* SET GRAPHICS MODE; FBUF 1 */
        drawmode(1);
        identify(&dx, &dy); /* INTERACTIVE MODE; USER CONTROL OF VIDEO
CURSOR */
        sum=search(&dx, &dy);         /* CALCULATE INTENSITY OF SPOT */
        printf("energy=%d\tintensity=%d\n", energy,sum);
        fprintf(fptr,"%d\t%d\n", energy, sum);
   }
   putch(7);       /* BEEPS TO SIGNAL END OF SINGLE SPOT ANALYSIS */
   printf("Hit escape to exit. Hit any other key to continue.\n");
 }
 fclose(fptr);
}


/* identify() */
/* THIS FUNCTION ALLOWS THE USER TO POSITION THE VIDEO CURSOR */
/* ABOUT THE DIFFRACTION SPOT */

int identify(int *mx, int *my)
{
   int dx, dy, key, key2, sum;
        dx=*mx;
        dy=*my;
        move(dx,dy); /* MOVE CENTER OF VIDEO CURSOR TO PIXEL COORD'S */
        circle(10);
        while((key=getch()) != 32){   /* "space bar" */
                if (key == 113){       /* IF "q" IS HIT */
                    break;                 /* THEN EXIT TO OPERATING SYSTEM */
                }
                opmode(1,1);
                printf("Hit enter to center the cursor on the spot center\n");
                if(key==0){
                    key2=getch();
                    if(key2==83){         /* DEL KEY*/
                        circle(10);
                        rmove(-10,0);
                        circle(10);
```

201

```c
        dx=dx-10;        /* MOVE CURSOR 10 PIXELS TO LEFT */
    }
    if(key2==72){        /* UP ARROW KEY*/
        circle(10);
        rmove(0,-1);
        circle(10);
        dy=dy-1;                /* MOVE CURSOR 1 PIXEL UP */
    }
    if(key2==71){        /* HOME KEY*/
        circle(10);
        rmove(0,-10);
        circle(10);
        dy=dy-10;        /* MOVE CURSOR UP 10 PIXELS */
    }
    if(key2==75){        /* LEFT ARROW KEY*/
        circle(10);
        rmove(-1,0);
        circle(10);
        dx=dx-1;         /* MOVE CURSOR 1 PIXEL TO LEFT */
    }
    if(key2==77){        /* RIGHT ARROW KEY*/
        circle(10);
        rmove(1,0);
        circle(10);
        dx=dx+1;         /* MOVE CURSOR 1 PIXEL TO RIGHT */
    }
    if(key2==81){        /* PAGE DOWN KEY*/
        circle(10);
        rmove(10,0);
        circle(10);
        dx=dx+10;        /* MOVES CURSOR 10 PIXELS TO RIGHT */
    }
    if(key2==80){        /* DOWN ARROW KEY*/
        circle(10);
        rmove(0,1);
        circle(10);
        dy=dy+1;         /* MOVE CURSOR 1 PIXEL DOWN */
    }
    if(key2==79){        /* END KEY*/
        circle(10);
        rmove(0,10);
        circle(10);
        dy=dy+10;        /* MOVES CURSOR 10 PIXELS DOWN */
    }
}
```

```c
        if(key==13){    /* <enter> */
            printf("x=%d\t\ty=%d\n", dx, dy);
            opmode(0,0);            /* SET I/O MODE; FBUF 0 */
            sum=search(&dx, &dy);
            *mx= dx;
            *my= dy;
            printf("Strike the space bar to analyze\n");
            printf("the remaining energies\n");
        }
        opmode(0,0);                /* SET I/O MODE; FBUF 0 */
    }
}
/* search() */
/* THIS FUNCTION SEARCHES FOR THE PIXEL WITH THE LARGEST
INTENSITY */

int search(int *dx, int *dy)
{
    float bgd;
    int count1, count2, dx0, dy0, dxmax, dymax, imax, intensity;
    int x, y, xdif, ydif;
    dx0=*dx - BOUND;        /*                                   */
    dy0=*dy - BOUND;        /*      INITIALIZE VARIABLES     *    
    imax=pixr(*dx, *dy);    /*                                   */
    dxmax=*dx;              /*                                   */
    dymax=*dy;              /*                                   */
    x=*dx;
    y=*dy;

/* MOVE CIRCLE CENTER TO DXMAX, DYMAX */
    opmode(1,1);
    xdif= dxmax - x;
    ydif= dymax - y;
    circle(10);
    rmove(xdif, ydif);
    circle(10);
    opmode(0,0);

/* FIND TOTAL SPOT INTENSITY MINUS BACKGROUND INTENSITY */
    bgd=backgd(dxmax, dymax);
    intensity=inten(dxmax, dymax, bgd);
    printf("x=%d\t\ty=%d\t\tintensity=%d\t\tbgd=%d\n\n", dxmax, dymax, intensity, bgd);
    return (intensity);
}
```

```c
/* backgd() */
/* THIS FUCTION CALCULATES THE AVERAGE BACKGROUND */
float backgd(int dx,int dy)
{
    float bkgd;
    int   bgd,bound,count3,count4,decimal,flag,i,ix,iy;
            bkgd=0;
            bound=BACKGDBOUND*2+1;
            for(i=0;i<bound;i++){
                ix=dx-BACKGDBOUND;
                iy=dy-BACKGDBOUND+i;
                bkgd+=pixr(ix,iy);
                ix=dx+BACKGDBOUND;
                bkgd+=pixr(ix,iy);
                iy=dy-BACKGDBOUND;
                ix=dx-BACKGDBOUND+i;
                bkgd+=pixr(ix,iy);
                iy=dy+BACKGDBOUND;
                bkgd+=pixr(ix,iy);
            }
            bkgd/=64;
            printf("\t\tbackground=%.3f\n",bkgd);
            return(bkgd);
}


/* inten() */
/* DETERMINES THE TOTAL INTENSITY MINUS THE BACKGROUND
INTENSITY OF A SPOT */
int inten(int dx, int dy, float bkgd)
{
    int count3,count4,count5,count6,count7,decimal;
    int bound,i, j, ix, iy, finalsum, flag,sumint;
    float intensity,sum;

            sum=0;
            bound=INTENSITY_BOUNDS*2+1;
            for(i=0;i<bound;i++){
                for(j=0;j<bound;j++){
                    ix=dx+i-INTENSITY_BOUNDS;
                    iy=dy+j-INTENSITY_BOUNDS;
                    intensity=pixr(ix,iy)-bkgd;
                    sum+=intensity;
                }
            }
            sumint=sum;
```

```
            printf("intensity=%d\n",sumint);
            return(sumint);
}
```

Data Analysis Program which uses automated tracking based on finding the first moment of the intensity of a spot

```c
/* mtestxbar.c */
/* This program tracks the diffraction spots by positioning the integration window */
/* about the x, y coordinate for which the first moment of 2-D intensity is a minimum */

#include <stdio.h>
#include <stdlib.h>
#include <im2to3.h>
#include <math.h>

#define BOUND 8
#define BACKGDBOUND 8
#define INTENSITY_BOUNDS 8
#define CMLIM 5
#define SEARCH_LIMIT 2
#define RADIUS 8          /* radius of cursor */

int identify(int *, int *, int *);
int search(int *, int *, int *);
void firstmoment(int *,int *);

main()
{
    unsigned char ovr[15],transpal[256];
    char base[8],filename[12],outfile[12];
    int i,j,numimage,key1,sum,dx,dy;
    int energy,final,inc,ini,start,tracking;

    FILE *fptr;
    for(i=0;i<15;i++){
        ovr[i]=200;
    }
    for(i=0;i<256;i++){
        transpal[i]=i;
    }
    init(0xd000,0x300);
    video(1,1);
    olutlay(0,ovr,ovr,ovr,transpal,transpal,transpal);
    outpath(0,-1,1,2);
    clear(1,0);
```

```c
printf("Enter initial energy (eV)\n");
scanf("%d",&ini);
printf("Enter final energy (eV)\n");
scanf("%d",&final);
printf("Enter energy increment (eV)\n");
scanf("%d",&inc);
printf("Enter base of file name\n");
scanf("%s",base);
printf("Hit escape to exit. Hit any other key to continue\n");

 while((key1=getch()) != 27 ){          /* "esc" */
    printf("The Background bound/Integration bound =%d/%d\n", BACKGDBOUND,
INTENSITY_BOUNDS);
    printf("Enter output file name\n\t");
    scanf("%s",outfile);
    fptr=fopen(outfile,"w");
    printf("Do you want (1)automated or (2)manual tracking?\n");
    scanf("%d", &tracking);
    start=0;
    for (energy=ini; energy<=final;energy+=inc){
        if (key1 == 113){
            break;
        }
        if (energy==ini){
                dx=246;
                dy=250;
        }
        sprintf(filename,"%s.%d",base,energy);
        printf("%s\n",filename);
        opmode(0,0);           /* SET I/O MODE; FBUF 0 */
        fromdisk(filename);
        opmode(2,0);           /* SET PROCEESSING MODE */
        clear(1,0);            /* CLEAR FBUF 1, OVERLAY BUF, TO 0 */
        opmode(1,1);           /* SET GRAPHICS MODE; FBUF 1 */
        drawmode(1);
        if(start==0 || tracking==2){
            identify(&dx, &dy, &tracking); /* INTERACTIVE MODE; USER CONTROL
OF VIDEO CURSOR */
        }
        if (start==1 && tracking==1){
            move(dx,dy);
            circle(RADIUS);
        }
        start=1;
```

```c
            sum=search(&dx, &dy, &tracking);   /* CALCULATE INTENSITY OF SPOT */
            printf("energy=%d\tintensity=%d\n", energy,sum);
            fprintf(fptr,"%d\t%d\n", energy, sum);
        }
      putch(7);        /* BEEPS TO SIGNAL END OF SINGLE SPOT ANALYSIS */
      printf("Hit escape to exit. Hit any other key to continue.\n");
    }
  fclose(fptr);
}


/* identify() */
/* THIS FUNCTION ALLOWS THE USER TO POSITION THE CURSOR */
/* ABOUT THE SPOT */

int identify(int *mx, int *my, int *tracking)
{
    int dx, dy, key, key2, sum, track;
        dx=*mx;
        dy=*my;
        track=*tracking;
        move(dx,dy); /* MOVE CENTER OF VIDEO CURSOR TO PIXEL COORD'S*/
        circle(RADIUS);
        while((key=getch()) != 32){   /* "space bar" */
                if (key == 113){       /* IF "q" IS HIT */
                    break;              /* THEN EXIT TO OPERATING SYSTEM */
                }
                opmode(1,1);
                printf("Hit enter to center the cursor on the spot center\n");
                if(key==0){
                    key2=getch();
                    if(key2==83){          /* DEL KEY */
                        circle(RADIUS);
                        rmove(-10,0);
                        circle(RADIUS);
                        dx=dx-10;       /* MOVE CURSOR 10 PIXELS TO LEFT */
                    }
                    if(key2==72){          /* UP ARROW KEY*/
                        circle(RADIUS);
                        rmove(0,-1);
                        circle(RADIUS);
                        dy=dy-1;        /* MOVE CURSOR 1 PIXEL UP */
                    }
                    if(key2==71){          /* HOME KEY */
                        circle(RADIUS);
                        rmove(0,-10);
```

207

```c
            circle(RADIUS);
            dy=dy-10;        /* MOVE CURSOR UP 10 PIXELS */
        }
        if(key2==75){        /* LEFT ARROW KEY */
            circle(RADIUS);
            rmove(-1,0);
            circle(RADIUS);
            dx=dx-1;         /* MOVE CURSOR 1 PIXEL TO LEFT */
        }
        if(key2==77){        /* RIGHT ARROW KEY */
            circle(RADIUS);
            rmove(1,0);
            circle(RADIUS);
            dx=dx+1;         /* MOVE CURSOR 1 PIXEL TO RIGHT */
        }
        if(key2==81){        /* PAGE DOWN KEY */
            circle(RADIUS);
            rmove(10,0);
            circle(RADIUS);
            dx=dx+10;        /* MOVES CURSOR 10 PIXELS TO RIGHT */
        }
        if(key2==80){        /* DOWN ARROW KEY */
            circle(RADIUS);
            rmove(0,1);
            circle(RADIUS);
            dy=dy+1;         /* MOVE CURSOR 1 PIXEL DOWN */
        }
        if(key2==79){        /* END KEY */
            circle(RADIUS);
            rmove(0,10);
            circle(RADIUS);
            dy=dy+10;        /* MOVES CURSOR 10 PIXELS DOWN */
        }
    }
    if(key==13){    /* <enter> */
        printf("x=%d\t\ty=%d\n", dx, dy);
        opmode(0,0);          /* SET I/O MODE; FBUF 0 */
        sum=search(&dx, &dy, &track);
        *mx= dx;
        *my= dy;
        printf("Strike the space bar to analyze\n");
        printf("the remaining energies\n");
    }
}

}
```

```
/* search() */
/* THIS FUNCTION SEARCHES FOR THE PIXEL WITH THE LARGEST
INTENSITY */

int search(int *dx, int *dy, int *tracking)
{
   int bgd;
   int count1, count2, dx0, dy0, dxmax, dymax, intensity;
   int cursor_set, x, y, xdif, ydif;
   dx0=*dx - BOUND;              /*                           */
   dy0=*dy - BOUND;              /*      INITIALIZE VARIABLES  */
   dxmax=*dx;                    /*                           */
   dymax=*dy;                    /*                           */
   x=*dx;
   y=*dy;
   if (*tracking==2){
       printf("Do you want (1)automated or (2)manual cursor set?\n");
       scanf("%d", &cursor_set);
   }
   if (*tracking==1 || cursor_set==1){
       opmode(0,0);  /* SET I/O MODE; FBUF 0 */
       firstmoment(&dxmax, &dymax);  /* activated 4/9/91 */
   }
   printf("xmax=%d\tymax=%d\n", dxmax, dymax);
/* MOVE CIRCLE CENTER TO DXMAX, DYMAX */
   *dx=dxmax;
   *dy=dymax;
   opmode(1,1);
   xdif= dxmax - x;
   ydif= dymax - y;
   circle(RADIUS);
   rmove(xdif, ydif);
   circle(RADIUS);
   opmode(0,0);
/* FIND TOTAL SPOT INTENSITY MINUS BACKGROUND INTENSITY */
   bgd=backgd(dxmax, dymax);
   intensity=inten(dxmax, dymax, bgd);
   printf("x=%d\t\ty=%d\t\tintensity=%d\t\tbgd=%d\n\n", dxmax, dymax, intensity, bgd);
   return (intensity);

}


/* firstmoment() */
/* THIS FUNCTION FINDS THE PIXEL WITH THE SMALLEST FIRST MOMENT*/
/* IN THE INTENSITY*/
```

```c
void firstmoment(int *dx, int *dy)
{
    float Ixbar,Iybar,deltaIxbar,deltaIybar,sumintensity;
    float mindeltaIcm,deltaIcm;
    int xtemp,ytemp,xmin,ymin,xold,yold,i,j,k,l,lim,limit,intensity,x,y;
    long int  Ix, Iy;
    lim=CMLIM*2+1;
    xold=*dx;
    yold=*dy;
    mindeltaIcm=10000;
    xmin=0;
    ymin=0;
    Ix=0;
    Iy=0;
    printf("xold=%d\tyold=%d\n\n",xold,yold);
    limit=SEARCH_LIMIT*2+1;
    for(k=0;k<limit;k++){
        xtemp=*dx+k-SEARCH_LIMIT;
        for(l=0;l<limit;l++){
          ytemp=*dy+l-SEARCH_LIMIT;
          Ix=0;
          Iy=0;
        /* CALCULATE Ix */
          intensity=0;
          sumintensity=0;
          for(i=0;i<lim;i++){
                x=xtemp+i-CMLIM;
                for(j=0;j<lim;j++){
                    y=ytemp+j-CMLIM;
                    intensity=pixr(x,y);
                    Ix+=( (long int)intensity*x);
                    sumintensity+=intensity;
                }
          }
          Ixbar=(float)(Ix/sumintensity);
        /* CALCULATE Iy */
          intensity=0;
          for(i=0;i<lim;i++){
            y=ytemp+i-CMLIM;
            for(j=0;j<lim;j++){
                x=xtemp+j-CMLIM;
                intensity=pixr(x,y);
                Iy+=((long int)intensity*y);
            }
```

210

```c
        }
        Iybar=(float)(Iy/sumintensity);
        deltaIxbar=Ixbar-xtemp;    /* calculate difference between center of */
        deltaIybar=Iybar-ytemp;    /* mass and window center              */
        deltaIcm=sqrt((double)(pow(deltaIxbar,2)+pow(deltaIybar,2)));
        if((k==0) && (l==0)){
            mindeltaIcm=deltaIcm;
        }
        if(deltaIcm < mindeltaIcm){
                mindeltaIcm=deltaIcm;
                xmin=xtemp;
                ymin=ytemp;
        }
    }
}
if((xmin==0) && (ymin==0)){
    xmin=xold;
    ymin=yold;
}
*dx=xmin;
*dy=ymin;
}


/* backgd() */
/* THIS FUCTION CALCULATES THE AVERAGE BACKGROUND */
int backgd(int dx,int dy)
{
    int   ave,bkgd,bkgdcount,bound,i,imax,itemp,j,k,xtemp,ytemp;
    int   count[256];
    char  bkgdfile[12];

    for(i=0;i<256;i++){
        count[i]=0;
    }
    imax=0;
    bkgdcount=0;
    ave=0;
    bound=BACKGDBOUND*2+1;
  /* TOP STRIP */
    for(j=0;j<bound;j++){
        xtemp=dx-BACKGDBOUND+j;
        ytemp=dy-BACKGDBOUND;
        itemp= pixr(xtemp,ytemp);
        count[itemp]++;
        if(count[itemp]>count[imax]){
```

211

```c
                imax=itemp;
            }
            bkgdcount+=itemp;
        }
/* BOTTOM STRIP */
    for(j=0;j<bound;j++){
        xtemp=dx-BACKGDBOUND+j;
        ytemp=dy+BACKGDBOUND;
        itemp=pixr(xtemp,ytemp);
        count[itemp]++;
        if(count[itemp]>count[imax]){
                    imax=itemp;
        }
        bkgdcount+=itemp;
    }
/* LEFT STRIP */
    for(k=1;k<(bound-1);k++){
        xtemp=dx-BACKGDBOUND;
        ytemp=dy-BACKGDBOUND+k;
        itemp=pixr(xtemp,ytemp);
        count[itemp]++;
        if(count[itemp]>count[imax]){
            imax=itemp;
        }
        bkgdcount+=itemp;
    }
/* RIGHT STRIP */
    for(k=1;k<(bound-1);k++){
        xtemp=dx+BACKGDBOUND;
        ytemp=dy-BACKGDBOUND+k;
        itemp=pixr(xtemp,ytemp);
        count[itemp]++;
        if(count[itemp]>count[imax]){
            imax=itemp;
        }
        bkgdcount+=itemp;
    }
    bkgd=imax;
    ave=((float)bkgdcount/(((BACKGDBOUND*2)+1)*4-4)+.5);
    printf("\t\tbackground=%d which occurred %d times\n",bkgd,count[imax]);
    printf("\t\taverage bkgd=%d\n", ave);
    return(ave);
}

/* inten() */
```

```
/* DETERMINES THE TOTAL INTENSITY MINUS THE BACKGROUND
INTENSITY OF A SPOT */
int inten(int dx, int dy, int bkgd)
{
    int count3,count4,count5,count6,count7,decimal;
    int bound,i, j, ix, iy, finalsum, flag;
    int intensity,sum;

    sum=0;
    bound=INTENSITY_BOUNDS*2+1;
    for(i=0;i<bound;i++){
        for(j=0;j<bound;j++){
            ix=dx+i-INTENSITY_BOUNDS;
            iy=dy+j-INTENSITY_BOUNDS;
            intensity=pixr(ix,iy)-bkgd;
            sum+=intensity;
        }
    }
    printf("intensity=%d\n",sum);
    return(sum);
}
```

Interpolation Program

```
/* interpol.c                                                    */
/*                                                               */
/* this program reads an input file which lists energies and     */
/* beam currents                                                 */
/*                                                               */
/*    e.g. (eV) (µA)   this line does not appear in the file      */
/*          40  0.5                                              */
/*          50  0.6                                              */
/*          60  0.7                                              */
/*           .    .                                             */
/*           .    .                                             */
/*           .    .                                             */
/*                                                               */
/* and interpolates in 2 eV increments. The interpolated list    */
/* is written to a file which the user names. As the program     */
/* stands it is used for interpolating a beam current calibration */
/* but may be modified slightly for other purposes.              */

#define LIMIT 200     /* max number of elements in arrays */
#define INCREMENT 2   /* interpolation increment */
```

```c
#include <stdio.h>
#include <stdlib.h>

FILE *fptr;
char filename[15];
int i,flag,j,count,n;
int y[LIMIT],energy[LIMIT];
float m,current[LIMIT],x[LIMIT],z[LIMIT];


main()
{
    printf("Enter the file name to be read\n\t");
    scanf("%s", filename);
    count=0;
    fptr=fopen(filename,"r");
    while(fscanf(fptr,"%d %f", &energy[count], &current[count]) != EOF){
        printf("energy= %d\tcurrent= %.2f\n",energy[count],current[count]);
        count+=1;
    }
    printf("count = %d\n",count);
    fclose(fptr);
    printf("Enter name of output file\n\t");
    scanf("%s", filename);
    fptr=fopen(filename,"w");
    z[0]=current[0];
    fprintf(fptr,"%d\t%.3f\n", energy[0], z[0]);
    i=1;
    printf("%d\t%.3f\n", energy[0], current[0]);
    for(j=0;j<(count-1);j++){
        m=(current[j+1]-current[j])/(energy[j+1]-energy[j]);
        n=1;
        flag=0;
        while(flag != 1){
            printf("energy[%d]= %d\t", i, (energy[0]+INCREMENT*i));
            z[i]=current[j]+INCREMENT*m*n;
            fprintf(fptr,"%d\t%.3f\n", (energy[0]+INCREMENT*i), z[i]);
            printf("m= %.3f\tcurrent = %.3f\n", m,z[i]);
            if(z[i] >= current[j+1]){
                flag=1;
            }
            i+=1;
            n+=1;
        } .
    }
}
```

214

```
fclose(fptr);
}
```

IV Curve Normalization Program

```
/* ivnorm.c */
/* this program uses an input file with a list of files */
/* corresponding to each indidual beam to be normalized */

#include <stdio.h>
#include <process.h>

#define LIM 200


FILE *fptr, *fptr2;
char filename[15],filename2[15],filename3[15],key,newfile[15];

int count,dummy,i,index,j,lastinit,maxcount;
int erg[50],energy[100],intensity[100],norminten[100];
float current[LIM], h, k;

main()
{
  printf("Enter name of beam current file (include extension): ");
  scanf( "%s", filename2);
  printf("Enter name of beam list file (include extension): ");
  scanf("%s", filename3);
  fptr2 = fopen( filename3, "r");
  lastinit = 1000;
  while( fscanf (fptr2, "%s %f %f", filename, &h, &k) != EOF ){
   if((fptr= fopen(filename,"r")) == NULL ){
        printf("Can't open file %s\n", filename);
        exit();
   }
   printf("filename is %s (%f %f)\n", filename, h, k);
   count=0;
   while(fscanf(fptr,"%d %d", &energy[count], &intensity[count]) != EOF ){
        count+=1;
   }
   fclose(fptr);
   printf("count=%d\n", count);
/* if the energy range for the current beam is different from the previous */
/* beam then read in the new energy range                          */
```

```c
    if( (energy[0] < lastinit) || (maxcount != count) ){
        fptr=fopen(filename2, "r");
        i=0;
        fscanf(fptr,"%d %f", &erg[i], &current[i]);
        while( erg[i] != energy[0]){
            i++;
            fscanf(fptr, "%d %f", &erg[i], &current[i]);
        }
        current[0]= current[i];
        printf("energy=%d\tcurrent[%d]=%.3f\n", energy[0], 0, current[0]);
        j=1;
        while( j < count){
            fscanf(fptr,"%d %f", &dummy, &current[j]);
            printf("energy=%d\tcurrent[%d]=%.3f\n", dummy, j, current[j]);
            j++;
        }
        fclose(fptr);
    }


    sprintf(newfile,"i%s", filename);
    printf("newfile is %s\n",newfile);
    fptr= fopen(newfile,"w");
    for(i=0;i<count;i++){
        norminten[i]=(intensity[i]/current[i]);
        printf("energy = %d\tintenstity = %d\tnormalized intensity = %d\n",
energy[i],intensity[i],norminten[i]);
        fprintf(fptr,"%d\t%d\n",energy[i],norminten[i]);
    }
    printf("count = %d\n", count);
    fclose(fptr);
    lastinit = energy[0];
    maxcount = count;
  }
  fclose(fptr2);
}
```

Program which generates LEED experimental files

```c
/* compile.c */
/* This program accepts an input file containing the file names and   */
/* (h,k) indices for each beam.                                       */
/* Last modified 2/18/92          AUTHOR: David Jentz                 */

#include <stdio.h>
```

```c
#include <math.h>
#include <process.h>

#define INCREMENT 2

FILE *fptr, *fptr2;
double change_line, int_part;
char string[80], key, filename[15], masterfile[20];
float factor, fenergy, fintensity, h, k;
int beam_number, count1, count2, i, energy[100], intensity[100], selection;

main(){
    factor=1;
    printf("Enter the master filename\n");
    gets(masterfile);
    printf("Enter one line of strings up to 80 characters\n");
    printf("Example:p(2x2)S Re(0001); T=300K; normal incidence\n");
    gets(string);
    fptr2= fopen("beamlist.fil", "r");
    fscanf(fptr2, "%d", &beam_number);
    fptr=fopen(masterfile,"w");
    fputs(string, fptr);
    count1=0;
    while(fscanf(fptr2, "%d %s %f %f", &beam_number, filename, &h, &k) != EOF){
        count1+=1;
    }
    fprintf(fptr,"\n%3d", count1);
    fclose(fptr);
    fclose(fptr2);
    fptr=fopen(masterfile, "a");
    fptr2=fopen("beamlist.fil", "r");
    count1=0;
    while(fscanf(fptr2, "%d %s %f %f", &beam_number, filename, &h, &k) != EOF){
        change_line= modf((double)((float)count1/25.0), &int_part);
        if(change_line < 0.04)
            fprintf(fptr, "\n");
        fprintf(fptr, "%3d", beam_number);
        count1+=1;
    }
    fprintf(fptr, "\n(1F10.1,1F10.1)\n");
    fclose(fptr);
    fclose(fptr2);
    fptr2=fopen("beamlist.fil", "r");
    while( fscanf(fptr2, "%d %s %f %f", &beam_number, filename, &h, &k) != EOF){
        if((fptr=fopen(filename,"r")) == NULL){
```

```c
            printf("Can't open file %s\n", filename);
            exit();
        }
        printf("\nreading file %s\n", filename);
        printf("h=%.4f\tk=%.4f\n", h, k );
        count1=0;
        while(fscanf(fptr,"%d %d", &energy[count1], &intensity[count1]) != EOF){
            if(count1>0)
                if(energy[count1] - energy[count1-1] != INCREMENT) {
                    printf("energy=%d is missing from file %s\n", (energy[count1-1] +
                                                    INCREMENT), filename);
                    printf("Hit any key to continue or 'q' to quit\n");
                    if((selection = getch()) == 113 )    /* if 'q' is hit exit program */
                        exit();
                }
            count1+=1;
        }
        fclose(fptr);
        printf("writing to %s\n", masterfile);
        fptr=fopen(masterfile,"a");
        fprintf(fptr,"%8.3f%8.3f\n",h,k);
        printf("h=%8.3fk=%8.3f\n",h,k);
        fprintf(fptr,"%3d%13.4e\n",count1,factor);
        for(i=0;i<count1;i++){
            fenergy = energy[i];
            fintensity = intensity[i];
            fprintf(fptr,"%10.1f%10.1f\n", fenergy, fintensity);
        }
        fclose(fptr);

    }
    fclose(fptr2);
}
```

IV Curve Averaging Progam

```c
/* ivave.c */
/* this program uses an input file which contains a list of files       */
/* which corresponds to each individual beam which is to be averaged    */
/* last modified 2/18/92                 AUTHOR: David Jentz     */

#include <stdio.h>
#include <math.h>
#include <process.h>
```

218

```c
#define INCREMENT 2

char  base[5], filename1[15], filename2[15], filename3[15], filename4[15];
int   beamcount, beamnum, Energy_points, i, j, l, Iavemin, minerg;
int   maxerg, maxcount;
int   count[200], energy[200], Isum[200], Iave[200], offset;
int   erg[10][200], intensity[10][200];
float h, k, r;
FILE  *fptr1, *fptr2, *fptr3, *fptr4;

main(){
  printf("Enter name of beam list file (include extension): ");
  scanf("%s", filename1);
  printf("Enter value to offset intensities (enter 0 if no offset is desired): ");
  scanf("%d", &offset);
  printf("Enter base of output file: ");
  scanf("%s", base);
  fptr1 = fopen( filename1, "r");
  i+=0;
  minerg=1000;
/* READ INDIVIDUAL BEAMS TO BE AVERAGED */
  while( fscanf (fptr1, "%s %f %f", filename2, &h, &k) != EOF ){
    if((fptr2= fopen(filename2,"r")) != NULL ){
        r= (float)((double)pow(h,2) + (double)pow(k,2));
        printf("filename is %s (%f %f) r=%f\n", filename2, h, k, r);
        j=0;
        while(fscanf(fptr2,"%d %d", &erg[i][j], &intensity[i][j]) != EOF ){
/* check if there are any missing energies */
          if(j>0){
            if((erg[i][j] - erg[i][j-1]) != INCREMENT)
                printf("energy= %d is missing from data file %s\n", (erg[i][j-1] +
                                                INCREMENT), filename2);

          }
          printf("energy= %d\tintensity= %d\n", erg[i][j], intensity[i][j]);
          j+=1;
        }
        printf("%d intensities in data file %s\n", j, filename2);
        if(minerg>erg[i][0])
            minerg=erg[i][0];
        if(maxcount< j)
            maxcount=j;
    }
    else
        printf("Can't open file %s\n", filename2);
```

219

```c
        fclose(fptr2);
        i+=1;
      }
    fclose(fptr1);  /* close beam list file */
    beamnum=i;
/* check if there are at least 2 beams to average and if not exit program */
    if(beamnum<2){
      printf("Not enough beams to analyze\n");
      exit();
    }
    maxerg= minerg + (maxcount-1)*INCREMENT;
    printf("minimum energy = %d\tmaximum energy = %d\n", minerg, maxerg);
    if(h<0)
        h=0-h;
    if(k<0)
        k=0-k;
    h*=4;
    k*=4;
/* AVERAGE BEAMS */
/* initialize counters */
    for(i=0;i<beamnum;i++)
        count[i]=0;
    printf("number of beams is %d\n", beamnum);
    Energy_points= 1+(float)(maxerg-minerg)/(float)INCREMENT;
    printf("number of energy points is %d\n", Energy_points);
    Iavemin=0;                        /*initialize minimum intensity value */
/* loop over energies */
    for(l=0;l<Energy_points;l++){
      Isum[l]=0;                      /* initialize sum of intensities */
      energy[l]=minerg + l*INCREMENT;
/* loop over beams */
        beamcount=0;
        for(i=0;i<beamnum;i++){
          j=count[i];
          if(erg[i][j] == energy[l]){
              Isum[l]+=intensity[i][j];
              count[i]+=1;
              beamcount+=1;
          }
        }
        Iave[l]=(float)Isum[l]/(float)(beamcount);
        if(Iave[l]<Iavemin)
          Iavemin=Iave[l];
    }
    printf("Iavemin= %d\n", Iavemin);
```

220

```c
/* WRITE BEAM ENERGIES AND AVERAGED INTENSITIES TO OUTPUT FILE*/
    sprintf(filename3,"a%s%x%x.dat", base, (int)h, (int)k);
    printf("filename is %s\n", filename3);
    fptr3=fopen(filename3,"w");
    sprintf(filename4,"z%s%x%x.dat", base, (int)h, (int)k);
    printf("filename is %s\n", filename4);
    fptr4=fopen(filename4,"w");
    for(l=0;l<Energy_points;l++){
        if(Iavemin<0){    /* offset negative intensities */
            Iave[l]-=Iavemin;
            fprintf(fptr3,"%d %d\n", energy[l], (Iave[l]+=offset));
            fprintf(fptr4,"%d %d\n", energy[l], (Iave[l]-=offset));
        }
        else{                /* don't offset intensities */
            fprintf(fptr3,"%d %d\n", energy[l], (Iave[l]+=offset));
            fprintf(fptr4,"%d %d\n", energy[l], Iave[l]-=offset);
        }
    }
    fclose(fptr4);
    fclose(fptr3);
}
```